Spring 2021

Physical Modeling of Backward Erosion Piping Phenomenon in a Geotechnical Centrifuge

William Fernando Ovalle Villamil

PHYSICAL MODELING OF BACKWARD EROSION PIPING PHENOMENON IN A GEOTECHNICAL CENTRIFUGE

by

William Fernando Ovalle Villamil

Bachelor of Science
Universidad de Los Andes, Colombia, 2012

Master of Science
Universidad de Los Andes, Colombia, 2014

Submitted in Partial Fulfillment of the Requirements

For the Degree of Doctor of Philosophy in

Civil Engineering

College of Engineering and Computing

University of South Carolina

2020

Accepted by:

Inthuorn Sasanakul, Major Professor

Sarah Gassman, Committee Member

Charles Pierce, Committee Member

Alicia Wilson, Committee Member

Cheryl L. Addy, Vice Provost and Dean of the Graduate School

DEDICATION

To my parents Marco and Mary Luz, and my siblings Andrés, Juan, José and Camila. Without you, this would have been impossible. Thanks for your unconditional support.

ACKNOWLEDGEMENTS

I would like to sincerely thank Dr. Inthuorn Sasanakul for her advisement and support during the development of this investigation. Her contribution to this project and to my development as a researcher is invaluable. I would also like to thank Dr. Sarah Gassman, Dr. Charles Pierce and Dr. Alicia Wilson for participating as committee members in the evaluation of this dissertation, and for their contributions to improve this work. I am deeply grateful for your time and participation.

I wish to thank Emad Gheibi, Ryan Starcher, Muwafaq Awad, Pitak Ruttithivaphanich and Siwadol Dejphumee for their support during different moments of my doctoral studies. Likewise, I would like to acknowledge the contributions in different technical aspects from Russel Inglett and Dr. John Dickerson.

I would also want to acknowledge the unconditional support in moments of great need from Hunter Stalker, Yohanna Mejía, Érika Rengifo, Melek Yildiz, Juan Cruz, Luisa Malagón, Vafa Soltagharaei, Albert Ortiz, Tayrín Hurtado, William Vélez, Ana Gallego, Mábel and Tyler Davis, Jean Franco, Gabriel Pérez, Nathalie López, Hugo Velandia, Dr. Juan Caicedo and the group of Colombianos en Columbia.

Finally, I would like to thank my beloved family, whose support and love was key to this accomplishment. I will always be thankful.

ABSTRACT

Backward erosion piping is a mechanism of internal erosion that has been widely recognized as a potential hazard for water-retaining structures, such as dams and levees, that are founded on granular materials. Backward erosion piping initiates toward the downstream zone of the structure by the concentration of flow at an exit point acting as drainage, which leads to a localized loosening of the soil and eventually to a continuous migration of grains from the foundation following a piping path pattern. Such piping path extends backward toward the impoundment once a certain critical hydraulic condition is met, resulting in the loss of stability of the structure and leading to failure.

Despite the numerous studies aimed to provide new insights into backward erosion piping prediction, detection and remediation, there is still a need to develop experimentally validated methodologies that allow linking results from physical and analytical models to field behavior. This is due to, among others, the difficulty to replicate the field behavior in small-scale models and the limited understanding of parameters that are interrelated and affect the evolution of the phenomenon.

The geotechnical centrifuge modeling technique has the potential to model complex geotechnical mechanisms and stress conditions that occur in large-scale prototypes (i.e., field conditions) using models with reduced scale, which saves cost and time in model construction. This is done by imposing a simulated gravitational acceleration field to the model that is higher than the Earth's gravity applied to the

prototype. However, the use of centrifuge modeling to study backward erosion piping is limited due to the complexity of the phenomenon and the limited understanding of the effects of the increased gravitational acceleration field on parameters, such as head and pressure losses, flow regime and critical hydraulic conditions. A few research studies have attempted to assess backward erosion piping in the geotechnical centrifuge, but the associated scaling effects are still insufficiently explored or validated.

The goal of this study is to advance the understanding of the backward erosion piping phenomenon by implementing the geotechnical centrifuge modeling technique. A series of centrifuge modeling experiments were performed to model the different mechanisms involved during the development of backward erosion piping. The scaling effects derived from the implementation of this technique are evaluated to allow the interpretation, conformation and validation of existing theoretical scaling laws. Results from this study provide new insights into the impact of exit drainage and seepage length on the global and local hydraulic conditions developed during different phases of the phenomenon. Critical hydraulic conditions were obtained and compared with data available in the literature. Overall, this study provides a new experimental protocol and analysis procedure for conducting centrifuge modeling studies of backward erosion piping. This study is a first step towards the full understanding of the complex field conditions.

TABLE OF CONTENTS

LIST OF TABLES

LIST OF FIGURES

LIST OF SYMBOLS

A, B Forchheimer coefficients (alternatively a and b).

B_p Buoyant force acting in a grain.

B_t Buoyant force acting in a soil volume.

C_B Empirical constant in the Line of Creep method.

C_L Empirical constant in the Weighted Creep method.

C_u, C_g Gradation coefficients from a grain-size distribution.

d_{50} Mean diameter of a soil volume.

d_c, D Diameter of an exit-hole.

d_{eff} Effective diameter of a soil volume.

e Void ratio in a soil volume.

f Darcy's friction factor.

F_d Seepage drag force acting on a grain.

Ff Friction factor in a porous medium based on Muskat (1938) and Stephenson (1979).

F_G Geometrical shape factor in Sellmeijer's Rule method.

Fo Forchheimer number.

Fo_{critic} Critical Forchheimer number to exceed the laminar flow domain.

F_p Resultant force in a grain due to intergranular contacts.

f_{pore} Friction factor in a porous medium.

F_R Resistance factor in Sellmeijer's Rule method.

F_S Scale factor in Sellmeijer's Rule method.

F_s Seepage force due to differential pressure acting on a grain.

F_t Resultant force due to lateral friction acting in a soil volume.

g_{Earth} Earth's gravitational acceleration.

g_{model} Simulated gravitational acceleration in a centrifuge model.

G_s Specific gravity.

h_i Hydraulic head in location i.

h_{up} Hydraulic head in an upstream reservoir.

Δh Head loss due to flow between two reference points spaced a distance L.

i Hydraulic gradient between two reference points spaced a distance L (i.e., $i = \Delta h/L$).

$i_{5\ cm}$ Local hydraulic gradient across a segment of 5 cm upstream an exit-hole.

i_{cr} Critical hydraulic gradient indicating the onset of a critical condition.

i_{cr-FVM} Critical hydraulic gradient to induce the first visible movement.

i_{cr-TH} Critical hydraulic gradient to induce the total heave.

i_{cr-exp} Centrifuge experimental scaling factor for critical hydraulic gradient.

i_{Global} Global hydraulic gradient between two reservoirs.

i_{j-k} Hydraulic gradient between two reference j and k.

i_L Local hydraulic gradient between an upstream reservoir and an exit-hole.

i_{sat} Hydraulic gradient used for saturation.

k Darcy's permeability constant.

K Kozeny-Carman constant.

K' Constant representing the porous shape within a soil volume.

K_0 Coefficient of lateral earth pressure at rest.

L Linear distance in a centrifuge model or prototype.

n Porosity of soil volume.

N Increment of gravitational acceleration with reference to Earth's gravity (i.e., $N = g_{model}/g_{Earth}$).

ΔP Pressure loss due to flow between two reference points spaced a distance L.

$\overline{(\Delta P)}$ Normalized pressure loss.

ΔP_{amb} Pressure loss in ambient flow conditions.

ΔP_H Pressure loss across an exit-hole.

ΔP_p Differential pressure across a grain.

$\overline{(\Delta P)}_{FVM}$ Normalized pressure loss at the first visible movement.

$\overline{(\Delta P)}_{TH}$ Normalized pressure loss at the total heave.

$\Delta P/\Delta L$ Pressure gradient due to flow between two reference points spaced a distance L.

$^{\Delta P}/_{\Delta L_{cr}}$ Critical pressure gradient.

R_{critic} Critical Reynolds Number indicating the limit of validity of Darcy's law.

Rn Reynolds Number in a porous medium based on Muskat (1938) and Stephenson (1979).

R_{pore} Reynolds Number in a porous medium.

S_b Specific surface area per unit volume of particles in contact with fluid in a soil volume.

S_p Total seepage force acting in a grain.

S_t Total seepage force acting in soil volume.

T Time variable in a centrifuge model or prototype.

v Velocity of flow.

v_{critic} Critical velocity of flow indicating the transition to a nonlaminar flow domain.

W' Submerged weight of grains.

W_p Weight of a grain.

W_t Weight of solid fraction in soil volume.

X_m Magnitude of a variable X in a centrifuge model.

X_p Magnitude of a variable X in a prototype (i.e., 1g condition).

$\boldsymbol{X}$ Centrifuge scaling law of a variable X (i.e., $\boldsymbol{X} = X_m/X_p$).

γ_w Unit weight of water.

μ Dynamic viscosity of a fluid.

ρ Density of the soil.

ρ_w Density of water.

σ'_m Mean effective stress.

σ_v Total vertical stress.

σ'_v Effective vertical stress.

τ Tortuosity constant in a soil volume.

τ_c Critical seepage viscous shear stress that induces grain movement.

ϕ' Drained friction angle of the soil.

CHAPTER 1

INTRODUCTION

Water-retaining structures are one of the most important civil engineered structures because of their direct benefits to society. These structures are used for energy generation, irrigation, water supply/management, flood control, control of watersheds and recreation. Consequently, they play an important role in the organization, economy, safety and development of modern society (Biswas and Tortajada 2001; Di Baldassarre et al. 2013). The exploitation of rivers and other water bodies using water-retaining structures is essential to improve the living conditions of human beings, and fewer human settlements would be supported by rivers in absence of these structures (Altinbilek 2002). For instance, one-fifth of the world power generation is contributed by dams and this is the main energy source in over 55 countries (Yöskel 2009). Only the United States registers more than 90,000 dams (USACE 2016), with more than 85% made of earthen materials, and a total of 47,349 levees are used for flood protection in a length of nearly 29,900 miles of major rivers and water bodies (USACE 2018).

Despite the importance of water-retaining structures to human life and the modern techniques used for their design, construction, maintenance and operation, several hazards continue to affect these structures, especially those made of earthen materials. Extreme natural events, structural defects or animal activity, are some examples of potential triggers of breach in earthen dams and levees that may result in catastrophic consequences. This was experience in New Orleans in 2005 with the failure of the levees

on the 17th Street Canal during hurricane Katrina (Ubilla et al. 2008; Sasanakul et al. 2008) and in the state of South Carolina where 51 regulated earth dams breached due to a major flooding in the central and coastal areas in 2015 (Sasanakul et al. 2017).

Studies of case histories of embankments and dikes with noticeable damage or structural failure in the United States, the Netherlands and other countries indicated that the most frequent failure mechanisms involve some form of erosion due to flow of water (Foster et al. 2000; Danka and Zhang 2015). One of the most recurrent failure mechanisms is internal erosion observed in nearly 46% of the cases, in which the mechanism known as backward erosion piping is frequent. This mechanism initiates towards the downstream toe of the structure with the concentration of flow in an exit point causing a localized loosening of the foundation soil (Bonelli 2013). If a certain critical hydraulic condition is achieved, migration of soil grains from the foundation begins, leading to the formation of micropipes that increase in length from the exit point and toward the impoundment. Eventually, the flow across the foundation concentrates in the micropipes and the erosion rate of grains increases, causing a condition of instability and the hydraulic failure of the foundation. Such failure condition corresponds to the scenario where the water-retaining structure is uncapable of maintaining the impoundment water level.

The impact of backward erosion piping in the safety of earthen structures is widely recognized. Hence, the design and construction of geotechnical structures often include the analysis of safety against the mechanism of backward erosion piping (Technical Advisory Committee 1999; USACE 2000; USDIBR 2014; Van Beek 2015). Nonetheless, the evaluation and remediation of this phenomenon based on field

observations are challenging as this phenomenon is difficult to be detected before the failure and any post-failure information that may allow studying the mechanism is usually washed away shortly after the breach (Costa and di Prisco 1999; Richards and Reddy 2007). To overcome this challenge, extensive research studies have been developed using analytical and experimental approaches to model backward erosion piping as an alternative to field studies. However, despite the valuable insights obtained in recent years, there is still a misconnection between the analytical and numerical works and the results from physical models (Sellmeijer et al. 2011; van Beek et al. 2012; Van Beek 2015), in addition to the lack of experimentally validated theories suitable to extrapolate laboratory testing to field behavior (Schmertmann 2002).

Since the late 1990s, the geotechnical centrifuge modeling technique has been remarkably useful to overcome the limitations to develop physical models of complex geotechnical structures and phenomena resembling a stress state closer to that existing in-situ (e.g. Lin et al. 1994; Nichols and Goodings 2000; Suah and Goodings 2001; Goodings and Abdullah 2002; Han and Goodings 2006; Taylor 2018). However, the remarkable potential of this technique has not been successfully used to study erosion mechanisms, such as backward erosion piping, due to several factors, but the most important is the limited experience that hinders the adequate interpretation of results from centrifuge models.

This dissertation focuses on the use of the geotechnical centrifuge modeling technique as an innovative alternative to develop experimental studies of backward erosion piping. This chapter presents and describes the background and motivation to

develop this research, followed by the objectives proposed and the contribution to the field of civil engineering.

1.1 INVESTIGATION OF BACKWARD EROSION PIPING

Figure 1.1 shows a concept map summarizing the state of the art of the investigation of backward erosion piping using field observations, analytical and numerical methodologies, and physical modeling techniques. Regardless of the methodology, the research studies have mainly focused on the determination of the hydraulic conditions that lead to failure by backward erosion piping, usually using estimations of the critical hydraulic head and the critical hydraulic gradient. Other aspects that are often studied are the effects of different parameters that may affect the initiation and development of the phenomenon, such as soil properties or the geometry and configuration of the structure.

Given the challenge of developing detailed studies in the field, field works are limited and have focused mainly on the statistical assessments of documented case histories to estimate the frequency of occurrence of the different erosion-driven failure mechanisms (e.g., Foster et al. 2000; Danka and Zhang 2015), and occasionally to characterize the phenomenon (Van Beek et al. 2011). On the other hand, analytical studies of this phenomenon date to the beginning of the 20th century to assess the piping potential in foundations of concrete and masonry structures (e.g., Bligh 1910; Lane 1935). More detailed analytical studies using extensive experimental data were developed towards the end of the 20th century allowing less conservative and more accurate estimations of both local and global critical hydraulic gradients (e.g., Sellmeijer 1988; Schmertmann 2000). More analytical and numerical studies were developed after the

beginning of the 21st century taking advantage of the improvement of computational capabilities and the availability of more experimental data (e.g., Ojha et al. 2001, 2003; Wan and Fell 2004a, 2004b; Fell and Wan 2005; Sellmeijer et al. 2011;). Such studies included new parametric assessments, such as the elapsed time during the development of backward erosion piping, but the main scope remained on developing methodologies to estimate critical hydraulic gradients.

The first experimental works were developed towards the end of 20th century using small-scale physical models of dikes (de Wit et al. 1981, 1984), allowing the observation of the different phases comprising backward erosion piping and providing new insights of the effects of soil properties, geometry and configuration of the structure, and a first glance of the limitations due to modeling at a reduced scale. After the beginning of the 21st century, experimental research has been conducted using different configurations and sizes of models, mainly for parametric assessments, and discretizing specific phases during the development of backward erosion piping (e.g., Reddi et al. 2000; Ghiassian and Ghareh 2008; Bendahmane et al. 2008; Fleshman and Rice 2013, 2014; Yang and Wang 2017; van Beek et al. 2008, 2010, 2011). Despite the valuable insights obtained, the interpretation of experimental results remains unclear due to the challenge of understanding the scale effects in physical models, the effects of heterogeneity of the soil from micro- to macro-scales, and the uncertainty associated to soil properties, such as grain size and grain shape (Bonelli 2013). Furthermore, direct comparison with results from analytical models is difficult due to, among others, the use of fixed geometries in analytical models (Sellmeijer et al. 2011; van Beek et al. 2012).

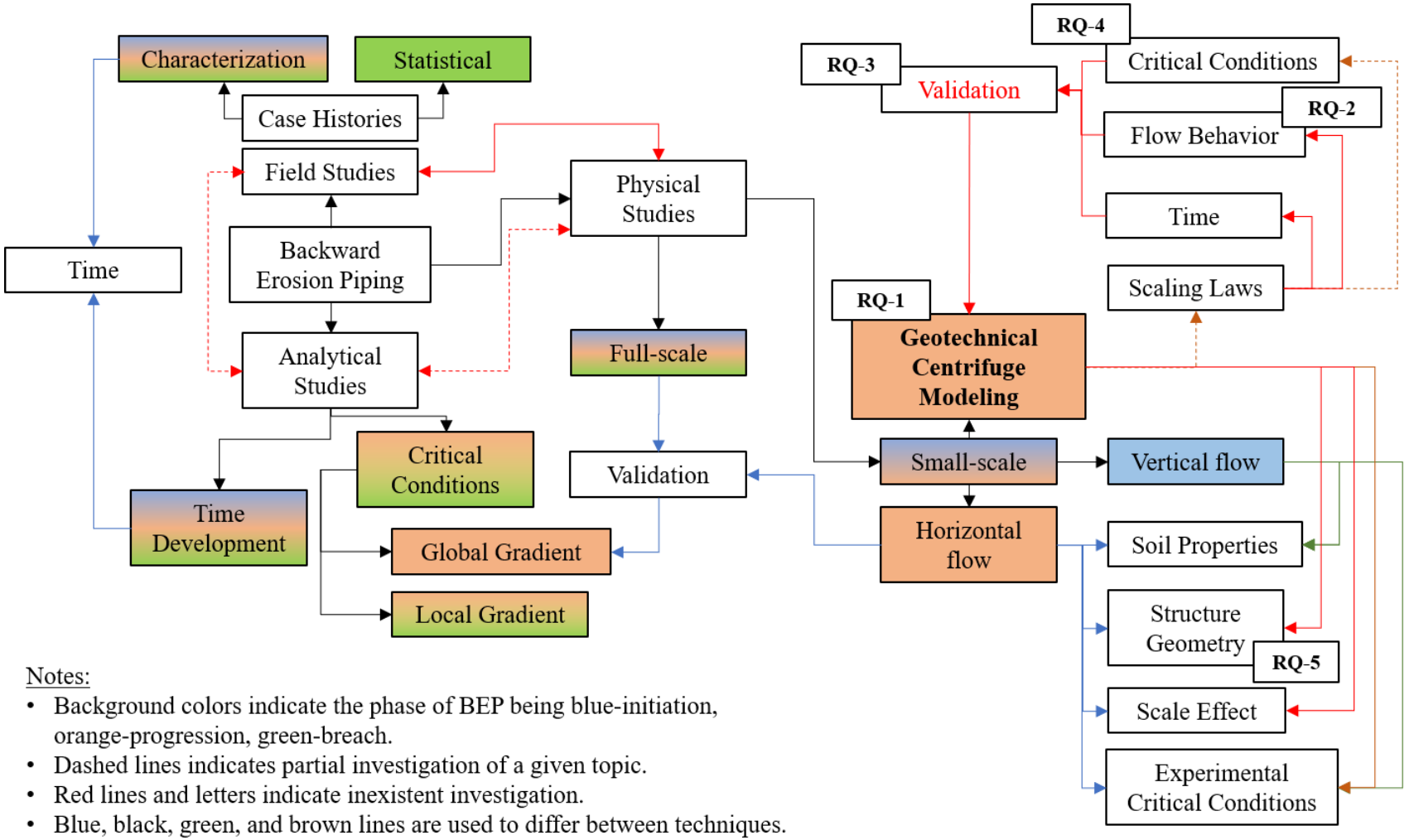

Figure 1. 1 Summary of research on backward erosion piping.

Full-scale physical models have also been used to investigate backward erosion piping and to improve and validate analytical methodologies using the advantage of analyzing the phenomenon under field conditions (van Beek et al. 2010, 2011; Sellmeijer et al. 2011). Although full-scale models reduce the scale effects to the minimum and possibly mitigates the uncertainty from other sources typical of small-scale models, such as soil properties or configuration of the structure, the cost and time required are usually unfeasible.

A useful technique to improve the current experimental framework for studying backward erosion piping is the geotechnical centrifuge modeling. This technique has been extensively used as an alternative to full-scale physical models to analyze complex behaviors of geotechnical structures (e.g., Gajan et al. 2005; Murillo et al. 2009; Lanzano et al. 2012; Stewart et al. 2015). Through this technique, a small-scaled model inside a centrifuge is subjected to an increased gravitational acceleration field greater than Earth's gravity, allowing simulating field-like environments always that adequate similarity conditions are satisfied (Taylor 2018). This advantage constitutes an important opportunity to improve the understandings of scaling effects in physical models of backward erosion piping, as well as to develop new experimental protocols to address other challenges for modeling this phenomenon. Notwithstanding, centrifuge modeling has only been effectively used in limited occasions for the investigation of backward erosion piping (van Beek et al. 2010; Leavell et al. 2014; Koito et al. 2016) and other mechanisms of internal erosion (e.g., Marot et al. 2016). A detailed assessment of the implications of modeling erosion mechanisms under increased gravitational acceleration fields only exist using analytical approaches and without any experimental validation

(e.g., Goodings 1982, 1984, 1985; Dong et al. 2001; Bezuijen and Steedman 2010). The lack of experience in centrifuge modeling have hindered the interpretation of existing centrifuge results and have led to questioning the potential of this technique for successfully modeling backward erosion piping or any other geotechnical phenomena involving erosion.

The main goal of this study is to develop a systematic assessment of the physical modeling of backward erosion piping using the geotechnical centrifuge modeling technique. The study considers the different phases comprising the phenomenon and explores the main challenges and limitations associated to centrifuge modeling of backward erosion piping. The scaling effects consequence of modeling under increased gravitational acceleration fields are evaluated using new and extensive sets of experimental results that are compared with analytical assessments and existing results from experimental studies obtained using alternative modeling techniques. The study focuses on the determination of the global and local critical hydraulic conditions leading to failure by this phenomenon and the assessment of the behaviors observed.

1.2 RESEARCH OUTLINE

1.2.1 PROBLEM STATEMENT

The geotechnical centrifuge modeling technique is widely recognized to be a powerful tool for developing both non-parametric (i.e., studies considering the entire geotechnical structure, such as physical models of levees or foundations) and parametric studies (i.e., studies focused on specific variables, such as the time for wave propagation in dynamic analysis or the time for diffusion in consolidation processes). However, the feasibility of using this technique for physical modeling of erosion mechanisms, such as

backward erosion piping, has been questioned due to the numerous potential scaling conflicts that have been identified through theoretical analysis. These theoretical scaling conflicts mainly derive from the difficulty to satisfy similarity of time-related variables, such as velocity of flow or erosion rate, among the different events that are considered occurring simultaneously during backward erosion piping, such as laminar and turbulent seepage flow and grain transport. However, the practical implications of using centrifuge modeling to model backward erosion piping are unknown due to the lack of extensive and detailed experimental evidence that validate or disprove the existing theoretical considerations. Hence, the actual feasibility of using this approach is still unknown. Furthermore, the limitations identified for centrifuge modeling of this phenomenon are also applicable to the experimental methodologies used in the literature.

1.2.2 Research Questions

Based on the problem statement described, the following main research question is proposed for this dissertation:

- RQ – 1: What are the practical implications of developing experimental models of backward erosion piping using the geotechnical centrifuge modeling technique?

The following additional research questions are also derived:

- RQ – 2: What are the seepage flow conditions and behaviors reproduced in physical models under increased gravitational acceleration fields?
- RQ – 3: How is the mechanism of backward erosion piping reproduced in centrifuge models?

- RQ – 4: What is the effect of the centrifuge gravitational acceleration field on the critical hydraulic gradients for backward erosion piping?
- RQ – 5: What are the potential centrifuge scaling effects on the development of backward erosion piping using geotechnical centrifuge?

1.2.3 Research Objectives

Based on the problem statement and the research questions, the following objectives are proposed for this study:

I. Evaluate the effects of centrifuge gravitational acceleration in the characteristics of flow through granular materials represented by the relationship between the hydraulic gradient and the velocity of flow.

II. Evaluate the development of the backward erosion piping mechanism in small-scale models under different levels of gravitation acceleration.

III. Evaluate the scaling behavior of main flow parameters during the development of backward erosion piping in centrifuge models.

IV. Evaluate the potential scaling conflicts associated to physical modeling of backward erosion piping using the geotechnical centrifuge.

V. Develop an interpretation protocol for physical models of backward erosion piping using the geotechnical centrifuge modeling technique.

1.2.4 Research Methodology and Research Topics

The methodology used in this dissertation is mainly experimental and the experiments were reproduced inside the geotechnical centrifuge facilities of the University of South Carolina. In some occasions, experimental results are compared to results from analytical methods available in the literature and to results from simple

numerical models developed using the computational tool SEEP/W. Specific details of the methodologies used are presented later in this document. Likewise, detailed descriptions of the literature are provided in the next chapter.

To address the research questions and objectives proposed, this dissertation is divided into four main sections or research topics as described next:

1.2.4.1 Research Topic I: Evaluation of Flow Characteristics through Cohesionless Materials in Centrifuge Environments

In geotechnical and geological engineering, groundwater flow or flow through earth structures is analyzed using Darcy's Law, assuming a permanent viscous or laminar condition in which the velocity of flow is linearly proportional to the hydraulic gradient. This assumption is valid when the velocities of flow experienced in these structures are relatively low. However, the flow behavior may exhibit nonlinearities in some field conditions, including breakwater structures and rapid flooding (e.g., Gelhar et al. 1992; Nielsen 1992; Kreibich et al. 2009), or in laboratory conditions, such as geotechnical centrifuge modeling (Khalifa et al. 2002).

In the case of centrifuge modeling, a small-scale model is subjected to a gravitational acceleration field of N times Earth's gravity. If the same soil and fluid in the full-scale prototype are used in the model, the velocity of flow in the model will increase N times higher than the velocity of flow in the prototype (Laut 1975; Garnier et al. 2007). As a result, the velocity of flow may exceed the limit for laminar flow and the flow behavior in the model may diverge from the one expected in geotechnical structures. Therefore, the limit of validity for the laminar flow and the flow behavior in centrifuge environments have an important impact on the implementation and interpretation of

physical models of backward erosion piping. Such limit of validity of Darcy's law and the laminar flow regime is usually estimated based on Forchheimer's Law and the concept of critical Reynolds number, R_{critic}, but its interpretation remains ambiguous, not only for geotechnical centrifuge modeling, but for any physical model involving flow.

The first stage of this study focused on investigating the effects of changes in the gravitational acceleration field on the behavior of flow through fine-grained sands that are typically used for geotechnical centrifuge modeling studies. This stage also established a connection between the different theoretical approaches available in the literature that have a valid application for centrifuge modeling. This was done by performing a series of centrifuge permeability tests at different levels of gravitational acceleration and using different granular materials. The effects of the characteristics of the porous media and centrifuge acceleration on the flow behavior were evaluated. The results show that the parameters relevant to Forchheimer's Law remained constant regardless of the centrifuge acceleration. The values of R_{critic} were obtained in a range from 0.2 to 11 and varied depending on the characteristics of material. The limit of validity of Darcy's Law occurred for lower velocities of flow in fine-grained materials, but it remained constant regardless of the gravitational acceleration field.

1.2.4.2 Research Topic II: Assessment of Centrifuge Models of the Initiation of Backward Erosion Piping due to Upward Flow

It is typical to develop physical models of backward erosion piping resembling the entire foundation of a structure. This type of model addresses the critical hydraulic condition to extend a pipe through the total seepage length until the failure occurs. However, backward erosion piping is recognized to develop in different phases and the

initiation phase occurs at a noticeably smaller scale for which the grain-to-grain behavior becomes important. The assessment of this phase is difficult while using models of the entire foundation mainly because of the challenge of estimating hydraulic gradients near the exit points (Fleshman and Rice 2013, 2014).

To evaluate the behavior associated only to the initiation phase of backward erosion piping, some research studies assessed the hydraulic behavior expected to occur during this phase by using one-dimensional experiments, usually inducing an upward flow condition through a column of sands (Fleshman and Rice 2013, 2014; Yang and Wand 2017; Peng and Rice 2020). The critical hydraulic conditions determined from these studies are presented as the true critical conditions for backward erosion piping and are fundamental for understanding this phenomenon. Previous experimental studies evaluated different aspects of the phenomenon, including the effect of grain-size distribution and particle shape (e.g., Fleshman and Rice 2014; Yang and Wang 2017). However, this type of analysis has not been performed using the geotechnical centrifuge modeling technique and consequently the effect of gravitational acceleration is unknown. Therefore, relevant parameters for physical modeling of backward erosion piping, such as localized hydraulic gradients triggering the phenomenon or the seepage stresses acting on the grains, both under increased gravitational acceleration fields, are still required.

The second stage of this study addressed the internal erosion induced by upward flow that typically occurs during the initiation phase of backward erosion piping. This stage of the study focused on the assessment of the centrifuge scaling behavior of models under different gravitational acceleration fields. A series of centrifuge tests were performed by maintaining the same model dimensions, soil and fluid properties and at

centrifuge gravity ranging from 1g to 30g. The results from these tests were also compared with results under Earth's gravity or 1g. Two critical hydraulic gradients associated with the first visible movement of sand particles and the total heave were obtained. The critical hydraulic gradients obtained for the first visible movement of grains agreed with a theoretical scaling law derived for this phase of the phenomenon. However, this theoretical scaling was not applicable to the total heave due to the expansion of the models. Regardless, the critical gradients for first visible movement and total heave were 0.56–0.99 and 1.16–2.44, respectively, and these results agreed with numerical and experimental values available in the literature. The seepage induced stresses at the granular level were estimated and it was found that 16% of the critical total seepage stress was contributed by the viscous shear stress, while the remaining 84% was contributed by differential pressure across the grain.

1.2.4.3 Research Topic III: Assessment of the General Behavior Occurred in Centrifuge Models of Backward Erosion Piping

Previous centrifuge modeling studies of backward erosion piping are available in the literature but are limited (e.g., van Beek et al. 2010; Leavell et al. 2014; Koito et al. 2016). Some of these studies present a useful assessment of specific parameters, such as the estimation of critical hydraulic gradients, but generally without addressing relevant aspects, such as the implications of modeling this phenomenon under an increased gravitational acceleration field. As a result, detailed analyses of backward erosion piping are very limited and experimental validation of theoretical assessments of centrifuge scaling laws related to this phenomenon, which are available in the literature, has not

been performed (Goodings 1982, 1984, 1985; Dong et al. 2001; Bezuijen and Steedman 2010).

The third stage of this study addressed the characteristics observed in centrifuge models of backward erosion piping and provided a detailed analysis of the behavior observed at different phases of erosion based on in-flight video recordings and post-test observations, along with local and global pressure loss measurements. This stage of the study presents the results from a series of centrifuge modeling tests using simplified small-scale models following the typical configurations used in the literature. The models were prepared with the same soil and the same model dimensions and were tested under different levels of centrifuge gravitational acceleration. The critical hydraulic conditions leading to failure by backward erosion piping were evaluated using global and local perspectives, and the results were used to partially assess the effects of the exit-hole size and the changes in the centrifuge gravitational acceleration.

The results showed that the overall mechanism that was modeled is similar to the mechanism described in previous small-scaled experimental studies. In addition, the results showed that the exit-hole size has minimal impact on the critical hydraulic gradient but affects the characteristics of the piping path and the amount of eroded material. The critical hydraulic gradient that initiated the erosion decreased slightly as the centrifuge gravitational acceleration increased. The values of the critical hydraulic gradient, which was studied locally and globally, ranged between 0.15 and 0.40 and fell within a range of estimates from typical analytical methods.

1.2.4.4 Research Topic IV: Evaluation of the Effects of Gravitational Acceleration, Exit-hole Size and Seepage Length in Centrifuge Models of Backward Erosion Piping

The fourth and final stage of this study, which expanded the scope of the third stage, aimed to provided new insights into the physical modeling of backward erosion piping by improving the understanding of the effects of parameters that are recognized to influence the development of this phenomenon in the field. This stage focused on three main variables: the seepage length, the size of the exit-hole and the magnitude of the gravitational acceleration field imposed in the models, relative to Earth's gravity, and the testing protocol was designed to evaluate the scaling behavior and the time of development of the phenomenon.

The analysis focused on the backward erosion piping that initiates at an exit-hole, resembling a crack in an impervious cover layer, and that progresses backwards to form micropipes across a foundation made of uniform, fine-grained sand. The results showed two typical behaviors in function of the seepage length, comprising a steady evolution with an identifiable progression of piping in models with shorter seepage length, and a rapid evolution with no identifiable progression in the remaining models. Despite the difference, the global hydraulic gradients were very similar and the change in value was rather caused by the size of the exit-hole. The gravitational acceleration field caused a decrease in the critical gradients, but the overall difference in value was 0.1 which is minimum compared with typical values from the literature. Overall, the behavior observed is acceptable compared to conventional physical models and the results from centrifuge models were close to full-scale estimations, which highlights the great potential of this technique to model erosion mechanisms.

1.3 CONTRIBUTION AND PRACTICAL IMPLICATION

The main contribution of this study is to provide a detailed systematic analysis of the backward erosion piping mechanism reproduced in centrifuge models, which was validated with results from other modeling techniques. The effects of centrifuge gravitation acceleration were assessed rigorously in this study and to an extent that was not considered in previous research studies.

The assessment of the global and local hydraulic conditions experienced during the backward erosion piping process can be used for the calibration of existing analytical and numerical models of this phenomenon, as well as for the development of new modeling techniques. In addition, the development of an experimental methodology to study backward erosion piping using the geotechnical centrifuge is fundamental for the design of physical models assessing mitigation options, as well as for studying other internal erosion mechanisms.

Together with the study of flow through porous media in centrifuge environments, this study provides a new opportunity for the application of centrifuge modeling for studies of transport phenomena in the fields of chemical and environmental engineering. Likewise, the outcomes of this study are in support of significant geotechnical engineering advances in design, assessment, and mitigation of dams, dikes, levees and other water retaining structures, to improve their resistance to storm surge and flooding events.

1.4 LIST OF PAPERS AND STRUCTURE OF DISSERATION

This dissertation presents results that have been already published or are currently under revision in peer-reviewed journals and international conferences. A total of four journal papers are presented in separate chapters of this dissertation, two of which were published and two are currently under revision. In addition, two papers were published as special publications from conference meetings, and one more is accepted for publication.

Peer-reviewed journals:

1. Ovalle-Villamil, W., and Sasanakul, I. (2018) "Investigation of Non-Darcy Flow for Fine Grained Materials." *Journal of Geotechnical and Geological Engineering*, https://doi.org/10.1007/s10706-018-0620-x, Jul. 2018.
2. Ovalle-Villamil, W., and Sasanakul, I. (2020) "Assessment of Centrifuge Modeling of Internal Erosion Induced by Upward Flow Conditions." *International Journal of Physical Modeling in Geotechnics*, 1 - 40.
3. Ovalle-Villamil, W., and Sasanakul, I. (2020) "Centrifuge Modeling Study of Backward Erosion Piping with Variable Exit." *Journal of Geotechnical and Geoenvironmental Engineering* (In Review).
4. Ovalle-Villamil, W., and Sasanakul, I. (2020) "Effects of Seepage Length on Centrifuge Models of Backward Erosion Piping with Variable Exit." (In Preparation).

Special publications from conference meetings:

1. Ovalle-Villamil, W., and Sasanakul, I. (2018) "A new insight into the behaviour of seepage flow in centrifuge modelling." Physical Modelling in Geotechnics, Volume 1: *Proc. of the 9th International Conference on Physical Modelling in Geotechnics (ICPMG 2018)*, London, United Kingdom, July 2018, pp.259.

2. Ovalle-Villamil, W., and Sasanakul, I. (2019) "Observation of Piping Erosion Initiation in a Centrifuge Model," *Geo-Congress 2019, 8th International Conference on Case Histories in Geotechnical Engineering*, Philadelphia, Pennsylvania, U.S., 2019.
3. Ovalle-Villamil, W., and Sasanakul, I. (2021) "Centrifuge Modeling of the Backward Erosion Piping Process," Accepted to: *10th International Conference on Scour and Erosion ICSE 10*, Arlington, Virginia, U.S., 2021.

The format of this dissertation follows a manuscript style. Chapter 1 shows an introductory outline of the motivation and methodology proposed for this investigation. Chapter 2 shows a summary of the background necessary to understand the mechanism of backward erosion piping and the state of the art of the research associated to this phenomenon. Chapters 3 to 6 present the investigation developed for each research topic proposed on the bases of the original research papers mentioned above. Chapter 7 presents the summary and conclusions derived from this investigation, along with recommendations for related future work. In addition, Appendices A to E present additional information related to the centrifuge device used in this investigation, sensing devices and test procedures followed.

CHAPTER 2

BACKGROUND AND LITERATURE REVIEW

The background and literature review relevant to this dissertation are presented in this chapter. The chapter is divided into five main sections. The first section includes an overview of the Geotechnical Centrifuge Facilities located at the University of South Carolina, which were used for the most part of this study. The second section presents the background and relevant theories of geotechnical centrifuge modeling oriented to physical modeling of flow and erosion mechanisms. The third section includes a detailed description of the mechanisms of backward erosion piping leading to failure of water-retaining structures due to internal seepage. The fourth section presents an overview of the theories describing the mechanics of flow through porous media applicable to geotechnical materials. The fifth and final section includes a summary of the most relevant research works reproduced for assessing backward erosion piping using both experimental and analytical approaches.

2.1 GEOTECHNICAL CENTRIFUGE FACILITIES

The Department of Civil and Environmental Engineering of the University of South Carolina received a significant improvement in 2011 that not only created new research opportunities for graduate students and faculties but provided a modern tool with high potential for education in different academic levels. Such improvement was the donation of a geotechnical centrifuge from the University of Maryland that now is part of the geotechnical research laboratory at UofSC. With this centrifuge, UofSC is now part

of a limited community of researchers capable of performing centrifuge modeling studies in geotechnical engineering.

The UofSC centrifuge was originally a Genisco 1230-1 device with a 1.30 m radius arm and symmetrical platforms rated at nearly 13.6 g-ton (30,000 g-lb). This small-sized centrifuge is specifically designed for small models with short preparation times, which makes this device ideal for parametric studies where models are built and tested quickly. This also allows multiple models to be constructed focusing on a broad range of parameters, making these facilities ideal for education and research, not only in geotechnical engineering, but with potential for application in different areas of civil engineering.

The centrifuge was originally built and used by NASA until 1982 when it was relocated to the University of Maryland. From 1982 to 2010, several geotechnical modeling research activities were conducted with this device, including, among others, the evaluation of the effects of backfill properties on the stability of geotextile-reinforced vertical walls (Suah and Goodings 2001), the effects of freezing over heave and consolidation of clays (Han and Goodings 2006), sinkhole development using sand and karst limestone (Goodings and Abdullah 2002), behavior of soils subjected to grout bulb injection at different depths (Nichols and Goodings 2000), and cratering and soil loosening due to explosive detonations modeled with pentaerythritol tetranitrate (Lin et al. 1994). The centrifuge was later relocated to the University of South Carolina in 2011 and has been actively upgraded and used since then.

A sketch of the geotechnical centrifuge at UofSC is shown in Figure 2. 1. The radius, r, from the central axis of the centrifuge to the basket floor is 1.3 m (51 inches).

The useful area of the baskets is 61-by-61 cm^2 (24-by-24 in^2) and they can accommodate models with up to 61 cm (24 inches) in height. The speed range capacity of this device is 0 to 400 RPM, which can be translated to a range of increment of gravitational acceleration by:

$$N = \frac{r}{9.81\ m/s^2}\left(2\pi\frac{RPM}{60}\right)^2 \qquad \text{Eq. 2. 1}$$

where N = increment of gravitational acceleration with reference to Earth's gravity (i.e., $N = g_{model}/g_{Earth}$); r = radius of rotation; and RPM = radial acceleration in revolutions per minute.

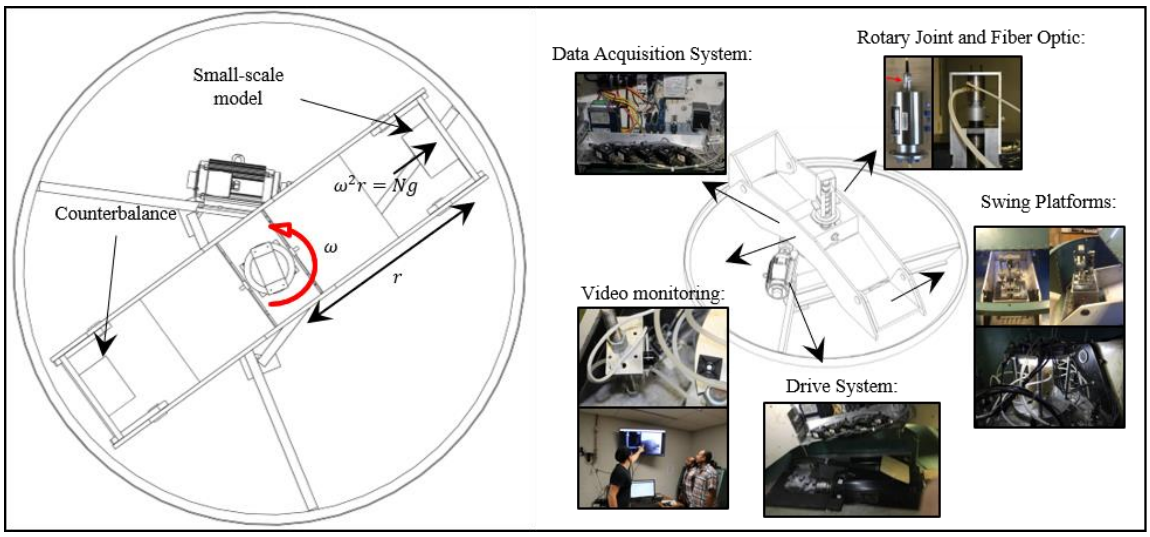

Figure 2. 1 Geotechnical centrifuge at the University of South Carolina.

The range of N that the centrifuge can operate is shown in Figure 2. 2a, as a function of RPM. It is observed that this centrifuge can perform experiments under values of N up to 230g, where g = 9.81 m/s^2. (i.e., Earth's gravity). The centrifuge capacity in terms of maximum acceleration multiplied by the maximum payload is 13.6 g-ton (30,000 g-lb) based on the manufacturer literature. Using the range of N aforementioned, the maximum payload can be estimated as shown in Figure 2. 2b. A maximum payload of

68 kg (150 lbs) is allowed at 200g, while 136 kg (300 lbs) is allowed at 100g. Further information and details regarding the components and operation of the geotechnical centrifuge at UofSC are included in Appendix A.

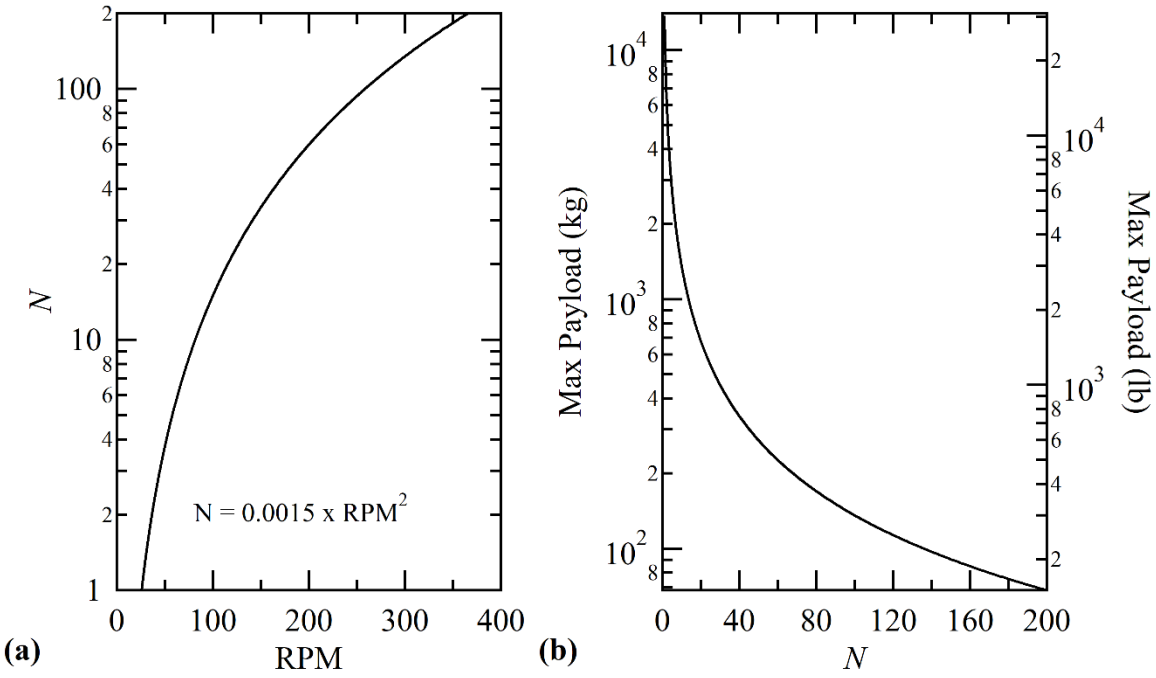

Figure 2. 2 (a) Induced gravitational acceleration by centrifuge radial acceleration and (b) maximum payload in centrifuge models.

2.2 GEOTECHNICAL CENTRIFUGE MODELING TECHNIQUE

2.2.1 SCALING LAWS FOR CENTRIFUGE MODELING

In physical modeling of geotechnical structures, the element tested is a small-scale model of a structure, or a section of it, which is usually refer to as the prototype. It is fundamental for a good modeling practice that the event reproduced in the small-scale model and that reproduced in the prototype are "similar". Similarity between the model and the prototype is represented by a series of appropriate scaling factors or scaling laws. For instance, the time factor, T_v, that is used to analyze the consolidation process in

cohesive soils, is a scaling factor that relates the consolidation process experienced in a controlled, laboratory experiment using a small portion of the soil (i.e., a small-scale model), with the consolidation expected to occur in the field (Taylor 2018).

The scaling factors or scaling laws in centrifuge modeling practice are defined for any variable X as the ratio between its magnitude in the centrifuge small-scale model, X_m, and that in the prototype, X_p, and are expressed as functions of the gravitational acceleration ratio, N. It is noted that N is a scaling factor that relates the gravitational acceleration field induced in the model with that acting on the prototype, which corresponds to Earth's gravity. In this study, the scaling laws and scaling factors are presented in bold fonts for clarity of the reader. Hence, a scaling law for any variable X is defined as $\boldsymbol{X} = X_m/X_p$.

A major limitation of using small-scale models in geotechnical engineering is the major challenge of replicating in-situ stress states at reduced scales. Therefore, the stresses that govern the mechanical behavior of soils in the field are hardly reproduced in small-scale models and similarity between model and prototype is difficult to achieve, as shown in Figures 2. 3a and 2. 3b. This limitation is generally overcome using full-scale models, but the cost and time required for their design, construction and testing represent additional challenges as they are not always feasible for research projects. The geotechnical centrifuge modeling technique provides an alternative solution by exposing a small-scale model to an inertial radial acceleration field that simulates an increased gravitational acceleration field N times stronger than Earth's gravity. As shown in Figure 2.3c, the self-weight of the model inside the centrifuge is increased to reach a stress state similar to that in the field (Kim et al. 2013). Hence, for the scenario presented in Figure

2. 3b, $\boldsymbol{a} = 1$ and $\boldsymbol{\sigma_v} = N^{-1}$; while for the scenario presented in Figure 2. 3c, $\boldsymbol{a} = N$ and $\boldsymbol{\sigma_v} = 1$.

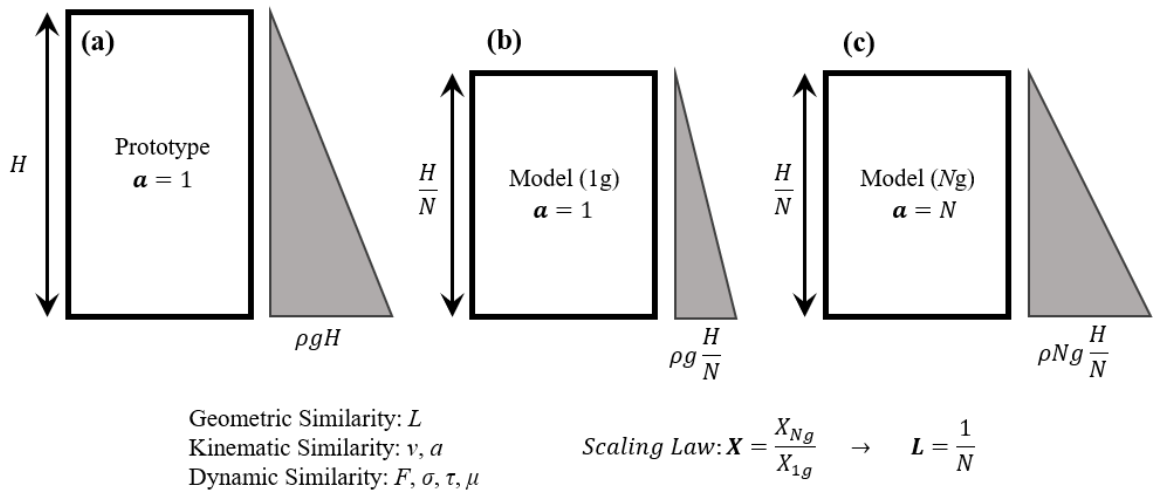

Figure 2. 3 Stress variation in reduced scale models: (a) prototype condition; (b) small-scale model at Earth's gravity; and (c) small-scale model under a centrifuge gravitational acceleration field of N times Earth's gravity.

Similar stress states in model and prototype (i.e., $\boldsymbol{\sigma_v} = 1$) are satisfied for homologous depths represented by a constant scaling law of linear distances of $\boldsymbol{L} = N^{-1}$, always that a similar density is maintained (i.e., $\boldsymbol{\rho} = 1$). Taylor (2018) defined this as the basic scaling law of centrifuge modeling. Cargill and Ko (1983) defined this ratio of lengths as the scaling law for geometric similarity and stated that dynamic and kinematic similarities should also be satisfied to properly reproduce a prototype condition. Dynamic similarity refers to the ratio of forces, and kinematic similarity refers to the ratio of velocities and acceleration.

Dimensional analysis of the scaling law of gravitational acceleration, $\boldsymbol{a}$ (length over squared time), allows deriving a scaling law for time as $\boldsymbol{T} = N^{-1}$, which implies scaling velocity as $\boldsymbol{v} = 1$. Such scaling laws are useful for modeling dynamic events, such

as earthquake loading or wave motion in offshore structures (e.g. Schofield 1981). Nonetheless, it is widely accepted that the velocity of flow increases in centrifuge models with $\boldsymbol{L} = N^{-1}$ by a factor of $\boldsymbol{v} = N$ (Laut 1975). Hence, the scaling of time becomes $\boldsymbol{T} = N^{-2}$ for problems involving seepage or transient flow (Garnier et al. 2007). The difference in both definitions of $\boldsymbol{T}$ is commonly referred to as a scaling conflict of the time variable and often requires special attention in centrifuge modeling (Joseph et al. 1988; Santamarina and Goodings 1989; Kutter 1995). For instance, physical models involving different time-dependent phenomena, such as liquefaction of sands due to earthquake loading or sediment transport due to action of waves, require additional strategies to solve the conflict, such as reducing the viscosity in the fluid to reduce the permeability of the soil and the velocity of flow (Dewoolkar et al. 1999, 2001; Ling et al. 2003). A summary of the basic scaling laws in centrifuge modeling is presented in Table 2. 1 (Madabhushi 2014).

Table 2. 1 Basic scaling laws for centrifuge modeling in geotechnical engineering.

Variable	Scaling Law	Variable	Scaling Law
Stress	$\boldsymbol{\sigma} = 1$	Volume	$\boldsymbol{V} = N^{-3}$
Density	$\boldsymbol{\rho} = 1$	Mass	$\boldsymbol{M} = N^{-3}$
Length	$\boldsymbol{L} = N^{-1}$	Force	$\boldsymbol{F} = N^{-2}$
Velocity	$\boldsymbol{v} = 1$	Time - diffusion	$\boldsymbol{T} = N^{-1}$
Acceleration	$\boldsymbol{a} = N$	Time - dynamic	$\boldsymbol{T} = N^{-2}$

2.2.2 The "Modeling of Models" approach

For geotechnical phenomena for which prototype data is not available, such as the case of backward erosion piping and other internal and surface erosion mechanisms, validating results from physical and analytical models is challenging. Consequently, there

is often a misconnection between experimental work and the field behavior. The approach known as "Modeling of Models" is a useful technique to verify scaling effects by comparing the behavior of different models of the same prototype but tested under different gravitational accelerations. If similarity rules are satisfied, the behavior predicted should be the same for every model tested. Taylor (2018) used the work of Ko (1988) to explain the principle behind this approach using the sketch shown in Figure 2. 4.

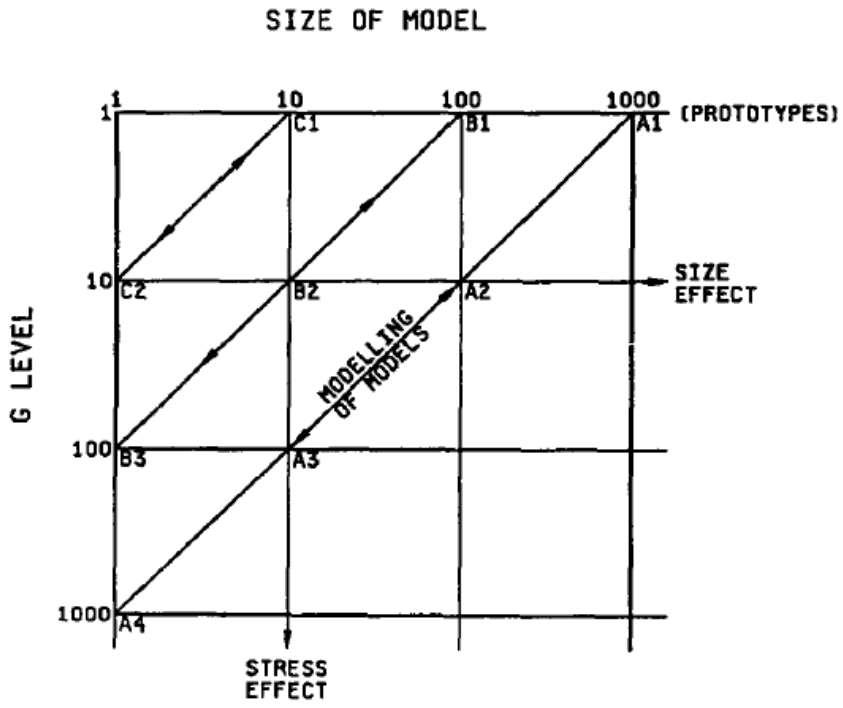

Figure 2. 4 Concept of "Modeling of Models".

As shown, a prototype with 10 m in height can be modeled at full scale under Earth's gravity (i.e., $\boldsymbol{a} = 1$), at a 1/10th scale with $\boldsymbol{a} = 10$, and at a1/100th scale with $\boldsymbol{a} = 100$, and the behavior in all scenarios should be similar. However, this strategy would satisfy only geometric similarity conditions. Other phenomena involving kinematic and

dynamic similarity requires further analysis of more factors, such as scaling of particle size or fluid properties. The "Modeling of Models" approach has been successfully used to validate centrifuge scaling laws in studies of shallow foundations on cohesionless soils (e.g. Ovesen 1980), response of piles (e.g. Ko et al. 1984; Terashi et al. 1989; Hamilton et al. 1991), among others.

2.2.3 Centrifuge modeling of erosion mechanisms

Different approaches have been used to determine scaling laws for centrifuge modeling of erosion mechanisms in soils and granular media. Goodings (1982, 1984, 1985) focused on erosion problems due to surface flow by decoupling this mechanism into four, namely seepage, mass movement, surface flow, and initiation of erosion. Each phenomenon was analytically compared using three ideal models: a full-scale model (i.e., $\boldsymbol{a} = 1$, $\boldsymbol{L} = 1$), a small-scale model under Earth's gravity ($\boldsymbol{a} = 1$, $\boldsymbol{L} = N^{-1}$), and a small-scale model in a centrifuge environment ($\boldsymbol{a} = N$, $\boldsymbol{L} = N^{-1}$). As expected, the author noted a conflict in similarity for the time variable between laminar seepage (i.e., $\boldsymbol{T} = N^{-2}$) and mass movement (i.e., $\boldsymbol{T} = N^{-1}$), and proposed a solution on the basis of scaling the permeability of the soil per $\boldsymbol{k} = N^{-1}$ by reducing the size of the particles by $\boldsymbol{d_{10}} = N^{1/2}$. Under this correction, the scaling of time for surface flow also agreed with seepage and mass movement (i.e., $\boldsymbol{T} = N^{-1}$). However, the author also highlighted that surface flow could not be replicated in similarity using small-scaled models at Earth's gravity due to the challenging scale effects. On the other hand, the initiation of erosion and sediment transport was analyzed using the model of Shields (1936) and the author noted that particles should be scaled by $\boldsymbol{d_{50}} = N^{-1}$ for adequate modeling, which results in a conflict with the previous scaling law proposed. Hence, a prototype event involving

seepage, surface flow, and mass movement could be modeled correctly using centrifuge modeling, but modeling these mechanisms simultaneously with the initiation of erosion is of great difficulty.

Dong et al. (2001) also noted the necessity for scaling particle size to meet similarity rules for problems involving particle mobility, a condition that is often difficult to meet unless the particles in the prototype are relatively large. In this work, an alternative approach was used based on the assumption that soil transport is associated with the turbulent flow with large amounts of sediments on suspension. Hence, using the Relative Fall Velocity criterion (Dean 1973), and dimensional analysis, the authors proposed scaling the kinematic viscosity of the fluid by $\boldsymbol{\eta} = N$ for fine sands, and by $\boldsymbol{\eta} = N^{-1}$ for coarse sands, to satisfy the similarity for time ($\boldsymbol{T} = N^{-1}$) in sediment transport and subsoil processes. More recently, Bezuijen and Steedman (2010) analyzed the scaling laws for seepage in laminar and turbulent flow based on different scaling factors of diameter and highlighted those that may be used for studying dynamic problems.

The scaling laws for centrifuge modeling of flow and erosion using small-scaled models, as described in this section, are summarized in Table 2. 2. It is of remarkable importance to consider that despite the different theoretical approaches used to derive these scaling laws, experimental data that fully validates these laws is not available (Dong et al. 2001; Garnier et al. 2007), which highlights the importance of developing detailed experimental research to provided new insights into the physical modeling of erosion mechanisms using the geotechnical centrifuge technique.

Table 2. 2 Theoretical scaling laws for flow phenomena ($\boldsymbol{L} = N^{-1}$).

Mechanism	Author	Scaling Law				
		$\boldsymbol{d}$	$\boldsymbol{v}$	$\boldsymbol{k}$	$\boldsymbol{t}$	$\boldsymbol{\eta}$
Seepage - Laminar Flow	Goodings (1982, 1984, 1985)	1	N		N^{-2}	
	Bezuijen and Steedman (2010)	1	N	1	N^{-2}	
		$N^{-1/2}$	1	N^{-1}	N^{-1}	
		N^{-1}	N^{-1}	N^{-2}	1	
		1	1	N^{-1}	N^{-1}	N
		$N^{-1/2}$	N^{-1}	N^{-2}	1	N
		N^{-1}	N^{-2}	N^{-3}	N	N
Seepage - Turbulent Flow	Bezuijen and Steedman (2010)	1	$N^{1/2}$	$N^{-1/2}$	$N^{-3/2}$	
		$N^{-1/2}$	$N^{1/4}$	$N^{-3/4}$	$N^{-5/4}$	
		N^{-1}	1	N^{-1}	N^{-1}	
Mass Movement - Laminar Flow	Pokrovsky and Fryodorov (1936)				N^{-1}	
	Goodings (1982, 1984, 1985)	$N^{-1/2}$	1	N^{-1}	N^{-1}	
Surface Flow	Goodings (1982, 1984, 1985)		1		N^{-1}	
Sediment Transport/Erosion	Goodings (1982, 1984, 1985)	N^{-1}			N^{-2}	
	Dong et al. (2001)	$N^{-1/3}$	$N^{1/3}$			
		N^{-1}	1		N^{-1}	
		1	1		N^{-1}	N
		N^{-1}	1		N^{-1}	N^{-1}

2.3 OVERVIEW OF BACKWARD EROSION PIPING

2.3.1 INTERNAL EROSION IN GEOTECHNICAL STRUCTURES

Erosion is a potential failure mechanism of water-retaining structures. A study by Danka and Zhang (2015) with a sample population of 503 dikes from United States, Hungary, Germany, China, and the Netherlands, related erosion to 83% of the total failure scenarios. Foster et al. (2000) analyzed the failure mechanisms and accidents in earth embankments constructed after 1950 in Australia, France, India, Japan, New

Zealand, Norway, United Kingdom, United States, and other countries. This extensive study indicated that 94.5% of the failure mechanisms involved some form of erosion. The most recurrent mode observed in this study was overtopping, together with other forms of external erosion, with a frequency of 48.4%. Internal erosion, or the erosion through the soil structure due to internal seepage, was also found to be a regular failure pattern, over slope stability problems, liquefaction, and earthquakes, and was related to 46.1% of the cases studied.

The internal erosion mechanism presented by Foster et al. (2000) was referred to as “piping”, and it was defined as a process entirely driven by internal seepage in which the detachment and transport of soil grains occur within and earthen structure, afterwards forming small pipes through the soil matrix. The process initiates at an exit point located somewhere near the toe of the embankment (namely downstream zone) and then progresses through the earth structure or its foundation until reaching the impoundment (namely upstream zone). This mechanism is rather one type, or a combination of two or more types, of the broader phenomenon known as internal erosion (Bonelli 2013). Internal erosion is the process of transport and migration of grains constituting the soil structure due to the action of internal flow, inducing a change in the hydraulic and mechanical characteristics of an earthen structure (Bendahmane et al. 2008). Internal erosion develops in different phases comprising initiation, continuation, progression to form a pipe, and initiation of the breach. Nonetheless, internal erosion may initiate at different locations and may develop in different patterns, depending on the mechanism involved and the characteristics and configuration of the water-retaining structure.

As shown in Figure 2. 5, the initiation of internal erosion develops following four main mechanisms (Bonelli 2013): contact erosion, suffusion, backward erosion piping, and concentrated leak erosion. Contact erosion occurs when flow through the interface between coarse-grained and fine-grained soils results in the migration of the finest particles. Earth structures with protection filters are prone to develop this mechanism. Suffusion refers to the removal of finer particles in gap-graded soils. Concentrated leak erosion occurs when flow lines concentrate in a specific orifice increasing the seepage forces in the vicinity. Structures with tensile cracks due to desiccation, differential settlement, or any other localized fracture, are exposed to this mechanism. Erosion due to concentrated leak may initiate inside the earth structure or in the upstream zone, for example, when cracks exist in the core (Figure 2. 5a) or in a concrete facing, respectively. Backward erosion occurs when a fracture or exit point for seepage exists or is created in the downstream zone (Figure 2. 5b). Concentrated seepage in the exit point fluidizes the soil and initiates the transport of grains. Erosion progresses to form micropipes extending through the foundation in opposite direction of flow. This mechanism requires a cohesionless soil, usually with uniform gradation (Schmertmann 2000; Bonelli 2013). Erosion progressing backwards could also occurs across the structure due to cracking across the core (Figure 2. 5c).

Despite the efforts to categorized and evaluate the likelihood of failure by internal erosion mechanisms, field evidence to assess the modes of internal erosion is very limited or inexistent due to the difficulties to visually recognize and distinguish the initiation and progression in the field (e.g., Costa and di Prisco 1999). Any sign or indication of the existence of any mechanism disappears when the structure breaches (Richards and Reddy

2007). Moreover, more than one mechanism may occur simultaneously, such as suffusion and contact erosion, or in sequence, such as concentrated leak and backward erosion. Notwithstanding, design, construction and maintenance guidelines for water-retaining structures, such as levees or dams, include various aspects related to the development of piping (Technical Advisory Committee 1999; USACE 2000; USDIBR 2014).

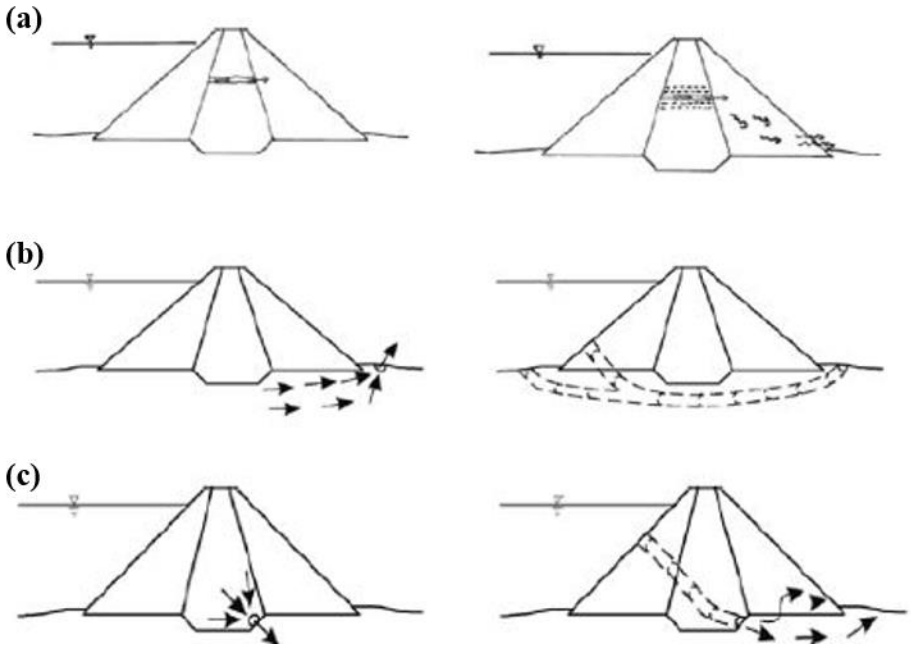

Figure 2. 5 Examples of internal erosion patterns (Bonelli 2013):
(a) initiated in the core – progresses through the embankment towards the downstream zone; (b) initiated at the downstream zone – progresses through the foundation or embankment towards the upstream zone;
(c) initiated in a crack in the core – progresses through the embankment towards the upstream zone.

2.3.2 MECHANISM OF BACKWARD EROSION PIPING

On the basis of observations of physical models of backward erosion piping at different scales, the phenomenon has been identified to develop following five typical phases (Bonelli 2013): (1) seepage, (2) initiation, (3) progression of piping, (4) widening of pipes and (5) failure of the foundation. This process is described in Figure 2. 6 for the

case of an impervious, water-retaining structure overlying a sandy foundation. As shown in Figure 2. 6a, the phase of seepage occurs due to the differential head, Δh, across the distance, L, between the impoundment and the downstream drainage, which causes water to flow across the foundation of the structure. Seepage occurs continuously, regardless of the value of Δh and the global hydraulic gradient acting across the foundation (i.e., $i_{global} = \Delta h / L$), and the flow conditions beneath the structure are predominantly laminar and one-dimensional, as expected for underground flow.

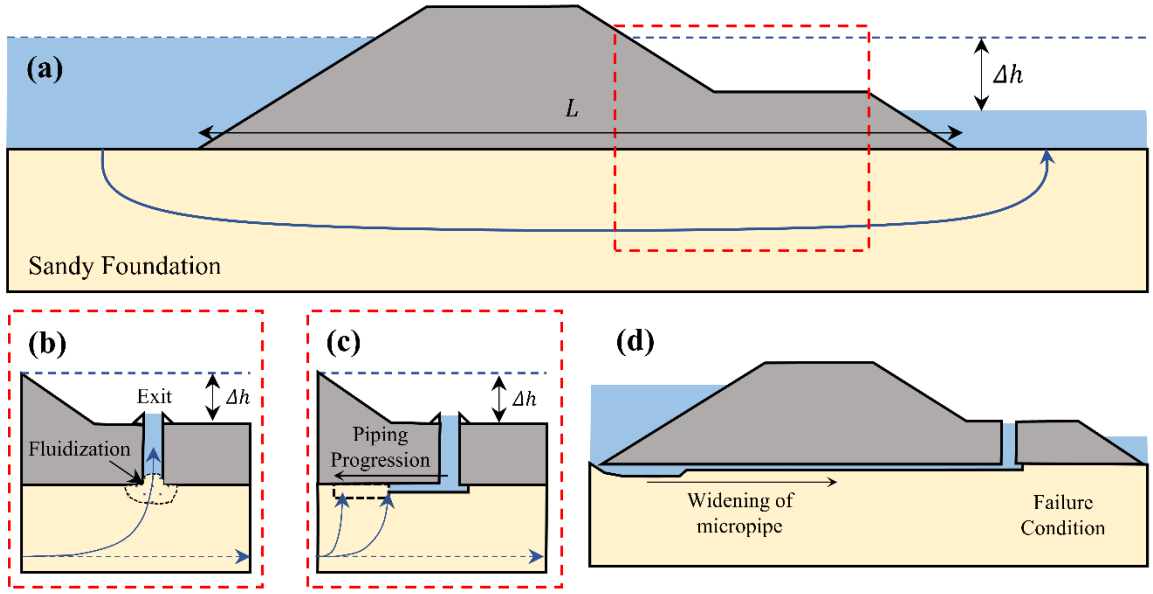

Figure 2. 6 Phases experienced in the backward erosion piping mechanism: (a, b) seepage and initiation; (c, d) progression and widening of pipe; and (e) breach of foundation.

The flow conditions beneath the structure become more complex when an exit drainage exists in the downstream zone, as shown in Figure 2. 6b. Such exit may be due to desiccation, rooting, or animal burrows, which cause cracks to form across an impervious cohesive layer, or may be part of the configuration of the structure, such as a drainage ditch or a trench, or simply the absence of an impervious cover layer on the downstream zone (see Figure 2. 7). Regardless of the type of exit, the initiation phase

takes place when the seepage forces due to emerging flow fluidize the soil in the vicinity of the exit (Alsayadani and Clayton 2014; Fleshman and Rice 2013, 2014; Ovalle-Villamil and Sasanakul 2020). Such fluidization of the soil essentially increases the local porosity at the exit and reduces the flow resistance, which induces a state of incipient motion on the grains (Fleshman and Rice 2014; Peng and Rice 2020). The formation of sand boils in the downstream zone is usually an evidence of fluidization of the soil during the initial stages of backward erosion piping (Kolb 1975; Li et al. 1996; Mazzoleni et al. 2013), as observed on some levees near the Mississippi River (see Figure 2. 8).

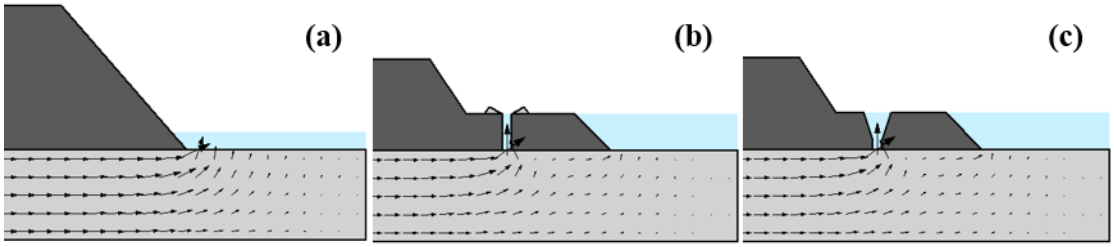

Figure 2. 7 Examples of configuration of downstream zone: (a) no cover layer; (b) cover layer with hydraulic fracture; (c) cover layer with ditch.

Figure 2. 8 Sand boil during flood event in Mississippi River Valley (Li et al. 1996; Alfortish et al. 2012).

After the initiation, the migration of soil grains from the foundation to the exit may begin, as shown in Figure 2. 6c, leading to the formation of micropipes that extend in length towards the impoundment during the progression phase. Bonelli (2013) described this phase using two steps. In the first step, the migration of grains to the exit continues until reaching an equilibrium phase in which the extension of the micropipes stops. An additional increase in Δh reactivates the process until a new equilibrium phase develops. In the second step, the migration of grains continues with no equilibrium phase. In this step, the progression continues until the micropipes reach a critical length, after which the seepage forces across the piping path are large enough to widen its size and cause the structural and hydraulic failure of the foundation, as shown in Figure 2. 6d.

Although the phases described previously have were observed in different experimental studies (van Beek et al. 2011, 2015), the progression of piping is found to be different depending on the size of the model and the type of exit (Van Beek et al. 2015). Large-scale experiments and some small-scale experiments with small exit areas have shown a stepped progression, in which the pipe increased in length but eventually stopped at an equilibrium phase, as described in the previous paragraphs. Hence, additional increases of hydraulic gradient are required to extend the micropipes to a critical condition. This mechanism is called progression-dominated. In contrast, the piping initiates and progresses to a critical condition for the same value hydraulic gradient and without any intermediate equilibrium in many small-scale models (Van Beek 2015; Van Beek et al. 2015). This mechanism is called initiation-dominated. To the authors' knowledge, no clear explanation of the conditions that lead to either progression or initiation-dominated behavior has been reported.

2.4 MECHANICS OF FLOW THROUGH POROUS MEDIA

2.4.1 PRESSURE GRADIENT AND VELOCITY OF FLOW IN POROUS MEDIA

The relationship between the pressure gradient, $\Delta P/\Delta L$, or the hydraulic gradient $i = \Delta h/\Delta L$, and velocity of flow, v, is used to describe the behavior of flow through porous media. This relation represents the pressure drop, ΔP, or head drop, Δh, in the medium for a given velocity of flow along a distance ΔL. If the velocity of flow is very low, the relationship is linear describing a flow governed by viscous forces, and is represented by Darcy's Law:

$$\frac{\Delta P}{\Delta L} = \frac{\rho_w g}{k} v \qquad i = \frac{v}{k} \qquad \text{Eq. 2. 2}$$

where k = Darcy's permeability; ρ_w = density of fluid; and g = gravitational acceleration. Note that the relationship between pressure gradient and hydraulic gradient is a function of the gravitational acceleration as $\Delta P = \Delta h \rho_w g$.

If the velocity of flow is higher, the flow is governed by both viscous and inertial forces and the gradient-velocity relation is nonlinear. This relationship is represented by Forchheimer's Law as:

$$\frac{\Delta P}{\Delta L} = Av + Bv^2 \qquad i = av + bv^2 \qquad \text{Eq. 2. 3}$$

where A, B, a and b = Forchheimer coefficients. These coefficients are highly dependent on the flow regime where the pressure gradients and velocity of flow are measured. Figure 2. 9 presents an example of flow regimes based on experimental data by Fand et al. (1987) and presented by Burcharth and Christensen (1991). In this figure, the coefficient *A*" is directly related to Darcy's permeability if the velocity of flow is sufficiently low. If the gradient-velocity relation is only measured within the Forchheimer regime, the coefficient A taken from the linear term may not be related to Darcy's

permeability. This explanation is also true for fully turbulent flow where the coefficients *A'* and *B'* may be derived but cannot be directly related to *A* and *B* in Eq. 2. 3.

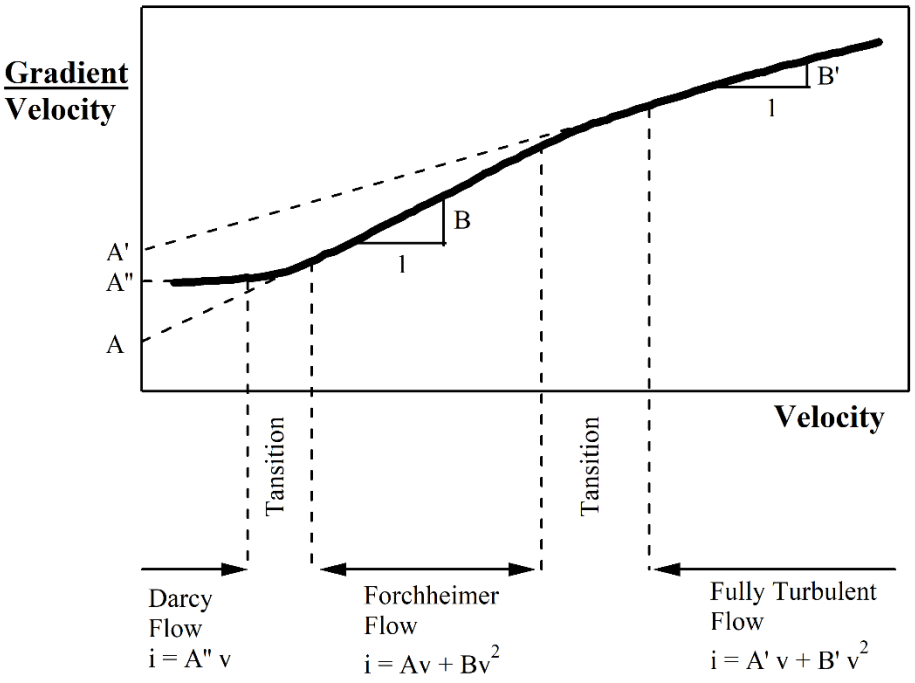

Figure 2. 9 Regimes of flow in porous media and flow coefficients.

Previous research studies have been performed to develop relationships between the physical characteristics of the porous media and the Forchheimer coefficients. For simplicity, the flow though porous media is described in the same manner as flow through pipes assuming that a set of tortuous capillaries composes the medium. These capillaries are comparable to pipes, with dimensions obtained based on the physical characteristic of the porous medium.

Using the concept of hydraulic radius (Carman 1956; Richardson et al. 2002), the average diameter of the capillaries can be expressed as:

$$d_c = 4\frac{n}{S_b} = \frac{4}{S}\frac{n}{(1-n)} \qquad \text{Eq. 2. 4}$$

where d_c = average diameter of capillaries; n = void fraction or porosity; S_b = surface area in contact with the fluid per unit volume of porous medium; and S = geometrical specific surface area per unit volume of particles. Following the assumption that the particles are spherical with effective diameter d_{eff} (Carrier 2003), a representative S for porous media is given by $6/d_{eff}$.

According to Carman (1956), the Hagen-Poiseuille equation $\left(\frac{\Delta P}{L_{pipe}} = \frac{32\mu}{d_{pipe}^2} v_{pipe}\right)$ used to describe the viscous flow in pipes can be rewritten for porous media assuming that $d_{pipe} \approx d_c$, $L_{pipe} \approx \tau \Delta L$, and $v_{pipe} \approx v\tau/n$, obtaining:

$$\frac{\Delta P}{\Delta L} = K'\tau^2 \mu \frac{S^2(1-n)^2}{n^3} v \qquad \text{Eq. 2. 5}$$

where τ = tortuosity; μ = dynamic viscosity; K' = constant representing the porous shape; and the term $K'\tau^2$ = empirical Kozeny-Carman constant K. The parameter K has been estimated to be close to 5 for unconsolidated media based on approximate values of τ and K' of $\sqrt{2}$ and 2.5, respectively. Nonetheless, Xu and Yu (2008) suggested that K is a function of the void fraction with values from 1 to 2 for a relatively low porosity and increases sharply as porosity increases. Given the linear relationship between pressure gradient and velocity of flow, Eq. 2. 5 is only applicable to the viscous flow regime.

A more general expression for all flow regimes can be derived using Darcy-Weisbach equation for pipes $\left(\frac{\Delta P}{L_{pipe}} = \frac{f}{2}\frac{\rho}{d_{pipe}} v_{pipe}^2\right)$, obtaining:

$$\frac{\Delta P}{\Delta L} = \frac{f}{2}\rho\tau^3 \frac{S(1-n)}{n^3} v^2 \qquad \text{Eq. 2. 6}$$

where f = Darcy's friction factor. In Eq. 2. 6, the pressure gradient varies with the square of velocity and is independent of the viscosity of the fluid. It is known from the flow through pipes that f varies with the velocity and regime of flow. However, the evaluation

of this parameter is very limited for porous media. Comiti and Renaud (1989) used Nikurdase formula to establish a constant value of 0.194.

Trussel and Chang (1999) mentioned that an exponential function, such as Eq. 2. 6, fits nonlinear flow data as well or better than Forchheimer's Law. However, based on the study of Ergun and Orning (1949), the transition from viscous to inertial conditions of flow is smooth and a two-term, nonlinear function would represent better the different domains of flow in most packed systems. Hence, following Forchheimer's Law, a two-term equation can be derived with the combination of Eq. 2. 5 and Eq. 2. 6 as:

$$\frac{\Delta P}{\Delta L} = K'\tau^2\mu\frac{S^2(1-n)^2}{n^3}v + \frac{f}{2}\rho\tau^3\frac{S(1-n)}{n^3}v^2 \qquad \text{Eq. 2. 7}$$

where Forchheimer coefficients A and B are:

$$A = K'\tau^2\,\mu\,\frac{S^2\,(1-n)^2}{n^3} \qquad B = f\frac{\rho\tau^3}{2}\frac{S\,(1-n)}{n^3} \qquad \text{Eq. 2. 8}$$

Different methods for using Eq. 2. 7 and Eq. 2. 8 have been proposed based on experimental data. Ergun (1952) proposed constant values of 4.2 and 0.3 for the terms $K'\tau^2$ and $f\tau^3/2$, respectively. Kovacs (1981) proposed values of 4.0 and 0.4 for the same terms. Kadlec and Knight (1996) and Sidiropoulou et al. (2007) proposed various empirical functions of diameter of particles and porosity for estimating A and B directly. Other authors, such as Comiti and Renaud (1989), proposed using constants for K' and f of 2.0 and 0.194, respectively, and proposed empirical functions for τ and S. A summary of the methods cited is presented in Table 2. 3.

This study proposes using a similar approach to Comiti and Renaud (1989) to investigate nonlinear flow though porous media in a centrifuge environment, using Eq. 2. 8. Instead of assuming constant values of K' and f, all the variables are left as originally written and only the tortuosity, τ, is approximated. If some particles in the media are

assumed unrestrictedly overlapped, τ can be determined as proposed by Bo-Ming and Jin-Hua (2004) as:

$$\tau = \frac{1}{2}\left[1 + \frac{1}{2}\sqrt{1-n} + \sqrt{1-n}\frac{\sqrt{\left(\frac{1}{\sqrt{1-n}}\right)^2 + \frac{1}{4}}}{1-\sqrt{1-n}}\right] \quad \text{Eq. 2. 9}$$

Eq. 2. 9 presents τ as a function of the porosity and this approach allows investigating the characteristics of the porous media represented by the porous shape factor, K', and the Darcy's friction factor, f.

Table 2. 3 Analytical models describing flow through porous media.

Model	Equation	Reference
$i = v/k$	Eq. 2. 2	Darcy's Law
$i = av + av^2$	Eq. 2. 3	Forchheimer's Law
$\frac{\Delta P}{\Delta L} = KC\,\mu\,\frac{S^2\,(1-n)^2}{n^3}v$	Eq. 2. 5	Carman (1956)
$i = 36\frac{\mu}{\rho g}\,\frac{(1-n)^2}{n^3}\frac{1}{d^2}v + 1.75\frac{1}{g}\frac{(1-n)}{n^3}\frac{1}{d}\,v^2$	Eq. 2. 10	Ergun and Orning (1949); Ergun (1952)
$i = 144\frac{\mu}{\rho g}\,\frac{(1-n)^2}{n^3}\frac{1}{d^2}v + 2.4\frac{1}{g}\frac{(1-n)}{n^3}\frac{1}{d}\,v^2$	Eq. 2. 11	Kovacs (1981)
$B = 0.0968\tau^3\rho S\frac{1-n}{n^3};\ A = 2\tau^2\mu S^2\frac{(1-n)^2}{n^3}$	Eq. 2. 12	Comiti and Renaud (1989)
$i = 225\frac{\mu}{\rho g}\,\frac{(1-n)}{n^{3.7}}\frac{1}{d^2}v + 2\frac{1}{g}\frac{(1-n)}{n^3}\frac{1}{d}\,v^2$	Eq. 2. 13	Kadlec and Knight (1996)
$a = 0.00333d^{-1.5}n^{0.06};\ b = 0.1943d^{-1.265}n^{-1.1414}$	Eq. 2. 14	Sidiropoulou et al. (2007)
$A = K'\tau^2\,\mu\,\frac{S^2\,(1-n)^2}{n^3};\ B = f\frac{\rho\tau^3}{2}\frac{S(1-n)}{n^3}$	Eq. 2. 7	This study

2.4.2 Limit of validity of Darcy's Law

The transition from viscous to non-viscous conditions of flow for porous media is expected to be difficult to identify (Burcharth and Christensen 1991). The Moody diagram, a relationship between the Friction Factor and the Reynolds Number, has been

widely used to evaluate the transition. The Friction Factor is a theoretical parameter used to predict the energy loss in a pipe based on the velocity of flow and the resistance due to friction. The Reynolds Number is a dimensionless parameter obtained from dimensional analysis representing the relation between inertial and viscous forces due to flow. In a logarithmic space of Friction Factor as function of Reynolds Number, the viscous domain is represented by a linear relationship. As Reynolds Number increases, the relationship becomes nonlinear indicating the transition to a non-viscous domain. The critical Reynolds Number (R_{critic}), indicating the end of the linear relationship, is used to define the limit of validity of Darcy's Law.

The interpretation of the Friction Factor and the Reynolds Number in porous media relies on the author's preferences. Comiti et al. (2000) stated that the most convenient way to determine the transition from viscous flow is using the simplified equation:

$$f_{pore} = \frac{\alpha}{R_{pore}} + \beta \qquad \text{Eq. 2. 15}$$

where α = 16; β = 0.194; and f_{pore} and R_{pore} = Friction Factor and Reynolds Number given by:

$$f_{pore} = \frac{\Delta P}{\Delta L v^2} \frac{2}{\rho\, \tau^3} \frac{n^3}{S(1-n)} \qquad R_{pore} = \frac{4\, \rho\, \tau v}{\mu\, S\, (1-n)} \qquad \text{Eq. 2. 16}$$

Eq. 2. 15 and Eq. 2. 16 were used by Khalifa et al. (2000) to evaluate scaling laws for flow in centrifuge modeling, and by Wahyudi et al. (2002) to evaluate the Darcy and non-Darcy flow through different sands. Goodings (1994) used more simplified definitions of Reynolds Number and Friction Factor, based on the studies of Muskat (1938) and Stephenson (1979), to evaluate the effect of the transitions in flow regime for centrifuge models. The definitions used are:

$$Ff = \frac{iDgn^2}{v^2} \qquad R_n = \frac{\rho v D}{n\mu} \qquad \text{Eq. 2. 17}$$

where i = dimensionless hydraulic gradient; and D = representative diameter of particle in the medium. Recently, Salahi et al. (2015) used the definition of Reynolds Number in Eq. 2. 17 to investigate nonlinear flow through crushed and rounded gravels.

Despite the differences of interpretation, most research studies reported R_{critic} between 1 and 10 for the limit of validity of Darcy's Law (Bear 2013). Goodings (1994) and Khalifa et al. (2000) suggested R_{critic} values between 3 and 11, while Comiti et al. (2000) suggested a value of 4.9. Salahi et al. (2015) estimated R_{critic} to be as high as 30.

A different methodology is proposed by Zeng and Grigg (2006) who used experimental or empirical parameters instead of the Reynolds Number and the Friction Factor. The Forchheimer number, Fo, is here introduced as:

$$Fo = \frac{k_i \beta' \rho v}{\mu} = \frac{B}{A}\, v \qquad \text{Eq. 2. 18}$$

where k_i = intrinsic permeability; β' = non-Darcy coefficient; and A and B = Forchheimer coefficients. It is noted that Fo is the result of comparing the pressure gradients for viscous and non-viscous flow. The critical Forchheimer number for overcoming viscous domain is given by:

$$Fo_{critic} = \frac{E_c}{1 - E_c} = \frac{B}{A}\, v_{critic} \qquad \text{Eq. 2. 19}$$

where E_c = critical difference indicating the transition; and v_{critic} = critical velocity at the transition. Zeng and Grigg (2006) proposed a value of Fo_{critic} of 0.11 for a 10% difference between viscous and non-viscous gradient at the transition.

2.5 MECHANICS OF EROSION DUE TO SEEPAGE

2.5.1 GRAIN MOTION DUE TO SEEPAGE-INDUCED FORCES

Shields (1936) studied the shear stress driven by a unidirectional streamflow required to initiate the transport of an individual grain on a granular bed. The author defined the Shields parameter as the critical ratio between the shear stress on top of the bed inducing the grain motion and the resisting submerged weight of the grain. The Shields parameter is given by:

$$\theta_c = \frac{\tau_c}{[(\rho_s - \rho_w) g\ d]} \qquad \text{Eq. 2. 20}$$

where θ_c = Shields parameter; τ_c = critical shear stress; ρ_s = grain density; ρ_w = fluid density; g = gravitational acceleration; and d = representative grain diameter of the bed. The Shields parameter is often presented in the form of diagram and as a function of the grain Reynolds Number given by:

$$R_e^* = u_c^* \frac{d}{\nu} \qquad u_c^* = \sqrt{\frac{\tau_c}{\rho}} \qquad \text{Eq. 2. 21}$$

where R_e^* = grain Reynolds Number; ν = kinematic viscosity of the fluid; and u_c^* = critical shear velocity. It is noted that R_e^* is different than the Reynolds Number obtained with Eq. 2. 16 and Eq. 2. 17 because u_c^* reflects the velocity of flow at the bed surface.

Despite being a widely used method for estimating the shear stress inducing sediment transport, Cao et al. (2006) considered that the Shields diagram is sometimes difficult to interpret and requires a trial and error procedure to determine the critical shear stress. Therefore, the authors proposed explicit formulations for the Shields parameter using the Logarithmic Matching Method (Guo 2002). The Shields parameter is then expressed in terms of the grain Reynolds Number as:

$$\theta_c = 0.1414\, R_e^{*-0.2306} \qquad R_e^* \leq 6.61$$

$$\theta_c = \frac{\left[1 + 0.0223\, R_e^{*2.8358}\right]^{0.3542}}{3.0946\, R_e^{*0.6769}} \qquad 6.61 \leq R_e^* \leq 282.84 \qquad \text{Eq. 2. 22}$$

$$\theta_c = 0.045 \qquad R_e^* \geq 282.84$$

Other empirical expressions have been proposed to facilitate the estimation of the Shields parameter or the shear stress (e.g., Beheshti and Ataie-Ashtiani 2008). One example is the analysis of a unidimensional stream flow that was used by White (1940) to determine the local shear stress on top of a granular bed, by analyzing the equilibrium of forces in the grains under incipient motion. Such shear stress is given by:

$$\tau = \alpha\eta\frac{\pi}{6}\rho' g d \tan\phi \qquad \text{Eq. 2. 23}$$

where τ = shear stress for equilibrium; α = experimental coefficient for low flow velocities; η = packing coefficient; ρ' = submerged density of the grain; g = gravitational acceleration; d = diameter of grains; and ϕ = angle of repose of grains on top of the bed. Using different configurations of flume type test and horizontal flow with granular materials, the author concluded that the shear stress varied as a function of the grain diameter and the tangent of ϕ.

Indraratna and Radampola (2002) analyzed the movement of particles in granular filters due to internal filtration by assuming that the filters were a set of unconnected conduits. The authors suggested that the particle movement may occur in three scenarios depending on the size of the porous throat. First, the particle will move and then become stationary. Second, the particle will be completely washed out from the filter. And third, the particle will move and then clog a pore with a smaller diameter than the grain. The

critical hydraulic gradient, defined as the hydraulic gradient required for particle movement, is defined in this study as:

$$i_{cr} = \frac{2}{3\gamma_w}\frac{d^2}{(d^2 + 0.375\, d_0^2)}(\gamma')[\cos\alpha\,(f) + \sin\alpha] \qquad d < d_0$$

$$i_{cr} = \frac{2}{3}\frac{\gamma'}{\gamma_w}[\cos\alpha\,(f) + \sin\alpha] \qquad d > d_0 \qquad \text{Eq. 2. 24}$$

where i_c = critical hydraulic gradient; γ_w = unit weight of fluid; γ' = submerged unit weight of eroding particles; d = particle diameter; d_0 = minimum pore diameter; f = coefficient of friction of the eroding particles; and α = inclination of the conduit. Different from the work of Shields (1936) and White (1940), this method considers particle motion due to internal seepage instead of surface flow. Nonetheless, as the authors concluded, the model is not valid to represent erosion of cohesive materials.

2.5.2 Critical hydraulic gradient for the initiation of backward erosion piping

As shown in Figure 2. 6, the initiation of backward erosion piping occurs when the pore pressures due to concentrated seepage across an exit point near the downstream toe of the levee exceed the stresses providing internal stability to the foundation soil (Alsaydalani and Clayton 2013; Fleshman and Rice 2014). The concentration of flow leads to suspension of grains in a fluidization-like process near the exit point and to the formation of sand boils that facilitate the grain transport from the foundation (Robbins et al. 2020), as shown in Figure 2. 8. This process can be described by an evaluation of the forces and stresses acting in the soil surrounding the exit point. Figure 2. 10 idealizes the exit point as a defect in a cohesive, low permeable layer underlain by a sandy foundation (Bonelli 2013). Vertical upward flow is anticipated underneath the exit point (Schmertmann 2000; Fleshman and Rice 2014). For simplicity, the volume of soil subjected to fluidization and sand boiling beneath the exit point is modeled as a cylinder

with the size of the defect, as shown in Figure 2. 10a and 2. 10b. Considering this volume as a continuum, forces per unit volume acting in the soil include: the weight of the solid fraction, W_t; the buoyant force, B_t; the total seepage force, S_t; and the resultant force due to lateral friction with the surrounding soil, F_t. Since the direction of F_t is opposite to the direction of soil movement (Israr et al. 2016), the forces per unit volume resisting the initiation are W_t and F_t, while the driving forces are B_t and S_t.

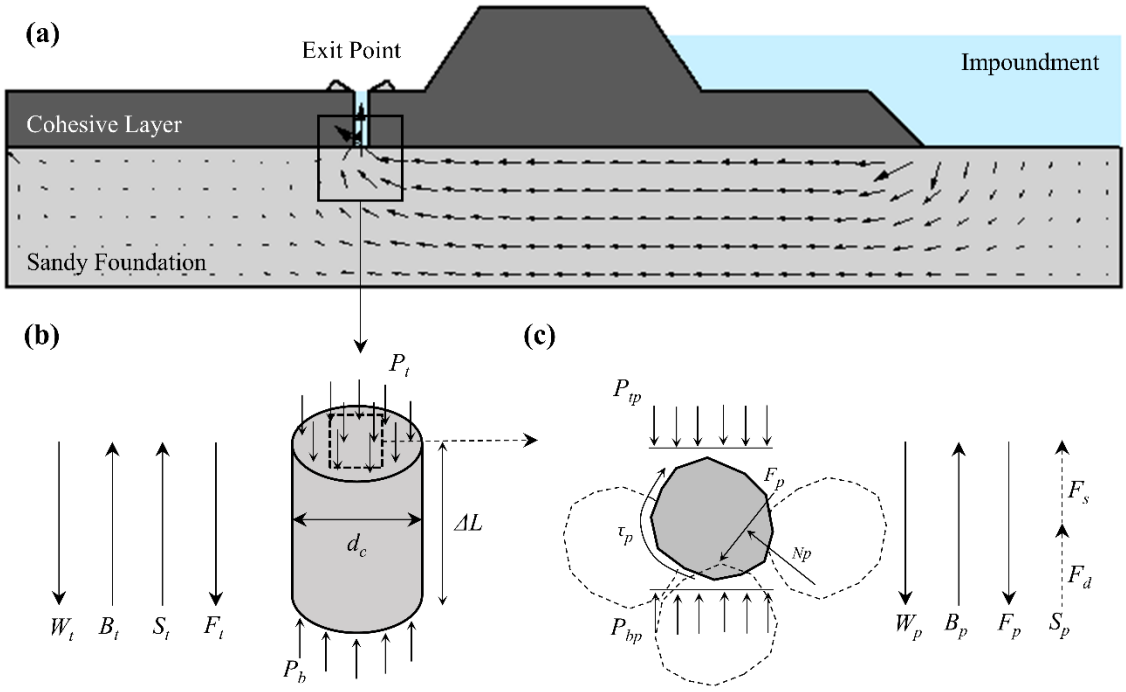

Figure 2. 10 Forces and stresses during the initiation of backward erosion piping: (a) schematic of flow through the foundation of a structure, (b) forces per unit volume of soil, and (c) forces at granular level in the surface.

By limit equilibrium, the critical condition for the initiation can be defined as (Indraratna and Radampola 2002):

$$\sum F_i = W_t - B_t + S_t - F_t = 0 \qquad \text{Eq. 2. 25}$$

where $W_t = g\rho_w G_s(1-n)$; $B_t = g\rho_w(1-n)$; $S_t = \Delta P/\Delta L$; $F_t = \left(\frac{4}{d_c}\right)\sigma'_m K_0 tan\phi'$; ρ_w = density of water; g = Earth's gravity; n = porosity; G_s = specific gravity; d_c = representative cross-sectional diameter of the crack in the cover layer; ΔP = pressure loss in a distance ΔL; σ'_m = mean effective stress; K_0 = coefficient of lateral earth pressure at rest; and ϕ' = drained friction angle of the soil.

Rearranging the terms in Eq. 2. 25, an expression for the pressure gradient and hydraulic gradient at limit equilibrium is derived as:

$$i_{cr} = \frac{1}{g\rho_w}\left(\frac{\Delta P}{\Delta L}\right)_{cr} = (1-n)(G_s-1) + \frac{1}{g\rho_w}\left(\frac{4}{d_c}\right)\sigma'_m K_0 \tan\phi' \qquad \text{Eq. 2. 26}$$

where i_{cr} and $(\Delta P/\Delta L)_{cr}$ are the critical hydraulic gradient (dimensionless) and the critical pressure gradient for the initiation of backward erosion piping, respectively. As shown in Eq. 2. 26, i_{cr} is not only a function of soil properties but also a function of the size of the exit point. For instance, in an exit point with no cover layer that can be idealized as a crack with infinite size ($d_c \rightarrow \infty$), Eq. 2. 26 is equivalent to the analytical method of heave by Terzaghi (1922) in which $i_{cr} \approx 1$. In contrast, as the size of the crack decreases ($d_c \rightarrow 0$), i_{cr} and $(\Delta P/\Delta L)_{cr}$ increase.

It must be highlighted that Eq. 2. 26 describes a condition of limit equilibrium between the seepage forces inducing soil movement and the resisting internal forces in a volume of soil with definite dimensions. Nonetheless, the initiation of backward erosion piping is expected to occur at level of grains for which the force equilibrium is more complex, and it is not represented by Eq. 2. 26. Therefore, Eq. 2. 26 is used to assess the scaling behavior of the models tested in this study, but it is not expected to describe the results obtained.

2.5.3 SEEPAGE FORCES AND STRESS IN THE GRAINS

As shown in Figure 2. 10c, the forces in an individual grain located on the surface of the control volume include (Fleshman and Rice 2014): the weight of the grain, W_p; the buoyant force, B_p; the resultant force due to intergranular contacts, F_p; and the total force due to seepage, S_p. The total seepage force acting on the grain is hypothesized as a combination of two components (White 1940; Bear 1972): a seepage force due to differential pressure on the top and the bottom of the grain, F_s, and a drag force due to viscous tangential forces acting on the surface area of the grains, F_d. Assuming that S_t is evenly distributed among the grains, then:

$$S_t = \sum F_s + \sum F_d \qquad \text{Eq. 2. 27}$$

where $\sum F_s$ and $\sum F_d$ = sum of the seepage and drag forces acting on each individual grain in the volume, respectively. If F_s is assumed evenly distributed on the solid fraction of the volume (i.e., $V_s = V_t\ [1 - n]$), an average estimation of F_s and F_d per grain can be obtained from:

$$F_s = \frac{\sum F_s}{NG} = \frac{\Delta P}{\Delta L}\frac{(1-n)V_t}{NG}$$
$$F_d = \frac{S_t - \sum F_s}{NG} = \frac{\Delta P}{\Delta L}\frac{n\,V_t}{NG} \qquad \text{Eq. 2. 28}$$

where V_t = total volume of soil; and NG = number of grains in the volume of soil. The fraction corresponding to each force is uncertain as it depends on many factors that cannot be easily determined experimentally at the granular level, including local velocity of flow, porosity, and other factors that may vary at this scale, such as grain size and shape. White (1940) assumed that only F_d acts on the grain for a laminar flow condition, while only F_s acts on the grain for a turbulent flow condition. However, such assumptions

are valid for surface erosion under horizontal flow of granular beds but not necessarily for the flow conditions modelled in this study. To the best of the author's knowledge, the assessment of these forces under upward flow and their correlation under horizontal or upward flow conditions have not been assessed in the literature. It must be highlighted that the directions of forces and stresses shown in Figure 2. 10 do not represent the actual resultant directions. These directions are intended to represent whether each individual stress in the system drives or resists grain motion with reference to the direction of flow.

2.6 ANALYTICAL MODELS OF BACKWARD EROSION PIPING

Before the theory of Flow Nets was formalized in 1937 by Arthur Casagrande (Richards and Reddy 2007), Bligh (1910) proposed the Line-of-Creep method to assess the piping potential along the interface between the structure and the soil. In this theory, a preferential flow path, in which the flow follows Darcy's Law, exits along the perimeter of the structure that is in contact with the foundation soil. Under this scenario, the stability against piping is defined as:

$$c_B = \frac{L_B}{\Delta h} \qquad \text{Eq. 2. 29}$$

where c_B = empirical percolation factor recommended for stability; L_B = preferential flow length; and Δh = global head loss across the structure.

Years later, Lane (1934) updated the Line-of-Creep method by including more experimental data and establishing a distinction between the flow across the soil-structure interface and the flow through the soil itself. The stability against piping using this model, which is known as the Weighted-Creep method, is given by:

$$c_L = \frac{L_L}{\Delta h} \qquad \text{Eq. 2. 30}$$

where c_L = empirical safe weighted creep ratio; and L_L = minimum safe flow length.

The main difference between the Lane-of-Creep and the Weighted-Creep methods is the interpretation of the flow path, which is arbitrary reduced in the latter, as shown in Figure 2. 11 (Terzaghi et al. 1996; Richards and Reddy 2007). Nonetheless, both methods determine the critical values of hydraulic gradient for piping based on correlations of the foundation soil type through the empirical factors c_B and c_L.

After the experimental work of de Wit et al. (1981), which is described in the next subsection, the analytical model known as Sellmeijer's Rule (Sellmeijer 1988) was proposed on the basis of visual observations of experiments of horizontal flow under increasing hydraulic gradients across a container filled with sand. General observations from the experiments include the formation of sand boils with fluidized sand for a certain increment of hydraulic gradient (see section 2.3.2), and the transport of sand grains from the foundation soil to the sand boils reaching equilibrium unless a new increment was applied. After reaching the equilibrium phase for several increments of hydraulic gradient, such phase did not occur anymore, and the erosion continued until failure. This moment was defined by Sellmeijer (1988) as the failure of the model.

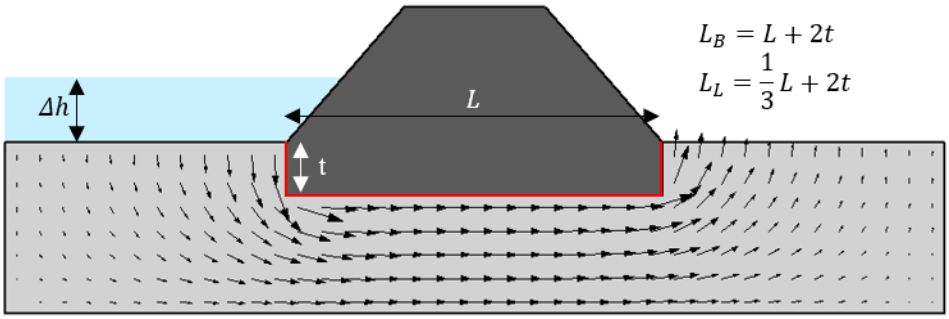

Figure 2. 11 Definition of safety lengths in the Lane-of-Creep and the Weighted-Creep methods.

Based on these observations, a fixed two-dimensional geometry representative of the experiments was designed as shown in Figure 2. 12. Then, a model for the limit equilibrium for the progression of backward erosion was derived analogically to the works by Bligh (1910) and Lane (1935) but covering groundwater flow through the soil, flow through the erosion channel or pipe, and the equilibrium of sand particles in the channel. The critical hydraulic gradient using the Sellmeijer's Rule method is then defined as (Sellmeijer and Koenders 1991; Koenders and Sellmeijer 1992):

$$\frac{\Delta h_c}{L} = \frac{1}{c} = F_R\, F_s\, F_G$$

$$F_R = \eta \frac{\gamma_p'}{\gamma_w} \tan\phi \qquad F_S = \frac{d_{70}}{\sqrt[3]{\kappa L}} \qquad \text{Eq. 2. 31}$$

$$F_G = [0.68 - 0.1 \ln(\eta F_S)] \left(\frac{D}{L}\right)^{\frac{0.28}{\left(\frac{D}{L}\right)^{2.8} - 1}}$$

where Δh_c = global critical head loss; L = seepage length; c = erosion coefficient; F_R = resistant factor; F_S = scale factor; F_G = geometrical shape factor; η = packing coefficient (White 1940); γ_p' = submerged unit weight of particles; γ_w = unit weight of fluid; θ = bedding angle of grains; k = hydraulic permeability; d_{70} = representative grain size; and D = height of sand layer.

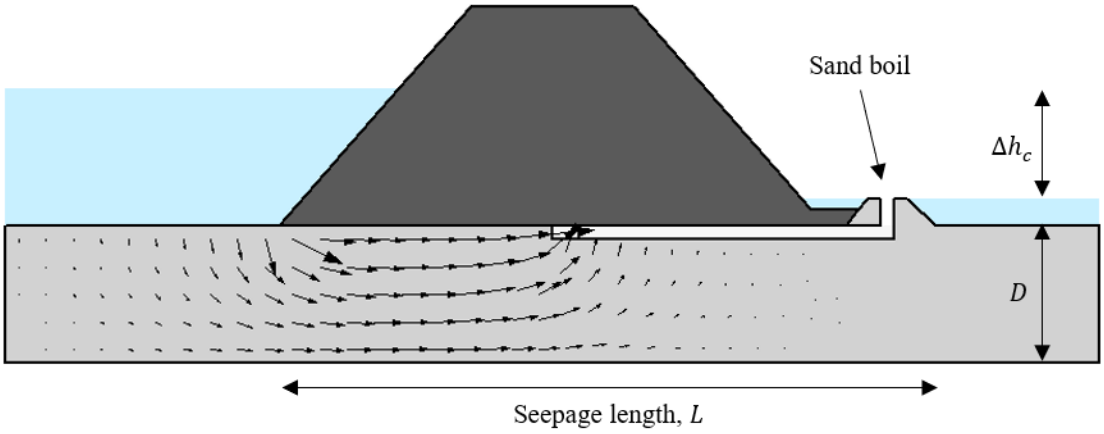

Figure 2. 12 Representative geometry for the Sellmeijer's Rule.

The Sellmeijer's Rule method was later modified using multivariate analysis of results from small-scale, medium-scale, and full-scale experiments of backward erosion piping (Van Beek et al. 2010, 2011; Sellmeijer et al. 2011). The modified factors F_R, F_S, and F_G for the new Sellmeijer's Rule are given by:

$$F_R = \eta \frac{\gamma_p'}{\gamma_w} \tan\phi \left(\frac{RD}{RD_m}\right)^{0.35} \left(\frac{U}{U_m}\right)^{0.13} \left(\frac{KAS}{KAS_m}\right)^{-0.02}$$

$$F_S = \frac{d_{70}}{\sqrt[3]{\kappa L}} \left(\frac{d_{70_m}}{d_{70}}\right)^{0.6} \qquad \text{Eq. 2. 32}$$

$$F_G = 0.91 \left(\frac{D}{L}\right)^{\frac{0.28}{\left(\frac{D}{L}\right)^{2.8}-1}+0.04}$$

where RD = relative density; U = coefficient of uniformity d_{60} / d_{10} ; KAS = roundness of the grains; and the suffix m = mean value. Despite the improvements that included considerations of relative density, gradation and particle shape, the authors reported that the effect of the grain size was still unknown. The same conclusion was mentioned by Van Beek et al. (2012) while implementing the new Sellmeijer's Rule to multilayered aquifers. In this study, although the numerical calculations agreed with some results from physical models, a gap between the numerical and experimental analyses still existed.

Before the improvements on the new Sellmeijer's Rule, Schmertmann (2000) used the original version of this method and an extensive set of experimental results from flume tests to design the Point Method. This method allows estimating the factor of safety against piping at any point of an expected progression path. To do so, a flow net analysis of the structure determines the local hydraulic gradients (i_x) experienced at various points x along the path. Afterwards, i_x is compared with a reference critical local hydraulic gradient (i_{px}) required for extending a pipe until the upstream zone. The factor of safety against piping is given by:

$$F_{px} = \frac{i_{px}}{i_x} \quad \text{Eq. 2. 33}$$

where F_{px} = factors of safety against piping at a point x. The magnitude of i_{px} is usually determined from experimental results of critical global hydraulic gradients ($\overline{(i_{pmt})}$) and the application of several correction factors. Hence, F_{px} can also be expressed as:

$$F_{px} = \frac{[(C_D C_L C_S C_Z C_k C_\gamma C_B)(C_G \overline{i_{pmt}})]C_\alpha}{(C_G C_R) i_x} \quad \text{Eq. 2. 34}$$

where C_D = correction factor for depth-length ratio; C_L = correction factor for total pipe length; C_S = correction factor for grain size; C_k = correction factor for permeability; C_Z = correction factor for underlayer with high permeability; C_γ = correction factor for density; C_B = correction factor for width of dam; C_α = correction factor for inclination; C_R = correction factor for dam axis curvature; and C_G = correction factor to adapt the experimental global gradients to local and field conditions.

Schmertmann (2000), and later Parekh et al. (2016), highlighted the importance of analyzing backward erosion piping using microscale observations of the hydraulic behavior to investigate this phenomenon. Schmertmann (2000) also highlighted the importance of the coefficient of uniformity in the critical gradient required for backward erosion progression. It was found that the experimental critical global gradient increased when the sand became less uniform; that is, as the coefficient of uniformity (d_{60} / d_{10}) increased. Nonetheless, it must be considered that a different mode of internal erosion may be developed in soils with non-uniform gradations.

Ojha et al. (2001) also made use of the Sellmeijer's Rule to calibrate a model for piping progression in terms of the porosity in the eroded sand. This model relates the Darcy's Law with the Kozeny-Carman equation for permeability (Carman 1956) and

estimates the pressure loss between the top of a water reservoir and an existing sand boil. The critical global head loss is described as:

$$\frac{H_{critic_1}}{H_{critic_2}} = \frac{a + b\left[\frac{(1-n_1)^p}{(n_1)^q}\right]}{a + b\left[\frac{(1-n_2)^p}{(n_2)^q}\right]} \quad \text{Eq. 2. 35}$$

where H_{critic_i} = critical head associated to a porosity n_i; p and q = 1 or 0 depending on the model for permeability and hydraulic gradient; and a and b = empirical constants. Ojha et al. (2003) later expanded this concept to adapt the critical hydraulic gradient as a function of the porosity of the soil to the Lane-of-Creep method.

Among the most common methods to estimate the critical values of the global hydraulic gradient, i_{global}, that lead to backward erosion piping, the Lane-of-Creep and the Weighted-Creep methods and the Sellmeijer's Rule are to be highlighted primarily because they are currently used in practice (Richards and Reddy 2007; van Beek et al. 2015). In addition, the study of the time for development of backward erosion by Fell et al. (2003) is of noticeable application. This work used a database of case studies and field observations to propose a logical framework to estimate the time required for piping to initiate and progress until failure considering three phases. It must be mentioned that this is an analysis of rates of development rather than actual measurements of time. Nonetheless, it was later used to analyze the probability of failure due to backward erosion piping (Fell and Wan 2005).

2.7 PHYSICAL MODELING OF BACKWARD EROSION PIPING

Physical modeling of backward erosion piping have been developed using models with different characteristics and have focused on the investigation of the effects of specific parameters on the critical hydraulic gradient leading to failure by this

phenomenon, i_{cr}, such as soil properties or the geometry of the structure (e.g., Fleshman and Rice 2013; Van Beek et al. 2011, 2014, 2015; Ovalle-Villamil and Sasanakul 2020, 2021), as well as to validate or improve existing analytical criteria (e.g., Schmertmann 2000; Sellmeijer et al. 2011). Regardless of the scope, the backward erosion piping process that was modeled in these studies began at a predefined exit for drainage and then progressed backwards across the interface between a sandy foundation and an impervious cover layer, towards a water source located upstream. Based on the setup used, the experimental approaches used in the literature can be classified as two- and three-dimensional experiments, depending on the flow distribution developed, as shown in Figure 2. 13.

Two-dimensional experiments model the flow conditions across the foundation of a water-retaining structure with two typical drainage configurations in the downstream zone. First, a structure with no cover layer in the downstream zone in which the foundation soil is exposed and constitutes an open exit, as shown in Figure 2. 13a; and second, a structure with a cover layer in the downstream zone in which the foundation soil is partially exposed, but the exit area is limited, such as in structures with a transversal trench or ditch, as shown in Figure 2. 13b. The flow lines in these experiments ideally remain parallel in a plan view of the structure, but two directions of flow develop in the cross-section. Three-dimensional experiments model the flow conditions across the foundation of a water-retaining structure with a cover layer in the downstream zone, which presents a localized exit point that resembles a hydraulic fracture, such as a crack or an animal burrow, as shown in Figure 2. 13c. The flow lines in these experiments

display two directions in the cross-section view but also in the plan view, as a result of the concentration of flow at the exit-hole.

Other studies used a one-dimensional configuration to model the hydraulic conditions inside the exit-hole, using a simplified perspective represented by cylindrical sand specimens. In these experiments, the flow followed a permanent upward direction, as shown in Figure 2. 13d. It is noted that these experiments described a localized initiation of backward erosion piping, in which a sand boil develops inside the exit-hole and prompts the formation of a piping path, and the outcomes from these models are not necessarily comparable with those obtained from two- and three-dimensional models.

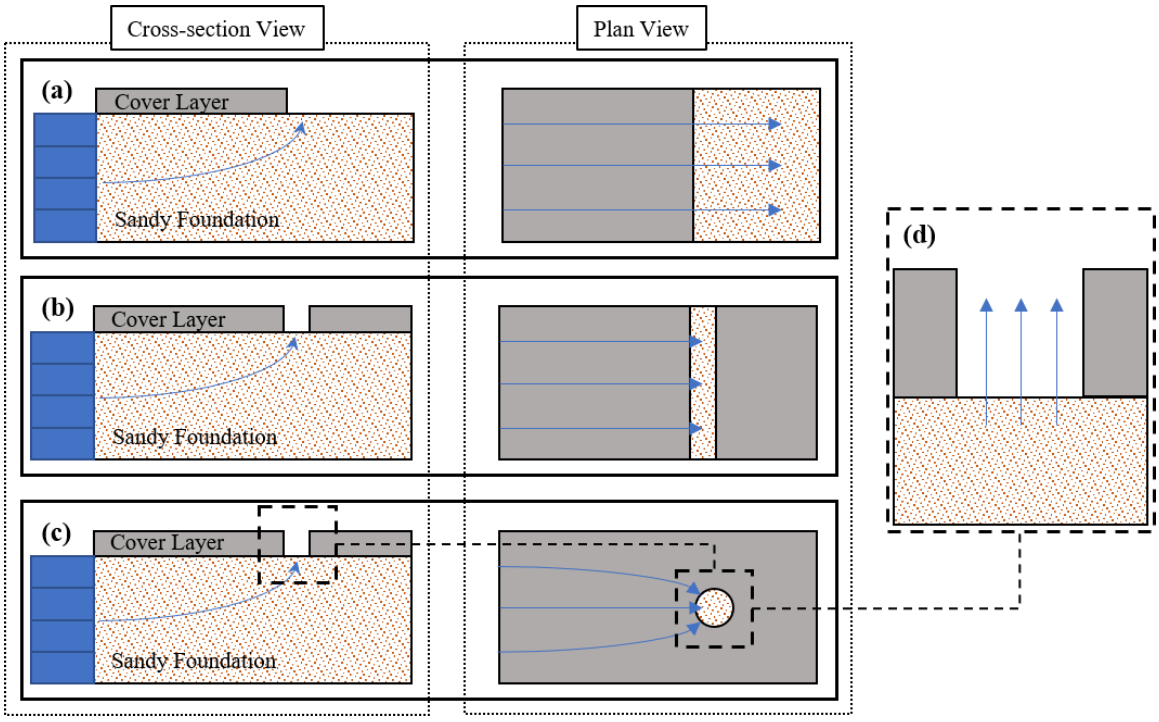

Figure 2. 13 Flow directions in physical models of backward erosion piping: (a) open exit, (b) ditch/trench exit, (c) exit-hole, and (d) one-dimensional.

It is also noted that alternative techniques have also been used to study the mechanism of backward erosion including triaxial devices (Bendahmane et al. 2008; Richards and Reddy 2012), flume-type tests (Sharif et al. 2015), among others. Likewise,

related phenomena, such as heave (Fontana 2008; Philipe and Badiane 2013) or suffusion (Marot et al. 2012), have been widely modeled.

2.7.1 One-dimensional experiments

Fleshman and Rice (2013, 2014) developed a series of experimental models to analyze the initiation phase of backward erosion piping and to evaluate the magnitude of i_{cr} across a column of sand leading to the initiation phase of piping erosion. These studies focused on modeling the flow conditions near a crack that are difficult to analyze using two- and three-dimensional experiments. These flow conditions and the experimental setup used are shown in Figure 2. 14 and Figure 2. 15, respectively. During test, upward flow was induced through soil specimens with a diameter, d_c, of 5.1 cm and a length, ΔL, of 12.7 cm until a seepage-induced failure occurred. A silicon coating was used on the interface between the soil specimens and the sample container to prevent preferred flow paths in the sides and to provide a frictional interface with the soil. The behavior was summarized in four typical phases: first visible movement described as a slight heave of the surface of the specimen, heave progression, sand boil formation, and total heave representing an unstable condition for which the entire specimen heaves upwards. The average i_{cr} obtained ranged from 1.32 to 1.47 in the phase of first visible movement, and 1.95 to 2.99 at total heave. The authors noted that a greater i_{cr} was required for sands with greater specific gravity and unit weight, as well as for well-graded sands and sands with angular shapes. Yang and Wang (2017) developed a similar study using cylindrical specimens with d_c of 10.5 cm and ΔL of 15 cm. This study did not use a coating at the soil-container interface and determined average values of i_{cr} from 0.81 to 1.02 for the first visible movement, and 0.93 to 1.21 for the total heave.

Peng and Rice (2020) evaluated the magnitude of i_{cr} to induce a transition from the original density to a loosened state in different sands, also using the experimental setup shown in Figure 2. 15, but with slightly greater specimens with a diameter, d_c, of 10.2 cm. Together with an inverse analysis of the experimental results using finite element models, the critical gradients estimated ranged from 0.65 to 1. It was also observed that the critical gradients increased with the overburden pressure, and such increase was greater in angular soils.

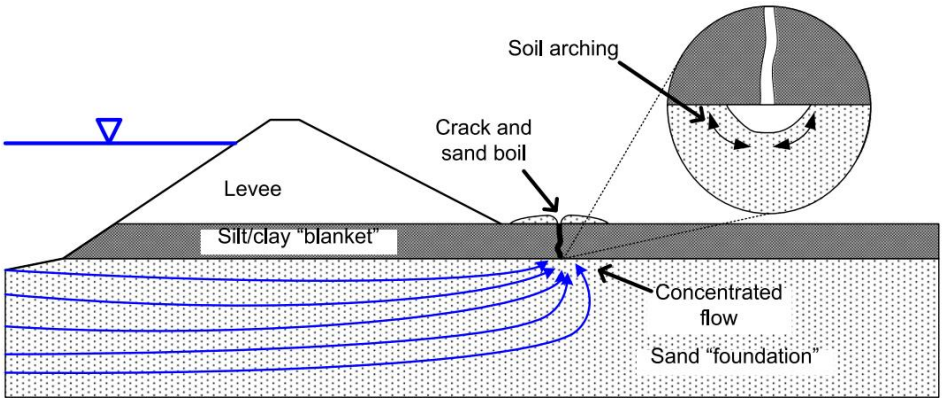

Figure 2. 14 Sketch of the exit point for one-dimensional experiments by Fleshman and Rice (2014).

Ovalle-Villamil and Sasanakul (2019) observed the initiation of piping erosion in centrifuge using cylindrical specimens of uniform, fine-grained sands and with d_c of 10.8 cm and average ΔL of 14 cm. A silicon coating was placed in the soil-container interface as used by Fleshman and Rice (2013, 2014). The values of i_{cr} for 1g tests for the first visible movement and the total heave were nearly 1 and 1.25, respectively, and increased by approximated factors of N in centrifuge tests at increased gravity Ng. This study highlighted that the total expansion of the specimen from the first visible movement to total heave decreased significantly in the centrifuge tests compared to 1g tests.

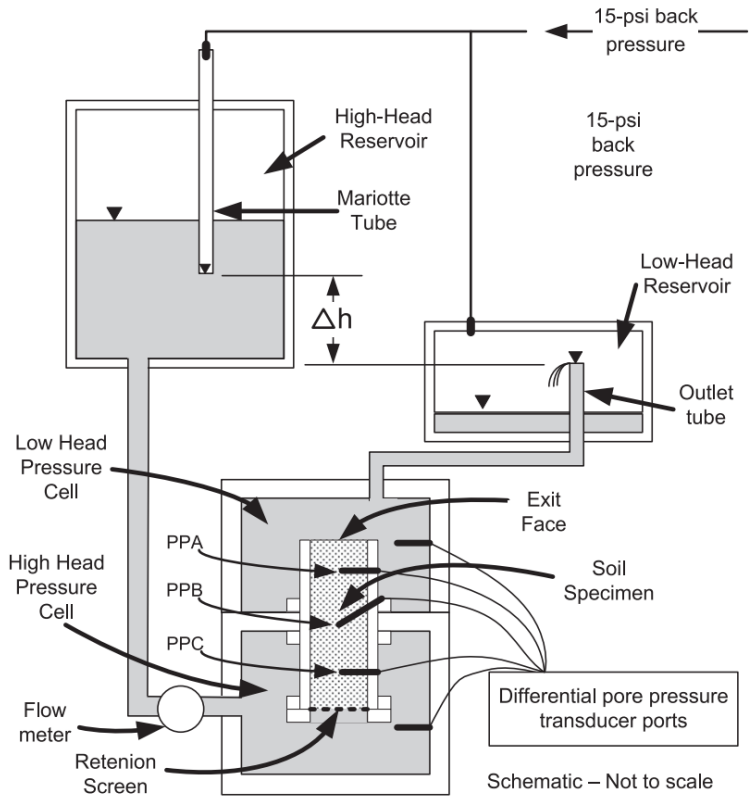

Figure 2. 15 Sketch of experimental setup in Fleshman and Rice (2013, 2014).

Tao and Tao (2017) used an alternative modelling approach based on a coupled computational fluid dynamics and discrete element method (CFD-DEM) to study the initiation of piping erosion through a micro-mechanical perspective. Their models replicated the experimental setup of Fleshman and Rice (2014) using cylindrical specimens with d_c of 2.76 cm and ΔL of 6.83 cm and studied two uniform gradations of sands composed of perfect spheres. The phases of first visible movement, heave progression and total heave were observed and values of i_{cr} obtained ranged from 0.82 to 1.67 in the phase of first visible movement, and 1.57 to 2.23 at total heave.

2.7.2 TWO-DIMENSIONAL EXPERIMENTS

Some experiments by de Wit et al. (1981) studied the effects of the soil type, relative density, type of exit and scale of model by using small-scaled, rectangular models subjected to horizontal flow, as shown in Figure 2. 16. The models with an open exit had seepage lengths of 0.8 m, 1.2 m, 2.4 m and 4.5 m, while models with a ditch type of exit had seepage lengths of 0.9 m and 2.7 m. Both types of model used clay cover layers and the models resembling a ditch type of exit had a ditch length of 5 cm. The foundation soils used had mean diameters, d_{50}, that ranged from 0.19 mm to 0.75 mm. Regardless of the size of the model and type of exit, the values i_{cr} triggering the phenomenon typically ranged from 0.16 to 0.43, but values as low as 0.09 and as high as 0.76 were also obtained. This study also highlighted that the critical hydraulic gradient required to extend a pipe to the upstream zone increased for coarser grains, denser sands, higher friction angles, and smaller exit points. Authors also approached the scaling effect by testing two models composed of the same soil but scaling the geometry by a factor of 3. They observed that the gradient required for backward erosion piping decreased with decreasing the scale of the models. In addition, it was observed by increasing the load in the clay cover layer that the effective stress in the soil had little effect in the critical gradients (van Beek 2015).

Silvis (1991) tested models using rectangular specimens and using a ditch type of exit with 0.5 m in length, as shown in Figure 2. 17. The seepage length varied for each experiment with values of 6 m, 9 m and 12 m, and the soil tested had a d_{50} of 0.21 mm. A steel plate was used as cover layer and a part was replaced by acrylate to allow visual observations of the piping process. The values of i_{cr} triggering the phenomenon were

0.04, 0.07 and 0.12 for seepage lengths of 9 m, 12 m and 6 m, respectively. The values of i_{cr} at failure were 0.12, 0.14 and 0.36 for the same order of seepage lengths. Results from this study were used for validation of the Sellmeijer's Rule analytical method (Sellmeijer 1988) and allowed observing a staged evolution of piping in which further increments of hydraulic gradient are required to extend the length of piping to a critical condition.

Full-scale experiments by Van Beek et al. (2011) also used a two-dimensional configuration with an open exit and tested a levee with a height of 3.5 m and a seepage length of 15 m, as shown in Figure 2. 18. The foundation soils had values of d_{50} of 0.15 mm and 0.20 mm. The hydraulic gradients obtained ranged from 0.08 to 0.11 at the initiation phase of the piping process, while values of i_{cr} ranged from 0.12 to 0.15. It was noted that sand boils formed for hydraulic gradients between 0.06 and 0.11.

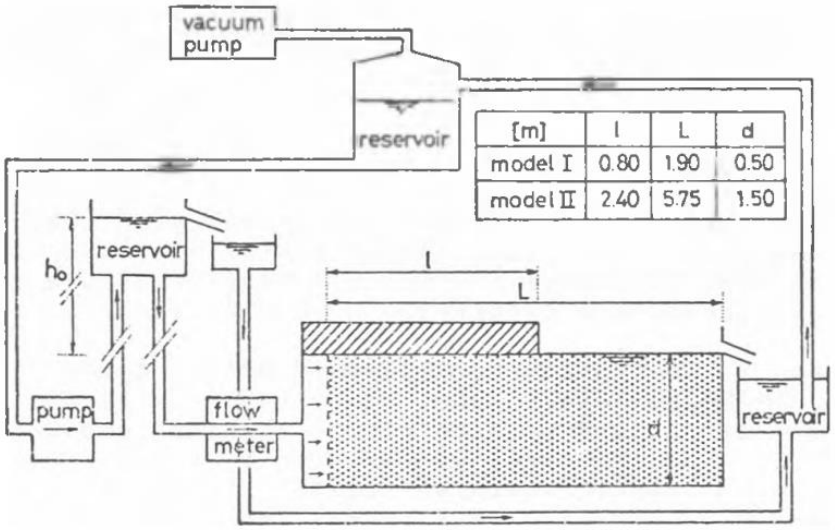

Figure 2. 16 Sketch of experimental setup in de Wit et al. (1981).

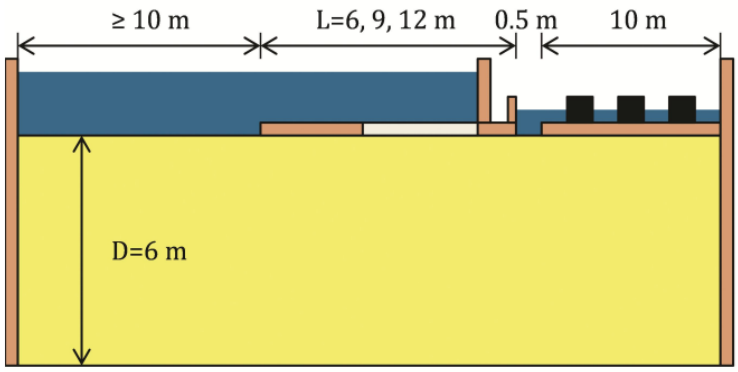

Figure 2. 17 Sketch of experimental setup in Silvis (1991).
Taken from Van Beek (2015).

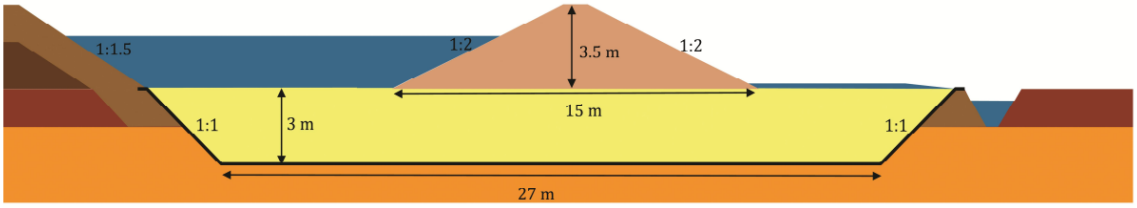

Figure 2. 18 Sketch of full-scale experiments by Van Beek et al. (2011).

Van Beek et al. (2010) developed an investigation of backward erosion piping in centrifuge models to observe the effects of increasing the gravitational acceleration field. The first model consisted of a sand foundation underlain by a plastic, transparent cover and was tested at 30g by increasing the hydraulic gradient across the specimen until sand transport was observed. The total seepage length and the thickness of the sand foundation were 35 cm and 10 cm, respectively, and an open exit was used to initiate the erosion (Bonelli 2013). The second model resembling a levee system with similar dimensions and exit type was tested at 80g. The critical global hydraulic gradients obtained in the first and second models were 0.33 and 0.23, respectively. This study showed that the

critical gradient decreases as the value of N increases due to the development of nonlaminar flow across the piping path.

Koito et al. (2016) developed a similar study of backward erosion piping in centrifuge models by modeling two levee systems with 20 cm in length and 5 cm and 2.5 cm in thickness of foundation soil. Both centrifuge models were tested at 50g and an open exit was used to initiate the erosion. The critical global hydraulic gradients obtained increased as the thickness of the foundation decreased, with average values of 0.214 and 0.333 for thickness values of 5 cm and 2.5 cm, respectively. This study highlighted that multiple piping paths with meandering behaviors may develop in the models, and the critical path does not necessarily follow the shortest seepage path (Horikoshi et al. 2019).

2.7.3 THREE-DIMENSIONAL EXPERIMENTS

Experiments by de Wit et al. (1981) displaying a three-dimensional configuration used rectangular soil specimens with 5.75 m in length, 0.5 m in width, 1.5 m in height, and a circular exit-hole across the clay cover layer with exit-hole diameters of 40 mm and 100 mm located at a distance of 2.4 m and 4.5 m from the upstream reservoir. The values of i_{cr} triggering the phenomenon ranged between 0.17 and 0.20, but sand boils occurred for hydraulic gradients between 0.11 and 0.15. The failure of the models occurred for the same magnitude of i_{cr} that initiated the phenomenon. This study highlighted that the exit-hole gradually filled with sand grains while the tests progressed, but the accumulation stopped until a greater hydraulic gradient was induced. Once the deposited sand exceeded the surface of the cover layer, the piping progressed until failure without further increments of gradient. This behavior was also observed by Miesel (1978) in experiments with larger exit-hole sizes (van Beek 2015).

Hanses (1985) also used three-dimensional experiments to investigate the effects of geometric variations in homogeneous and multilayered specimens using the experimental setup sketched in Figure 2. 19. The experiments used rectangular specimens with three typical sets of dimensions but a constant exit-hole diameter of 6 mm. The first set had 0.96 m in length, 0.24 m in width and 0.24 m in height. The second set had 0.9 m in length, 0.083 m in width and 0.165 m in height. The third set had 3.52 m in length, 0.33 m in width and 0.66 m height. The seepage lengths used were 0.7 m, 0.6 m and 2.6 m for the first, second and third set of experiments, respectively. The foundation soil had a d_{50} of 0.33 mm. The average values i_{cr} triggering the phenomenon were 0.18, 0.32 and 0.10 for the first, second and third sets of experiments, respectively. This study highlighted the development of two types of erosion, defined as primary erosion (i.e., erosion at the tip of the pipe due to local fluidization) and secondary erosion (i.e., widening and deepening of the pipe).

Van Beek et al. (2014) and Van Beek (2015) presented results from several three-dimensional experiments with seepage lengths of 0.3 m and 1.3 m, and with exit-hole diameters of 6 mm, 12 mm and 20.5 mm, as shown in Figure 2. 20. The values of d_{50} used ranged from 0.13 mm to 0.38 mm and the values of i_{cr} obtained ranged from 0.16 to 0.70, but the piping initiation was identified for hydraulic gradients between 0.04 and 0.20. Van Beek et al. (2014) highlighted that the influence of the grain size on i_{cr} was rather limited always that the gradation of the soil was uniform, as expected for backward erosion piping (Schmertmann 2000; Bonelli 2013), and its value only increased slightly as the diameter of the exit-hole increased. The value of i_{cr} tended to decrease as the size of the model increased, as also observed by de Wit et al. (1981).

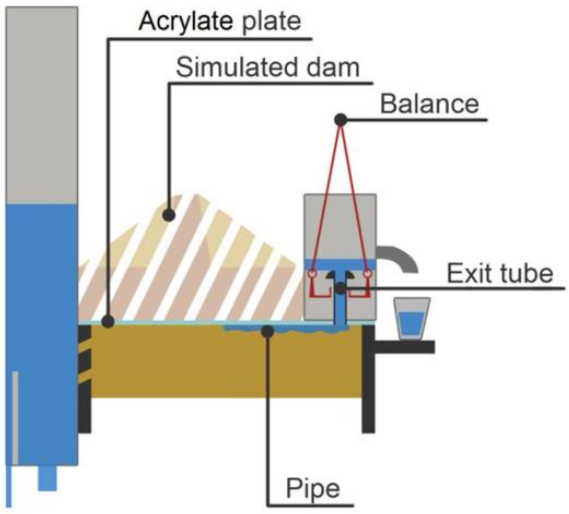

Figure 2. 19 Sketch of experimental setup in Hanses (1985). Taken from Van Beek (2015).

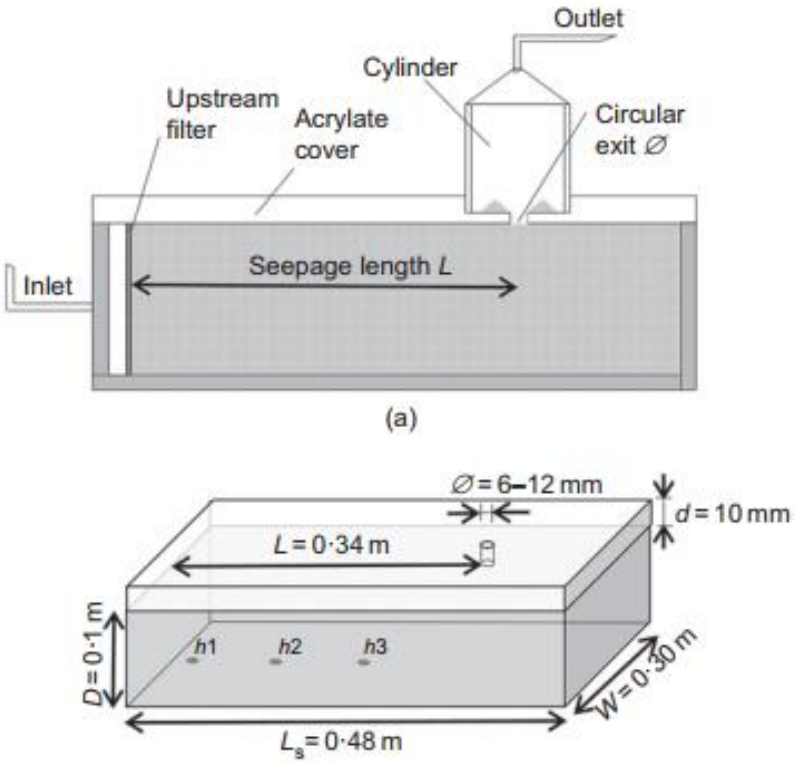

Figure 2. 20 Sketch of experimental setup in Van Beek (2015) and Van Beek et al. (2014, 2015).

Leavell et al. (2014) presented results from three centrifuge models tested at different levels of gravitational acceleration. The first two models simulated a levee foundation with 12.7 cm in thickness and 96.5 cm in length. A clay blanket with 2.5 cm in thickness was placed on top of the models and an exit-hole with 0.9 cm in diameter was used to initiate the erosion at a distance of 45.7 cm from the upstream reservoir. The third model had the same dimensions, but the thickness of the foundation was reduced by 2.5 cm and an additional clayey sand layer was added between the foundation and the clay blanket. Although values of critical hydraulic gradients are not reported in this study, post-failure visual observations of the three models showed that piping only occurs on the surface of the foundation. This study also highlighted that centrifuge models of backward erosion piping should be designed to be simplistic and to minimize the value of N as the scale effects become more significant as the gravitational acceleration field increases.

2.7.4 CRITICAL HYDRAULIC GRADIENT FROM PHYSICAL MODELS

Figure 2. 21 shows the estimations of i_{cr} obtained using two- and three dimensional experiments as functions of the ratio between the cross-sectional exit area, A_{Exit}, and that of the soil grains, A_{Grains}, and the results are discretized by the seepage length, L. The values of i_{cr} represent the hydraulic gradient reported when the failure of the models occurred, which corresponds to the moment when the foundation failed to maintain the impoundment. It is noted that the symbols in Fig. 2 represent the average value of i_{cr} from different models with same dimensions and soil, and the error bars indicate the range of values obtained. Results from full-scale experiments (Van Beek et al. 2011) and from centrifuge models tested at 50g (Koito et al. 2016) and 80g (Van Beek

et al. 2010) are presented as horizontal lines because an estimation of A_{Exit}/A_{Grain} is not available.

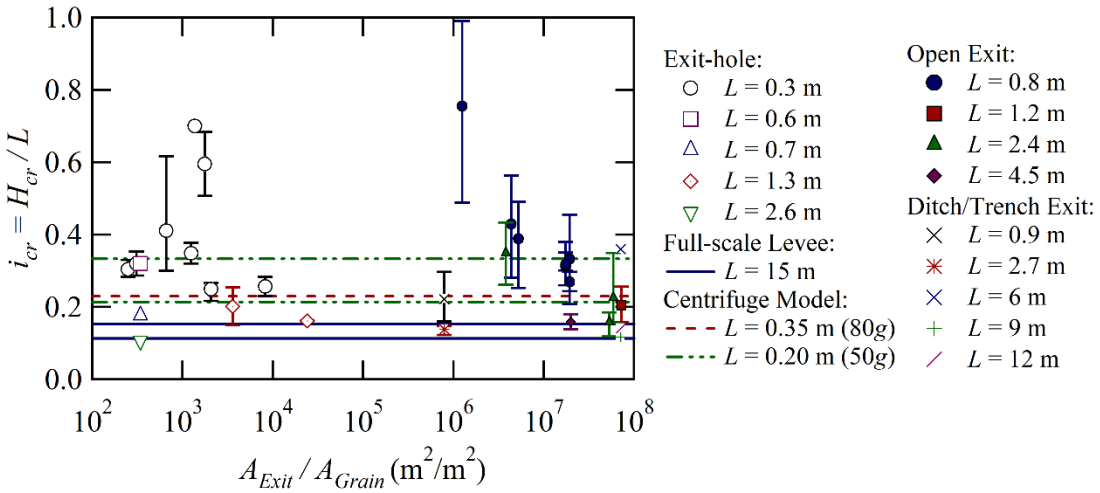

Figure 2. 21 Critical hydraulic gradients (at failure) from physical models of backward erosion piping.

It is observed that values of i_{cr} as low as 0.11 and as high as 1.0 were obtained from physical models of backward erosion piping and there was no clear tendency among the results that could capture the effects of seepage length, grain size and exit size. Variations in the value of i_{cr} for identical experiments were as high as 0.5 and 0.25 in experiments with a two- and three-dimensional configurations, respectively, and the grater variations occurred in models with shorter L. Nonetheless, most of the results ranged between 0.1 and 0.4, regardless of the type of model, and two general trends could be identified. First, the value of i_{cr} displayed a decreasing tendency as A_{Exit}/A_{Grain} increased, which indicates that i_{cr} decreased as the exit area increased. Second, the value of i_{cr} also displayed a decreasing tendency as L increased. There were not enough results to determine a reliable tendency in function of the gravitational acceleration field in centrifuge models, but it was observed that a lower value of i_{cr} was estimated in the

model tested a greater gravity level, even though the L was greater. It is also noted that the values of i_{cr} from centrifuge models were closer to the results from full-scale models, compared the models with similar dimensions.

CHAPTER 3

FLOW BEHAVIOR IN CENTRIFUGE MODELS OF COHESIONLESS MATERIALS[1, 2]

[1]Ovalle-Villamil, W., and Sasanakul, I. (2018) "Investigation of Non-Darcy Flow for Fine Grained Materials." *Journal of Geotechnical and Geological Engineering*, https://doi.org/10.1007/s10706-018-0620-x, Jul. 2018.

[2]Ovalle-Villamil, W., and Sasanakul, I. (2018) "A new insight into the behaviour of seepage flow in centrifuge modelling." *Physical Modelling in Geotechnics, Volume 1: Proc. of the 9th International Conference on Physical Modelling in Geotechnics (ICPMG 2018),* London, United Kingdom, July 2018, pp.259.

3.1 INTRODUCTION

Understanding the phenomenon of flow through granular materials and man-made porous media has a remarkable impact on applied engineering and industrial applications. Several research studies have been undertaken to investigate the characteristics of flow through porous media and proposed empirical expressions to describe the relationship between pressure gradient and velocity of flow (e.g., Comiti and Renaud 1989; Wahyudi et al. 2002; Mathias et al. 2008; Mesquita et al. 2012; Andreasen et al. 2013; Dukhan et al. 2014). In geotechnical and geological engineering, groundwater flow or flow through earth structures is analyzed using Darcy's Law, assuming a permanent viscous condition in which the velocity of flow is linearly proportional to the hydraulic gradient. This assumption is valid when velocities of flow experienced in these structures are relatively low. However, the flow behavior may exhibit nonlinearities in some field conditions including breakwater structures and rapid flooding (e.g., Gelhar et al. 1992; Nielsen 1992; Kreibich et al. 2009), or in laboratory conditions such as geotechnical centrifuge modeling (Khalifa et al. 2002). Consequently, studies of phenomena involving erosion due to flow of water using the centrifuge modeling technique must consider analyzing the flow conditions under increased gravitational acceleration fields.

The Forchheimer's law has been proposed to describe non-viscous flow in porous media using a nonlinear relationship to relate gradient and velocity of flow using a combination of viscous and inertia terms. Several researchers, such as Ergun (1952), Macdonald et al. (1979), Kadlec and Knight (1996), Sidiropoulou et al. (2007), and others, have used extensive experimental results to relate Forchheimer's Law to fluid properties and porous media characteristics. However, despite the remarkable advances

for modeling flow in porous media, some limitations remain. First, previous studies used experimental results obtained mostly from materials with particle sizes ranging from gravels to medium sands. Results for fine to very fine sands, usually used for centrifuge modeling, are limited. Second, the approaches describing both viscous (e.g., Kozeny 1927; Carman 1937, 1956), and non-viscous flow (e.g., Comiti and Renaud 1989), require crude assumptions of material properties that are not easily obtained, such as tortuosity or the porous shape. Furthermore, the determination of the limit between viscous and non-viscous flow varies among the researchers (Khalifa et al. 2000; Ovalle-Villamil and Sasanakul 2018).

In centrifuge modeling, a scaled model is subjected to a gravitation acceleration field of N times Earth's gravity (i.e., $\boldsymbol{a} = N$). If the same soil and fluid in the full-scale prototype are used in the model (i.e., $\boldsymbol{\rho_s} = \boldsymbol{\rho_w} = 1$), the velocity of flow in the model is increased N times higher than the velocity of flow in the prototype (i.e. $\boldsymbol{v} = N$) to ensure similarity in the events modeled (Laut 1975; Garnier et al. 2007). As a result, the flow velocity may exceed the limit of viscous conditions of flow. A unique value of Reynolds Number of 1 has been used to limit the validity of Darcy's Law in centrifuge models (Arulanandan et al. 1988; Singh and Gupta 2011). However, this limit does not account for the characteristics of the porous media or the different interpretations of the Reynolds Number.

This study provides new insights into the impact of physical properties of porous media on the non-Darcy flow. The research focuses on an investigation of fine-grained sands typically used for geotechnical centrifuge modeling studies. Mathematical expressions are established to describe the Forchheimer flow parameters and their

relationships with the characteristics of various porous media. Effects of centrifuge gravitation on flow behavior are evaluated and results are used for evaluating the limit of validity of Darcy's Law. The transition from Darcy's domain relating to the material properties is further analyzed and discussed using two different definitions of Reynolds Number.

3.2 EXPERIMENTAL METHODOLOGY

A series of permeability tests were conducted using a customized setup assembled in a 1.3 m-radius geotechnical centrifuge located at the University of South Carolina. The setup presented in Figure 3. 1 was designed to investigate the flow characteristics over a wide range of pressure gradients, and to allow precise measurements of gradient and velocity of flow within the specimen while subjected to levels of centrifuge gravity of 1g, 10g, 20g, and 30g. The permeameter located inside the centrifuge allows placing specimens with 0.07 m in diameter and 0.15 m in length. Glass marbles are located on the top and bottom of the specimen to ensure homogeneous distribution of flow. The air-water cylinder system located outside of the centrifuge is used to force water to flow into the specimen through one of the passages of the centrifuge rotary joint. Afterwards, the water is returned through the other passage to the cylinder system while the centrifuge is spinning.

The air-water cylinder system includes 3 cylinders, with 0.10 m of internal diameter and 0.30 m of stroke, allowing a storage capacity of 2.5 liters. The cylinders, namely head tank, atmospheric tank, and back-pressure tank are all connected in a closed system. Each cylinder comprises water and air chambers separated by a piston. The air chambers for the head tank and the back-pressure tank are connected to an air supply line,

while the air chamber for the atmospheric tank is connected to atmospheric pressure. The pressure gradient is applied to the specimen by increasing the air pressure at the head tank. Consequently, the water chamber can be pressurized to establish a flow through the specimen over a wide range of gradients. Two pressure sensors measure the pressure losses over a sample length of 0.13 m. The water flowing out of the sample is then driven to the water chamber of the atmospheric tank. A Linear Variable Differential Transformer (LVDT) is used to precisely measure displacement of the piston with time. Hence, the velocity of flow can be determined. The piston of the head tank and the atmospheric tank are connected to ensure the continuity of flow in and out of the specimen. The back-pressure tank is used for the specimen saturation described in the next section.

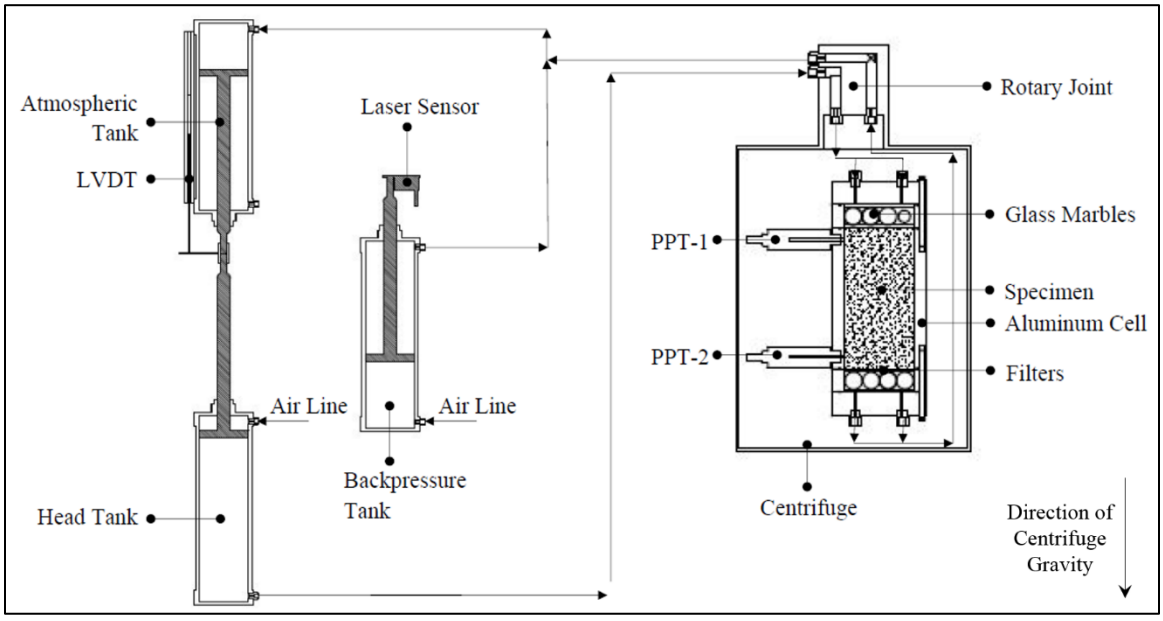

Figure 3. 1 Experimental setup for Research Topic 1 (not to scale).

The tests were performed by gradually increasing the pressure gradient, resulting in the change of velocity of flow with time at approximately 0.0004-0.001 m/s per

second. The effect of unsteady flow due the increase of flow velocity may be expected, as reported by Khalifa et al. (2002). However, steady state tests were performed on selected samples, and results agreed with results from the testing method used in this study. Therefore, the quasi-steady state flow condition is assumed to be valid, and a continuous relationship between gradient and flow velocity can be obtained by the discretization of time. Additional 1g bench tests were performed without spinning the centrifuge using the same setup previously described, but the system bypasses the rotary joint of the centrifuge.

3.3 SAMPLE PREPARATION AND MATERIAL PROPERTIES

Specimens were prepared by dry pluviation. Six layers with 25.4 mm of thickness were pluviated and each layer was carefully compacted using a rubber tamper to develop a homogeneous distribution of the specimen. To avoid migration of particles through the filters, the portion of the samples with grain size lower than 0.075 mm (No. 200 sieve) was removed. Specimens were saturated by flushing CO_2 through the sample at a very low pressure and then water was introduced into the sample from the base. Water was flushed through the system for an extended time until there was no evidence of air bubbles in the water lines. Back-pressure was then applied to the system using the back-pressure tank shown in Figure 3. 1. The change in volume of air, if any, was observed from the displacement of this piston. This process was repeated by incrementally increasing the back-pressure until there was no displacement.

This study focuses on fine-grained materials with an effective diameter, d_{eff}, ranging from 0.13 to 1.94 mm. These materials are Glass Beads (GB) and 3 sands from different geographic regions. These sands are Nevada Sand (NS), Columbia Sand (CS,

CSf), and Eau Claire Sand (ECS). Nevada Sand is a well-known fine laboratory sand native to Sierra Nevada region. Columbia Sand is silica sand native to Columbia, South Carolina. Eau Claire Sand is relative coarser silica sand native to Eau Claire, Wisconsin. Grain-size distributions of these materials are shown in Figure 3. 2. General characteristics including effective diameter, particle shape and gradation parameters are presented in Table 3. 1.

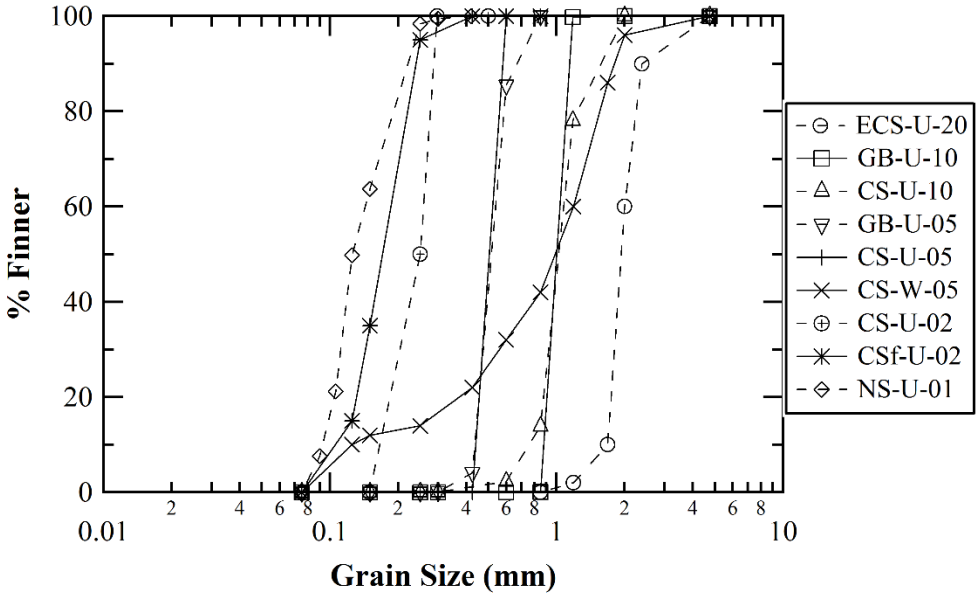

Figure 3. 2 Grain-size distributions of materials tested in Research Topic 1.

As shown on Figure 3. 2 and Table 3. 1, tests were performed with different test matrices (i.e. particle size, porosity, and gradation). A well-graded sample was tested in comparison with a uniformly graded sample having the same d_{eff} of 0.5 mm for Columbia sand. It is noted that Nevada Sand typically used in centrifuge modeling is the finest material tested with d_{eff} of 0.13 mm. A total of 9 samples were tested in centrifuge and additional 7 samples were tested using the bench test setup.

Table 3. 1 General characteristics of materials tested in Research Topic 1.

Sample ID	Effective Diameter d_{eff} (mm)	Particle Shape	C_u	C_g	Gradation
ECS-U-20	1.94	Subangular to Angular	1.20	0.97	Uniform
GB-U-10	1.00	Spherical	1.18	0.97	Uniform
CS-U-10	1.00	Subrounded to Subangular	1.41	1.04	Uniform
GB-U-05	0.52	Spherical	1.23	0.97	Uniform
CS-U-05	0.51	Subrounded to Subangular	1.20	0.97	Uniform
CS-W-05	0.44	Subrounded to Subangular	9.57	2.12	Well-Graded
CS-U-02	0.23	Subrounded to Subangular	1.56	0.97	Uniform
CSf-U-02	0.16	Subrounded to Subangular	1.75	1.06	Uniform
NS-U-01	0.13	Subrounded	1.54	0.95	Uniform

3.4 RESULTS AND DISCUSSION

3.4.1 VARIATION OF GRADIENT WITH VELOCITY OF FLOW

Figure 3. 3 shows the variation of the gradient in terms of pressure head, $\Delta P/\Delta L$ and distance head, i, in function of the velocity of flow for sample ECS-U-20. The data in this figure was obtained from both centrifuge and bench tests performed on two different specimens prepared at similar porosity. Due to some pressure loss through the centrifuge rotary joint, lower maximum gradients were achieved in the centrifuge tests. As a result of this limitation, the maximum resultant velocity measured in the bench tests was nearly two times greater (0.02 m/s). Despite the limitation, the velocity achieved in the centrifuge tests was high enough to reach non-Darcy flow in most of the specimens tested, and to account for potential velocities of flow experienced in different geotechnical and geological applications. Wide ranges of flow velocities for different field conditions, from very low to more than 1 m/s in coastal environment (e.g. Neilsen 1992), up to 1.5 m/s in flood conditions (e.g. Kreibich et al. 2009), and from 1.2×10^{-7} to

0.002 m/s in flow through aquifers (e.g. Gelhar et al. 1992), are experienced depending upon the flow conditions.

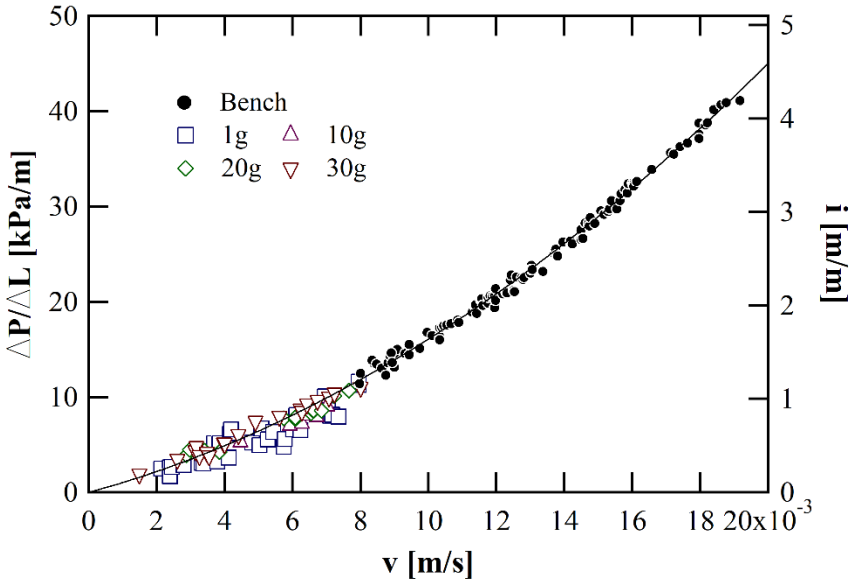

Figure 3. 3 Evolution of gradients against the velocity of flow for specimen ECS-U-20.

Hydraulic gradients and velocities experienced on both setups are compared and good agreement is observed for all the tests. Therefore, the results from bench tests are justified to use as an extension of the centrifuge testing results in order to observe the flow behavior at the maximum gradients and velocities possible. Figure 3. 4a and 3. 4b show the unified flow behavior experienced with the coarser ($d_{eff} \geq 0.5$ mm) and finer ($d_{eff} < 0.5$ mm) samples, respectively. The maximum velocity of flow of 0.016 m/s induced in the finest Columbia Sand (CSf-U-02) is translated to a dimensionless hydraulic gradient of 150. Markedly lower hydraulic gradients of up to 5 were induced with the coarser sand (ECS-U-20) at a velocity of nearly 0.02 m/s.

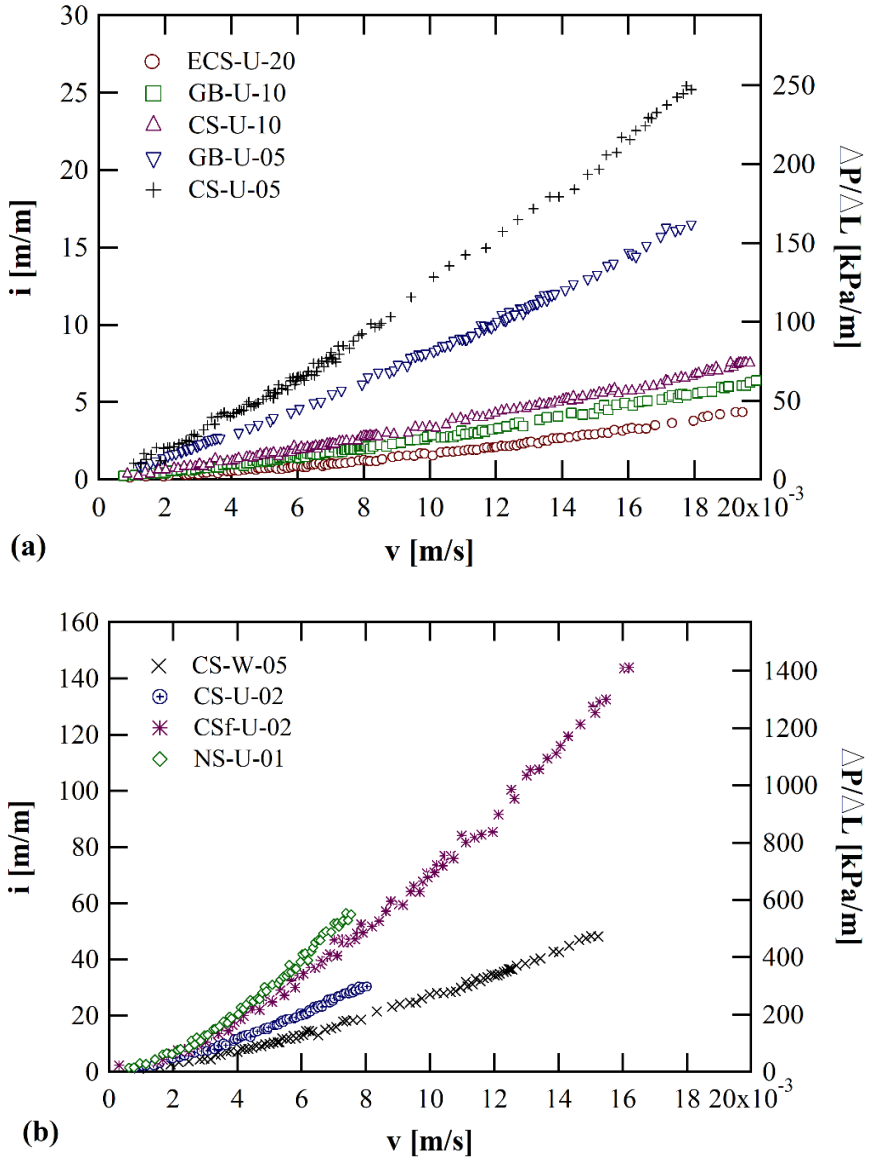

Figure 3. 4 Evolution of gradients against the velocity of flow for specimens with (a) $d_{eff} \geq 0.5$ mm, and (b) $d_{eff} < 0.5$ mm.

Observation of Figure 3. 4 allows the identification of nonlinear behavior in samples CS-U-05 and CSf-U-02. The transition from a linear relationship can be roughly seen beyond velocities within 0.006 and 0.008 m/s. However, the transition to non-Darcy

flow is difficult to identify in the remaining samples. A better evaluation of the occurrence of nonlinear flow is presented in the next section.

3.4.2 Determination of Forchheimer coefficients from nonlinear flow tests

The nonlinearity observed among the results obtained can be examined by normalizing the pressure gradients with the velocity of flow (MacDonald et al. 1979; Comiti and Renaud 1989), as shown in Figure 3. 5 for samples GB-U-10 and ECS-U-20. Two different flow behaviors are observed from the change in slope of these plots. In the plot for sample GB-U-10 (Figure 3. 5a), the initial slope appears to be steeper than the second slope. According to Dukhan et al. (2014), this change can be interpreted as the transition from a post-Darcy condition of flow, represented by the first slope, to a fully developed Forchheimer condition, represented by the final slope. This observation implies that the material experienced non-Darcy flow throughout the range of velocities tested. The plot for sample ECS-U-20 (Figure 3. 5b) shows a different behavior with an initial relatively flat slope that then increased at higher velocities. In this case, the initial horizontal portion represents a fully viscous flow for the range of velocities experienced in centrifuge, and the inclined portion represents the transition from this domain.

The normalization of pressure gradient presented in Figure 3. 5 also allows the determination of the Forchheimer coefficients A and B (Eq. 2. 3). As shown in the same figure, a linear least squares regression of the normalized gradients varying with the velocity results in a y-intercept and a slope equivalent to A and B, respectively. Table 3. 2 summarizes the values of these coefficients obtained for all samples from bench and centrifuge tests.

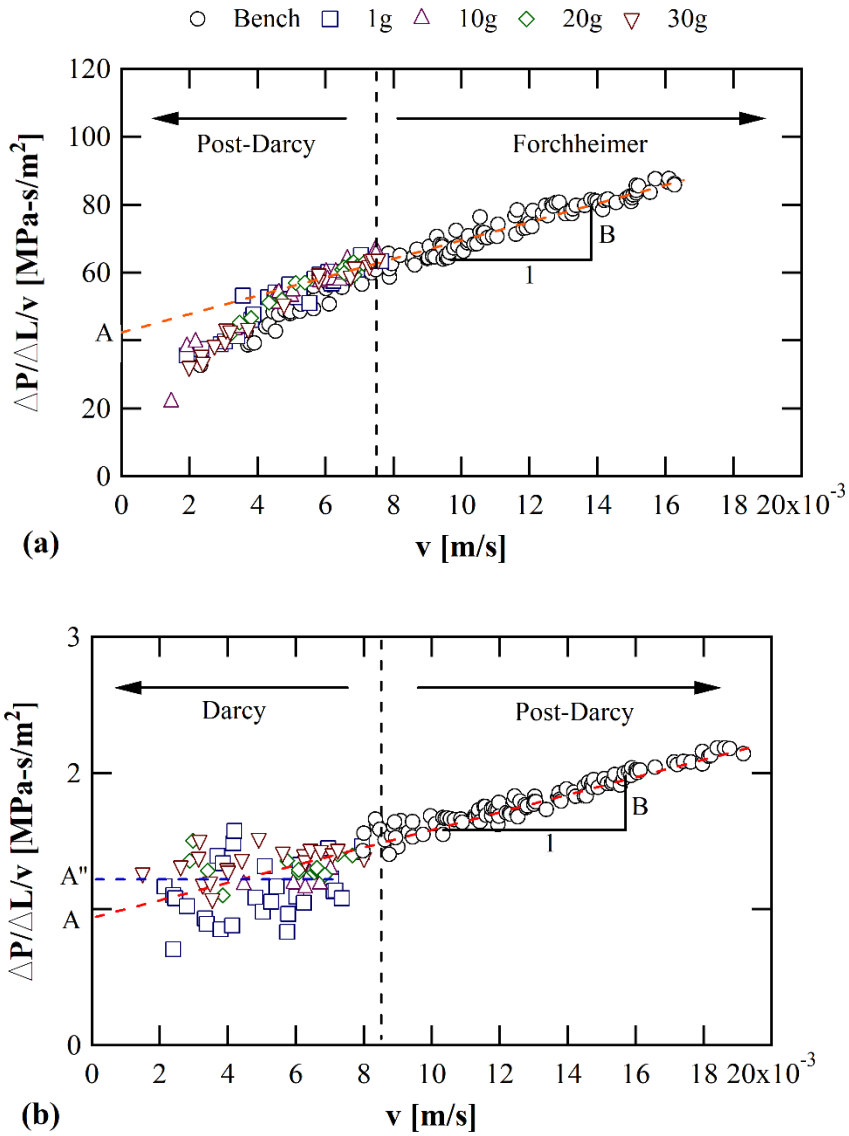

Figure 3. 5 Typical regimes of flow identified using normalized pressure gradients for specimens (a) GB-U-10 and (b) ECS-U-20.

Results in Table 3. 2 indicate that Forchheimer coefficients decreased as d_{eff} increased. The specimens with d_{eff} of 1.0 mm have A and B values ranging from 2 to 3 MPa-s/m^2 and 36 to 60 MPa-s^2/m^3, respectively, regardless of particle shape and gradation. By comparison, the specimens with d_{eff} of 0.5 mm have values of A and B

ranging from 6 to 30 MPa-s/m^2 and 233 and 915 MPa-s^2/m^3. It is important to note that although a few specimens presented initial viscous flow characteristics, coefficient A was estimated from the linear regression of the inclined line (Figure 3. 5b). Estimations of coefficient B greater than zero prove that the range of flow velocity used in this study was high enough to develop non-Darcy conditions of flow for all the samples.

Table 3. 2 Forchheimer coefficients A and B obtained in centrifuge and bench tests.

Sample	Porosity	S_b (mm^{-1})	Centrifuge Acceleration (Ng)	A (MPa-s/m^2)	B (MPa-s^2/m^3)
ECS-U-20	0.350	2.379	1	1.082	12.74
			10	1.184	5.27
			20	1.222	11.09
			30	1.212	31.56
	0.347	2.391	Bench	0.967	64.24
GB-U-10	0.368	3.784	1	2.230	37.80
			10	2.244	36.77
			20	2.121	60.27
			30	2.260	50.25
	0.380	3.716	Bench	2.152	49.16
CS-U-10	0.415	3.513	1	2.619	51.48
			10	2.525	59.81
			20	2.697	51.64
			30	2.785	57.15
	0.425	3.456	Bench	3.035	35.97
GB-U-05	0.365	7.357	1	6.651	233.35
			10	6.561	261.46
			20	6.520	265.44
			30	6.639	224.86
	0.373	7.265	Bench	6.673	138.52
CS-U-05	0.397	7.170	1	8.247	342.78
			10	9.098	261.73
			20	8.786	283.16
			30	7.815	441.02
	0.404	7.082	Bench	9.885	230.82

Table 3. 2 Forchheimer coefficients A and B obtained in centrifuge and bench tests (continuation).

Sample	Porosity	S_b (mm^{-1})	Centrifuge Acceleration (Ng)	A (MPa-s/m^2)	B (MPa-s^2/m^3)
CS-W-05	0.324	9.314	1	22.14	915.70
			10	22.50	680.02
			20	21.65	532.38
			30	21.27	538.40
	0.335	9.164	Bench	29.69	380.42
CS-U-02	0.405	15.784	1	16.03	2843.4
			10	16.82	2751.7
			20	16.54	2814.3
			30	16.31	2836.2
CSf-U-02	0.397	22.656	1	22.10	5940.7
			10	23.84	5707.5
			20	25.62	5352.4
			30	21.89	5690.3
	0.406	22.320	Bench	30.30	3722.0
NS-U-01	0.372	28.856	1	66.32	4009.3
			10	65.39	3721.0
			20	66.71	3770.2
			30	69.10	3429.4

3.4.3 Effect of centrifuge gravitational acceleration

Estimations of coefficients A and B in Table 3. 2 show differences among the specimens tested and the type of test. For instance, values of B are less consistent between centrifuge and bench tests. According to Bear (2013), different factors could lead to variations in these coefficients, such as the transition between the various flow regimes, the characteristics of the material, the experimental setup, or the uncertainties related to the flow phenomenon. Nonetheless, the values of Forchheimer coefficients appear to be consistent with centrifuge acceleration. In Figure 3. 3 and Figure 3. 5 discussed previously, the initial portions show the results obtained when the specimen

was subjected to centrifuge gravitation accelerations of 1g, 10g, 20g, and 30g. In these portions, the evolution of gradients and normalized gradients as functions of the velocity of flow present nearly identical behaviors despite the level of acceleration. This consistency with centrifuge gravitational acceleration indicates that the effect of gravity is small or nonexistent in the range of velocities tested.

Other researchers (e.g., Khalifa et al. 2000) made similar conclusions for Darcy's permeability, k, and indicated that some variations in the relationship between hydraulic gradients and velocity of flow might be observed due to compression of the specimen during the centrifuge spin up. In this study, the specimens were compacted to a very dense consistency to minimize the compression at high gravity. Therefore, the independence of the centrifuge gravitational acceleration on the gradient-velocity relation for Darcy's flow condition can be extended to non-viscous flow conditions for the range of gravity tested. It is important to consider that increasing the centrifuge acceleration may generate more noticeable effects of the change in the fluid viscosity.

3.4.4 Prediction of Forchheimer coefficients and Darcy's permeability

Forchheimer coefficients are dependent not only on the particle size and porosity but on other characteristics of the material, including particle shape and grain-size distribution. These characteristics are not explicitly included in the expressions describing the flow through porous media, as presented in Table 2. 3. However, such characteristics influence the distribution of voids and solids in the medium as well as the particle effective diameter. The surface area in contact with fluid, S_b, presented in Eq. 2. 4, can be used as a variable accounting for the effects of n and d_{eff} for each material

tested. Figure 3. 6 shows that the coefficients A and B increase as S_b increases. Curve-fitting functions of both A and B are provided with this plot.

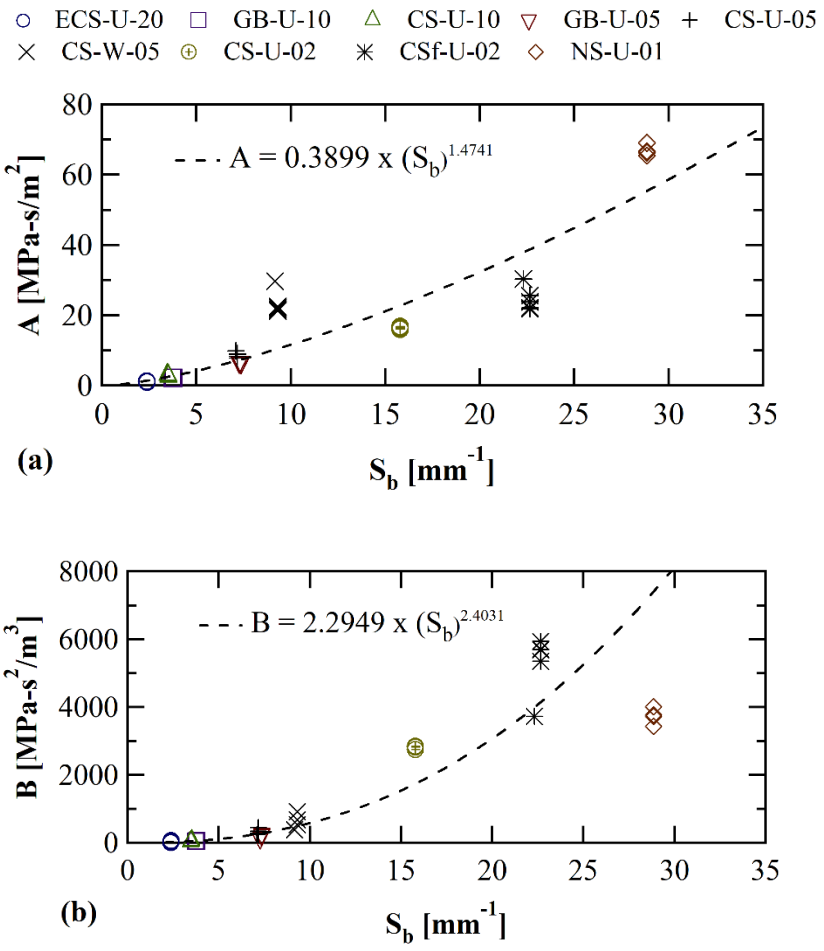

Figure 3. 6 Correlation between Forchheimer coefficient and surface are in contact with fluid: (a) coefficient A, and (b) coefficient B.

The curve-fitting functions in Figure 3. 6 are compared with experimental estimations of Forchheimer coefficients from different researchers, as presented in Figure 3. 7. Comiti and Renaud (1989) reported values of A and B for spherical marbles with diameters ranging from 1.0 to 5.0 mm, and velocities of flow up to 0.04 m/s. Macdonald et al. (1979) and Abbood (2009) developed flow analyses for glass beads, sands, gravels,

and other crushed materials with particle sizes ranging from 0.5 to 30 mm, and velocities of flow up to 0.022 m/s. Sidiropoulou et al. (2007), Moutsopoulos et al. (2009), Sedghi-Als et al. (2014), and Snoijers (2016), on the other hand, focused their works in coarse sands and gravels with particle sizes from 0.60 to 67 mm, and velocities of flow up to 0.03, 0.04, and 0.15 m/s, respectively. The porosities used in these studies range from 0.32 to 0.50.

It is observed in Figure 3. 7 that there is a small increase of the parameters A and B with respect to S_b, as reported in the previous works. Results for fine-grained sands from this study show a similar behavior extending toward high values of S_b. However, there was no data available in the literature for a comparison in this range. The values of the Forchheimer coefficients from other researchers are lower than the curve-fitting functions obtained in this study. This difference may be due to the velocity of flow used in the experiments. The maximum velocity of flow in this study was 0.02 m/s, while velocities of up to 0.15 m/s were achieved for some of the results in Figure 3. 7. This difference could lead to different regimes of flow, resulting in some differences in Forchheimer coefficients, as presented initially in Figure 2. 9.

The effect of the velocities of flow used to determine A and B is evaluated by comparing predictions of gradient-velocity relations using the curve-fitting functions presented in Figure 3. 6 and the models of Ergun (1952), Kovacs (1981), Kadlec and Knight (1996), and Sidiropoulou et al. (2007), presented in Table 2. 3. Non-Darcy flow behavior for Hostun Sand (Khalifa et al. 2002) and Ottawa Sand (Goodings 1994) is predicted, as shown in Figure 3. 8. Predictions from this study agree with the experimental results. The models of Ergun (1952), Kovacs (1981), and Sidiropoulou et al.

(2007) underestimate and the model of Kadlec and Knight (1996) overestimates the experimental data for the range of flow velocities up to 0.01 m/s.

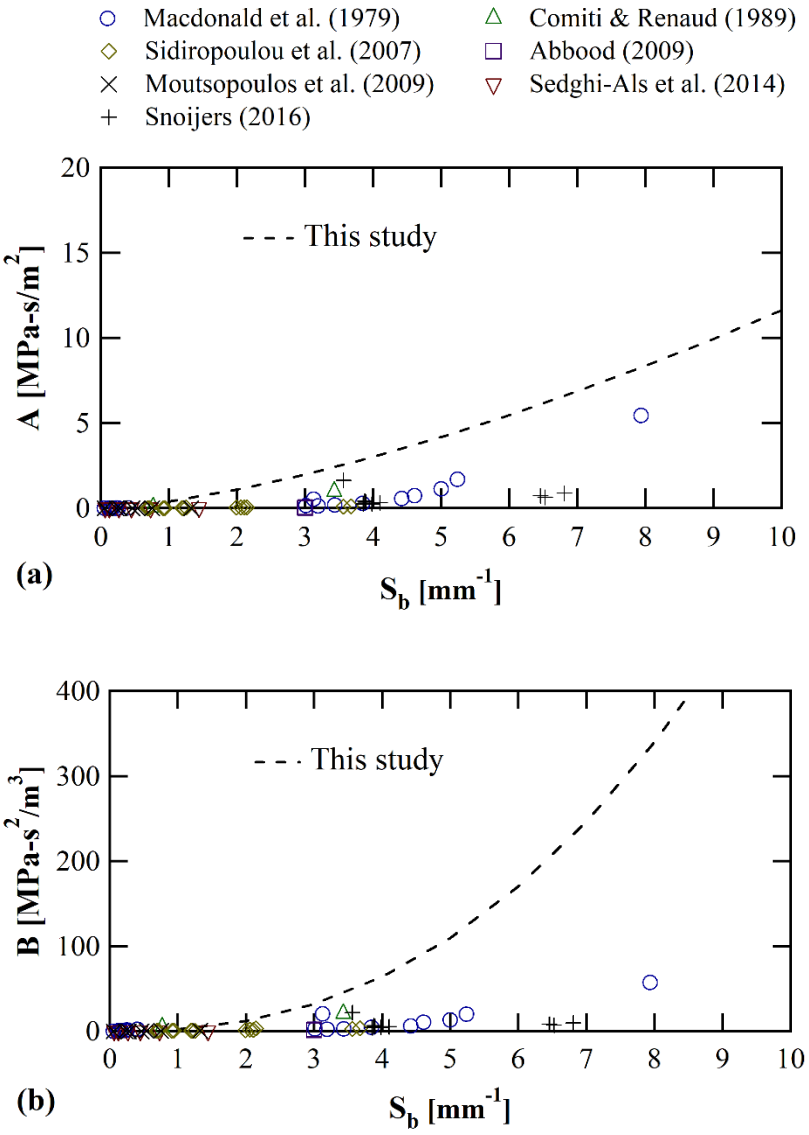

Figure 3. 7 Comparison between the empirical relationship of Forchheimer coefficients with others: (a) coefficient *A*, and (b) coefficient *B*.

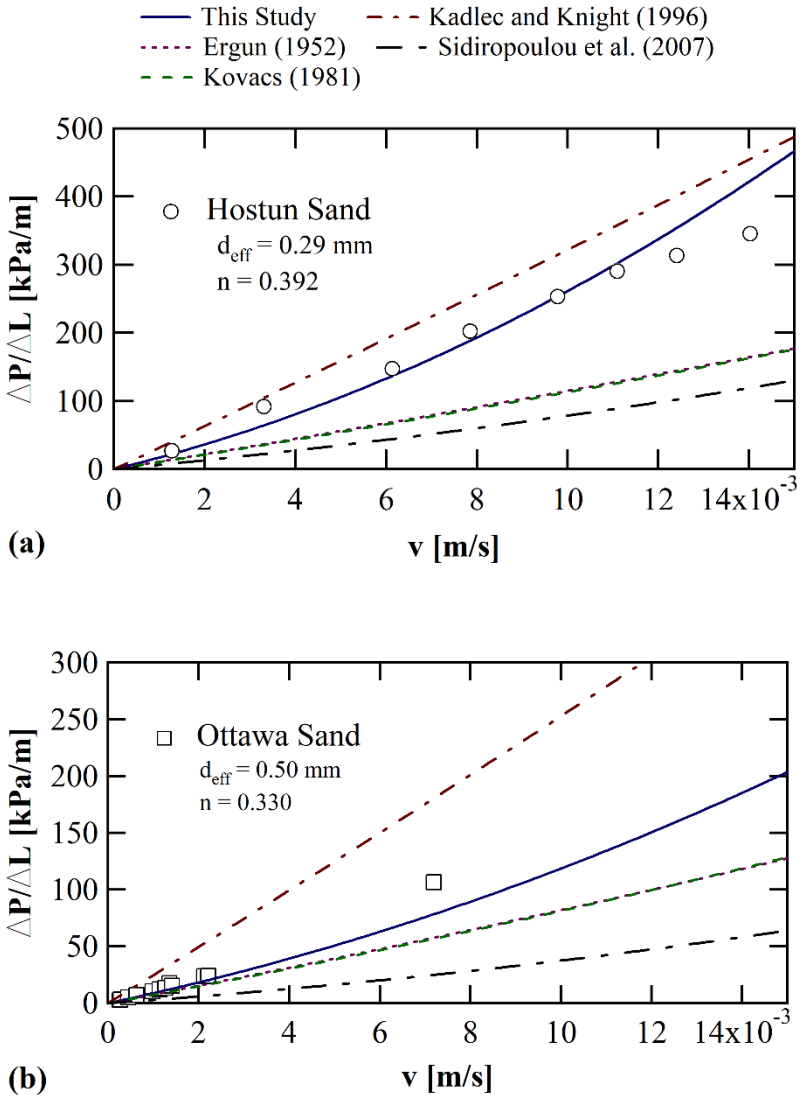

Figure 3. 8 Predictions of gradient-velocity relation for (a) Hostun Sand (Khalifa et al. 2000a, b), and (b) Ottawa Sand (Goodings 1994).

As shown in Figure 3. 8, the good prediction using the model developed in this study is valid for the range of velocity up to 0.02 m/s and it should not extend beyond this limit. This research focuses on the non-Darcy flow behavior of fine-grained sand at relatively lower velocities, such as those experienced in many geotechnical applications and in centrifuge modeling. The other models may be more appropriate for flow in

coarser materials at much higher velocity. The applicable range of flow velocities should be considered when selecting a model for predicting Forchheimer coefficients.

Values of coefficient *A* are used to estimate the Darcy's permeability, *k*, for each sample tested using Eqs. 2. 2 and 2. 8. Results are compared with other experimental values and the power law proposed by Chapuis (2004), as shown in Figure 3. 9. Although the regime of flow analyzed here is nonlinear, estimations of *k* are consistent with the literature due to the relatively lower range of velocities tested. This result verifies the use of coefficient *A* to represent the viscous domain of flow.

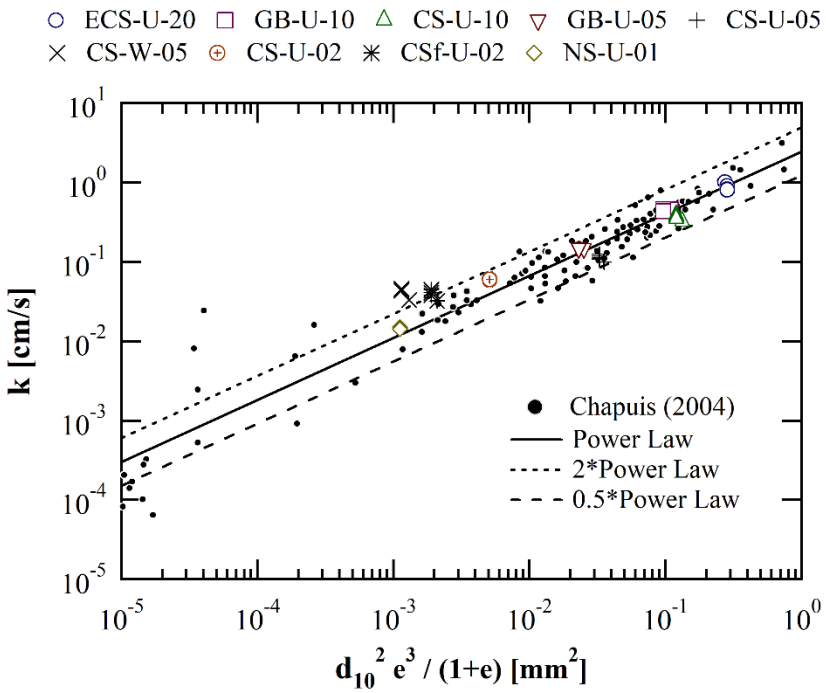

Figure 3. 9 Estimations of Darcy's permeability compared with Chapuis (2004).

3.4.5 APPROACH TO IDENTIFY THE LIMIT OF VISCOUS DOMAIN OF FLOW

The Moody diagram is a common method used to evaluate the transition between Darcy (viscous) and non-Darcy flow. Comiti et al. (2000) suggested using Eq. 2. 15 for estimating the limit of validity of Darcy's Law using α = 16 and β = 0.194. However, it is important to examine the parameters α and β proposed by Comiti et al (2000). By substituting Eq. 2. 7 into Eq. 2. 16, f_{pore} can be expressed as:

$$f_{pore} = \frac{8\,K'}{R_{pore}} + f \qquad \text{Eq. 3. 1}$$

In Eq. 3. 1, $\alpha = 8K'$ and $\beta = f$. This indicates that these parameters are related to the material properties and the flow characteristics. The values of α and β adopted in Comiti et al. (2000) result from using a constant value of K' of 2.0 assuming a circular pore shape, and a constant value of f of 0.194. However, values of K' are rather variable as indicated by Carman (1956), and the use of Nikurdase formula to estimate f may be questionable as observed by Comiti and Renaud (1989). In this study, parameters K' and f are calculated from the measured coefficients A and B.

First, the calculation begins with estimating values of the Kozeny-Carman constant, K, from Eq. 2. 8 as presented in Table 3. 3. The range from nearly 3.7 to 17.3 obtained seems to deviate from the reference value of 5, but it should be noted that most of these results remain within an acceptable range according to Xu and Yu (2008). Next, the values of tortuosity, τ, are calculated using Eq. 2. 9. For sands and glass beads with uniform grain-size distribution and rounded shapes, the range of tortuosity between 1.63 to 1.78 is acceptable in comparison with the results presented in Salem and Chilingarian (2000), for randomly packed spheres with porosity of 0.34 to 0.45. The tortuosity values

of 1.86 and 1.92 obtained for the angular sample ECS-U-20 and the well-graded sample CS-W-05, agree with the values obtained in Wahyudi et al. (2000) with similar arrangements of sands. Using the values of K and τ for each material, the porous shape factor, K', is then calculated. According to Carman (1956), K' ranges from 1.67 to 3.00 depending on the pore shape and eccentricity of the capillaries. Most of the results presented here are within or close to this range. In general, K' increases as d_{eff} increases, but a more pronounced increase was observed for sands than for glass beads. The effect of gradations is minimum as the value of K' for the well-graded sample (CS-W-05) is close to the value obtained for the uniform graded sample (CS-U-05).

Table 3. 3 Empirical porous media and fluid properties.

Sample ID	Kozeny-Carman constant K	Tortuosity τ	Shape Factor K'	f
ECS-U-20	8.036	1.86	2.316	0.303
GB-U-10	8.081	1.78	2.581	0.234
CS-U-10	17.29	1.63	6.489	0.475
GB-U-05	6.374	1.79	1.998	0.308
CS-U-05	11.32	1.69	3.977	1.074
CS-W-05	13.20	1.92	3.590	0.443
CS-U-02	4.373	1.67	1.560	5.038
CSf-U-02	3.748	1.68	1.322	4.650
NS-U-01	4.264	1.77	1.354	2.201

The values of Darcy's friction factor, f, were calculated from the measured coefficient B and the estimations of τ. Results obtained are also included in Table 3. 3. The values of f obtained are greater than the constant value of 0.194 used by Comiti and Renaud (1989), derived from the Nikurdase formula. In this study, the value of f is treated as a variable, according to the results of flow tests and the characteristics of the

materials. This result implies that a unique form of f_{pore} in Eq. 3. 1 is not considered possible.

The f_{pore} for viscous flow is derived by substituting Eq. 2. 5 into Eq. 2. 16, obtaining $f_{pore}|_{Darcy} = 8K^{'}/R_{pore}$. The transition from nonlinear flow is defined as the deviation, E_f, of f_{pore} from $f_{pore}|_{Darcy}$, given by:

$$E_f = \frac{f_{pore} - f_{pore}|_{Darcy}}{f_{pore}|_{Darcy}} \qquad \text{Eq. 3. 2}$$

Consequently, R_{critic} indicating the limit of validity of Darcy's Law can be expressed as:

$$R_{critic} = E_f \frac{8\,K'}{f} \qquad \text{Eq. 3. 3}$$

Eq. 3. 3 indicates that R_{critic}, based on Eq. 3. 1 (Comiti et al. 2000), varies according to K' and f. In this study, R_{critic} is estimated using an E_f value of 10% to represent the 10% deviation from Darcy's flow domain. The values of R_{critic} for each material tested in this study are presented as functions of S_b in Figure 3. 10. An average value of R_{critic} of 4.6 is obtained. Specimens with greater d_{eff} than 0.5 mm and lower S_b than 15 mm^{-1} have critical values between 2 and 11. Lower values are obtained for specimens with lower d_{eff} and greater S_b, indicating that transition occurs at lower velocities of flow. This behavior may be related to the size of the capillaries. The size of the flow paths in porous media composed of compacted fine grains is smaller than in flow paths with coarser particles. As stated in Fourar et al. (2004), the energy dissipation is greater in regions with small flow sections. Moreover, the size of these sections is

progressively reduced as the Reynolds Number increases due to the generation of eddies as the flow becomes more inertial.

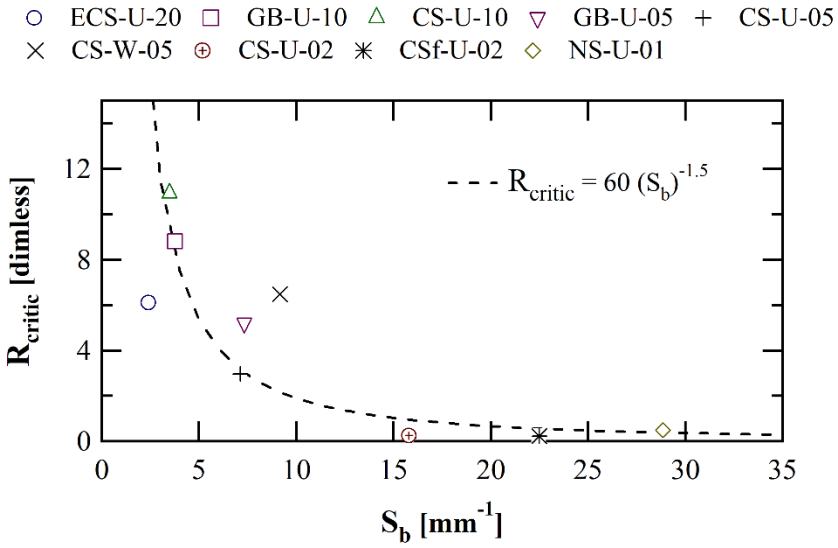

Figure 3. 10 Dependence of critical Reynolds Number to surface area in contact with fluid.

For an E_f value of 5%, values of R_{critic} obtained in this study range from 0.11 to 5.5, with an average value of 2.3. For an E_f value of 1%, values of R_{critic} obtained range from 0.02 to 1.1, with an average value of 0.46. Wahyudi et al. (2002) used a similar approach by assuming E_f values of 10%, 5%, and 1%, and reported R_{critic} average values of 9.2, 4.3, and 0.83, respectively, for sands with particle-sizes ranging from 0.16 mm to 0.63 mm. Khalifa et al. (2000) reported average values of R_{critic} of 9.7 and 4.9 using the same sands and E_f values of 10% and 5%, respectively. Differences between R_{critic} obtained in this study and Khalifa et al. (2000) and Wahyudi et al. (2002) are approximately one half. These differences are mainly due to the parameters α and β, as presented in Eq. 2. 15. Both Khalifa et al. (2000) and Wahyudi et al. (2002) assumed the

values of α = 16 and β = 0.194 based on the work of Comiti et al. (2000); hence, their results are similar. The assessment of the different methods to determine R_{critic} is discussed in the following section. Overall, results agree with the range from 3 to 11 proposed by Goodings (1994), except for the finer grained sands. The literature for the experimental evaluation of R_{critic} is very limited for fine sands.

3.4.6 Differences in formulations used for Reynolds Number

There are different formulations used to determine the Reynolds Number in the literature, as well as different criteria defining the limit of validity of Darcy's Law. Due to uncertainties related to the flow regime and the selection of parameters representing the materials, such as tortuosity or shape factors, it is important to acknowledge that the same value of R_{critic} may lead to an inconsistent estimation of the corresponding critical velocity of flow and hydraulic gradient.

The value of R_{critic} of 4.9 for E_f of 5% proposed by Khalifa et al. (2000), using the formulation of R_{critic} in Eq. 2. 16, and the range of values from 3 to 11 proposed by Goodings (1994), using the formulation of R_n in Eq. 2. 17, predict different values of critical velocity and hydraulic gradient. Figure 3. 11 presents a comparison of the proposed critical Reynolds Numbers and their corresponding values of gradient and velocity of flow for samples CS-U-10 and CSf-U-02. The dotted lines represent an approximation of the viscous or linear domain related to each critical value. All of the proposed R_{critic} values for the coarse sample CS-U-10 (Figure 3. 11a) are located within the initial straight portion of the plot, indicating the viscous flow regime. The upper limit of R_n = 11 proposed by Goodings (1994) predicts the limit of validity of Darcy's domain more accurately.

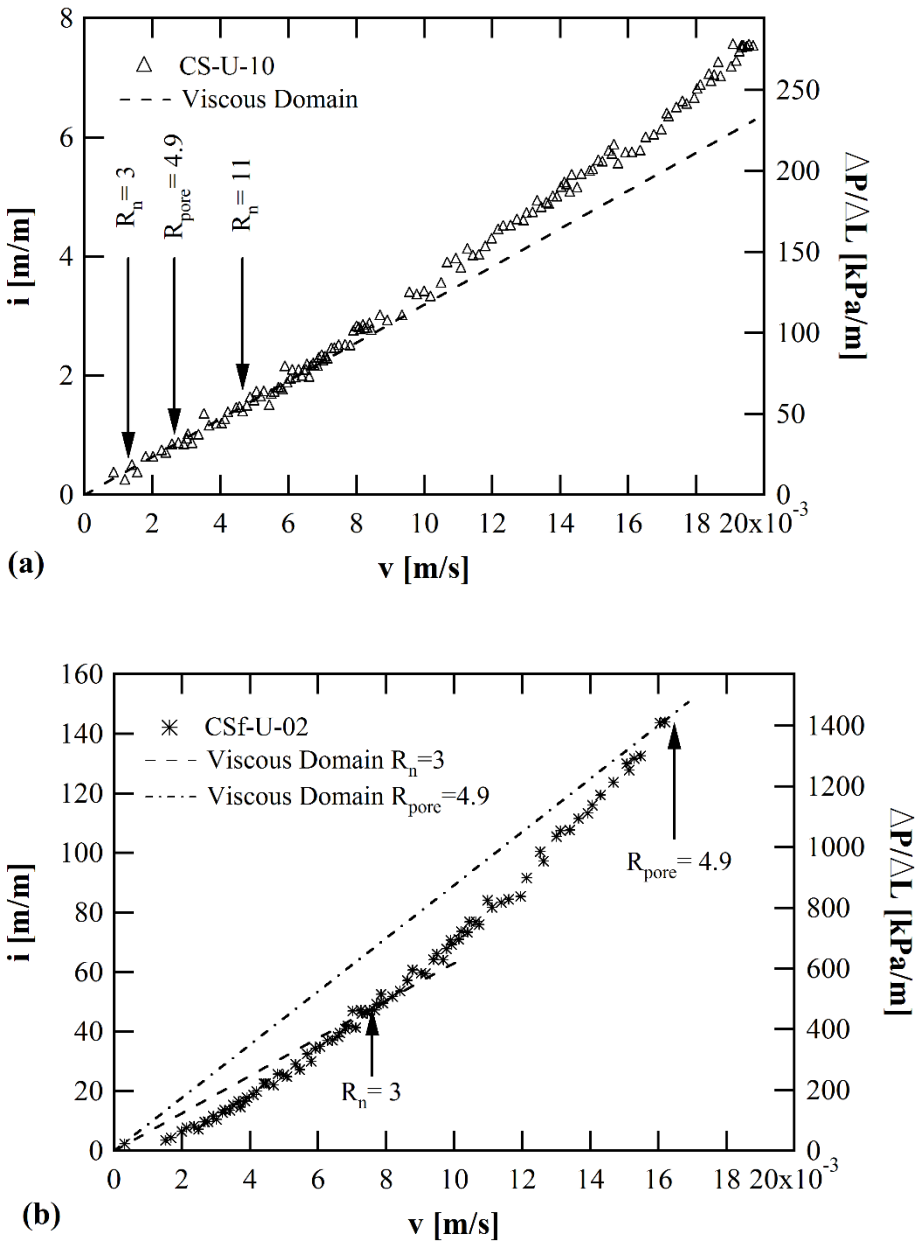

Figure 3. 11 Critical Reynolds Numbers and their corresponding values of velocity and gradient proposed by Khalifa et al (2000) and Goodings (1994) for (a) sample CS-U-10, and (b) sample CSf-U-02.

For the finer grained sample CSf-U-02 (Figure 3. 11b), all the proposed R_{critic} values are in the nonlinear region; thus, they overpredict the limit of validity of Darcy's domain. It is important to be aware that the difference in values of critical velocity of

flow and hydraulic gradient, predicted by the proposed R_{critic}, can be significant (up to 4 times difference in values of flow velocity). The concept of critical Reynolds Number may provide an approximation of where the Darcy's domain remains valid, but it is clear that a constant value of critical Reynolds Number should not be used for all soil types.

A more precise critical velocity was obtained from an alternative method proposed by Zeng and Grigg (2006), shown in Eqs. 2. 18 and 2. 19, using values of Forchheimer coefficients A and B. Table 3. 4 presents the calculated critical velocities and the corresponding critical hydraulic gradients from the measured A and B from this study. Overall, the critical velocity of flow ranging from 5.9×10^{-4} to 2×10^{-3} m/s, and the corresponding hydraulic gradients ranging from 0.2 to 26 are observed for the materials tested. It is interesting to note that the critical hydraulic gradient can be as low as 0.2 for coarser materials (ECS-U-20) and as high as 26 for finer and well-graded materials (CS-W-05). In general, this is to be expected as higher head loss occurs in fine-grained materials than in coarse-grained materials for the same velocity of flow. However, it is observed that there is no clear correlation between the critical velocity or hydraulic gradient and the effective grain size of the materials.

Table 3. 4 also presents the calculated values of R_{critic} using different formulations of Reynolds Number for the critical velocity and hydraulic gradient. The calculated values of R_{critic} vary depending upon the formulation used. For example, the critical velocity of 2×10^{-3} m/s for the sample ECS-U-20 yields three different values of R_{critic}: 9.22 for Eq. 2. 17, 7.38 for Eq. 2. 15 (α = 16 and β = 0.194), and 6.12 for Eq. 3. 1 (using K' and f derived from experimental data in this study). In general, the simple formulation in Eq. 2. 17 yields R_{critic} values higher than the values obtained by Comiti et

al. (2000), and higher than the values of coarse-grained materials from this study. Nonetheless, the same formulation predicts lower values for finer grained sands. The difference was derived from the parameters used for material properties and flow characteristics (τ, K' and f). For a comparison between Eq. 2. 17 and this study for the same value of R_{critic}, Eq. 2. 17, which is a simple and widely used formulation, would predict relatively higher critical velocity and hydraulic gradient resulting in a less conservative prediction of the limit of validity of Darcy's Law.

Table 3. 4 Critical flow properties and Reynolds Number.

Sample ID	v_{critic} (m/s)	i_{critic} (m/m)	R_{critic} Goodings (1994)	Comiti & Renaud (1989); Comiti et al. (2000)	This study
ECS-U-20	2.0×10^{-3}	0.241	9.22	7.38	6.12
GB-U-10	4.7×10^{-3}	1.154	12.5	9.10	8.82
CS-U-10	5.9×10^{-3}	1.879	13.9	12.7	10.9
GB-U-05	5.4×10^{-3}	4.101	7.47	6.55	5.20
CS-U-05	3.1×10^{-3}	3.187	3.95	5.88	2.96
CS-W-05	7.8×10^{-3}	26.03	10.1	8.48	6.50
CS-U-02	5.9×10^{-4}	1.091	0.33	1.34	0.25
CSf-U-02	7.6×10^{-4}	2.530	0.30	1.24	0.23
NS-U-01	2.0×10^{-3}	15.64	0.70	1.83	0.49

3.4.7 Remarks on flow through porous media in centrifuge models

This study demonstrates that the gradient-velocity relationship is independent of the centrifuge gravitational acceleration. Based on the results from the set of materials tested, modeling viscous flow in a centrifuge condition can be a challenge when the velocity of flow increases significantly. The nonlinear relationship between pressure gradient and velocity of flow is found at a relatively low velocity of flow. The use of

$R_{critic} \leq 1$ is acceptable but conservative for sands with d_{eff} greater than 0.5 mm. The same R_{critic} value should be used with caution for sand with d_{eff} less than 0.2 mm. Careful consideration should be taken when selecting a formulation for R_{critic} to calculate the critical velocity and hydraulic gradient as variations can be significant between different formulations. If fine sand with $d_{eff} \leq 0.2$ mm is desired for a centrifuge model, a series of permeability test should be conducted to characterize the flow behavior and the limit of validity of Darcy's Law, prior to model testing. Errors due to nonlinear flow behavior should be assessed and considered whether they would affect the model response in the centrifuge environment. If the test objective is to precisely measure the hydraulic gradient in a model, it is beneficial to obtain the Forchheimer coefficients for the desire range of velocities. These coefficients can also be estimated from the relationships provided in this study and results can be used to develop scaling laws accounting for the nonlinearity.

3.5 CONCLUSIONS

An experimental analysis of centrifuge nonlinear flow was reproduced in this study using sands and glass beads with different grain-size distributions, shapes and porosities, all represented by a unique surface area in contact with fluid per unit volume of specimen, S_b. Coefficients A and B in Forchheimer's Law increased with S_b in agreement with experimental results available in the literature. The accuracy in the predictions of Forchheimer coefficients depends on the range of velocities of flow used to derive the empirical correlations. Relationships proposed in this study were appropriate for predicting the flow behavior for velocities up to 0.02 m/s.

The definition of the limit of viscous flow, using the concepts of Reynolds Number and Friction Factor, varies depending on the judgment and preference of the authors. Reynolds Numbers calculated with the formulation used by Goodings (1994) and Salahi et al. (2015) led to higher values of R_{critic}, which resulted in less conservative predictions of the limit of validity of Darcy's Law. Results from this study using the proposed empirical relationship, based on the formulation of Comiti et al. (2000), show that R_{critic} decreases as S_b increases. The transition occurred for R_{critic} as low as 0.2 in materials with an effective particle size of 0.2 mm.

The empirical relationships of the Forchheimer coefficients A and B developed in this study can be used to estimate critical velocity and hydraulic gradient using the method proposed by Zeng and Grigg (2006). For the fine-grained materials tested in this study, the critical velocity lay within a narrow range between 5.9×10^{-4} to 2×10^{-3} m/s. The corresponding hydraulic gradient can be as low as 0.2 for relatively coarse material and as high as 26 for finer grained and well-graded material. There is no clear trend observed for the critical velocity or hydraulic gradient with effective particle size. The empirical relationships developed in this study can be used to predict R_{critic} and to account for the nonlinearity of flow behavior occurring in centrifuge modeling tests or other engineering applications.

CHAPTER 4

PHYSICAL MODELING OF THE INITIATION OF BACKWARD EROSION PIPING USING THE GEOTECHNICAL CENTRIFUGE[1, 2]

[1]Ovalle-Villamil, W., and Sasanakul, I. (2020) "Assessment of Centrifuge Modeling of Internal Erosion Induced by Upward Flow Conditions." *International Journal of Physical Modeling in Geotechnics*, 1 - 40.

[2]Ovalle-Villamil, W., and Sasanakul, I. (2019) "Observation of Piping Erosion Initiation in a Centrifuge Model," *Geo-Congress 2019, 8th International Conference on Case Histories in Geotechnical Engineering*, Philadelphia, Pennsylvania, U.S., 2019.

4.1 INTRODUCTION

Several research studies have been performed to improve the understanding of backward erosion piping, which often occurs in water-retaining structures, such as dams and levees, where the foundation soil is composed of a cohesionless soil, generally with a uniform gradation (Richards and Reddy 2012; Bonelli 2013). Nonetheless, the complex mechanisms involved in backward erosion piping present a challenge to the development and advancement of physical and numerical modeling techniques that can accurately replicate field conditions (Schmertmann 2002; Richards and Reddy 2007; Bonelli 2013). Physical modeling of the backward erosion piping has been extensively performed under relatively low stress conditions in flume tests to model two- and three- dimensional flow (e.g., De Wit et al. 1981; Sellmeijer et al. 2011; Van Beek et al. 2012, 2015), and in column tests to model one-dimensional flow (e.g., Fleshman and Rice 2013; Yang and Wang 2017). In addition, full-scale experiments were conducted where a full-scale levee model was instrumented and monitored through loading and failure (Van Beek et al. 2011). Although full-scale testing results are extremely useful, the associated cost and time only allows a limited number of tests and are impractical for parametric research studies.

The centrifuge modeling technique has been an effective tool for parametric studies as it allows many reduced-scale models to be tested with less effort than full-scale models. Studies using centrifuge modeling have been performed by a few researchers to investigate the backward erosion piping process (e.g., van Beek et al. 2010; Leavell et al. 2014; Koito et al. 2016). However, these studies did not assess scaling laws and flow conditions. Multiple flow conditions and erosion mechanisms occurring simultaneously

may take place within a centrifuge model during the combined phases of the backward erosion piping, resulting in scaling conflicts (Goodings 1982, 1984; Dong et al. 2001; Bezuijen and Steedman 2010). More research is needed to understand the scaling behavior of centrifuge models and more experimental analyses are needed to develop accurate interpretations of existing results.

This paper presents the centrifuge modeling of internal erosion induced by upward flow that typically occurs during the initiation phase of the backward erosion piping. The research focuses on the upward and laminar flow condition and provides detailed data analysis and interpretation to improve the understanding of centrifuge scaling laws applied specifically to these conditions. The testing program was designed to investigate the erosion process and systematically evaluate the effects of centrifuge gravity on the model behavior. Experimental results obtained are used to evaluate critical hydraulic gradients and scaling factors that are validated against adequate theoretical scaling laws and results available in the literature.

4.2 EXPERIMENTAL METHODOLOGY

A series of upward flow tests was performed in a 15g-ton geotechnical centrifuge located at the University of South Carolina using the customized setup shown in Figure 4. 1 and Figure 4. 2. The setup is composed of a customized cylindrical sample container and three video cameras located inside the centrifuge, and four air-water cylinders (namely head tanks) placed in parallel outside the centrifuge. The container is constructed using clear acrylic and allows placing specimens with a constant diameter, d_c, of 10.8 cm and variable length, ΔL, of up to 20 cm. A manifold and a porous steel plate are located at the base of the container to ensure a homogenous distribution of flow to the specimens. A

silicon coating was applied along the inner wall of the container to develop friction on the soil-container interface simulating the boundary conditions in the field (Fleshman and Rice 2013). The video cameras are used for continuously recording a top view and 2 side views of the specimens during testing.

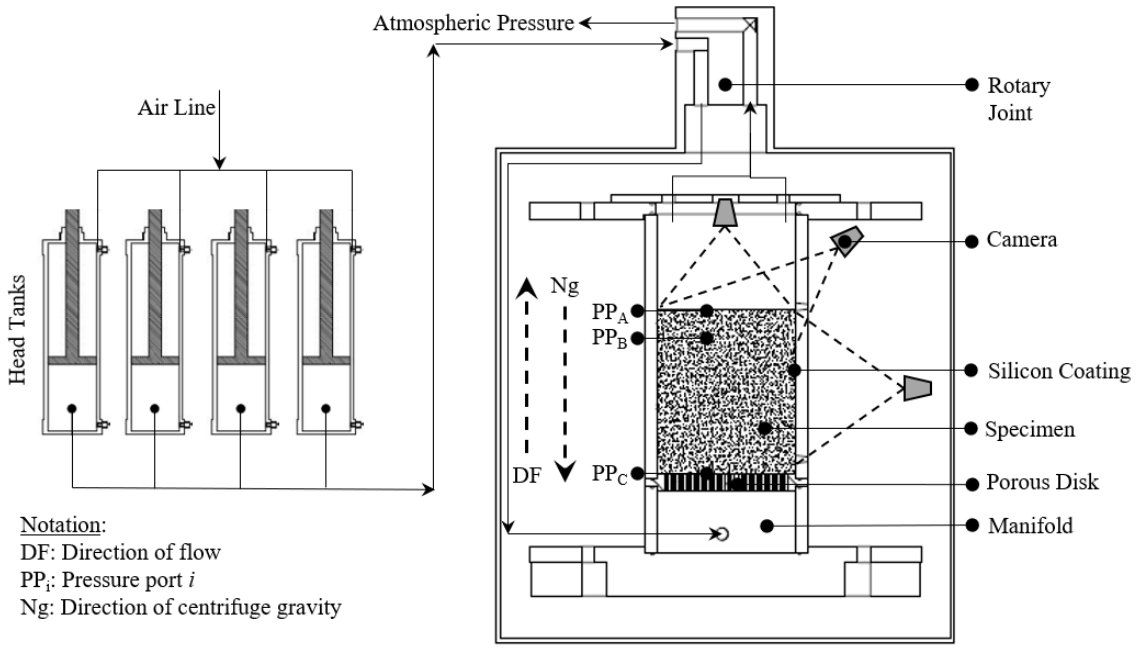

Figure 4. 1 Experimental setup in Research Topic 2 (not to scale).

The air-water cylinders allow a total storage capacity of 11.3 liters of water and are used to force water to flow into the specimen as detailed in the papers by Ovalle-Villamil and Sasanakul (2018a, 2018b, 2019). The air pressure in the head tanks is used to control the progression of the experiments and is increased to induce water flow to the base of the specimens through one passage of the centrifuge rotary joint. Water then flows upwards through the specimen and is driven outside the centrifuge through a different passage of the rotary joint open to atmospheric pressure. By increasing the air pressure in the head tanks, different pressure gradients and velocities of flow are induced

in the specimens. During test, stepped increments of air pressure are applied to the head tanks until the total heave is observed. A series of differential pressure sensors are used to measure local pressure loss across the total length of the specimen (PP_A-PP_C) and across a length of 1.6 cm from the surface (PP_A-PP_B), as shown in Figure 4. 1.

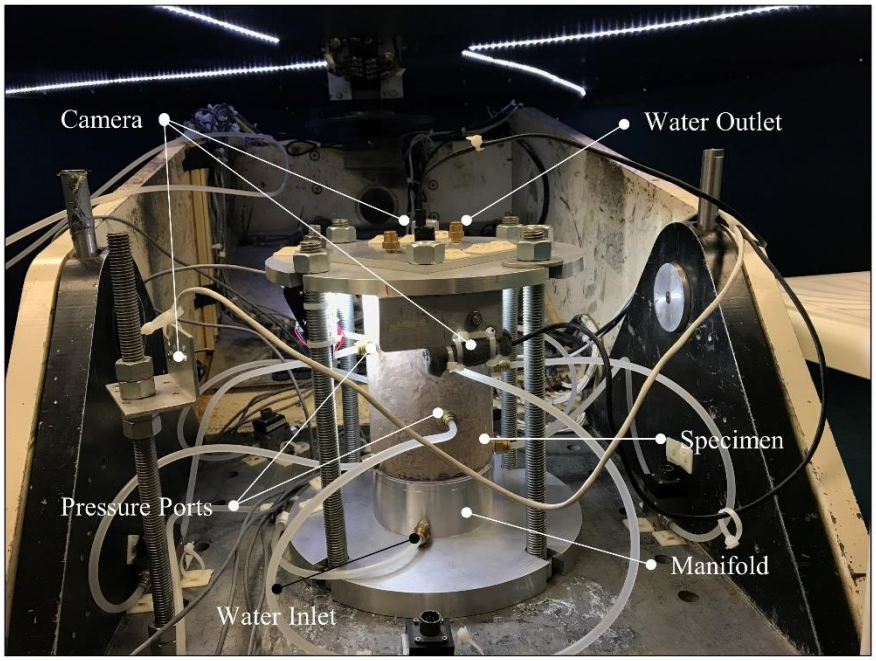

Figure 4. 2 Experimental setup in centrifuge basket.

4.3 SAMPLE PREPARATION AND MATERIAL PROPERTIES

Specimens were prepared by dry pluviation using a rubber tamper to compact six layers of equal weight and ensuring a homogenous distribution of density and bonding between layers. An average ΔL of 12.6 cm was used in this study. The specimens were saturated by flushing water in an upward direction at a very low gradient ($i_{sat} < 0.1$) to ensure no change in the initial porosity prior to testing. Any additional presence of air

inside the specimens is removed during the first increments of pressure gradient across the specimen.

The two types of uniform, fine-grained, cohesionless materials used in this study include Nevada Sand (NS), native to Sierra Nevada region, and Columbia Sand (CS), native to South Carolina. Table 4. 1 shows the properties of these materials, including soil gradation parameters (Casagrande 1948) and the effective diameter (Carrier 2003). Two different gradations of Nevada Sand were tested: a uniform sand mainly composed of coarse grains and effective diameter, d_{eff}, of 0.13 mm (i.e., NS-U-01); and a uniform sand with predominantly finer grains and d_{eff} of 0.04 mm (i.e., NS-U-001). A uniform gradation of Columbia Sand was tested with d_{eff} of 0.20 mm (CS-U-02).

Table 4. 1 General characteristics of sands tested in Research Topic 2.

Specimen ID	Effective diameter d_{eff} (mm)	Particle Shape	C_u	C_g	Gradation
NS-U-001	0.04	Subrounded	2.63	1.22	Uniform
NS-U-01	0.13	Subrounded	1.75	1.06	Uniform
CS-U-02	0.20	Subrounded to subangular	1.56	0.97	Uniform

Each specimen was tested at 10g, 20g, and 30g centrifuge gravitational accelerations. Additional bench tests were performed under Earth's gravity (1g) using the same setup, but the gradients were induced using the conventional constant-head permeability test procedure specified by ASTM D2434/68 (ASTM 2006). This modification in the experimental methodology was used to induce lower gradients in the

specimen and increase the amount of water available for flow than it is possible with the head tanks used in centrifuge tests. A total of 12 tests were performed in this study. Some of these tests were repeated to verify repeatability of the test method and reproducibility of the results.

4.4 RESULTS AND DISCUSSION

4.4.1 GENERAL OBSERVATIONS OF THE INITIATION OF BACKWARD EROSION PIPING

A qualitative description of the behavior observed by way of video recordings is presented in this section. Figure 4. 3 shows the behavior observed with specimen NS-U-001 tested at 1g. In this figure, the dashed lines are references of the initial location of the surface of the specimen, while the continuous line represents the location of the surface during test. Under small increments of global hydraulic gradient, i, there is no apparent movement of grains or deformation near the surface of the specimen indicating that the initial porosity remains (Figure 4. 3a). Further increments of i induce the stage of first visible movement in which a very small expansion of the surface of the specimen is observed (Figure 4. 3b). In this stage, the upward flow causes a reorganization in the granular structure until a new equilibrium state is achieved with an increased porosity. This process repeats for further increments of i until a preferential flow path or piping path is formed across the specimen in the stage of total heave (Figure 4. 3c). It must be noted that the total heave observed in this study is different than that proposed by Fleshman and Rice (2014) as the entire specimen did not heave upwards. Nonetheless, this phase corresponds to the final unstable condition before failure in agreement with the literature. The expansion observed after the first visible movement is not uniform or symmetric with respect to the central, vertical axis of the specimen. This indicates that

the reorganization of grains caused non-uniform increments of porosity across the sample. Consequently, the piping path does not form across the center of the specimen as the flow concentrates in the regions with greater porosity. Tao and Tao (2017) observed a similar behavior using CFD-DEM models and highlighted that the regions with larger voids occurred near the container wall, maybe due to initial larger voids and a lower frictional resistance near the wall.

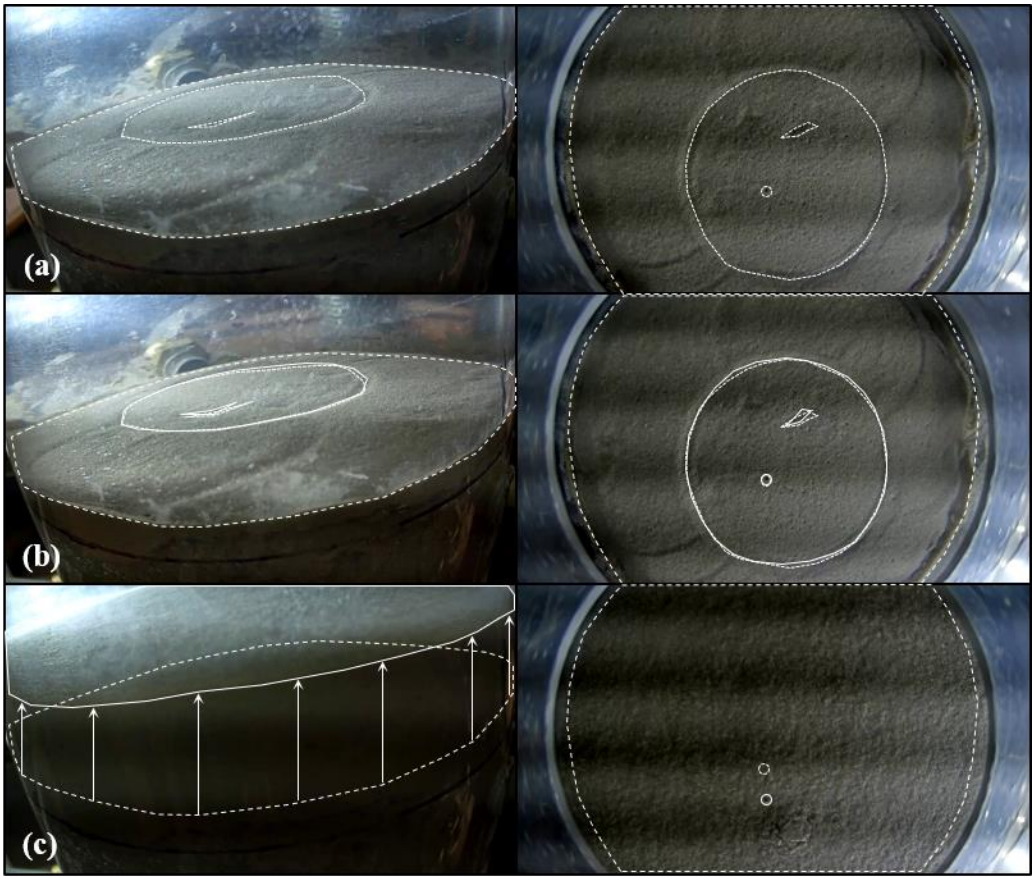

Figure 4. 3 Initiation of backward erosion piping in specimen NS-U-001:
(a) before first visible movement; (b) at first visible movement; (c) at total heave.

A similar behavior is observed at high g and with specimens NS-U-01 and CS-U-02. However, the expansion of the specimens after the first visible movement is

noticeably lower at high g in comparison with the tests at 1g, as shown in Figure 4. 4. This behavior indicates that the increase of porosity during the initiation of backward erosion piping is greater at 1g than at higher g, as also observed by Ovalle-Villamil and Sasanakul (2019). This behavior may be justified considering that although the motion of grains may follow different paths that are difficult to identify in the experiments, such as rolling/sliding or suspension, the settling process towards a new equilibrium state is a function of the grain mass, the grain-size and the stress distribution along the depth of the specimen due to centrifuge gravitational acceleration. Therefore, a smaller displacement of the grains is expected in centrifuge models due to the increased self-weight resulting in lower expansion. In addition, a phase of sand boil formation as described by Fleshman and Rice (2013, 2014) was not observed in this study. Nonetheless, as recognized by Fleshman and Rice (2014) and Tao and Tao (2017), this phase does not take place in every test performed.

4.4.2 HYDRAULIC GRADIENT AT 1G

The global hydraulic gradient, i, was calculated from the pressure loss across the specimen and measured using the differential pressure sensors, as shown in Figure 4. 2 (i.e., pressure loss across ports PP_A and PP_C). The velocity of flow, v, was estimated based on the initial permeability of the specimens and an approximated hydraulic gradient driving the flow. It is important to clarify that this hydraulic gradient is obtained from an approximated pressure loss between the manifold and the surface of the specimen and it is not necessarily equal to i. Figure 4. 5 shows the results for specimens NS-U-001, NS-U-01 and CS-U-02, tested at 1g. Specimen CS-U-02 shows a linear relationship between i and v from the beginning of the test until a magnitude of i of

nearly 0.54 obtained for the first visible movement. The relationship then deviates from the initial linear portion as less i was observed as v increased, until a magnitude of i of nearly 1.73 estimated for the total heave. Specimens NS-U-01 and NS-U-001 show a similar behavior with an initial linear relationship between i and v until the first visible movement at magnitudes of i of nearly 0.74 and 0.66, respectively. The total heave occurred at magnitudes of i of 1.40 and 2.44, respectively.

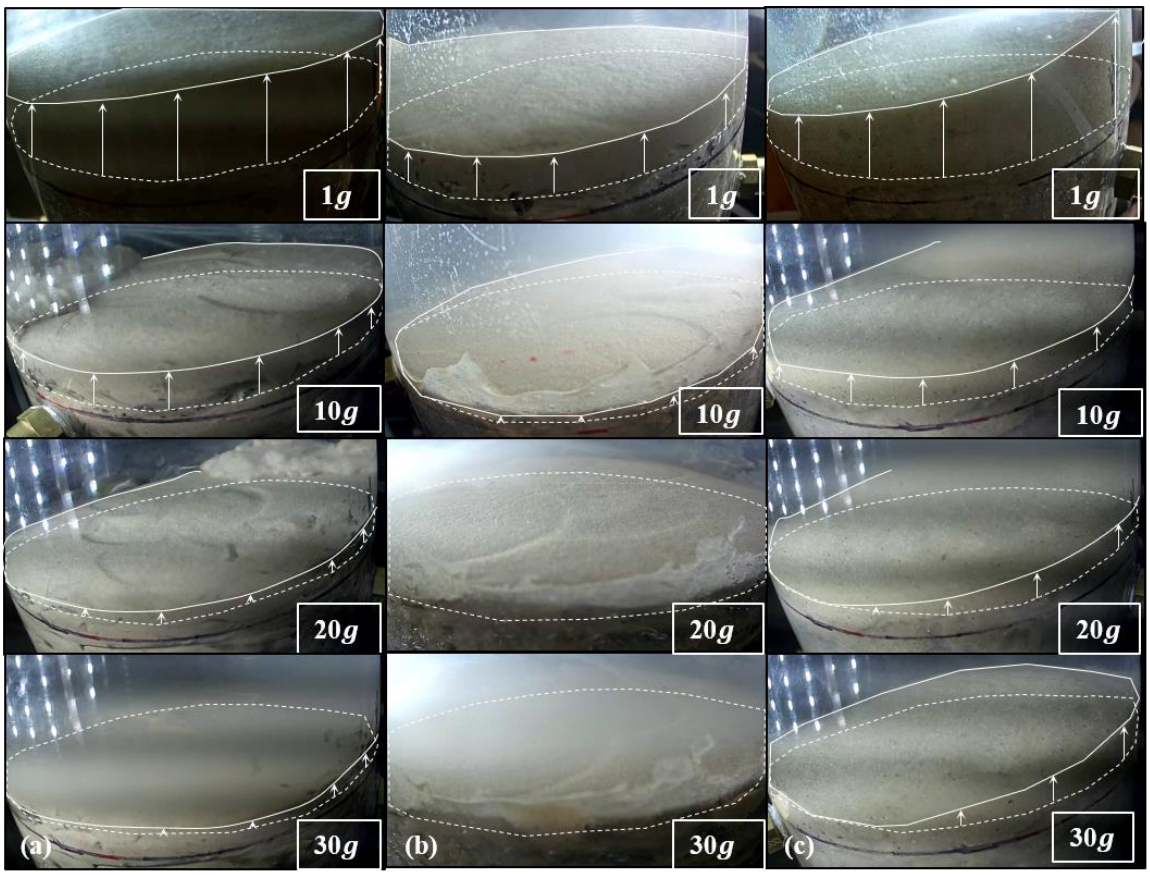

Figure 4. 4 Total heave at different centrifuge gravitational accelerations for:
(a) specimen NS-U-001; (b) specimen NS-U-01; (c) specimen CS-U-02.

Overall, the relationship between i and v remains linear until the first visible movement where the expansion of the column starts. As i increases and the expansion

progresses, the porosity increases and the rate of increasing of i as a function of v decreases. The magnitude of i reaches a maximum value at the total heave and decreases significantly immediately after. The magnitude of i at the moment of total heave is greater than 1 for every specimen tested indicating that the mechanism modeled is different than the uplift of a large soil mass. Such mechanism could be anticipated in a scenario without soil-container interface friction, as described by the method of heave by Terzaghi (1922).

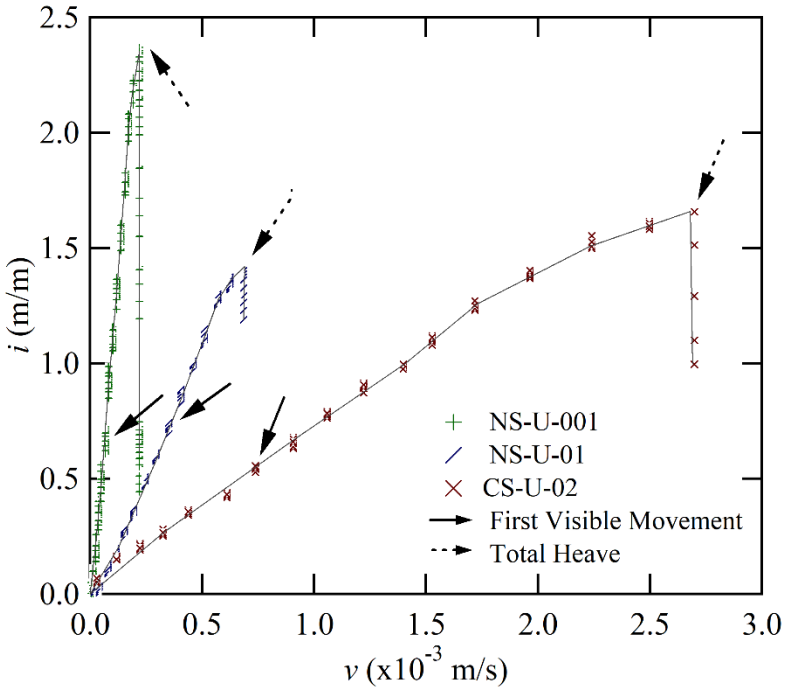

Figure 4. 5 Increments of hydraulic gradient with the velocity of flow for 1g experiments.

4.4.3 CRITICAL HYDRAULIC GRADIENT IN CENTRIFUGE MODELS

The behavior observed in centrifuge models and the critical global hydraulic gradients, i_{cr}, are presented in Figure 4. 6 to Figure 4. 8. The pressure loss across the

specimens, ΔP, was normalized by the submerged weight of grains, W', per cross-sectional area, A (i.e., $\Delta P \,/\, NW'A$, where N represents the increment of the gravitational acceleration), and the normalized pressure loss obtained, $\overline{\Delta P}$, is plotted as a function of v, as shown in Figures 4. 6a, 4. 7a and 4. 8a for the specimens NS-U-001, NS-U-01 and CS-U-02, respectively. The value of $\overline{\Delta P}$ essentially represents the ratio between driving and resisting forces during the initiation of backward erosion piping.

Figure 4. 6a, 4. 7a, and 4. 8a show that $\overline{\Delta P}_{FVM}$ at the first visible movement is similar and independent of gravity in specimens NS-U-001 and NS-U-01. However, $\overline{\Delta P}_{FVM}$ is greater at high g than at 1g in specimen CS-U-02. At the stage of total heave, $\overline{\Delta P}_{TH}$ decreases nearly 40, 20 and 30% at high g, relative to 1g, for the specimens NS-U-001, NS-U-01 and CS-U-02, respectively. The values of $\overline{\Delta P}_{FVM}$ and $\overline{\Delta P}_{TH}$ observed at high g are more consistent regardless of N. Overall, $\overline{\Delta P}_{FVM}$ varies from 0.50-0.95 and $\overline{\Delta P}_{TH}$ varies from 0.97-2.17.

The difference in values of $\overline{\Delta P}_{FVM}$ among different tests is due to several factors. For instance, the high value of $\overline{\Delta P}_{FVM}$ in the coarser specimen CS-U-02 tested at high g could be due to a possible non-laminar flow condition that may occur in the high g tests in which the flow velocity is noticeably greater than the velocity at 1g. Likewise, the magnitude of ΔP across the specimens at 1g is very small and the measurements are likely to be less accurate than at higher g. In addition, the visual identification of the first visible movement can be subjective as it is based on the first visible surface expansion of the specimens.

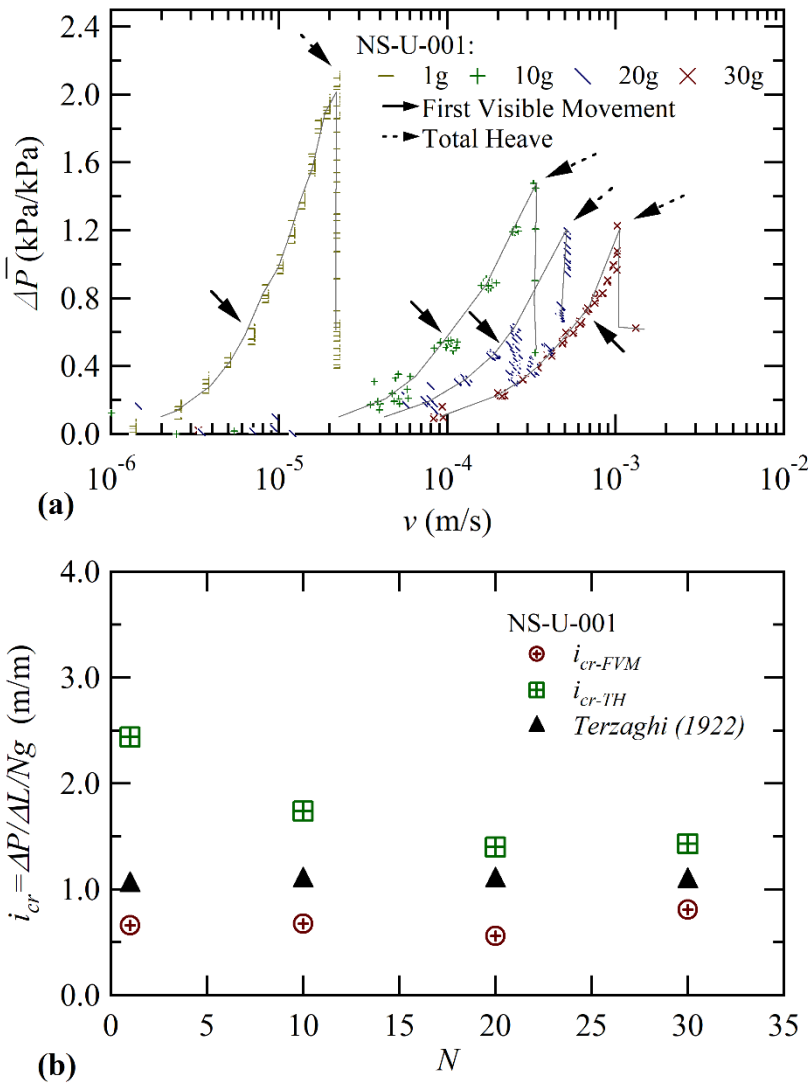

Figure 4. 6 (a) Increments of normalized pressured loss across the specimen with the velocity of flow and (b) variations of critical global hydraulic gradients with centrifuge gravity for specimen NS-U-001.

An average residual $\overline{\Delta P}$ of 0.60 is observed after the total heave for specimens NS-U-001 and NS-U-01, while an average value of 0.72 is observed for the specimen CS-U-02. The residual values lower than 1 indicate that the total weight of the grains per unit area, $NW'A$, is greater than the seepage stress, ΔP, after the total heave. This is justified considering that during the initiation of erosion only a portion of the soil is

fluidized forming a single preferential flow path (Kolb 1975; Li et al. 1996; Mazzoleni et al. 2014), but the total weight of grains in the specimen is not completely dragged by the fluid. Therefore, intergranular forces still exist in some sections of the specimens. It is interesting to note that the residual values of $\overline{\Delta P}$ are close to the values of $\overline{\Delta P}_{FVM}$ for specimens NS-U-001 and NS-U-01.

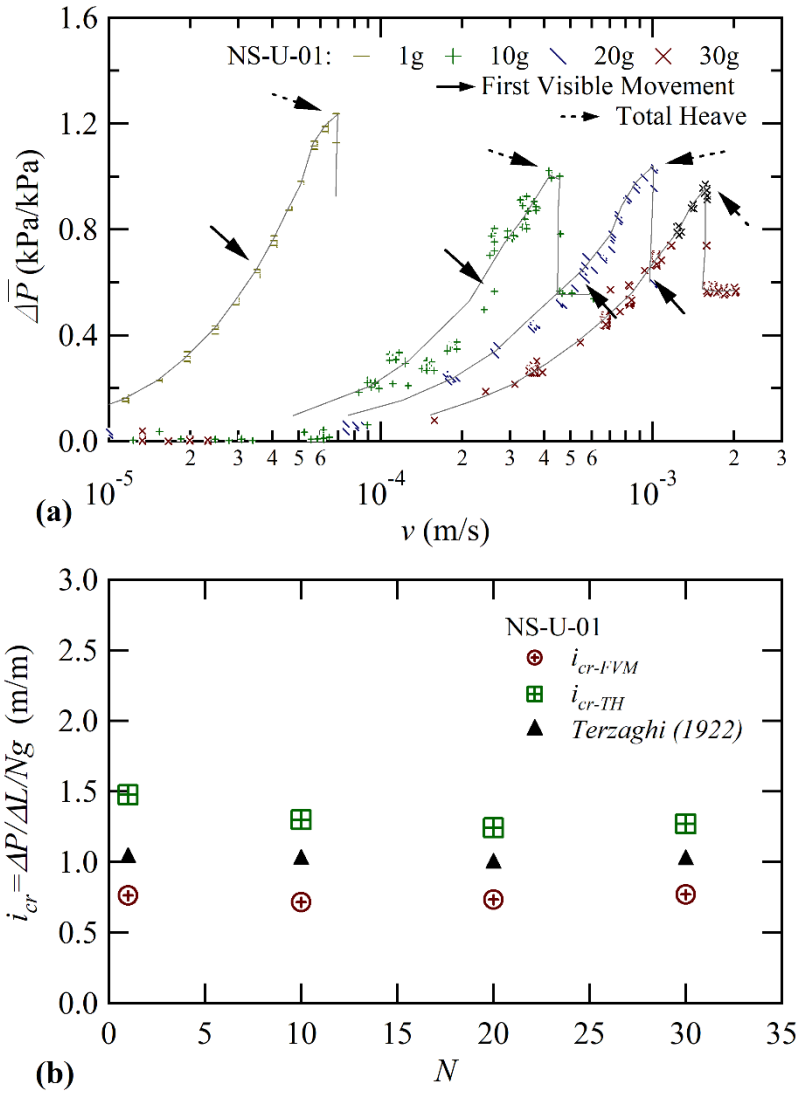

Figure 4. 7 (a) Increments of normalized pressured loss across the specimen with the velocity of flow and (b) variations of critical global hydraulic gradients with centrifuge gravity for specimens NS-U-01.

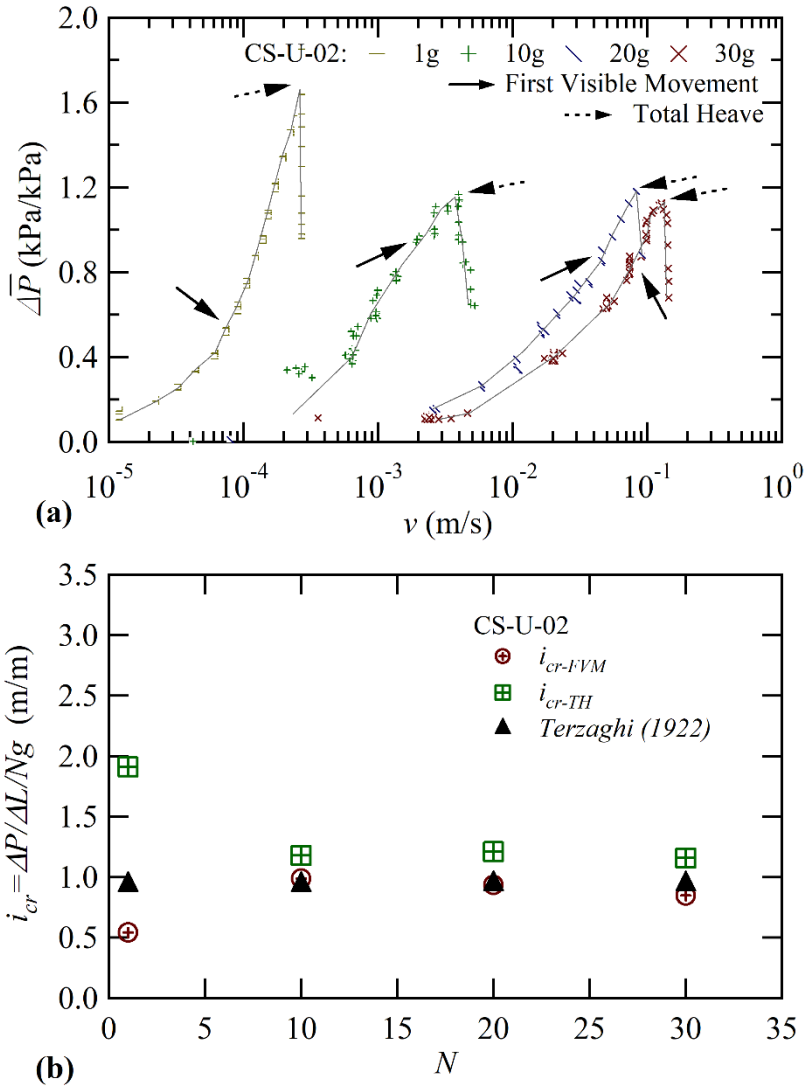

Figure 4. 8 (a) Increments of normalized pressured loss across the specimen with the velocity of flow and (b) variations of critical global hydraulic gradients with centrifuge gravity for specimen CS-U-02.

The results of $(\Delta P/\Delta L)_{cr}$ and i_{cr} obtained at the first visible movement (i.e., i_{cr-FVM}) and the total heave (i.e., i_{cr-TH}) are shown in Table 4. 2. The magnitude of $(\Delta P/\Delta L)_{cr}$ increases linearly with N, indicating that greater pressure gradients and velocities of flow are required to trigger the phenomenon as the effective stress across the specimen increases. A study by Richards and Reddy (2012) using true triaxial

experiments demonstrated that the critical velocity of flow to initiate piping increases as the major principal stress (applied in vertical direction) and the effective stress increase, in agreement with this study. The values of $(\Delta P/\Delta L)_{cr}$ result in fairly constant magnitudes of i_{cr} regardless of N, as shown in Figure 4. 6b, 4. 7b and 4. 8b.

Table 4. 2 Critical global gradients obtained in tests at 1g, 10g, 20g and 30g.

Sample	Porosity (n)	Centrifuge acceleration (Ng)	First Visible Movement		Total Heave	
			$(\Delta P/\Delta L)_{cr}$ (kPa/m)	i_{cr} (m/m)	$(\Delta P/\Delta L)_{cr}$ (kPa/m)	i_{cr} (m/m)
NS-U-001	0.370	1	6.475	0.660	23.94	2.440
d_{eff} = 0.039 mm	0.344	10	66.41	0.677	170.7	1.740
	0.344	20	109.9	0.560	274.7	1.400
	0.348	30	238.4	0.810	420.8	1.430
NS-U-01	0.374	1	7.500	0.765	14.50	1.478
d_{eff}= 0.130 mm	0.383	10	70.24	0.716	127.5	1.299
	0.400	20	144.2	0.735	243.8	1.243
	0.385	30	227.0	0.771	374.0	1.271
CS-U-02	0.429	1	5.329	0.543	18.75	1.911
d_{eff}= 0.199 mm	0.433	10	97.03	0.989	115.9	1.181
	0.428	20	183.7	0.936	237.9	1.213
	0.430	30	249.6	0.848	340.7	1.158

The experimental values of i_{cr-TH} are greater than the analytical method of heave by Terzaghi (1922) due to the boundary condition imposed (i.e., soil-container interface friction). In contrast, the values of i_{cr-FVM} are generally lower than the analytical method of heave, except for the coarser specimen CS-U-02, as shown in Figure 4. 8b. This

observation suggests that the increase of i required to advance from the incipient motion of grains to a sand boil state is lower as d_{eff} increases. Similar results reported by Yang and Wang (2017) show values of i_{cr} for the initial movement of grains and the total heave from 0.81 to 0.93, and 1.02 to 1.21, respectively, for sands coarser than CS-U-02. The values of i_{cr-FVM} are lower than the values obtained from the analytical method of heave. This implies that the initiation phase does not represent a global failure condition in which the effective stress is diminished. In this case, the critical values represent a local condition in which the seepage forces are great enough to drag the grains near the surface for which the interlocking forces are relatively low due to low confinement compared with the grains below the surface.

4.4.4 Assessment of similarities in centrifuge tests

The theoretical scaling law of $\boldsymbol{i_{cr}}$ = 1 is assessed using the results in Table 4. 2 and different experimental scaling factors, $\boldsymbol{i_{cr-exp}}$, determined using different ratios of gravitational accelerations (i.e., N=g_m/g_p), as shown in Table 4. 3. The experimental scaling factors obtained are also presented as functions of N in Figure 4. 9a and 4. 9b for the first visible movement and the total heave, respectively. The values of $\boldsymbol{i_{cr-exp}}$ for the first visible movement are closer to the theoretical scaling law with a mean magnitude of 1.14 and standard deviation of 0.30. The values of $\boldsymbol{i_{cr-exp}}$ between 1.5 and 2 obtained for the specimen CS-U-02 and for $N \geq 10$ may be due to non-laminar flow as discussed in the previous section. For the total heave, the values of $\boldsymbol{i_{cr-exp}}$ are more consistent but lower than the theoretical scaling law with a mean magnitude of 0.83 and standard deviation of 0.16. Since i_{cr-TH} is greater at 1g, values of $\boldsymbol{i_{cr-exp}}$ lower than N are expected for $N \geq 10$ (i.e., g_p = 1) at the stage of total heave.

Table 4. 3 Scaling factors for critical global hydraulic gradient with different ratios of prototype-model.

Gravitational acceleration ratio N	First visible movement			Total heave		
	NS-U-001	NS-U-01	CS-U-02	NS-U-001	NS-U-01	CS-U-02
N = 10: g_p = 1g, g_m = 10g	1.02	0.94	1.82	0.71	0.88	0.62
N = 20: g_p = 1g, g_m = 20g	0.85	0.96	1.72	0.57	0.84	0.63
N = 30: g_p = 1g, g_m = 30g	1.22	1.01	1.56	0.58	0.86	0.61
N = 2: g_p = 10g, g_m = 20g	0.83	1.03	0.95	0.81	0.96	1.03
N = 3: g_p = 10g, g_m = 30g	1.20	1.08	0.86	0.82	0.98	0.98
N = 1.5: g_p = 20g, g_m = 30g	1.44	1.05	0.91	1.02	1.02	0.95

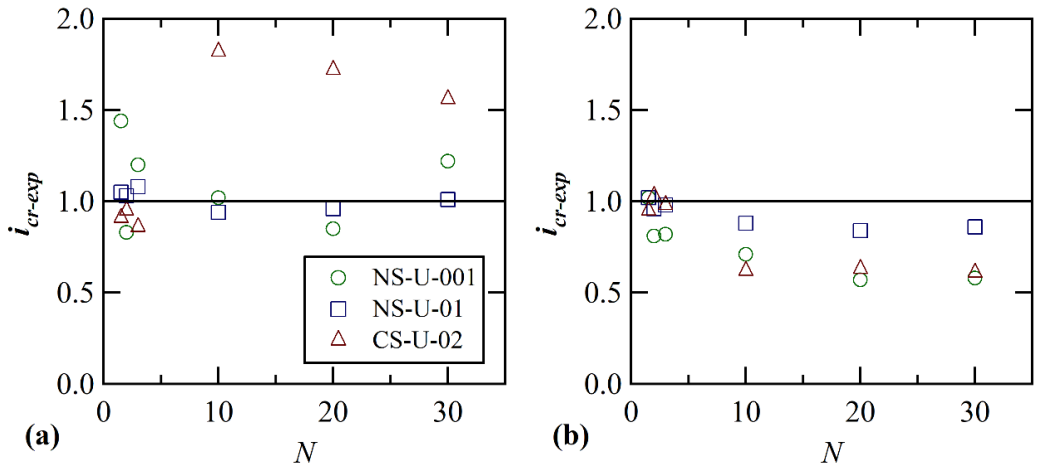

Figure 4. 9 Variations of scaling factors for critical global hydraulic gradient with centrifuge gravity: (a) first visible movement and (b) total heave.

Similarity between the models is maintained by ensuring the same flow regime (Goodings 1982, 1984, 1985; Bezuijen and Steedman 2010). The flow regime is typically assessed based on the relationships between the Friction Factor, F_f, and the Reynolds Number, R_n, through the Moody diagram (Goodings 1994; Ovalle-Villamil and Sasanakul 2018a, 2018b). Figure 4. 10 shows the evolution of F_f as a function of R_n obtained using the simplified functions of Muskat (1938) and Stephenson (1979). The values of R_n were calculated from the estimated values of v and may not be accurate because of the increase in porosity that occurs after the first visible movement. However, as presented previously, the change of porosity is small for the tests at high g.

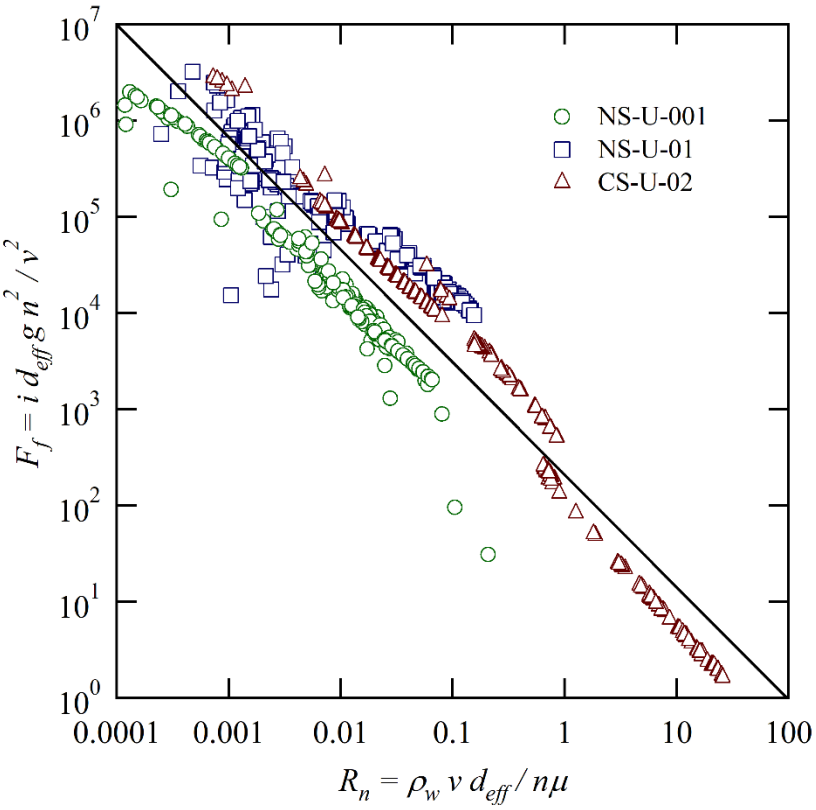

Figure 4. 10 Moody diagram from simplified functions of friction factor and Reynolds number (Muskat 1938; Stephenson 1979).

The relatively linear relationship between F_f and R_n shown in Figure 4. 10 indicates a continuous laminar flow condition (Comiti et al. 2000; Ovalle-Villamil and Sasanakul 2018a, 2018b). The estimated values of R_n are generally lower than 1 except for the specimen CS-U-02 tested at 20g and 30g. This observation implies that the same flow regime is maintained at centrifuge accelerations of up to 30g with the finer sands, but a slight deviation from laminar flow may have occurred in the coarser sand at centrifuge accelerations higher than 10g. It must be noted that a non-laminar flow condition is not identified in Figure 4. 10 as the relationship between F_f and R_n remains linear even for the greater values of R_n (Goodings 1994; Ovalle-Villamil and Sasanakul 2018a, 2018b).

4.4.5 Comparison of centrifuge results with the literature

To validate the experimental results of this study, the values of i_{cr-FVM} and i_{cr-TH} in Table 4. 2 are plotted as functions of the surface area of the grains in contact with the fluid per unit volume of specimen, S_b, as shown in Figure 4. 11. The parameter S_b is a normalized term accounting for effects of porosity and effective diameter (i.e., $S_b = 6\, d_{eff}^{-1}[1-n]$). Experimental data obtained for sands with different grain-size and gradation by Fleshman and Rice (2014) and Yang and Wang (2017), and numerical modeling results by Tao and Tao (2017) are compared with results from this study. It is noted that the values of i_{cr-FVM} and i_{cr-TH} in Table 4. 2 and Figure 4. 11 correspond to a prototype condition of 1g as $\boldsymbol{i_{cr}}$ = 1 and are comparable with the values from the literature.

Figure 4. 11a shows that i_{cr-FVM} decreases as S_b increases (i.e., d_{eff} and n decreases). This behavior indicates that a lower i is required to induce motion of grains in

soils with lower d_{eff}. In contrast, results from this study show that i_{cr-TH} increases as d_{eff} increases, as shown in Figure 4. 11b. This behavior is not observed in other studies. Values of i_{cr-TH} closer to 1 were obtained by Yang and Wang (2017), which are lower than the results from this study, Fleshman and Rice (2014), and Tao and Tao (2017). The difference may be due to the soil-container interface friction that was not considered in the study of Yang and Wang (2017). On the other hand, Fleshman and Rice (2014) and Tao and Tao (2017) obtained higher values of i_{cr-TH} than this study. This may be a consequence of the differences in grain-shape and grain-size distribution. The angular grain sand (Angular 20-30) from Fleshman and Rice (2014) shows higher average i_{cr} than the remaining specimens in Figure 4. 11b, indicating that the higher the angularity, the higher resistance against piping initiation. In addition, as indicated by Tao and Tao (2017) from a comparison between Uniform Sand and Ottawa 20-30, a higher resistance against piping is observed in this study with specimen NS-U-001.

The differences between the results from this study and the literature could also be due to the sample-size effect considering that a smaller sample container was used by Fleshman and Rice (2014) and Tao and Tao (2017). In addition, this study focuses on soils with low porosities ranging from 0.34 to 0.43 and more data are required to assess the effects of porosity. Figure 4. 11 also shows that the uncertainty in i_{cr} is relatively large. The value of i_{cr-TH} ranges from nearly 2.1 to 3 for Ottawa sand 20-30 (Fleshman and Rice 2014), and from nearly 1.4 to 2.5 for specimen NS-U-001 (this study). Tao and Tao (2017) indicated that the uncertainty in their results is a consequence of the rate of increment of i in their numerical models. It is possible that this factor contributes to the accuracy in experimental results. However, this study used step increments of i and

allowed enough time to reach equilibrium at each step. Overall, the results from this study compare reasonably well with data available in the literature.

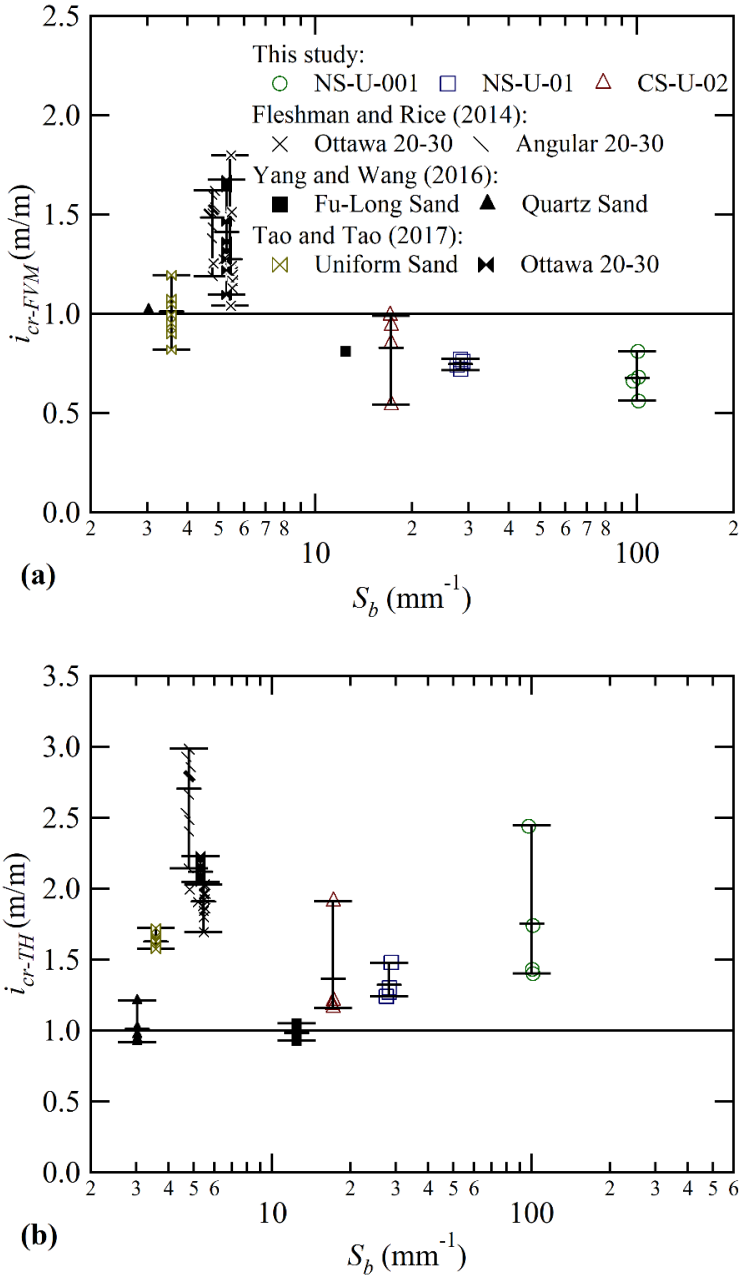

Figure 4. 11 Variations of prototype critical global hydraulic gradient with S_b for (a) first visible movement and (b) total heave.

4.4.6 SEEPAGE STRESSES AT LEVEL OF GRAINS

The assessment of seepage stresses at level of grains is performed considering the two components of the total seepage force, as shown in Figure 2. 10c. The seepage force due to differential pressure, F_s, and the drag force, F_d, were determined using Eq. 2. 28 for the first visible movement at the top portion of the specimen and are presented as functions of N in Figure 4. 12. The average magnitude and error bars representing variation of data are presented.

Significant uncertainty is observed for 1g tests with variations ranging from 1 to nearly 4 orders of magnitude. Less uncertainty is observed at high g and the results are more consistent. The uncertainty appears to be greater for the finest sand NS-U-001 and decreases as d_{eff} increases. More consistent results from high-g test emphasize the advantage of centrifuge testing in achieving more accurate measurements of seepage and drag forces since ΔP in the same segment increases proportional to N.

The results of F_s and F_d were used to estimate the differential pressure across the grain, ΔP_p, and the average viscous shear stress, τ_p, respectively. The two components of the total seepage stress are presented in Figure 4. 13a. The incipient motion of grains was determined by the first visible movement observed on the surface of the specimen. Both ΔP_p and τ_p increase as d_{eff} increases, indicating that a greater stress is required to displace coarser grains. For the upward flow condition, ΔP_p is greater than τ_p and the contribution for the total critical seepage stress is 84% and 16%, respectively. This behavior is opposite to the assumption proposed by White (1940) in which the viscous shear stress is dominant for the laminar flow regime. This could be due to the direction of

flow being different in this study and ΔP_p is less between the top and the bottom of the grain under horizontal laminar flow.

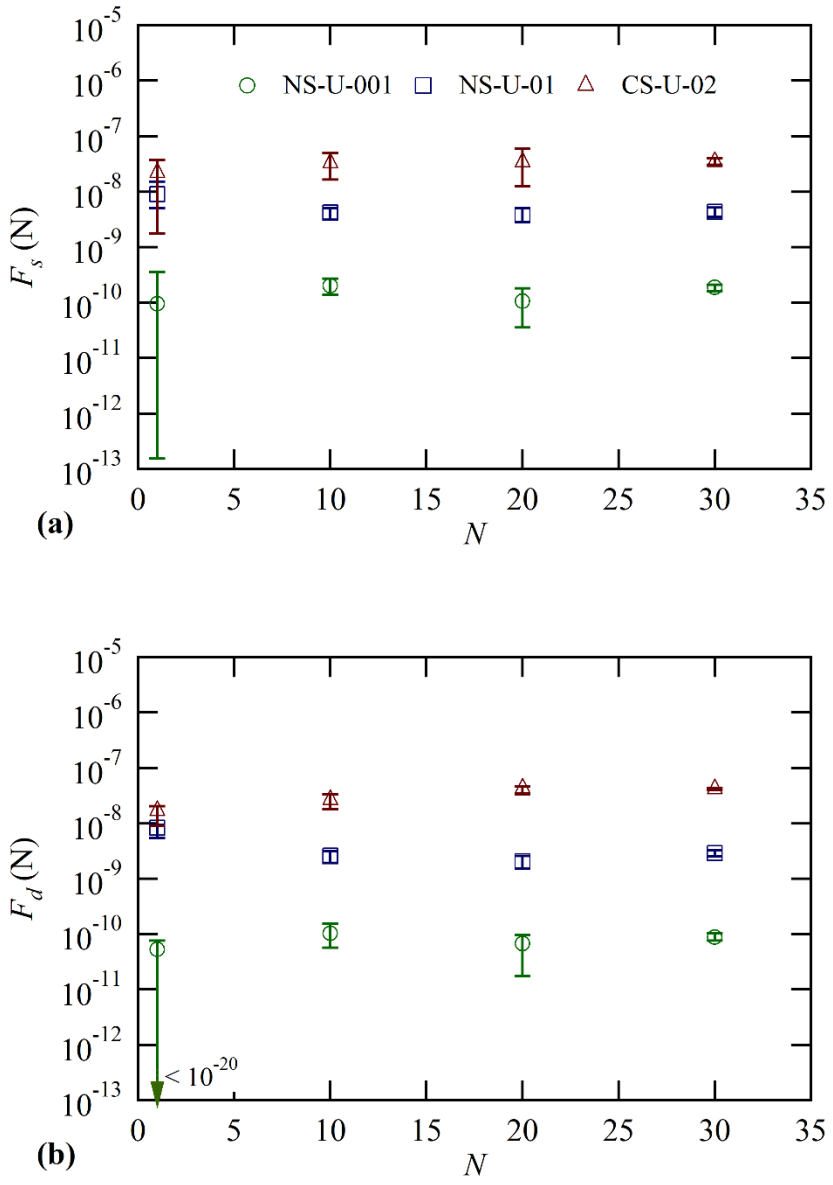

Figure 4. 12 Variations of seepage force at granular level with centrifuge gravity (a) seepage force due to differential pressure and (b) drag force.

The results of τ_p are presented as functions of d_{eff} in Figure 4. 13b and are compared with empirical values and experimental results available in the literature. It must be noted that values of ΔP_p are not available in the literature. White (1940) obtained values of τ_p from experiments of surface erosion of granular beds induced by the horizontal flow. Swamee and Ojha (1994) and Cao et al. (2006) obtained τ_p using empirical relationships based on the Shields parameter, particle size, and specific gravity of the grains. Santamarina (2003) and Ojha et al. (2003) obtained values of τ_p from simplified formulations describing flow through porous media based on Stoke's law (Santamarina 2003).

Figure 4. 13b shows that τ_p increases as d_{eff} increases and results from this study are in good agreement with the reference data. The values obtained for surface flow are generally higher. This observation may be justified considering that the resistance due to intergranular contacts may be lower under upward flow, while greater contact stresses may develop when an individual grain tends to rotate over a neighbor grain under horizontal flow. In this study, the values of τ_p obtained for the coarser sand CS-U-02 show good correlation with Swanmee and Ojha (1994) and Cao et al. (2006). Data from Santamarina (2003) and Ojha et al. (2003) is lower than the results from this study. This is expected because the formulations only account for the effective weight of the grain and the viscosity of the fluid. These formulations are often used in analytical and numerical models where grain motion is involved because of its simplicity and conservative results. Overall, it appears that theoretical values are lower than those obtained experimentally. The results of this study demonstrate that the centrifuge

modeling can be used to measure ΔP_p and τ_p and can be useful for future numerical modeling studies.

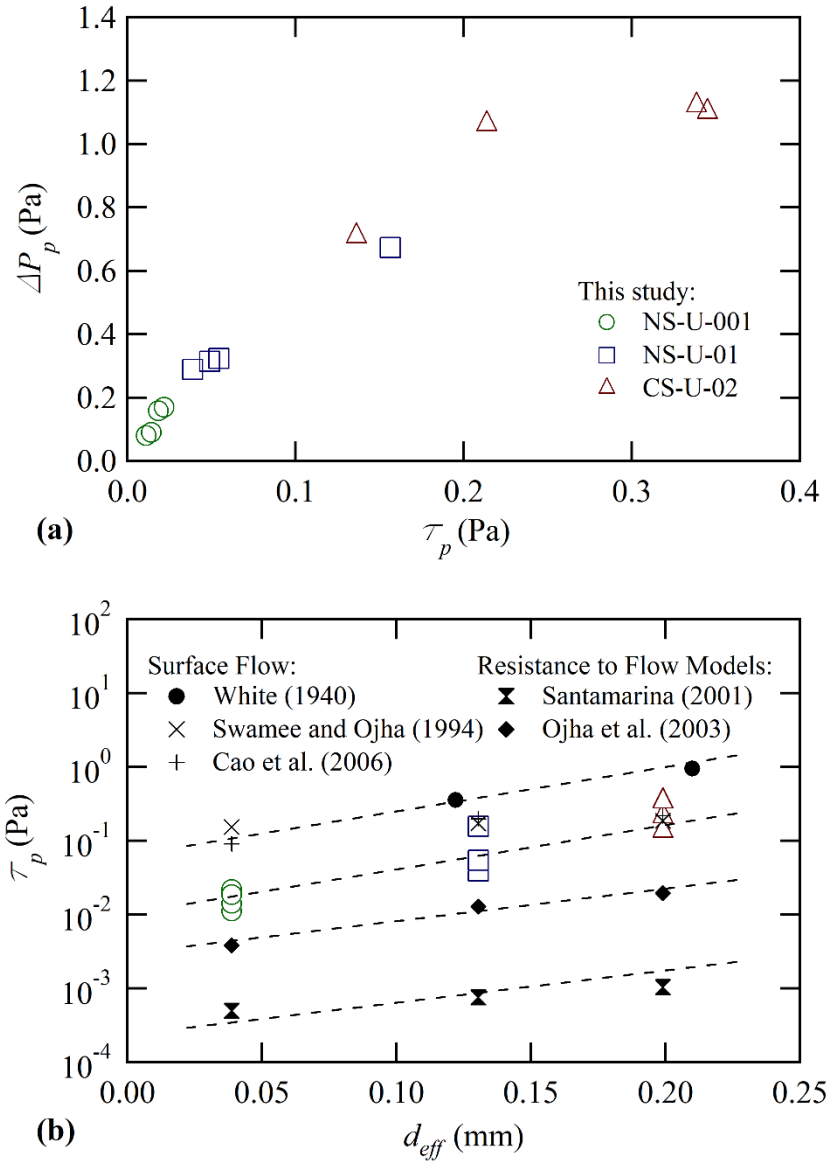

Figure 4. 13 Seepage stresses at granular level: (a) correlations between differential pressure and viscous shear stress, and (b) variations of viscous shear stress with effective diameter.

4.5 CONCLUSIONS

This study presents the centrifuge modeling of the initiation of backward erosion piping induced by upward, laminar flow through fine-grained sands. A customized experimental setup was designed to observe the development of the phenomenon and to monitor the hydraulic behavior across the entire specimen and the surface portion where the initiation is expected to occur. Tests were performed at various centrifuge accelerations without scaling grain-size, pore fluid and model dimensions, and the critical hydraulic gradients across the specimens ranged from 0.56-0.99 and 1.16-2.44, for the stages of first visible movement of grains and the total heave, respectively. Estimations of gradients within 1.6 cm near surface were used to evaluate the seepage forces and stresses at level of grains. It was observed that 16% of the critical total seepage stress was contributed by the viscous shear stress induced by the drag force, while the remaining 84% was contributed by differential pressure across the grain.

A theoretical centrifuge scaling law for the critical hydraulic gradient was derived by force equilibrium during the initiation of backward erosion piping using constant model dimensions and grain-size regardless of the centrifuge gravity. The theoretical scaling law agrees with the scaling factors obtained experimentally for the critical condition of first visible movement. Nonetheless, the scaling changes after this condition because of the continuous change of porosity during the expansion of the specimens and the possible development of non-laminar flow in the coarser material. Furthermore, the theoretical scaling law is accurate to compare models at different centrifuge accelerations, but it is less precise to predict the behavior at 1g. This is a consequence of the increase in effective stress associated to the increase in self-weight that leads to lower

deformations of the specimens at high g. Despite these observations, the experimental estimations of critical hydraulic gradients show good agreement with data available in the literature obtained using experimental methodologies and a numerical analysis based on the CFD-DEM method.

CHAPTER 5

PHYSICAL MODELING OF BACKWARD EROSION PIPING USING THE GEOTECHNICAL CENTRIFUGE[1, 2]

[1]Ovalle-Villamil, W., and Sasanakul, I. (2020) "Centrifuge Modeling Study of Backward Erosion Piping with Variable Exit." *Journal of Geotechnical and Geoenvironmental Engineering*, (In Review).

[2]Ovalle-Villamil, W., and Sasanakul, I. (2021) "Centrifuge Modeling of the Backward Erosion Piping Process," Accepted to: *10th International Conference on Scour and Erosion ICSE 10,* Arlington, Virginia, U.S., 2021.

5.1 INTRODUCTION

A detailed summary of the research related to backward erosion piping is presented in Bonelli (2013), which compiles relevant research performed by Bezuijen and Steedman (2010), Sellmeijer et al. (1991, 2011), Richards and Reddy (2008, 2010), and van Beek et al. (2011, 2012), as well as many others. This summary shows that although this phenomenon has been analyzed using different experimental and analytical methodologies and that important advances have been achieved to predict the critical hydraulic conditions that lead to failure by backward erosion piping, as well as the effects of different parameters in its development, relating the data from experimental studies to field behavior continues to be a challenge. Bonelli (2013) highlights that this challenge is not only due to the difficulties of applying experimental data directly to a field context but it is also a consequence of the limitations of the understanding of the differences between the mechanisms observed in the laboratory and the physical process that actually occurs in the field. These limitations are primarily linked to the uncertainty inherent in the use of physical models with a reduced scale. While these models are cost-effective and extremely valuable for parametric studies, they fail to reproduce the processes that are observed at full scale. Consequently, the current methods of assessing safety against backward erosion piping rely on simplified approaches that lead to conservative solutions (e.g., Bligh 1910; Lane 1935), or require complex inputs that are hardly available for standard engineering practice (e.g., Schmertmann 2000; Sellmeijer et al. 2011).

Geotechnical centrifuge modeling provides a method to produce more realistic field stress conditions and could enable a more realistic evaluation of backward erosion piping using small-scale models that conventional physical models cannot replicate.

Previous centrifuge modeling studies of backward erosion piping are available in the literature but are limited (e.g., van Beek et al. 2010; Leavell et al. 2014; Koito et al. 2016; Ovalle-Villamil and Sasanakul 2020, 2021). Some of these studies present a useful assessment of specific parameters, such as the estimation of critical hydraulic gradients, but generally without addressing relevant aspects, such as the effect of modeling erosion mechanisms under an increased gravitational acceleration field. As a result, detailed analyses of internal erosion mechanisms using centrifuge modeling, including backward erosion piping, are very limited. Furthermore, although theoretical assessments of centrifuge scaling laws related to this phenomenon are available, no experimental validation has been performed (Goodings 1982, 1984, 1985; Dong et al. 2001; Bezuijen and Steedman 2010).

This study presents the results of a series of centrifuge modeling tests of backward erosion piping using simplified small-scale models, which were prepared with the same soil and the same model dimensions and were tested under different levels of centrifuge gravitational acceleration. This investigation aims to improve the understanding of the backward erosion piping phenomena, as well as improve the centrifuge modeling testing protocol to study internal erosion. The critical hydraulic conditions leading to failure by backward erosion piping are evaluated using global and local perspectives, and the results are used to assess the effects of the exit-hole size and the changes in the centrifuge gravitational acceleration. A detailed description of the mechanisms reproduced in the models, along with a summary of the critical hydraulic gradients obtained, are presented and compared with typical, analytical estimations that are commonly used to assess safety against backward erosion piping.

5.2 EXPERIMENTAL METHODOLOGY

A customized testing setup was designed to simulate the hydraulic conditions experienced during the development of backward erosion piping inside a 15g-ton geotechnical centrifuge located at the University of South Carolina. The centrifuge models were prepared to replicate a confined sandy foundation underlying an impervious clay layer with a definable exit-hole. The erosion mechanism that was modeled began at the exit-hole and then progressed to form micropipes across the interface between the sand and clay layers that increased in length towards the upstream reservoir until failure occurred. In this study, failure was defined as the moment when the water level in the upstream reservoir could not be increased or maintained by the sandy foundation.

Figure 5. 1 shows a sketch of the experimental setup used in this study. The setup is composed of an aluminum box with two external reservoirs that were used as upstream and downstream reservoirs, along with a central reservoir that contained the model, as shown in Figure 5. 1a and 5. 1b. The central reservoir allowed for models with a length and a width of 31.5 cm. The upstream and downstream reservoirs had a length of 5 cm, a width of 31.5 cm, and a height of 30.5 cm. Drainage holes were perforated in the downstream reservoir at an elevation of 10 cm from the base of the container to maintain a constant water elevation during test. A series of circular holes with diameters of 0.32 cm were also perforated in the side walls of the central reservoir up to a height of 10 cm to ensure a homogeneous distribution of flow to the model. In addition, a No. 200 steel mesh was installed at the interfaces between the side walls and the models to prevent grain transport to the downstream and upstream reservoirs.

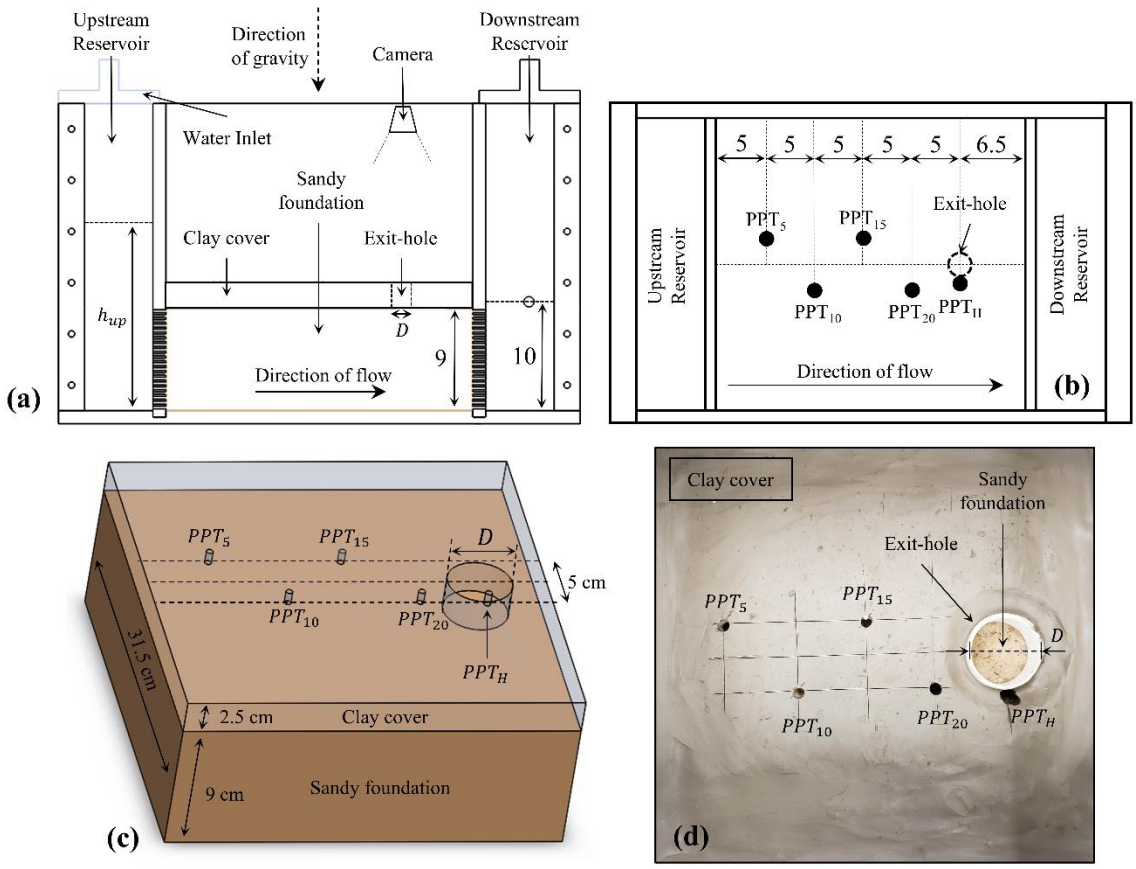

Figure 5. 1 Experimental setup in Research Topic 3: (a) lateral view, (b) plan view, (c) isometric view of model, and (d) plan view of model.

The testing setup allowed continuous measurements of pore water pressure to be taken at different locations across the surface of the sandy foundation through a series of miniature pressure sensors located at 5 cm (PPT_5), 10 cm (PPT_{10}), 15 cm (PPT_{15}), 20 cm, and 25 cm (PPT_H) from the upstream reservoir, as shown in Figure 5. 1b and 5. 1c. The center of the exit-hole was located at 25 cm from the upstream reservoir, near the location of PPT_H. Two additional pressure sensors were located in the upstream and downstream reservoirs (i.e., PPT_{Up} and PPT_{Down}), and a video camera was installed above the exit-hole to continuously record a top view of the models. During the test, the model was first

spun to a desired gravitational acceleration field, or g-level, at a rate of 4 g/min. Enough time was allowed for the sensor readings to stabilize. The water inlet located on top of the upstream reservoir was opened to increase the upstream head, h_{up}, and the global head loss across the model, $\Delta h = h_{up} - h_{down}$, inducing flow under different values of i_{global}. Several increments of h_{up} were induced until the failure occurred. The clay cover was immediately removed to conduct a post-failure visual assessment of the surface of the sandy foundation.

A total of nine models were tested at g-levels of 10g, 20g, and 30g, using exit-hole diameters, D, of 0.25 cm, 0.7 cm, 1.8 cm, 2.6 cm, and 4.9 cm. Several tests were repeated to ensure that the results are repeatable. Table 5. 1 shows the general information of each model that was tested. These g-levels were selected because a laminar flow condition could be maintained within this range with the Nevada Sand that was used in this study (Ovalle-Villamil and Sasanakul 2018). The gravitational acceleration field at 30g approached the maximum limit of laminar flow condition for this type of soil at the initial porosity.

Table 5. 1 General characteristics of centrifuge models in Research Topic 3.

ID	Centrifuge Acceleration Ng	D (cm)	ID	Centrifuge Acceleration Ng	D (cm)
Test 1	10	0.25	Test 6	10	2.6
Test 2	10	0.7	Test 7	20	2.6
Test 3	10	0.7	Test 8	30	2.6
Test 4	20	0.7	Test 9	10	4.9
Test 5	10	1.8			

5.3 SAMPLE PREPARATION AND MATERIAL PROPERTIES

The foundation soil that was used in this study was fine-grained Nevada Sand, native to the Sierra Nevada region. The soil was sieved before testing to remove grain sizes below 0.075 mm (No. 200 sieve), to achieve a uniform gradation (C_u = 1.75, C_g = 1.06), and to avoid internal erosion mechanisms that are typical of non-uniform gradations, such as suffusion (e.g., Marot et al. 2012). The foundation soil grains had an effective diameter, d_{eff}, of 0.13 mm after sieving.

The sandy foundation was prepared by placing four layers of dry sand with equal mass into the central reservoir, each one tampered manually with a steel hammer until a density of 1920 kg/cm^3 was achieved. The surface of each layer was carefully flattened with a steel flattening plate to provide a fully horizontal surface. The impervious layer that served as cover and provided overburden stress to the erodible sandy foundation was installed afterwards. In this study, the soil used as the impervious layer was a grey, low plasticity clay that is typically used in pottery and acquired in block form with a length of 30.5 cm, a width of 20.3 cm, and a height of 17.8 cm. The block was cut into several slabs with a thickness of 2.5 cm, and approximately 6 slabs were used in each model. The sides of the slabs were beveled to a nearly 45° angle to provide an overlap with a length of 2.5 cm, as used by Leavell et al. (2014). Based on video recordings and post-test observations, no leakage was observed through the clay layer, and it was in full contact with the sand layer during the tests.

For the saturation of the models, an acrylic plate with dimensions that were similar to the inner cross-section of the central reservoir was placed on top of the model, and a small surcharge of dead weight was added to provide adequate contact between the

sand and clay layers. The water level in the upstream reservoir was then increased until the water table was stable across the specimen at an elevation of nearly 4 cm from the base of the container. The surcharge was removed, and the exit-hole was created by carefully removing small cylindrical pieces of the clay layer, as shown in Figure 5. 1d. A plastic cylinder was then inserted at the exit-hole to maintain its size during testing. The sensors were also installed at the interface between the clay and the sand layers by removing cylindrical pieces of clay, and any remaining open spaces were filled as needed. The saturation continued by increasing the water level by small increments in the upstream reservoir until an initial water elevation of 10 cm was achieved across the model (i.e., Δh = 0). All models were saturated using de-air water.

5.4 RESULTS AND DISCUSSION

5.4.1 OBSERVATIONS FROM VIDEO RECORDINGS

Video recordings were used to visually describe the behavior observed as the tests progressed. Figure 5. 2 presents the top view of the exit-hole of the model in Test 6. Figure 5. 2a shows the initial hydrostatic condition across the model (i.e., Δh = 0). The behavior observed after the application of increments of h_{up} is summarized using three phases. Phase 1 refers to the event when the water level inside the exit-hole increases after increasing h_{up} and reaches an equilibrium level, as shown in Figure 5. 2b. A slight expansion of the surface of the soil was observed inside the exit-hole in Tests 6 to 9, with values of D of 2.6 cm and 4.9 cm. Due to the limited field of view, it is unknown if the same expansion occurred with a smaller D. Phase 2 refers to the event when the water level inside the exit-hole increases and exceeds the thickness of the clay layer, as shown in Figure 5. 2c. A continuous upward flow condition is established across the exit-hole

during this phase, but no grain transport occurs. Phase 3 refers to the event when the flow visually drags material from the foundation. The initial erosion observed consists of small amounts of grain suspended above the exit-hole, as shown in Figure 5. 2d. The amount of grain suspended increases as the test progresses, as shown in Figure 5. 2e, until a massive erosion of material occurs, as shown in Figure 5. 2f. This moment corresponds to the final erosion and failure of the model, which coincides with the sudden drop of h_{up}. It must be noted that the initial erosion is subjective due to the quality of the video recordings, but the final erosion is easily identified in the videos.

Phase 1 occurs from the beginning of the tests until h_{up} is high enough to induce a continuous upward flow condition across the exit-hole. The expansion of the surface that was observed in some tests within this phase is an indicator of the formation of a loosened zone near the exit-hole. According to Fleshman and Rice (2014), this behavior is attributed to the soil grains along the free surface reaching a state of incipient motion due to equilibrium between driving and resisting forces. Nonetheless, the movement of the grains is small, and consequently, the expansion of the surface is minimal. In addition, the expansion likely occurs as the water level inside the exit-hole is increasing and stops when equilibrium is achieved. In contrast, a more critical condition of flow is imposed on the soil grains once Phase 2 begins, mainly due to the existing continuous upward flow. The loosening of the soil in the vicinity of the exit-hole is expected to progress during this phase until the seepage forces acting on the grains exceed the resisting forces, and the erosion begins, which also indicates the initiation of Phase 3. It is expected that the piping initiation and progression occur within these two phases, even

though the erosion is not yet visible during Phase 2. The widening of the piping path and breach of the model occur during the final erosion at the end of Phase 3.

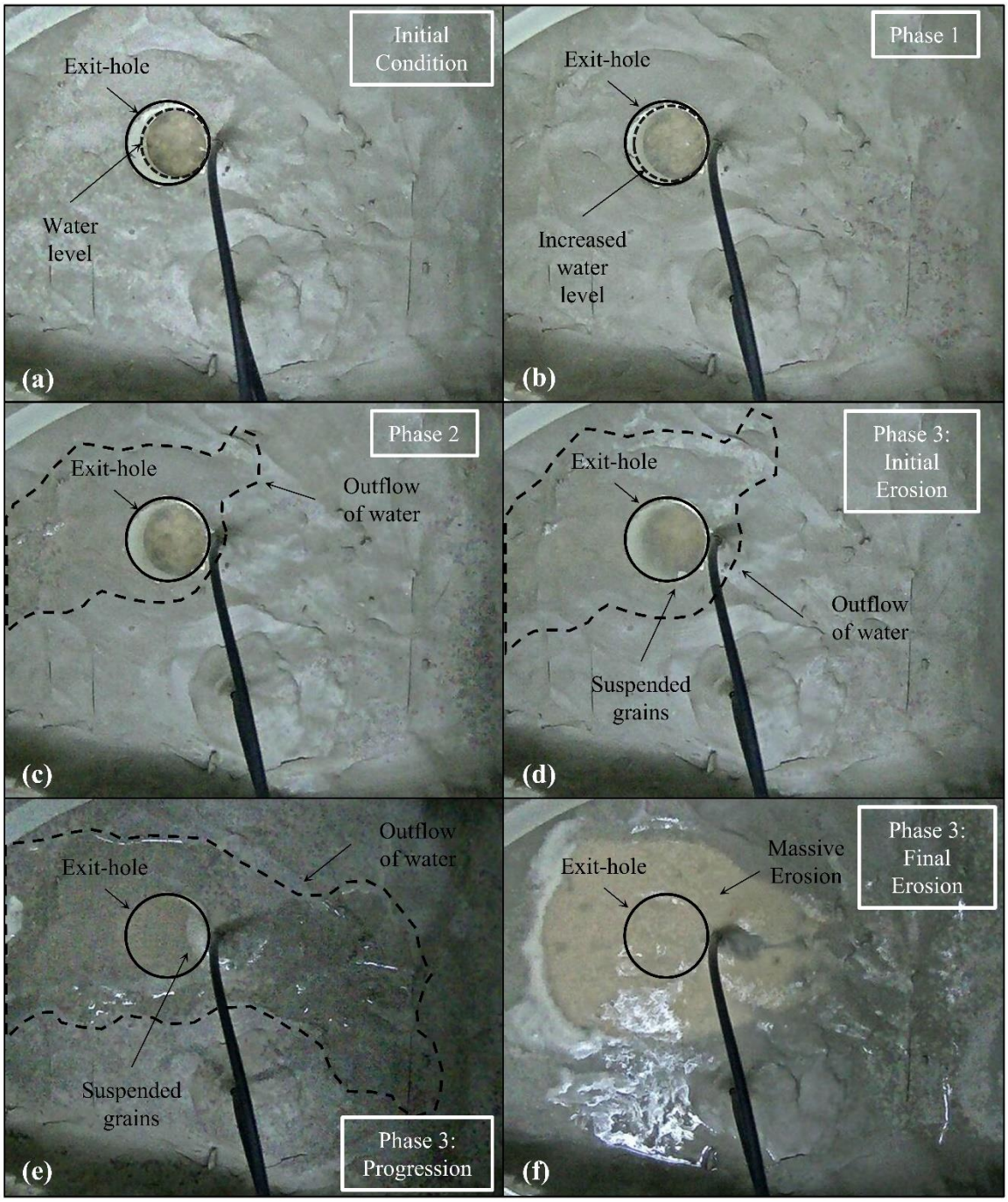

Figure 5. 2 Progression of backward erosion piping during Test 6: (a) initial conditions, (b) Phase 1, (c) Phase 2, (d) initial erosion in Phase 3, (e) progression of erosion in Phase 3, and (f) final erosion in Phase 3.

Table 5. 2 reports the occurrence of Phases 1 to 3 observed in the video recordings for each model. Although Phases 1 and 3 occurred in every model, Phase 2 was not always observed. In fact, Phase 2 only occurred in models tested at 10g with values of D < 4.9 cm. For these tests, the elapsed time between Phases 2 and 3 ranged from 8 seconds, for D = 0.7 cm, up to 2.6 minutes for D = 2.6 cm. In the remaining tests, the erosion started simultaneously with the development of a continuous upward flow condition. Hence, the initial erosion, as described previously, either occurred rapidly or did not occur.

Table 5. 2 Visual observations of centrifuge models.

ID	Phase 1	Phase 2	Phase 3		Failure Type	Crater Size (cm)	Pipe thickness (mm)
			Initial Erosion	Final Erosion			
Test 1	✓	✓	✗	✓	Type 4	2.5	None
Test 2	✓	✓	✓	✓	Type 1	4.5	5
Test 3	✓	✗	✗	✓	Type 1	4	5-25+
Test 4	✓	✗	✗	✓	Type 1	6	5-25+
Test 5	✓	✓	✓	✓	Type 1	6.5	30-40
Test 6	✓	✓	✓	✓	Type 2	6	70-80
Test 7	✓	✗	✗	✓	Type 1	3	10
Test 8	✓	✗	✗	✓	Type 4	None	None
Test 9	✓	✗	✗	✓	Type 3	None	40

5.4.2 POST-FAILURE OBSERVATIONS

A visual assessment of the surface of the specimens, which was performed after removing the clay layer, allowed for the identification of four types of failure patterns, as shown in Figure 5. 3. Type 1 displays a crater with diameters ranging from 2.5 cm to 6.5 cm at the location of the exit-hole, as shown in Figure 5. 3a. The main piping path connecting the exit-hole and the upstream reservoir was identified and followed a

meandering behavior. Signs of surface erosion over the surface of the specimen, along with one or more additional piping paths, were also identified. Type 2 displays a crater with dimensions that are similar to Type 1. However, a unique piping path towards the center of the model was observed with no meandering behavior, as shown in Figure 5. 3b. No signs of surface erosion are observed, but a clear widening of the main piping path exists. Type 3 shows a unique piping path towards the center of the specimen with no meandering behavior, as shown in Figure 5. 3c. This failure type also presents an accumulation of grains at the location of the exit-hole, forming a column of sand with a diameter similar to the exit-hole and a maximum height equal to the thickness of the clay cover layer. The grains appear to be deposited on the furthermost, downstream portion of the exit-hole, resulting in an uneven height across the diameter. Finally, Type 4 shows signs of surface erosion but not a clear piping path, as shown in Figure 5. 3d. The failure characteristics observed in each test are also presented in Table 5. 2.

The post-failure observations showed that the piping path is less meandered as D increases. No clear trend was found between the size of the crater observed and the value of D or the g-level. Nonetheless, an apparent correlation was found between the value of D and the accumulation of grains at the exit-hole. In this study, the accumulation only occurred for a value of D of 4.9 cm. For lower values of D, the foundation soil was removed as the piping progressed and was completely dragged out of the exit-hole. This behavior indicates that the seepage force dragging the soil was greater in tests with values of D lower than 4.9 cm. Consequently, the hydraulic gradient at the exit-hole and the exit velocity of flow when the erosion began were likely greater than those experienced with the greatest D.

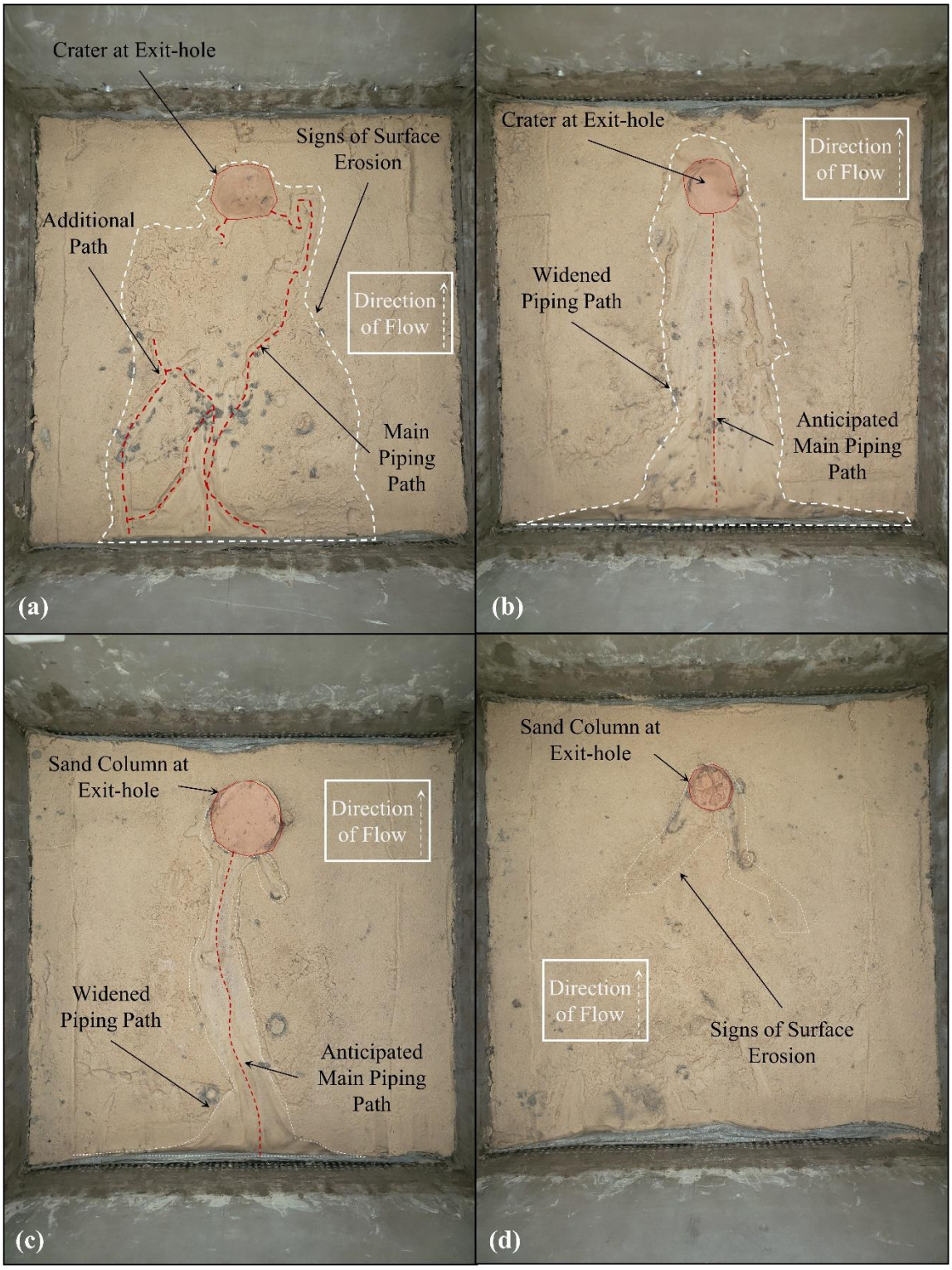

Figure 5. 3 Erosion patters in centrifuge models of backward erosion piping: (a) Type 1, (b) Type 2, (c) Type 3, and (d) Type 4.

5.4.3 EVOLUTION OF THE PIEZOMETRIC SURFACE

Figure 5. 4 shows the evolution of the piezometric surface observed during Phases 1 to 3 in Test 6 with D = 2.6 cm. The piezometric head at each port location was estimated from the pressure readings as $h_i = P_i / \gamma_w$, where P_i represents the pressure reading at the port location i and γ_w represents the unit weight of water. The dimensions were scaled to a prototype condition using an appropriate scaling law of $\boldsymbol{L} = N^{-1}$ (Taylor 2018). The datum in this figure is located at the interface between the sand and clay layers. Consequently, the piezometric head at the downstream reservoir, h_{down}, located at L = 3.15 m, was nearly 0.1 m and remained constant throughout the test. On the other hand, the piezometric head at the upstream reservoir, h_{up}, located at L = 0 m, increased as the test progressed.

During Phase 1, the slope of the piezometric surface was fairly constant between the upstream reservoir and the exit-hole location for values of h_{up} < 0.89 m (i.e., Δh < 0.77 m), as shown in Figure 5. 4a. The water level inside the exit-hole remained below the thickness of the clay cover layer for this range of h_{up}. This behavior indicates that the hydraulic gradient across the specimen remains nearly constant within this phase. These results were compared with results of a steady-state seepage analysis of the experimental setup using the program SEEP/W under an uncompressible flow condition. The numerical model assumed that no deformation of the sandy foundation occurred. Hence, no erosion or expansion within the model occurred. The experimental results showed good agreement with the numerical models for values of h_{up} < 0.76 m (i.e., Δh < 0.65 m). For greater values of h_{up}, slightly greater values of piezometric head were obtained in the

experiment, indicating that changes in the soil structure may have taken place, such as loosening, which was also observed in the video recordings.

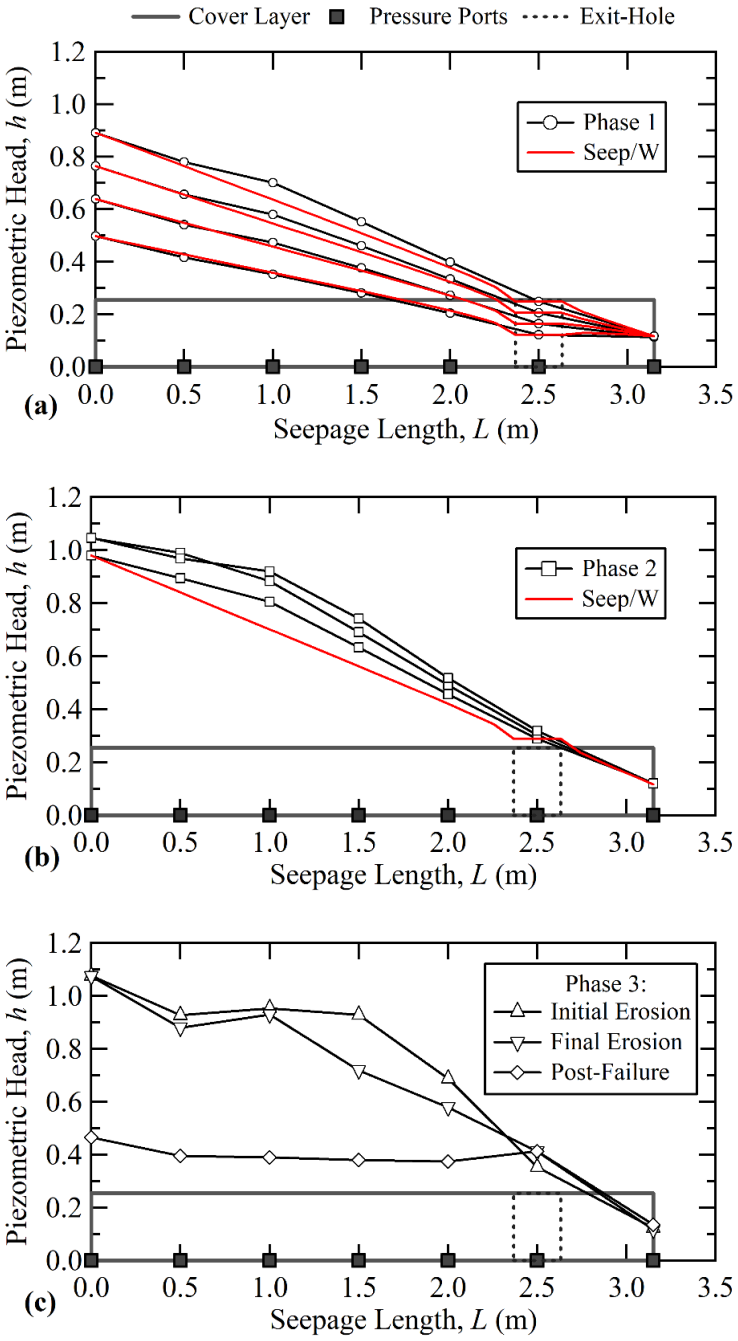

Figure 5. 4 Evolution of piezometric surface during backward erosion piping in centrifuge models: (a) Phase 1, (b) Phase 2 and (c) Phase 3.

Greater hydraulic gradients developed towards the exit-hole location as h_{up} increased within Phase 2, as shown in Figure 5. 4b. This behavior may be explained by considering that, during this phase, the exit-hole behaves like a relief well, and a greater concentration of pressure is anticipated in its vicinity. The piezometric surfaces within Phase 2 showed noticeable changes across the specimen with a sharper slope towards the exit-hole than near the upstream reservoir. The experimental piezometric head is greater than the piezometric head in the numerical model, which indicates that a loosening of the sandy foundation occurred, even though traces of erosion were not visible in the video recordings. Phase 2 continued until a maximum slope was reached towards the exit-hole, and a nearly flat slope was developed towards the upstream reservoir, as shown in Figure 5. 4c. At this moment, the initial erosion occurred as the first traces of grain suspension were visible, which also indicated the onset of Phase 3. A slight decrease in the gradient occurred near the exit-hole afterwards, as reflected by the decrease in the slope of the piezometric surface. Therefore, the erosion was anticipated to progress while the decrease in slope occurred, until a piping path was developed across the specimen and final erosion occurs. At this moment, h_{up} decreased sharply and the head loss between the upstream reservoir and the exit-hole was diminished, resulting in a fairly horizontal piezometric surface.

Phase 2 occurred for values of h_{up} between 0.98 m and 1.05 m, while Phase 3 occurred for a constant value of h_{up} of 1.10 m (i.e., Δh = 0.96 m). The most noticeable change in the localized hydraulic gradients (i.e., hydraulic gradients in different segments across the specimen) occurred within Phases 2 and 3 and may be the result of either the backward expansion of the loosened soil or the initiation and progression of the main

piping path. However, based on the visual assessment and comparisons with the numerical results, an expansion of the soil may have occurred for lower values of h_{up}. The behavior observed indicates that the critical condition was determined by a unique value of i_{global}. As discussed by Van Beek et al. (2014), this behavior is typical of initiation-dominated models, in which the critical hydraulic gradient for the initiation of backward erosion piping is much greater than that of the progression phase. Therefore, intermediate equilibrium was not observed during the progression.

5.4.4 Evolution of Global and Local Hydraulic Gradients

Local hydraulic gradients were estimated between different pressure ports, and the results obtained are shown in Figure 5. 5 as functions of the elapsed time in Test 6. Figs. 6a and 6b show the local hydraulic gradients for the segment $PPT_5 - PPT_H$ (i.e., i_{5-H}), the shortest segment nearest to the exit-hole, $PPT_{20} - PPT_H$ (i.e., i_{20-H}), a segment on the left side of the specimen between PPT_5 and PPT_{15} (i.e., i_{5-15}), a segment on the right side of the specimen between PPT_{10} and PPT_{20} (i.e., i_{10-20}), and the entire seepage length across the specimen between the upstream and downstream reservoirs (i.e., i_{global}). The onset of Phases 1 to 3 is also highlighted. Figure 5. 5a shows the evolution of the local hydraulic gradients from the beginning of the test until the onset of Phase 2, while Figure 5. 5b shows the results observed during the remaining testing time.

As shown in Figure 5. 5a, for the initial 81 minutes of the test and during Phase 1, the value of i_{20-H}, which corresponds to the segment closest to the exit-hole, increased at a greater rate than i_{5-15}, which corresponds to the segment further away. The difference in gradients between these two segments also increased as i_{global} increased. This behavior indicates that the local hydraulic gradient tends to increase at a greater rate

towards the location of the exit-hole, as described in Figure 5. 4. It is noted that i_{5-H} showed an average behavior for the remaining segments and was generally greater than i_{global}. This observation is justified, considering that i_{global} is obtained from Δh and is used as a control during the test, but it remains independent of the local flow conditions until failure occurs. In contrast, i_{5-H} accounts for the local changes that continuously occurred during the test, which indicates that the flow across the model is not necessarily represented by i_{global}.

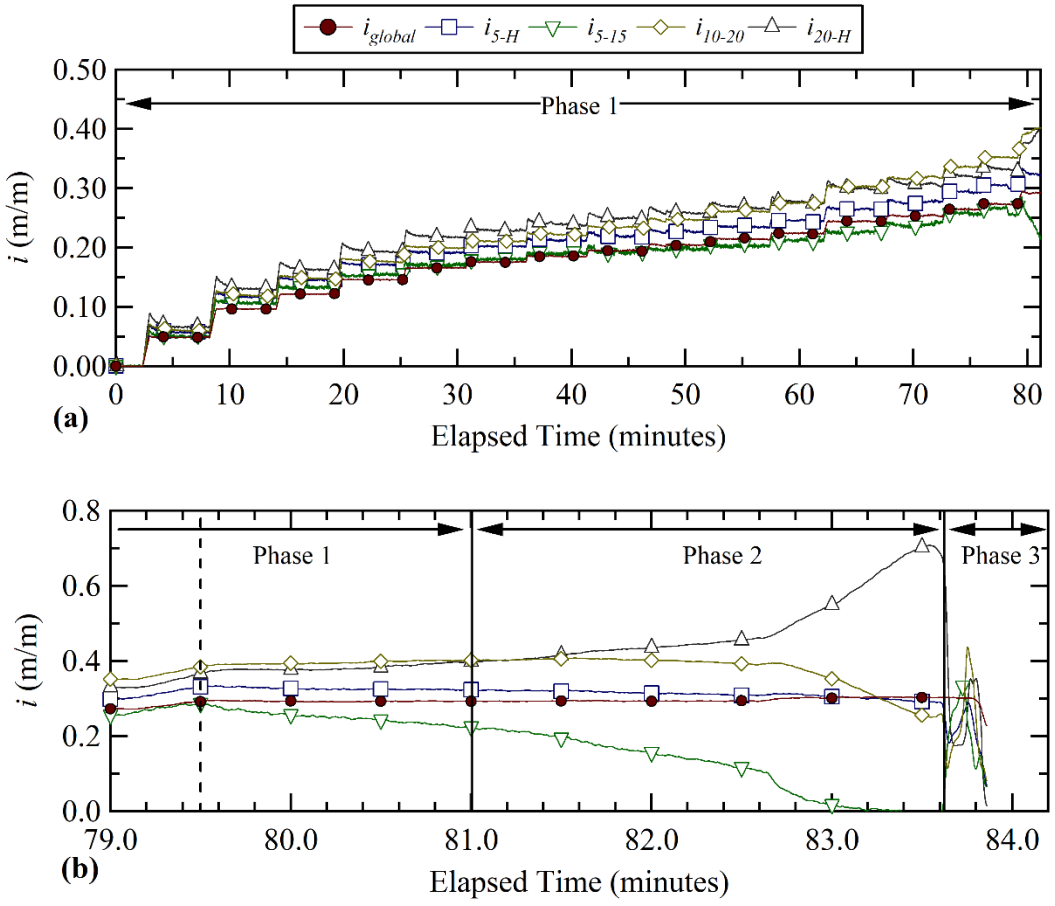

Figure 5. 5 Evolution of global and local hydraulic gradients: (a) Phase 1 and (b) Phases 1 to 3.

A change in the overall behavior takes place at 79.5 minutes, as shown in Figure 5. 5b. At this moment, the value of i_{20-H} began to increase at a greater rate than in the remaining segments, while the value of i_{5-15} began to decrease. These changes resulted in a relatively constant value of i_{5-H}, which indicates that the increase of i_{20-H} compensates for the decrease of i_{5-15}. The value of i_{20-H} remained constant through the end of Phase 1 and through Phase 2, but it increased sharply at 82.6 minutes until the end of Phase 2 and before the initial erosion. The local hydraulic gradient in the other segments decreased within this interval of time. During Phase 3 and after the initial erosion, the local hydraulic gradient in the segments reached fairly constant values and then dropped significantly after the final erosion. Although describing the evolution of the local hydraulic gradients is difficult during this phase due to the short amount of time that elapsed (12 seconds), it is anticipated that the widening of the piping path occurs within this period. In addition, the moment when the piping path reaches the upstream reservoir can be identified when the value of i_{global} decreases sharply. It is interesting to note that the gradient across both sides of the model is similar at the beginning of the test but increases more towards the location of PPT_5 and PPT_{15} than towards the location of PPT_{10} and PPT_{20}, as i_{global} increases. This behavior indicates that the flow is not symmetrical across both sides of the model, even though the erosion pattern observed after the test is located towards the center of the model.

5.4.5 Effect of the exit-hole size D

Figure 5. 6 shows the critical hydraulic gradients that were estimated as functions of D. This figure only displays the results obtained in tests at 10g, which allow for comparisons under the same conditions of self-weight. The critical hydraulic gradients

are presented for the entire length of specimen, $i_{cr_{Global}}$, the longest segment between pressure ports, $i_{cr_{5-H}}$, and the segment closest to the exit-hole, $i_{cr_{20-H}}$. Overall, the critical values ranged from 0.25 to 0.40, with average values of 0.26, 0.34 and 0.31 for $i_{cr_{Global}}$, $i_{cr_{5-H}}$ and $i_{cr_{20-H}}$, respectively. The value of i_{cr} appeared to be consistent for D < 4.9 cm, regardless of the segment. However, a slight decrease was observed for D = 4.9 cm. As highlighted in experimental studies of the initiation phase of backward erosion piping, which modeled the exit-hole using cylindrical columns of uniform sands (Fleshman and Rice 2014; Ovalle-Villamil and Sasanakul 2020), there was a contribution of the lateral confinement to the internal stability of the grains beneath the exit-hole. Based on the results obtained in this study, this contribution was greater as D decreased, and consequently, a lower hydraulic gradient was anticipated to cause grain motion as D increased. In addition, a greater cross-sectional area of the exit-hole facilitates the expansion of the soil, thus reducing the seepage stress that is required to initiate and progress the erosion.

The values of i_{cr} in Figure 5. 6 were also compared with estimates from the models of Bligh (1910), Lane (1934) and Sellmeijer et al. (1991), as described in Section 2.6 (Eqs. 2. 29, 2.30 and 2.31). It is important to note that these models incorporate some soil properties and the general geometry of the structure to predict the critical i_{global} but ignore the dimensions or the type of exit. Consequently, a constant critical value is obtained, regardless of D. The experimental values of i_{cr} obtained in this study fall within the range of the analytical estimates, indicating good agreement. However, estimates from the models of Bligh (1910) and Lane (1934) are noticeably lower than the experimental estimates, while the estimate from Sellmeijer et al. (1991) is closer but

slightly greater. The differences observed may be attributed to the simplicity of the models by Bligh (1910) and Lane (1934), which solely rely on the type of soil, compared to the more elaborate model developed by Sellmeijer et al. (1991). The average difference between the analytical and experimental estimates ranged from 23% to 78%. It must be noted that estimates of $i_{cr_{global}}$ from both analytical and experimental models do not accurately represent the critical local conditions. This finding is particularly important for the assessment of backward erosion piping, in which knowledge of the localized conditions is needed, as indicated in the method proposed by Schmertmann (2000), which relies on comparisons between analytical and experimental values of local hydraulic gradients.

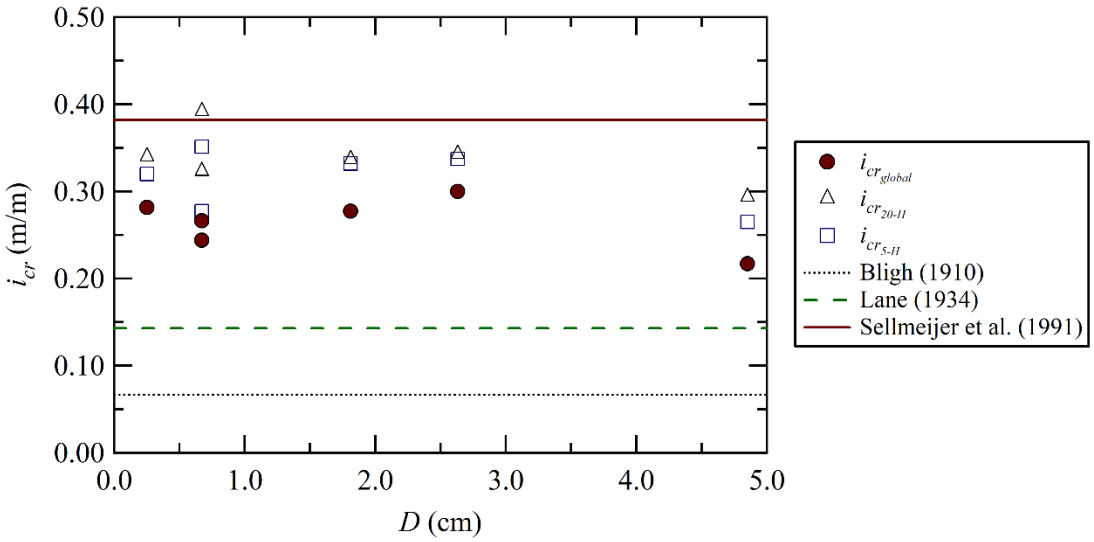

Figure 5. 6 Critical global and local hydraulic gradients in models at 10g.

Results from this study also show that the values of $i_{cr_{global}}$ remained nearly constant as D increased, indicating that the effect of D on the critical hydraulic gradient was minimal. This behavior is similar to that observed in the experimental study using

flume-type testing by Van Beek et al. (2015). In their study, a slight increase of 0.01 in the value of $i_{cr_{global}}$ was obtained as D increased from 6 mm to 12 mm. Despite this finding, results and observations from this study found that the characteristics of the piping path and the amount of material eroded are affected by D, as shown previously in Figure 5. 2 and Table 5. 2.

5.4.6 Effect of the centrifuge gravitational acceleration

Figure 5. 7 shows the critical hydraulic gradients obtained in different segments for Tests 2 and 4 with D = 0.7 cm and Tests 6 to 8 with D = 2.6 cm. Results are presented as functions of the g-level. Since the centrifuge models tested in this study use the same soil, the weight of the grains increased as the g-level for each model increased. The seepage force and the hydraulic gradient required to drag the grains are expected to increase in proportion to increases in the g-level (Bezuijen and Steedman 2010). However, results in Figure 5. 7 show a slight decrease of i_{cr} as the g-level increases, regardless of the local segment and the value of D. This behavior may be associated with a scaling effect of the seepage length, considering that by increasing the gravitational acceleration field in the models, a longer seepage length than the actual model size is simulated (Bezuijen and Steedman 2010; Taylor 2011). Consequently, a longer seepage length is modeled at 30g than at 10g, and a lower critical hydraulic gradient is anticipated, as observed in flume-type tests under Earth's gravity (Van Beek et al. 2015). It is important to note that the erosion that was reproduced in this study began after the water level inside the exit-hole exceeded the thickness of the clay cover. This condition could occur at lower values of Δh if the seepage length in the centrifuge model is decreased. Consequently, lower values of i_{cr} may be obtained as the seepage length

decreases. Further research on the effect of the seepage length in centrifuge environments is needed.

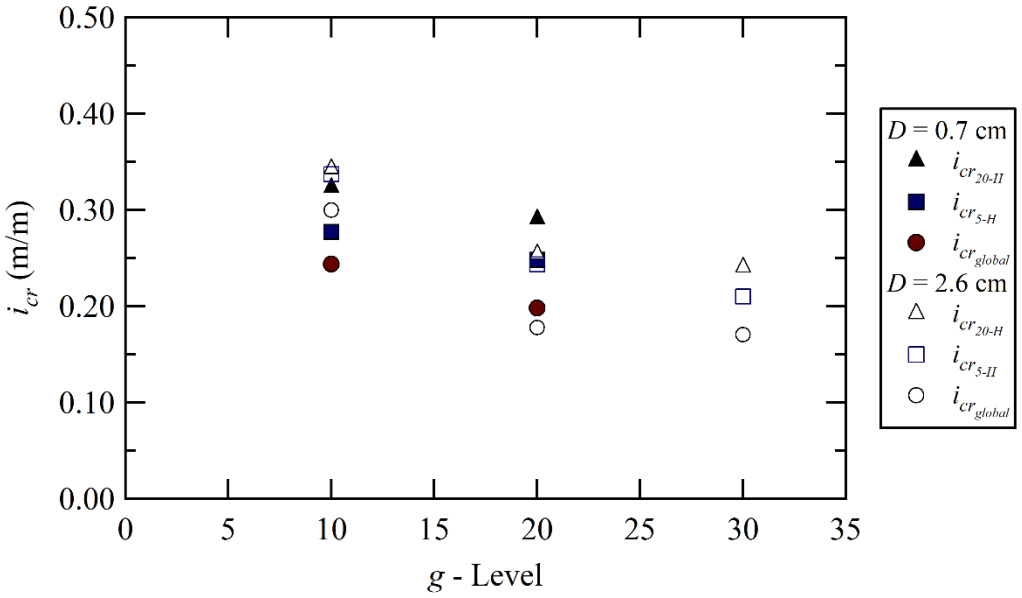

Figure 5. 7 Critical global and local hydraulic gradients in models at 10g, 20g and 30g.

Increasing the gravitational acceleration also affected the erosion pattern after the tests, as observed in Test 8 with a value of D of 2.6 cm and a g-level of 30g (i.e., Type 4), as presented in Table 5. 2 and Figure 5. 3. Although the failure in this model occurred, an identifiable piping path was not observed, which was seen in Tests 6 and 7 with a similar value of D but a lower g-level. Likewise, the amount of eroded material was noticeably lower at 30g. These observations suggest that the change in porosity before failure decreased as the g-level increased, and the phases of piping progression and widening are not clearly defined as final phases inducing a failure condition. This behavior may also be related to the occurrence of non-laminar flow, but its effects on the piping pattern remain unknown. It is important to note that the existence of the piping path in the model of Test

8 is possible, but it may be invisible or may have collapsed during the post-failure assessment. As reported by van Beek et al. (2015), the width of the piping path is approximately 30 times the size of the grains. As a result, an approximate width before widening of 0.4 mm is anticipated for the tests in this study.

5.5 CONCLUSIONS

This study presents the centrifuge modeling of backward erosion piping using small-scaled models with the same dimensions, soil type, and pore fluid. These models were tested at g-levels of 10g, 20g, and 30g. Detailed visual assessment of the centrifuge models showed that the erosion process consists of an initial seepage phase, followed by the formation of a loosened zone near the exit-hole that leads to the initiation, progression, and widening of a piping path between the exit-hole and the upstream reservoir. The piezometric surface evolved during the process from homogeneous linear behavior, indicating a constant distribution of head loss across the specimen, to a noticeably greater head loss towards the exit-hole than towards the upstream reservoir prior to erosion. The erosion occurred in two phases, with an initial erosion showing small traces of grains that were dragged from the foundation, and a final erosion with a markedly greater erosion rate. Both phases occurred for the same hydraulic gradient, suggesting an initiation-dominated mechanism, which is typical of small-scaled model observations.

The critical hydraulic gradient was evaluated for both local and global conditions, and values ranging from 0.15 to 0.4 were obtained. The critical hydraulic gradients remained constant as the size of the exit-hole increased, which has been shown in the literature, but a slight decrease was observed with the greatest exit-hole tested. In

addition, the critical hydraulic gradient slightly decreased as the g-level increased. The overall critical values obtained fell within a range of values that were estimated using common analytical methods, and average differences between the experimental and analytical estimates ranged from 25% to 78%. It was noted that centrifuge tests at a high g-level should be conducted with careful considerations of several unknowns, including the scaling effects of seepage length and the development of non-laminar flow. Nevertheless, this study provides new insights into the complex mechanisms of backward erosion piping.

CHAPTER 6

CENTRIFUGE MODELING OF BACKWARD EROSION PIPING IN MODELS WITH VARIABLE SEEPAGE LENGTH AND EXIT SIZE[1, 2]

[1]Ovalle-Villamil, W., and Sasanakul, I. (2020) "Effects of Seepage Length on Centrifuge Models of Backward Erosion Piping with Variable Exit." (In Preparation).

[2]Ovalle-Villamil, W., and Sasanakul, I. (2021) "Centrifuge Modeling of the Backward Erosion Piping Process," Accepted to: *10th International Conference on Scour and Erosion ICSE 10,* Arlington, Virginia, U.S., 2021.

6.1 INTRODUCTION

Backward erosion piping is an internal erosion mechanism that is widely recognized as a potential hazard for water-retaining structures founded on granular materials (Foster et al. 2000; Richards and Reddy 2007; Danka and Zhang 2015). Field assessment of backward erosion piping is challenging because the process is difficult to detect before failure and any post-failure information is usually washed away after the breach (Costa and di Prisco 1999; Richards and Reddy 2007). Challenges are also encountered during physical modeling of backward erosion piping because of the complexity of the phenomenon and the numerous factors affecting the results (Van Beek et al. 2014, 2015). Parametric studies have been performed to improve the understanding of the phenomenon and to validate existing analytical models (e.g., Schmertmann 2000; Sellmeijer et al. 2011), as well as to evaluate effects of several factors, including foundation soil properties and geometry of the structure (e.g., Van Beek et al. 2011, 2014, 2015; Ovalle-Villamil and Sasanakul 2020, 2021). Despite the difficulties and limitations, results from physical models have provided valuable information to advance the understanding of backward erosion piping and that helped in the development of predictive tools applicable for field conditions.

Studies of backward erosion piping generally modeled the erosion that begins at a predefined exit for drainage and then progressed backwards across the interface between a sandy foundation and an impervious cover layer. These studies used models with different scales, geometrical characteristics and testing procedures and were performed to meet specific objectives, such as assessing the scaling effects by varying the model dimensions, seepage length and size of the exit, but the results typically included

estimations of critical hydraulic gradients that lead to failure. The behaviors observed vary noticeably from model to model due to, among others, the differences in flow behavior relative to the characteristics of the experiment (Van Beek 2015), and an accurate evaluation of other parameters, such as grain size, is still challenging. The development of new experimental techniques to study backward erosion piping using alternative approaches is necessary to improve the understanding of this phenomenon.

The geotechnical centrifuge modeling technique has been extensively used to analyze complex behaviors of geotechnical structures as an alternative to full-scale experiments (e.g., Gajan et al. 2005; Murillo et al. 2009; Lanzano et al. 2012; Stewart et al. 2015), as well as to study soil behavior under different loading conditions using the advantage of modeling a realistic stress condition imposed by the centrifuge gravitational acceleration field (Taylor 2018). This technique has great potential to study internal erosion phenomena, including backward erosion piping, to observe their effects on the behavior of geotechnical structures and to evaluate existing mitigation measures. However, only a few studies have addressed the implications of centrifuge modeling of internal erosion phenomena, and these studies did not examine the scaling behavior required for centrifuge data interpretation. Therefore, more research is needed to effectively use centrifuge modeling to model backward erosion piping and to compare centrifuge results with results from previous research using models under Earth's gravity.

This study focuses on the backward erosion piping mechanism that initiates at a circular exit-hole, resembling a crack in an impervious cover layer in which the flow concentrates, and that progresses backwards to form micropipes across a foundation made of a uniform, fine-grained sand. The results are analyzed to describe the effects of

two relevant parameters that are broadly studied in the literature: the seepage length and the size of the exit-hole. In addition, the effect of the centrifuge gravitational acceleration field imposed in the models is evaluated. The behavior observed and the estimations of critical hydraulic gradients are compared with the results from physical models available in the literature.

6.2 EXPERIMENTAL METHODOLOGY

The models tested in this study followed a three-dimensional configuration and resembled a confined sandy foundation underlying an impervious clay layer with a cylindrical exit-hole. The models were tested at 10g, 20g and 30g using the 15g-ton geotechnical centrifuge located at the University of South Carolina. Details of the experimental setup used are shown in Figures 6. 1 and 6. 2. The setup is composed of an aluminum box with two external reservoirs, which were used as upstream and downstream reservoirs, along with a central reservoir that contained the models, as shown in Figures 6. 1 and 6. 2a. A series of circular holes with diameters of 0.32 cm were perforated on the inner walls of the external reservoirs up to a height of 10 cm to ensure a homogeneous distribution of flow to the models. A No. 200 steel mesh was installed at the interfaces between the side walls and the foundation soil to prevent grain transport to the reservoirs. Two additional drainage holes were perforated in the downstream reservoir at an elevation of 10 cm from the base of the container to maintain a constant water elevation during the tests. The central reservoir containing the specimens had a length and a width of 31.5 cm and a height of 30.5 cm.

The exit-hole diameter, D, in the models were 7 mm, 18 mm, 26 mm and 49 mm, and were located at distances from the upstream reservoir of 15 cm and 25 cm, which

also indicate the seepage lengths, L, modeled. A series of miniature pore pressure sensors were placed at different locations across the surface of the sandy foundation depending on the value of L, as shown in Figures 6. 2b and 6. 2c. The sensors were located at 5 cm (PPT_1), 10 cm (PPT_2), 15 cm (PPT_3), and 20 cm (PPT_4) from the upstream reservoir in models with L = 25 cm, while pairs of sensors were placed in parallel at distances of 5 cm (PPT_1 and PPT_2) and 10 cm (PPT_3 and PPT_4) from the upstream reservoir in models with L = 15 cm. An additional sensor was located near the location of the exit-hole (PPT_H) in every model and two more sensors were located inside the upstream and downstream reservoirs (i.e., PPT_{Up} and PPT_{Down}). A video camera was installed above the exit-hole to continuously record a top view of the models during test.

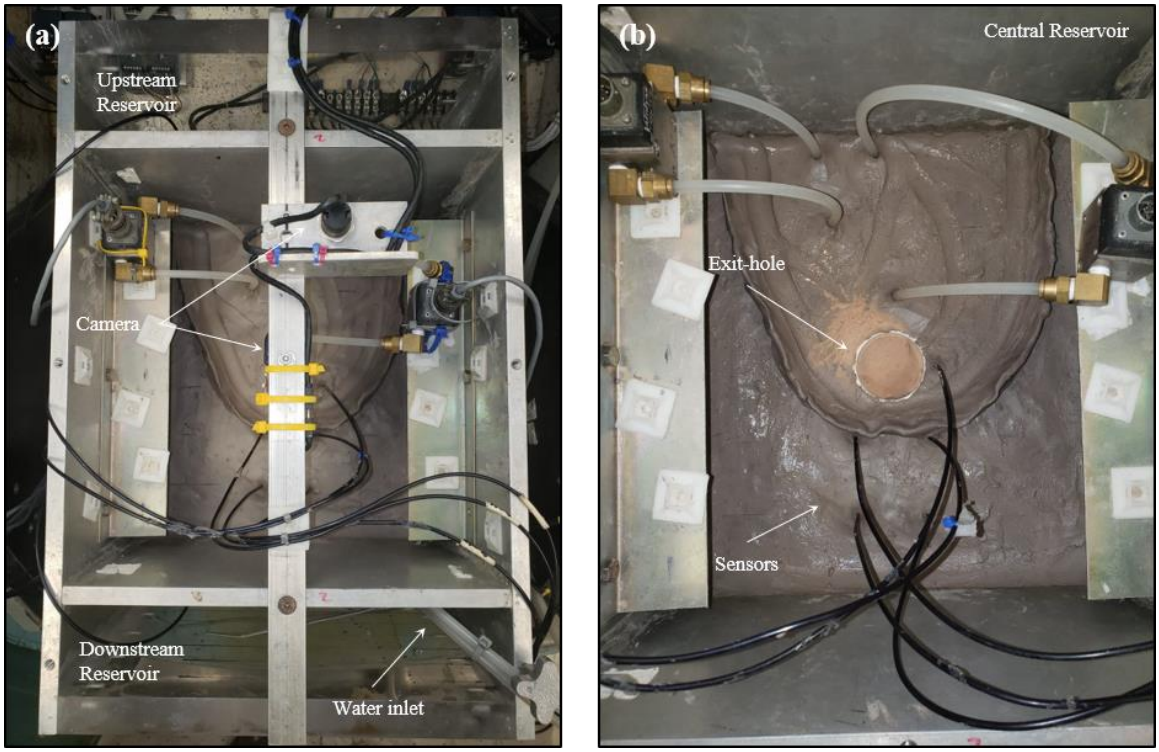

Figure 6. 1 Example of centrifuge model for experiments in Research Topic 4: (a) top view before failure, and (b) post-failure top view.

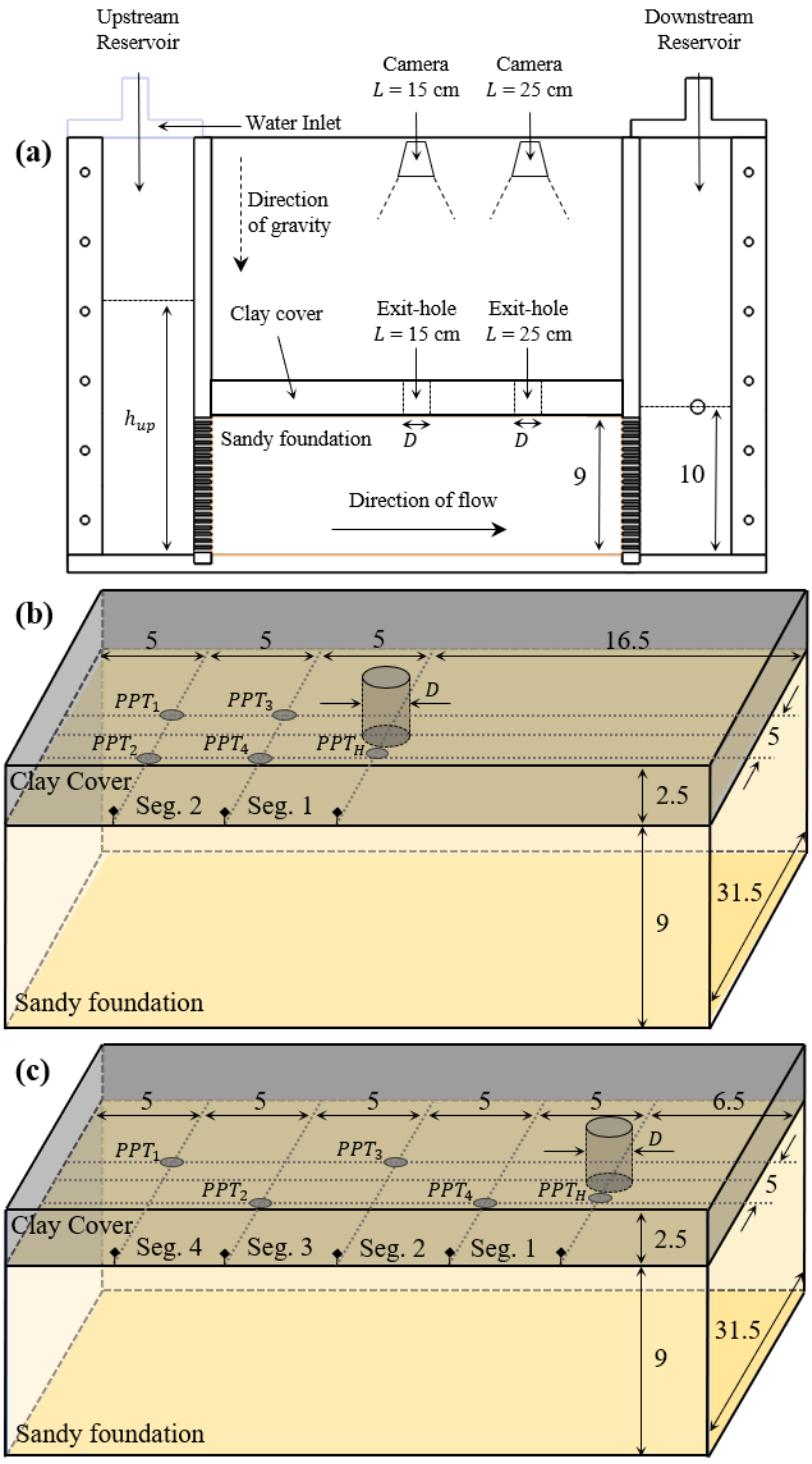

Figure 6. 2 Sketch of experimental setup for experiments in Research Topic 4: (a) side view, (b) model with L = 15 cm, (c) model with L = 25 cm (units in cm).

The tests began with spinning the models to a desired gravitational acceleration field, Ng, at a rate of 4 g/min. Enough time was allowed for the pressure sensor readings to stabilize. Afterwards, a water inlet located on top of the upstream reservoir was opened to increase the upstream head, h_{up}, inducing flow under different values of head loss between reservoirs, $\Delta h = h_{up} - h_{down}$. Several increments of h_{up} were induced until the failure occurred, which was identified as the moment when the foundation soil could not maintain the water level inside the upstream reservoir. A total of 12 tests were reproduced and the values of N, L and D in each model are shown in Table 6. 1.

Table 6. 1 General characteristics of centrifuge models tested for Research Topic 4.

Test No.	N (g_{model}/g_{earth})	L (cm)	D (mm)
1	$10g$	25	7
2	$10g$	25	18
3	$10g$	25	26
4	$20g$	25	26
5	$30g$	25	26
6	$10g$	25	49
7	$10g$	15	7
8	$10g$	15	18
9	$10g$	15	26
10	$10g$	15	49
11	$20g$	15	49
12	$30g$	15	49

6.3 SAMPLE PREPARATION AND MATERIAL PROPERTIES

The foundation soil that was used in this study was a fine-grained Nevada Sand, native to the Sierra Nevada region. The soil was sieved to achieve a uniform gradation (C_u = 1.75, C_g = 1.06) and to remove grain sizes below 0.075 mm (No. 200 sieve), which

resulted in a mean diameter, d_{50}, of 0.13 mm. The soil used as impervious cover layer was a grey, low plasticity clay typically used in pottery. The sandy foundation was prepared by tamping four layers of dry sand until a density of 1920 kg/cm3. The clay cover layer was prepared from approximately 6 slabs of clay with a thickness of 2.5 cm and was placed on top of the sand layer. The sides of the slabs were beveled to a 45° angle to provide overlap and prevent leaking (Leavell et al. 2014).

For the saturation of the models, an acrylic plate with similar dimensions than the inner cross-section of the central reservoir was placed on top of the model. A small surcharge of dead weight was added to provide adequate contact between the sand and clay layers. The water level in the upstream reservoir was then increased until the water table was stable across the specimen at an elevation of nearly 4 cm from the base of the container. The surcharge was removed, and the exit-hole was created by removing cylindrical pieces of the clay layer. A plastic cylinder was inserted at the exit-hole to maintain its size during testing. The sensors were also installed at the interface between the clay and the sand layers by removing cylindrical pieces of clay. Any remaining open spaces were filled as needed. The saturation continued by gradually increasing the water level in the upstream reservoir until an initial water elevation of 10 cm was achieved across the model (i.e., Δh = 0).

6.4 RESULTS AND DISCUSSION

The results and analysis from the models tested are presented in this section. The initial assessments were done under similar stress conditions using the results from models tested at 10g, as shown in Table 1, including the evolution of the piezometric surface, the analysis of the behaviors modeled, and the pressure loss and critical gradients

as functions of seepage length, L, and exit-hole size, D. Afterwards, the effects of modeling under an increased gravitational acceleration field are presented using the results from models at 10g, 20g and 30g.

6.4.1 Evolution of piezometric surface in centrifuge models

The evolution of the piezometric surface was analyzed to describe the global behavior modeled. The piezometric surface was determined from the pressure head at each port location shown in Figure 6. 2 and was estimated as $h = P/\gamma_w$, where P represents the pressure reading and γ_w represents the unit weight of water. Figure 6. 3 shows the results obtained in models with an exit-hole diameter, D, of 2.6 cm and seepage lengths, L, of 25 cm and 15 cm. The datum in this figure is located at the interface between the sand and clay layers. The values of h in the model with L = 15 cm are the average of the pressure readings at equivalent distances. The values of h at L = 0 m and L = 3.15 m correspond to the water head inside the upstream and downstream reservoirs, respectively (i.e., h_{up} and h_{down}). The dimensions in Figure 6. 3 were scaled to a prototype condition of 1g using an appropriate scaling law of $\boldsymbol{L} = N^{-1}$ (Taylor 2018).

The general behavior was first analyzed from the video recordings and three typical phases were identified. The initial phase (namely Phase 1) comprised the increments of h_{up} for which the water level inside the exit-hole remained below the surface of the clay cover layer. The second phase (namely Phase 2) comprised the increments of h_{up} for which continuous emerging flow occurred across the exit-holes as the water level exceeded the surface of the clay layer, but traces of erosion were not observed. The last phase (namely Phase 3) comprised the increments of h_{up} for which the erosion was visible in the video recordings and progressed until the failure of the model.

The evolution of the piezometric surfaces during these phases are presented in Figures 6. 3a, 6. 3b and 6. 3c, respectively.

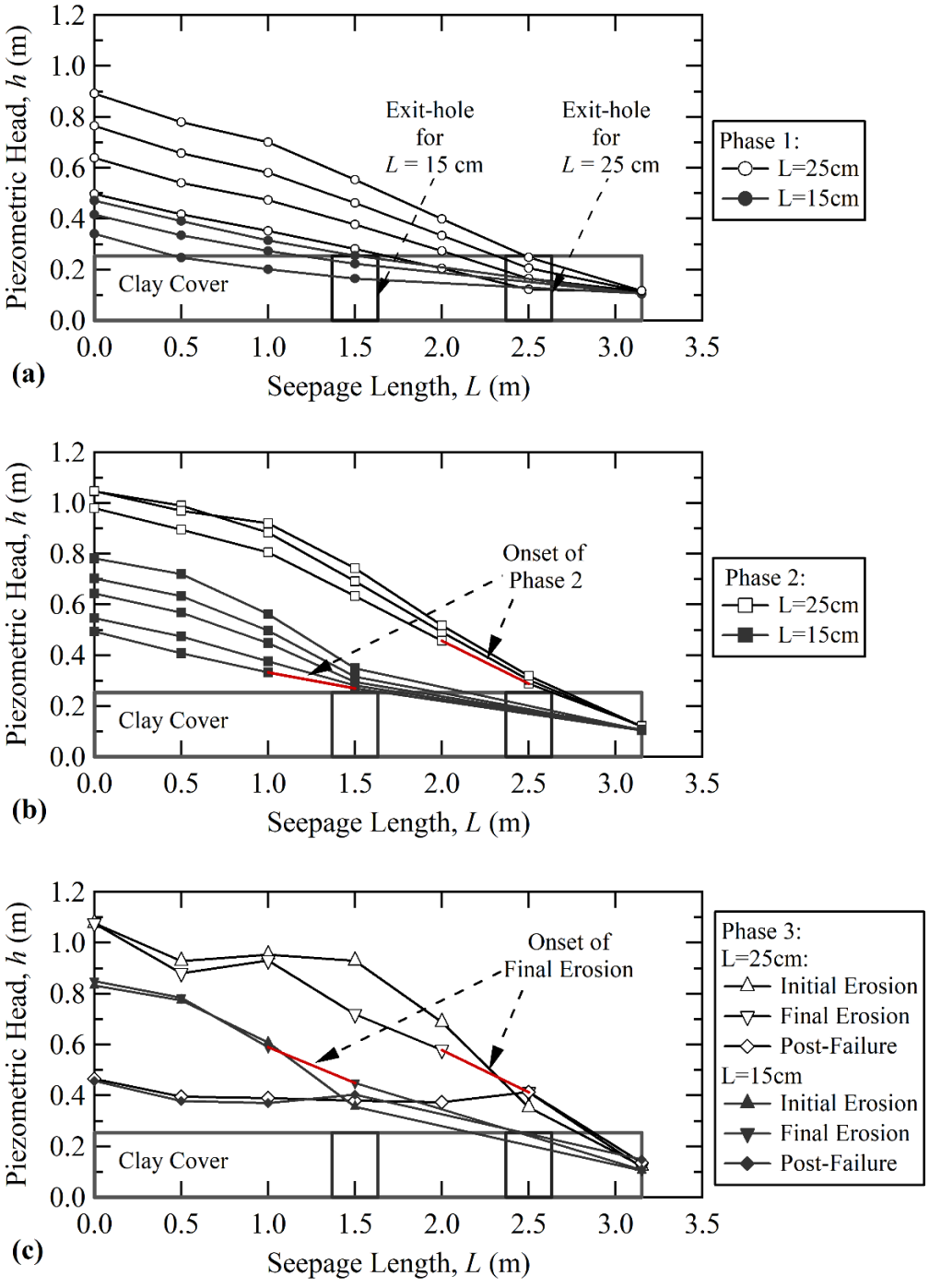

Figure 6. 3 Evolution of the piezometric surface during (a) Phase 1, (b) Phase 2 and (c) Phase 3.

As shown in Figure 6. 3a, Phase 1 developed from the beginning of the tests until a value of h_{up} of 0.47 m in the model with L = 15 cm, and until a value of h_{up} of 0.89 m in the model with L = 25 cm. The slope of the piezometric surface was constant between the upstream reservoir and the exit-hole in both models. The values of h_{up} within Phase 2 were greater in the model with L = 25 cm (0.98 m to 1.05 m) compared to the model with L = 15 cm (0.49 m to 0.78 m), as shown in Figure 6. 3b. For L = 15 cm, the slope remained constant for values of h_{up} of up to 0.54 m, and then the slope increased towards the exit-hole and decreased towards the upstream reservoir for values of h_{up} between 0.54 m and 0.78 m. The latter behavior also occurred for every value of h_{up} in the model with L = 25 cm. The slope towards the exit-hole increased in both models within Phase 2 until reaching a maximum value before the erosion was visible, but a greater number of increments of h_{up} was allowed in the model with shorter L. Finally, as shown in Figure 6. 3c, Phase 3 occurred for a relatively constant value of h_{up} of 0.85 m and 1.10 m in the models with L = 15 cm and L = 25 cm, respectively. Regardless of L, the slope of the piezometric surface slightly decreased between the first and final erosions, and then decreased sharply until reaching a horizontal residual slope that was similar in both models. This last reduction in slope was simultaneous with the decrease of h_{up} and indicated the failure of the models as they could not maintain the water level in the upstream reservoir.

The initial behavior displayed during Phase 1 reflects the seepage across the foundation that occurs during the normal operation of a water-retaining structure, even when an exit-hole exists somewhere in the downstream zone. In this case, the flow is driven from the impoundment to a drainage area predisposed by design, and the flow is

mainly horizontal below the structure with a constant head loss across the total seepage length. The exit-hole remains flooded within this phase and there is no change in the soil structure that may indicate erosion, but a localized increase of the head loss near the exit-hole may occur after increasing the head of the impoundment. A certain increase in the head of the impoundment must be met to change the seepage direction and to trigger a critical condition for backward erosion piping by redirecting the drainage to the exit-hole and by reducing the seepage length, as observed in Phase 2. This condition occurred for a lower water head as the exit-hole is closer to the impoundment. The seepage stress induced on the soil appears to be lower for lower seepage lengths as more increments of impoundment head were allowed before erosion in the model with a shorter seepage length. In addition, the failure occurred for a head in the impoundment that increased as the location of the exit-hole from the impoundment increased.

6.4.2 Effect of seepage length in the behavior of backward erosion piping

The typical behavior observed in all models started with the ambient condition, in which the seepage occurred across the foundation and to the downstream reservoir. Horizontal flow is observed below the clay layer with a constant pressure and head losses across the total seepage length. The exit-hole remained flooded during this condition, but there was no change in the porosity of the soil. Eventually, the deviation from the ambient condition occurred after increasing the head in the upstream reservoir to a certain level that caused a change in the seepage direction by redirecting the drainage to the exit-hole. This deviation decreased the seepage length and increased the pressure loss near the exit-hole, which triggered the condition for initiating backward erosion piping. After the

deviation, the erosion was initiated leading to the failure of the models, which was observed at a lower upstream head as the exit-hole was closer to the upstream reservoir.

The local pressure loss, ΔP, across different segments within a model was calculated from the pressure measurements and was normalized by the pressure loss under an ambient condition, ΔP_{amb}. The ambient condition is defined as a steady-state flow across the undeformed soil for which the local ΔP is linearly proportional to the global head loss imposed to the system (Fleshman and Rice 2014; Peng and Rice 2020). As proposed by Peng and Rice (2020), ΔP_{amb} was estimated from the linear regression of the initial portion of the curve of ΔP in a given segment versus the hydraulic head in the upstream reservoir, h_{up}. The normalization $\Delta P/\Delta P_{amb}$ was done for Segments 1, 2, 3 and 4, in models with L = 25 cm, and for Segments 1 and 2, in models with L = 15 cm, as shown in Figures 6. 2b and 6. 2c, respectively.

The evolution of $\Delta P/\Delta P_{amb}$ as a function of the elapsed time is presented in Figures 6. 4a and 6. 4b for the models tested at 10g, with L = 15 cm and with D = 7 mm and 49 mm, respectively. The values of h_{up} at different testing times are also displayed in these figures. For every value of D and for every segment, the values of $\Delta P/\Delta P_{amb}$ remained close to the ambient condition (i.e., $\Delta P/\Delta P_{amb}$ = 1) before emerging flow across the exit-hole was observed in the video recordings. This indicates that there was no change in the porosity of the soil. Afterwards, the value of $\Delta P/\Delta P_{amb}$ deviated from the ambient condition and two distinct behaviors were observed. The first behavior was observed in models with D = 7 mm, 18 mm and 26 mm, for which the value of $\Delta P/\Delta P_{amb}$ increased in Segments 1 and 2 as h_{up} increased, but a greater increase occurred in Segment 1, as shown in Figure 6. 4a between the minutes 24 and 52. This indicates that

ΔP increased in a greater magnitude towards the exit-hole after the emerging flow occurred. Furthermore, the increase of $\Delta P/\Delta P_{amb}$ in Segment 1 was greater as D increased, which indicates that ΔP near the exit-hole was greater as D increased. The value of $\Delta P/\Delta P_{amb}$ in both segments decreased after reaching a peak, regardless of the value of D, with a first peak in Segment 1 at the minute 52, and then in Segment 2 at the minute 55.4. This behavior indicates the initiation of erosion and progression of the piping path. The first decrease was through Segment 1 where ΔP decreased due to a localized reduction in flow resistance. The second decrease was through Segment 2 as the piping progressed. It is noted that small traces of sand were visually observed near the exit-hole at the peak in Segment 1. The decreasing in $\Delta P/\Delta P_{amb}$ observed for both segments continued until the failure occurred at the minute 61.8 in the model with D = 7 mm, as shown in Figure 6. 4a.

The second behavior was only observed in the model with D = 49 mm and is shown in Figure 6. 4b. As seen in previous models, the value of $\Delta P/\Delta P_{amb}$ increased and deviated from the ambient condition after the emerging flow was observed, at nearly 24 minutes of test. However, the value of $\Delta P/\Delta P_{amb}$ remained similar in both segments for the next three increments of h_{up}, between the minutes 24 and 27. Then, a greater increase of $\Delta P/\Delta P_{amb}$ was observed in Segment 2, between the minutes 27 and 62, while a decrease of $\Delta P/\Delta P_{amb}$ in Segment 1 was observed. This may be due to a partial reduction in the flow resistance due to soil loosening near the exit-hole, but not necessarily to piping as there was no sign of erosion from video recordings until the minute 62. The initiation and progression occurred as described in the previous models with an initial

peak in the value of $\Delta P/\Delta P_{amb}$ in Segment 1, towards the minute 62, and followed by a peak in Segment 2, towards the minute 63.2.

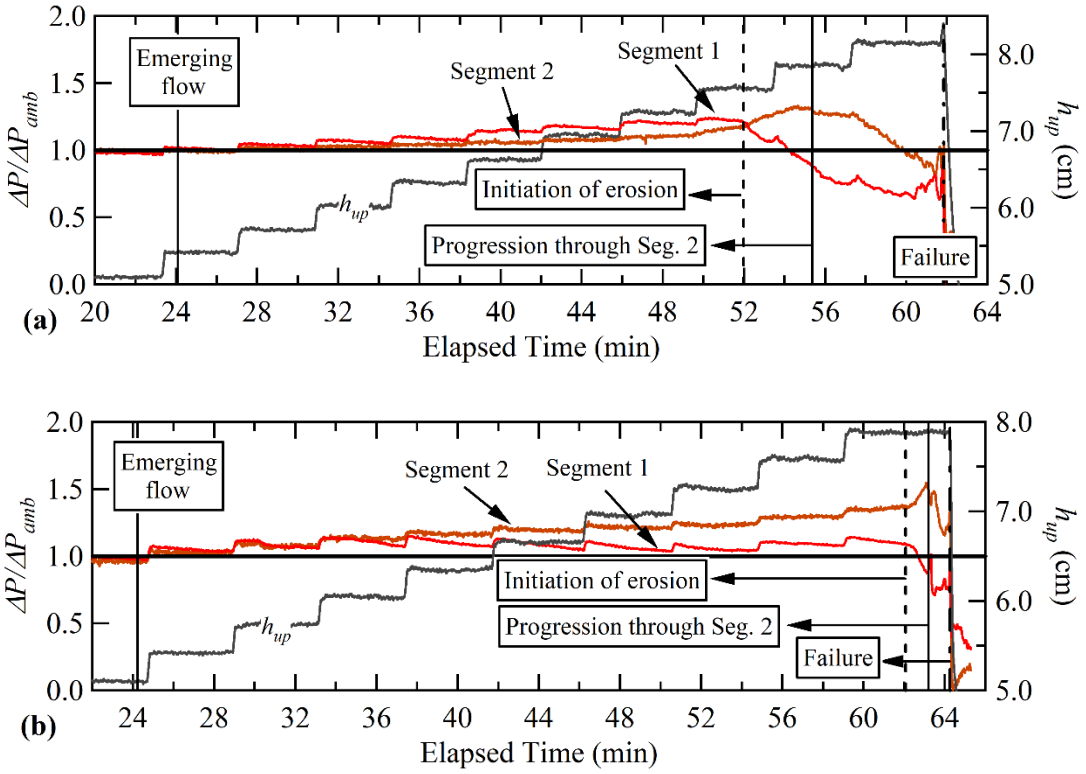

Figure 6. 4 Normalized pressure loss in models with L = 15 cm tested at 10g: (a) D = 7 mm and (b) D = 49 mm.

The results from models with L = 25 cm are shown in Figures 6. 5a and 6. 5b, for the model with D = 7 and 49 mm, respectively. Different from models with L = 15 cm, the deviation from the ambient condition in models with L = 25 cm occurred before the emerging flow across the exit-hole. Figures 6. 5a shows that although the values of $\Delta P/\Delta P_{amb}$ in Segments 1 and 2 increased after the deviation at the minute 47.5, Segments 3 and 4 showed a decrease in $\Delta P/\Delta P_{amb}$ within the same duration. This behavior shows that a decrease in ΔP occurred near the upstream reservoir likely due to the concentration of flow at the exit-hole, which changed the global seepage distribution (i.e. flow net).

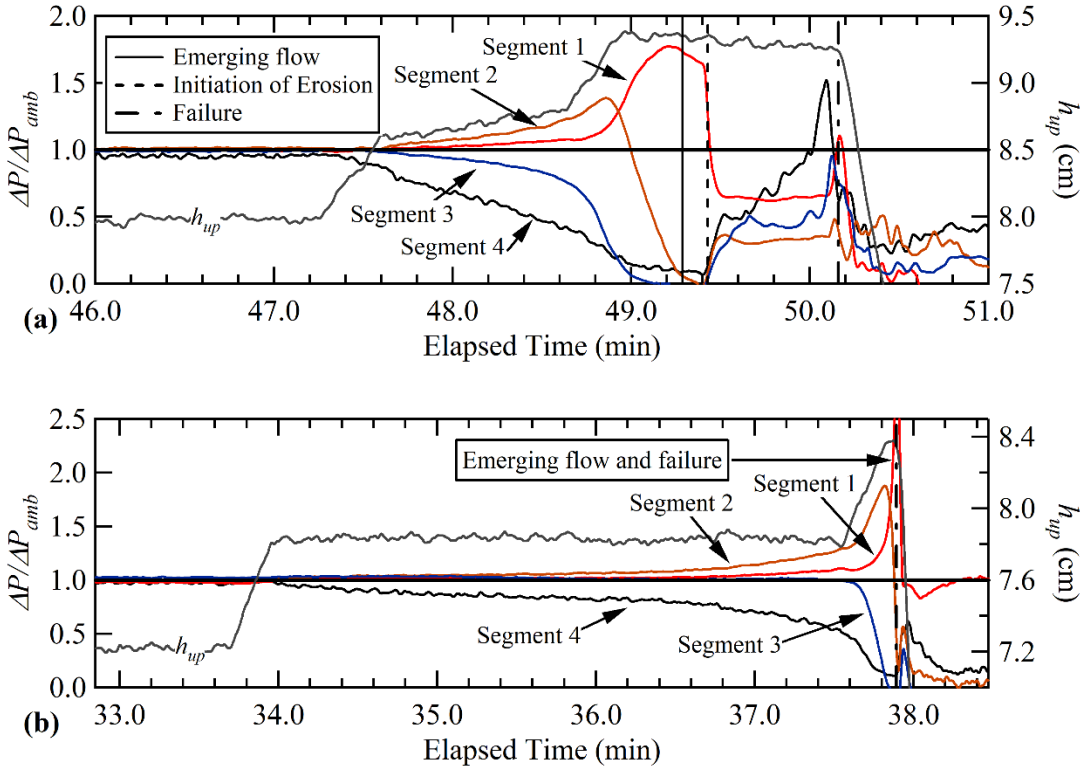

Figure 6. 5 Normalized pressure loss in models with L = 25 cm tested at 10g: (a) D = 7 mm and (b) D = 49 mm.

It is noted that the decrease in $\Delta P/\Delta P_{amb}$ observed near the upstream reservoir in the models could be interpreted as a local loosening in the soil due to the development of forward erosion typical of experiments with loose sands or models with gaps between the sand and cover layers (Van Beek 2015). However, an adequate bonding between the sand and clay layers was ensured in this study by means of loading the sample prior testing and increasing the gravitational acceleration field during test. Hence, as mentioned, the decrease in ΔP near the upstream reservoir was rather due to changes in the shape of flow lines as the flow concentrated at the exit-hole. It is noted that although the decrease of $\Delta P/\Delta P_{amb}$ was only observed in models with L = 25 cm, the results presented in Figure 6. 3 show that this also occurred in models with lower L = 15 cm.

Figure 6.5a also shows that there was no identifiable progression of piping in these models with L = 25 cm, but an initial massive erosion that coincided with the peak in Segment 1 (towards the minute 49.4 in Figures 6. 5a) was observed in the models with D = 7 mm, 18 mm and 26 mm. Afterwards, the value of $\Delta P/\Delta P_{amb}$ in all segments decreased to a similar value below the ambient condition and remained constant until a second and final massive erosion occurred (towards the minute 50.2 in Figures 6. 5a), indicating the failure of the model. The model with D = 49 mm showed a similar behavior than the remaining models with L = 25 cm, as shown in Figures 6. 5b, but the deviation from the ambient condition and the failure occurred shortly after the application of the last increment of h_{up}.

The main difference in the behavior of $\Delta P/\Delta P_{amb}$ between the models with different L is observed at each segment after the deviation from the ambient condition. A relatively slow and steady change in $\Delta P/\Delta P_{amb}$ occurred in the models with L = 15 cm, providing a clear observation of the initiation and progression of piping. In contrast, a rapid change in $\Delta P/\Delta P_{amb}$ was observed in the models with L = 25 cm. The deviation from the ambient condition presented in Figures 6. 4 and 6. 5 was caused by the change in flow direction towards the exit-hole, and the influence of L on the emerging flow conditions prior to the change in flow direction was clearly observed. For instance, the emerging flow occurred at a lower value of h_{up} in the models with L = 15 cm, indicating a lower exit velocity of flow at the exit-hole than in the models with L = 25 cm. Therefore, the greater values of h_{up} reached during emerging flow and the greater exit velocity of flow induced the critical conditions required to fail the models with L = 25

cm, which led to a first visible erosion involving a much larger amount of soil than in models with L = 15 cm.

6.4.3 Pressure loss across the exit-hole

The local hydraulic conditions in the exit-hole influence the hydraulic gradient across the foundation and consequently the development of backward erosion piping (Robbins et al. 2020). Since the flow across the exit-hole is mainly vertical and upward (Schmertmann 2020), and it is likely affected by its dimensions (Ovalle-Villamil and Sasanakul 2020), analyzing the effects derived from the value of D under this flow condition is of importance for this study. To address this, the local pressure loss in the exit-hole was analyzed using the ideal conditions shown in Figure 6. 6, as suggested by Robbins et al. (2020).

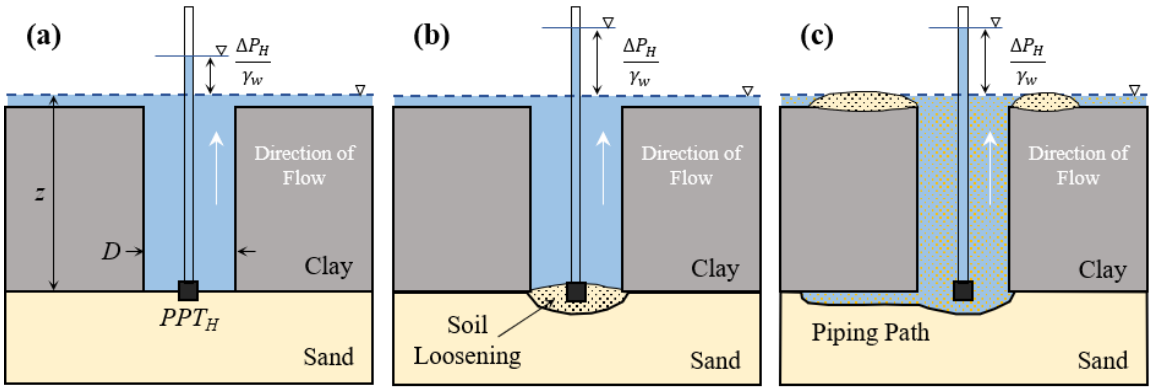

Figure 6. 6 Ideal head loss across an exit-hole during the initiation and progression of backward erosion piping: (a) emerging flow, (b) localized loosening of the soil, and (c) initiation and progression of piping.

In Figure 6. 6, the pressure loss between the bottom and surface of the exit-hole is estimated as $\Delta P_H = P_H - P_z$, where P_H is the pressure reading at the bottom of the exit-hole (i.e., at PPT_H in this study), and P_z is the hydrostatic pressure at the surface of the

sand layer. If there is no flow in the exit-hole, $\Delta P_H = 0$. When h_{up} increases to a certain level, ΔP_H also increases, resulting in flow across the exit-hole, and reaches a constant value until h_{up} increases again (Figure 6. 6a). If a local loosening occurs, the pressure loss in horizontal direction between the impoundment and the location of PPT_H decreases, resulting in an increase in ΔP_H across the exit-hole (Figure 6. 6b). A greater increase in ΔP_H is expected after the migration of grains begins due to piping as the flow concentrates towards the piping path and PPT_H increases significantly (Figure 6. 6c). The evolution of ΔP_H as a function of h_{up} obtained in the models tested at 10g is presented in Figure 6. 7. The value of P_z was estimated to be at the surface of the clay layer to resemble the moment of emerging flow.

Several behaviors were observed from the video recordings of the exit-hole, but three main stages are noteworthy: the emerging flow, the initiation of erosion and the failure, as shown in Figure 6. 8. The emerging flow was observed when the water visually raised above the surface of the clay layer. The initiation of erosion was observed when the first grains were visible above the exit-hole indicating the beginning of sand migration due to piping. The amount is vastly less in models with L = 15 cm than in models with L = 25 cm. The final erosion was observed when a massive amount of sand was visible at the exit-hole and this moment is considered the onset of failure. These stages were identified in correspondence to the evolution of ΔP_H as shown in Figure 6. 7.

In all models with L = 25 cm, the values of ΔP_H increased rapidly after the emerging flow was visible. The initiation of erosion at the exit-hole was observed almost simultaneously during the last increment of h_{up} and was followed by the final erosion. In both stages, a large amount of sand was observed. Because the phenomenon developed

rapidly, it was difficult to clearly evaluate a relationship between the values of ΔP_H and h_{up} during these stages. However, it is possible that when the value ΔP_H increased, soil loosening occurred prior to the initiation of erosion.

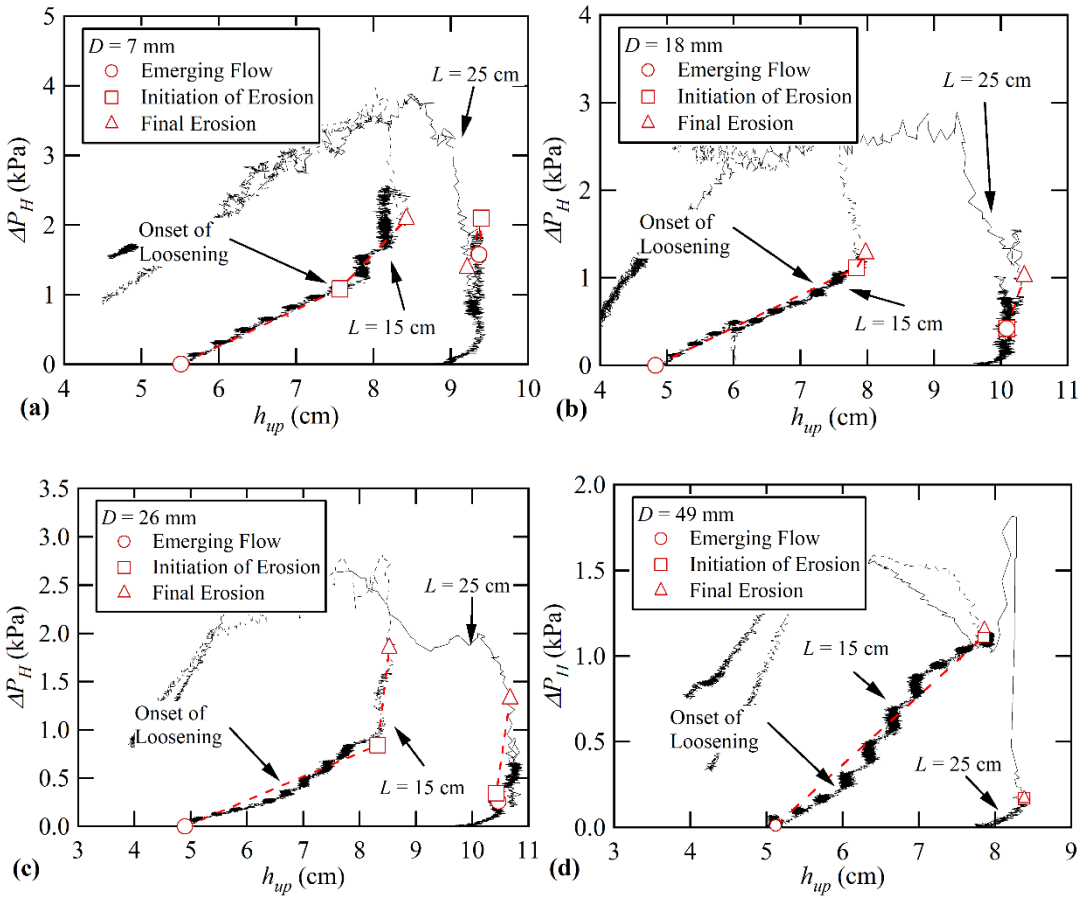

Figure 6. 7 Evolution of pressure loss across the exit-hole for models tested at 10g: (a) D = 7 mm, (b) D = 18 mm, (c) D = 26 mm, and (d) D = 49 mm.

For the models with L = 15 cm, several increments of h_{up} were induced after the emerging flow was observed and before the initiation of erosion was visible. The values of ΔP_H increased as h_{up} increased. During each increment of h_{up} up to values between 6 cm and 8 cm, the value of ΔP_H reached equilibrium at a constant value. Afterwards, and before the initiation of erosion was observed, the value of ΔP_H also increased as h_{up}

increased, but it did not reach equilibrium and continued to increase while h_{up} remained constant. This observation implies that soil loosening occurred at the bottom of the exit.

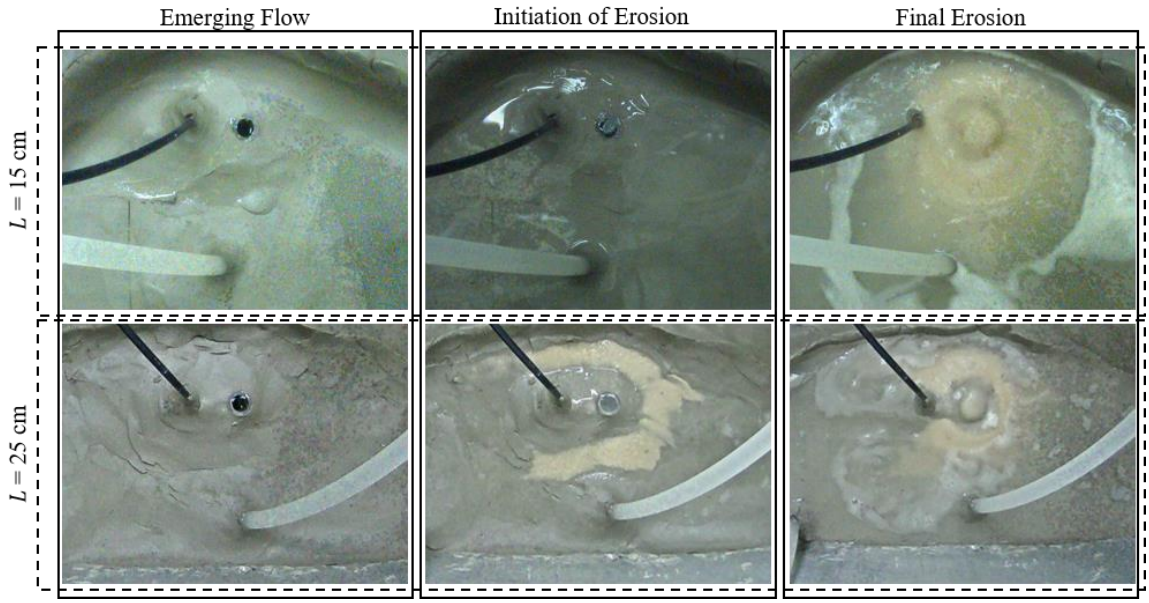

Figure 6. 8 Snapshots of the conditions of emerging flow, initiation of erosion and final erosion in models with D = 7 mm tested at 10g.

Comparing the range in values of h_{up} among models with different D, it was observed that more soil loosening occurred as D increased. Van Beek et al. (2014) and Van Beek (2015) discussed a possible explanation of this behavior using the bridging effect. Higher flow concentration is anticipated in a smaller exit-hole size because the grains are locked more tightly. As a result, a relatively high local pressure loss is required to loosen the soil in comparison with a large hole. In contrast, as D increases, the soil is more susceptible to expand. This effect is supported by the values of ΔP_H obtained in this study to represent the beginning of soil loosening taken from the point when the values of ΔP_H kept increasing while h_{up} remained constant. The values of ΔP_H of 1.08 kPa, 0.95

kPa, 0.42 kPa and 0.25 kPa for D = 7 mm, 18 mm, 26 mm and 49 mm, respectively, were obtained and verified that a lower vertical gradient caused the loosening as D increased.

Between the time the soil started to loosen and the final erosion, the values of ΔP_H were likely affected by the grains dragged outside the exit-hole as well as the grains suspended inside (Robbins et al. 2020). The values of ΔP_H observed for the initiation of erosion were about 1.08 kPa, 1.11 kPa, 0.84 kPa and 1.11 kPa for D = 7 mm, 18 mm, 26 mm and 49 mm, respectively. After the final erosion was visible and before the failure, a sudden increase in the values of ΔP_H occurred in all models, regardless of L. This increase occurred within a short period of time and may be a consequence of the flow concentrating on the piping path that resulted in the widening process. The values of ΔP_H representing the onset of final erosion were nearly 2.50 kPa, 1.26 kPa, 1.60 kPa and 1.14 kPa, for D = 7 mm, 18 mm, 26 mm and 49 mm, respectively. Similar trend is observed with D and is consistent with the behavior observed during the soil loosening. A summary of the ranges of values of h_{up} and ΔP_H for the different stages is presented in Tables 6. 2 and 6. 3.

6.4.4 Evolution of Hydraulic Gradient and Critical Condition

The critical hydraulic gradient, i_{cr}, was determined by analyzing the evolution of the hydraulic gradient, which was determined as $i = \Delta P_i / L_i / \gamma_w$, where ΔP_i and L_i are the pressure loss and the length of a given segment within a model, respectively. The gradients studied include: i_{Global}, which is a global hydraulic gradient calculated for the entire length of the model; i_L, which is a local hydraulic gradient calculated for the length between the upstream reservoir and the exit-hole; and $i_{5\ cm}$, which is local hydraulic gradient calculated for the Segment 1, as described in Figure 6. 2.

Table 6. 2 Summary of values of h_{up} and ΔP_H in models with L = 15 cm.

D (mm)	No emerging flow[b]		Emerging flow to onset of loosening			Loosening to final erosion		
	h_{up} (cm)	No. of Increments	h_{up} (cm)	ΔP_H (kPa)	No. of Increments	h_{up} (cm)	ΔP_H (kPa)	No. of Increments
7	0 - 5.5	6	5.5 - 7.6	0 - 1.08	7	7.6 - 8.2	1.08 - 2.50	3[a]
18	0 - 4.8	4	4.8 - 7.5	0 - 0.95	9	7.5 - 7.9	0.95 - 1.26	1
26	0 - 4.9	7	4.9 - 7.0	0 - 0.42	6	7.0 - 8.5	0.42 - 1.60	4 [a]
49	0 - 5.1	5	5.1 - 6.0	0 - 0.24	3	6.0 - 7.9	0.24 - 1.14	6

[a] Failure occurred during the application of last increment of h_{up}

[b] ΔP_H assumed to be zero

Table 6. 3 Summary of values of h_{up} and ΔP_H in models with L = 25 cm.

D (mm)	No emerging flow[b]		Emerging flow to final erosion		
	h_{up} (cm)	No. of Increments	h_{up} (cm)	ΔP_H (kPa)	No. of Increments
7	0 - 8.9	7	8.9 - 9.3	0 - 2.10	1
18	0 - 9.8	16	9.8 - 10.3	0 - 1.53	2 [a]
26	0 - 9.8	15	9.8 - 10.7	0 - 1.39	2
49	0 - 7.8	9	7.8 - 8.4	0 - 0.17	1

[a] Failure occurred during the application of last increment of h_{up}

[b] ΔP_H assumed to be zero

Variation of the hydraulic gradients with the normalized elapsed time are presented in Figures 6. 9 and 6. 10 for models tested at 10g with L = 15 cm and 25 cm, respectively. These figures show the variations experienced after soil loosening inside the exit-hole was identified. The elapsed time was normalized by the total testing duration after loosening to allow comparison of all models in the same figure. In addition, the values of i were scaled by N to present the results in a prototype condition.

Figures 6. 9 and 6. 10 also identify three critical conditions of erosion: soil loosening, initiation of erosion and failure. As shown previously, soil loosening was defined as when ΔP_H increased while i_{Global} (or h_{up}) remained constant. The initiation of erosion was defined as when the sand grains were visible at the exit-hole, also indicating the piping initiation. Failure was defined as when the failure is visually observed, and it corresponded to the significant reduction of i_{Global}. Table 6. 4 shows the critical values obtained in each condition.

For the models with L = 15 cm, the values of i_{Global} only increased slightly when the critical conditions changed from loosening to initiation of erosion and then to failure. The highest change was observed in the model with D = 49 mm in which the i_{Global} changed from nearly 0.15 to 0.21 from loosening to failure. The values of i_L and $i_{5\,cm}$ were mostly higher than the values of $_{Global}$ for all models, particularly for the conditions of loosening and initiation of erosion. At the failure condition, there was no clear trend as nearly half of the models showed lower values of i_L and $i_{5\,cm}$ compared to the values of i_{Global}. It is noted that in most of the models tested, the value of i_{Global} at failure did not always correspond to the last constant value of h_{up}. Therefore, the accuracy of i_{Global} at failure is relatively lower than that at the loosening and initiation conditions. The value of i_L increased from

the loosening to the initiation of erosion and decreased at failure. It is interesting to note that the rate of increase of i_L was influenced by the size of the exit-hole. For instance, in the models with D = 26 mm and 49 mm, the value of i_L increased 20 to 30% from loosening to initiation of erosion, while the model with D = 18 mm only increased 10% and there was a negligible change in the model with D = 7 mm.

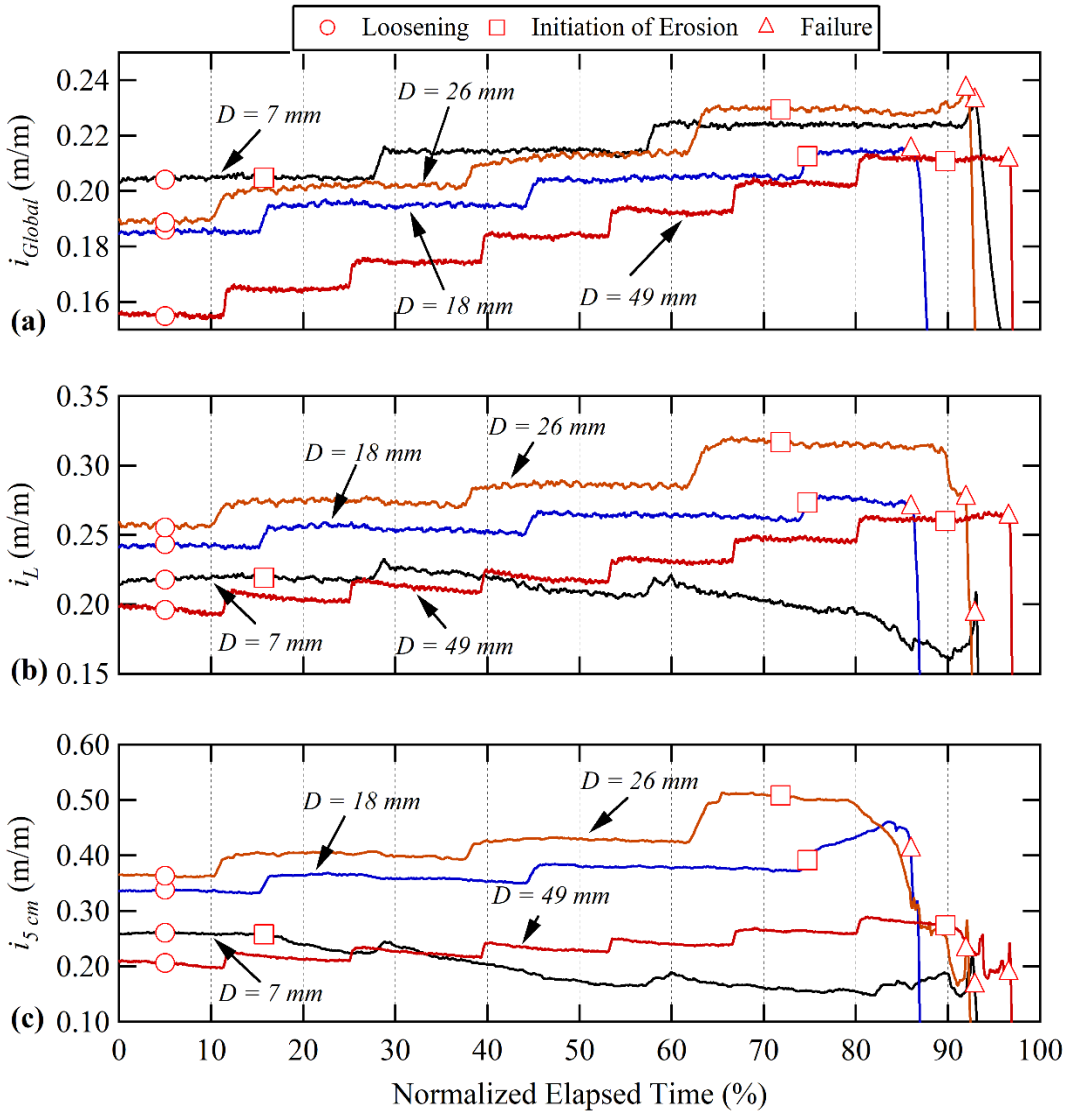

Figure 6. 9 Evolution of hydraulic gradients across different segments in models with L = 15 cm: (a) i_{Global}, (b) i_L and (c) $i_{5\,cm}$.

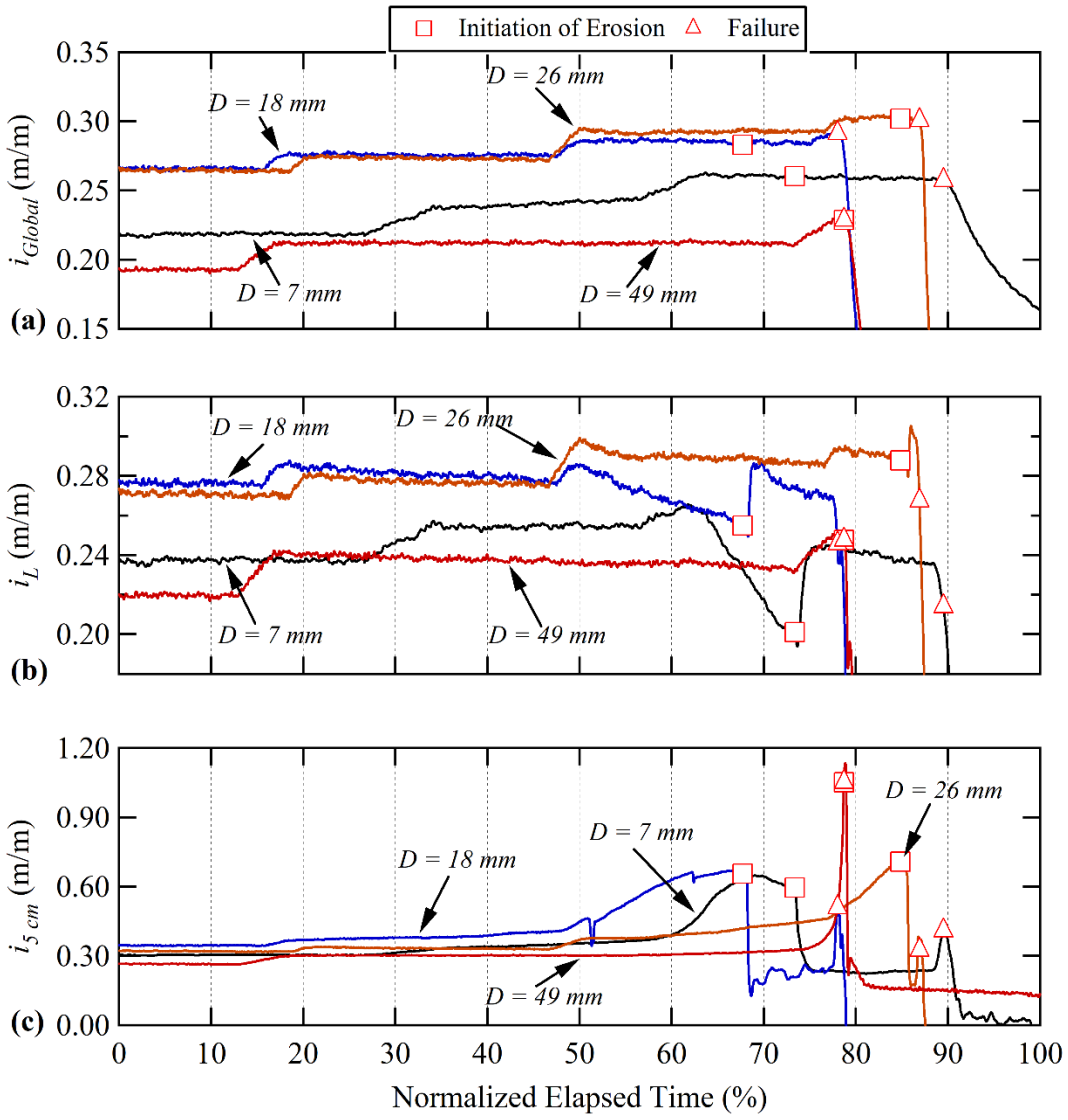

Figure 6. 10 Evolution of hydraulic gradients across different segments in models with L= 25 cm: (a) i_{Global}, (b) i_L and (c) $i_{5\,cm}$.

The values of $i_{5\,cm}$ were 20 to 60% higher than the values of i_L at the initiation of erosion. This observation is in exception to the model with D = 49 mm in which the difference between $i_{5\,cm}$ and i_L was negligible. By comparing the values of i_L and $i_{5\,cm}$ relative to the diameter of the exit-hole, it was found that both local gradients increased as D increased, once again in exception to the model with D = 49 mm. There is no clear

explanation for the outliner behavior of the model with D = 49 mm, but since this model had a relatively larger diameter than other models, it is possible that other unknown factors, such as the flow pattern at the exit-hole, could governed the behavior. More data is needed to assess possible factors affecting the behavior of relatively large exit-hole sizes in centrifuge models. Overall, two important aspects are derived from the centrifuge models. First, a noticeably greater value of local gradient occurred in comparison to the i_{Global}. And second, the exit-hole size influenced the change of local gradients during the transition from loosening to initiation of erosion.

Table 6. 4 Hydraulic gradients for the critical conditions of loosening, initiation of erosion and failure.

Model		Loosening			Initiation of Erosion			Failure		
L (cm)	D (mm)	i_{Global}	i_L	$i_{5\ cm}$	i_{Global}	i_L	$i_{5\ cm}$	i_{Global}	i_L	$i_{5\ cm}$
15	7	0.20	0.22	0.26	0.20	0.22	0.26	0.23	0.19	0.16
	18	0.19	0.24	0.34	0.21	0.27	0.39	0.21	0.27	0.41
	26	0.19	0.26	0.36	0.23	0.32	0.51	0.24	0.28	0.23
	49	0.15	0.20	0.21	0.21	0.26	0.27	0.21	0.26	0.19
25	7				0.26	0.20	0.60	0.26	0.21	0.41
	18				0.28	0.26	0.66	0.29	0.25	0.51
	26				0.30	0.29	0.71	0.30	0.27	0.33
	49				0.23	0.25	1.05	0.23	0.25	1.05

As described previously, the phenomenon developed rapidly in models with L = 25 cm. Therefore, the loosening was not clearly identified and only the values for the initiation of erosion and failure are presented in Figure 6.10 and Table 6. 4. Overall, the values of i_{Global}, i_L and $i_{5\ cm}$ in models with L = 25 cm were higher than the values observed in the models with L = 15 cm. Importantly, the values of $i_{5\ cm}$ were noticeably greater than the values of i_{Global} and i_L. For the initiation of erosion, the values of $i_{5\ cm}$ increased from 0.6 to 1.1 as D increased from 7 mm to 49 mm, and then decreased at

failure, in exception to the model with D = 49 mm. Overall, the values of $i_{5\ cm}$ at the initiation of erosion in the models with L = 25 cm were found to be 28 to 74% greater than the values observed in the models with L = 15 cm.

The critical gradients reported in Table 6. 4 and the evolution of gradients observed in Figures 6. 9 and 6. 10 highlighted the influence of the model geometry (i.e., seepage length and exit-hole size) on the flow conditions along the seepage length, which in turn impacted the critical local gradients. The pressure loss across a system represented by i_{Global} is generally used to evaluate the critical conditions. However, when a defect exists in the cover layer and provides an exit for water drainage, the values of i_L may be used to assess the critical conditions as it represents the average hydraulic gradient across the seepage length (i.e., between the upstream reservoir and the exit-hole). In this study, the initiation of erosion is considered as the most critical condition and can be observed with relatively higher accuracy than the failure itself. At the initiation of erosion, the critical global gradient, $i_{cr-Global}$, and the critical local gradient, i_{cr-L}, were found to be similar for all models regardless of the seepage length, as show in Table 6. 4. However, it is noticeable that i_{cr-L} was slightly higher than $i_{cr-Global}$ for the models with L = 15 cm. The impact of the seepage length is more pronounced for $i_{cr-5\ cm}$ at the initiation of erosion. The values of $i_{cr-5\ cm}$ were much higher in the models with longer seepage length. In this study, the values of $i_{cr-5\ cm}$ in the models with L = 25 cm were between 40 to 280% higher than the values observed in the models with L = 15.

6.4.5 Effect of Gravitational Acceleration Field

The pressure loss, ΔP, was considered initially for the assessment of the effect of centrifuge gravity in the centrifuge models prepared using the same soil and model

dimensions, and tested at 10g, 20g and 30g. For this assessment, the value of ΔP across Segment 1 was normalized by the value of N (i.e., $N = g_{model}/g_{Earth}$), and the results are presented as a function of h_{up} in Figure 6. 11. The first linear portion of $\Delta P/N$ observed was consistent for every value of N indicating that ΔP increased proportionally to N. Consequently, a linear scaling factor was applicable (i.e., $\boldsymbol{\Delta P} \approx N$). However, this condition was valid only until the initiation of erosion occurred. After that, a linear scaling factor was not applicable to ΔP as both increasing and decreasing behaviors in $\Delta P/N$ were observed for different tests.

Post-test observations also showed the effect of N on the amount of eroded soil after failure, as shown in Figure 6. 12. For the models with L = 25 cm, as shown in Figure 6. 12a, a lower amount of eroded soil was observed as N increased. At higher values of N, the amount of eroded soil was only visible and concentrated near the exit-hole and the piping path did not extend to the upstream reservoir. This behavior was not observed in the models with L = 15 cm, as shown in Figure 6. 12b. There is no clear explanation to the decrease in eroded soil as N increased, but it is a possible consequence of testing under a different stress level as N increased (i.e. different overburden and surcharge stress). It is noted that the scaling of soil erosion along the piping path is unknown and it is very difficult to assess. In addition, there are also differences in the flow condition and behavior during loosening, initiation of erosion and failure for the models with different seepage length, and the effect of seepage length may also contribute to the different erosion behavior.

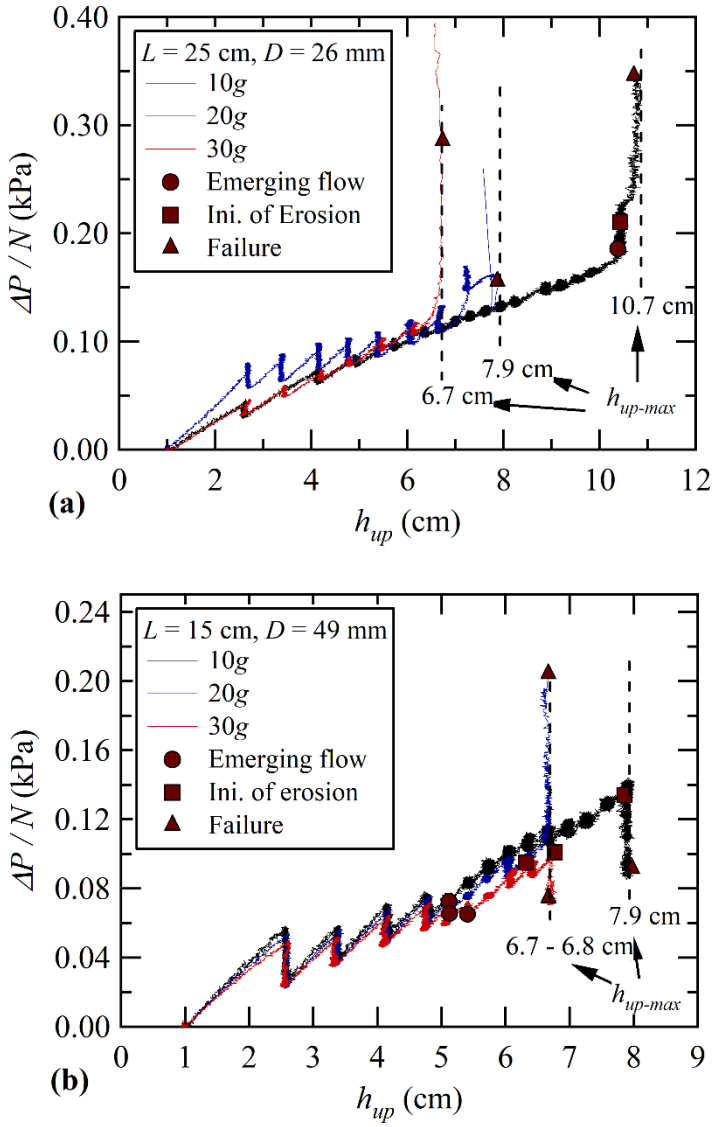

Figure 6. 11 Pressure loss normalized by N in Segment 1:
(a) D = 26 mm, L = 25 cm and (b) D = 49 mm, L = 15 cm.

Assessing the effect of N on the critical conditions leading to backward erosion piping is also challenging because the overall measurements of pressure loss may be in a range of a few kPa. The pressure loss is related to the amount of soil loosening and piping path. Therefore, it is expected to be dependent on the value of N. In this study, the values of $i_{cr-global}$ and i_{cr-L} were reported for the model with L = 15 cm and D = 49 mm and

for the model with L = 25 cm and D = 26 mm, as shown in Figure 6. 13. Variation of the critical gradients with N is observed. As the value of N increased, the critical gradient decreased, and it appears that the rate of change was slightly higher for the models with L = 25 cm. It is noted that although the dimensionless value of hydraulic gradient implies a scaling factor of $\boldsymbol{i}$ = 1, the values were not necessary expected to be constant with N. This is because the same soil, same overall dimensions and same diameter of exit-hole were used for all tests with different N, which indicates that the prototype dimensions were not the same. This observation implies that the scaling factor of 1 does not necessarily apply to these results. Nevertheless, the average difference in values between 10g and 30g is nearly 0.1 and such difference may be negligible considering the complexity of the phenomenon.

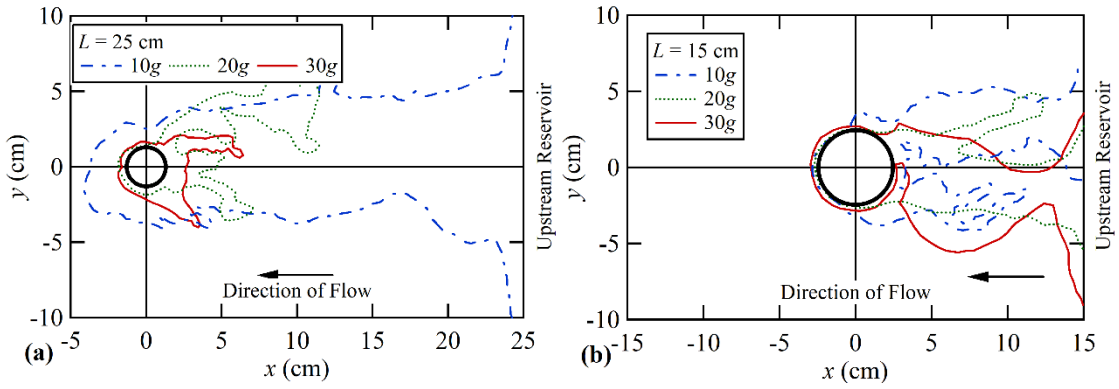

Figure 6. 12 Sketch of erosion patterns at different levels of gravitational acceleration: (a) D = 26 mm and (b) D = 49 mm.

The overall results obtained in this study were compared with the literature considering the effects of L and D. The critical hydraulic gradients in terms of i_{cr-L} during the initiation of erosion were compared with the values of i_{cr} from three-dimensional experiments reported in the literature and the results are presented in Figures 6. 14 and 6. 15. It is noted that the ratio between the cross-sectional area of the exit-hole,

A_{Exit}, and that of the soil grains, A_{Grains}, shown in Figure 6. 14, was reported to account for both exit-hole and grain sizes. In addition, the seepage lengths from the centrifuge models were presented in prototype dimensions (i.e., $\boldsymbol{L} = N^{-1}$) in Figure 6. 15 to allow direct comparison with experiments under Earth's gravity.

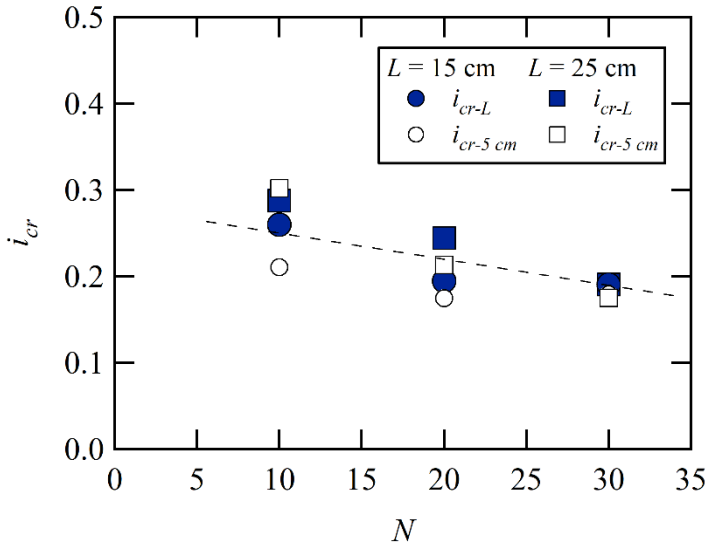

Figure 6. 13 Critical hydraulic gradients as functions of N.

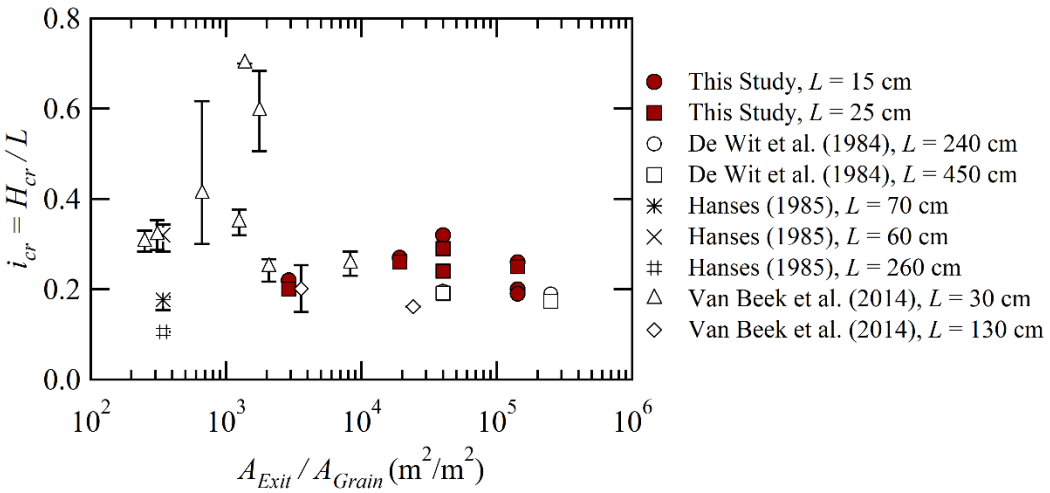

Figure 6. 14 Critical hydraulic gradients from physical models of backward erosion piping as a function of the ratio of cross-sectional areas of exit-hole and grain.

The results from this study were within an acceptable range comparing with results from other experiments. It is highlighted that results from full-scale experiments by Van Beek et al. (2011) showed values of i_{cr} between 0.12 and 0.15 for a seepage length of 15 m (Van Beek et al. 2011). The critical values from this study were closer to the full-scale results, compared to results from small- and medium-scale models available in the literature. This indicates that centrifuge modeling decreased the uncertainty in the estimation of i_{cr} from other models and facilitated observations and measurements at relatively small segments that are otherwise challenging.

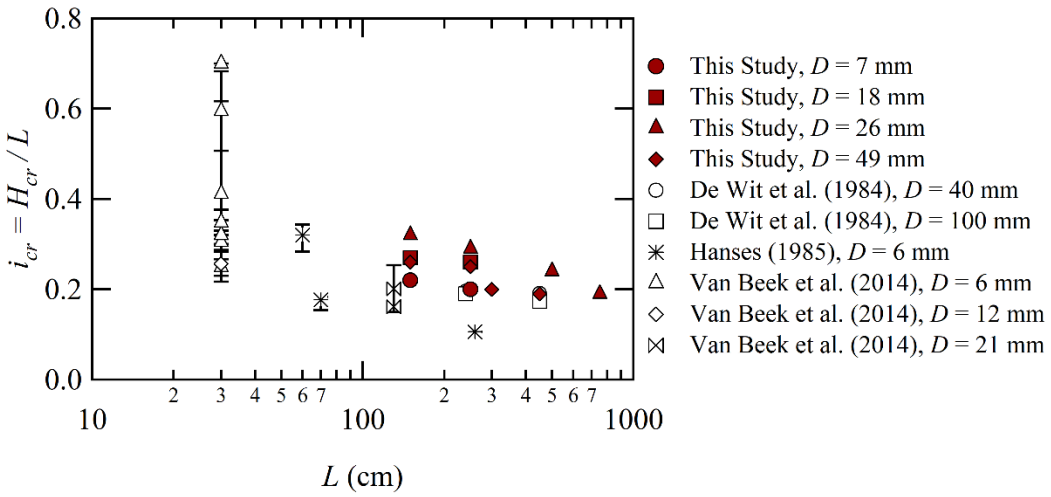

Figure 6. 15 Critical hydraulic gradients from physical models of backward erosion piping as a function of the seepage length in prototype condition.

One last aspect noted from the centrifuge models was the typical short duration observed between the initiation of erosion and the failure of the model. Some models with L = 15 cm showed times over 9 minutes, while times as low as 16 seconds were seen in models with L = 25 cm. There was no trend between the elapsed times and L or D, but the time decreased as N increased, as shown in Figure 6.16. Since the likely time for the

development in the field, within its initiation and the final failure, is three to 12 hours based on the method of Fell et al. (2003), and assuming a prototype condition of a sandy foundation with no filter protection and concentration of flow at an exit-hole, these theoretical times extrapolated to modeling conditions of 10g, 20g and 30g, using an appropriate scaling law of $\boldsymbol{t} = N^2$ (Goodings 1982, 1984; Taylor 2018), shows a rather good agreement with the experimental values in this study. Nonetheless, most of the times from experiments tested at 10g ranged from prototype times between one and three hours.

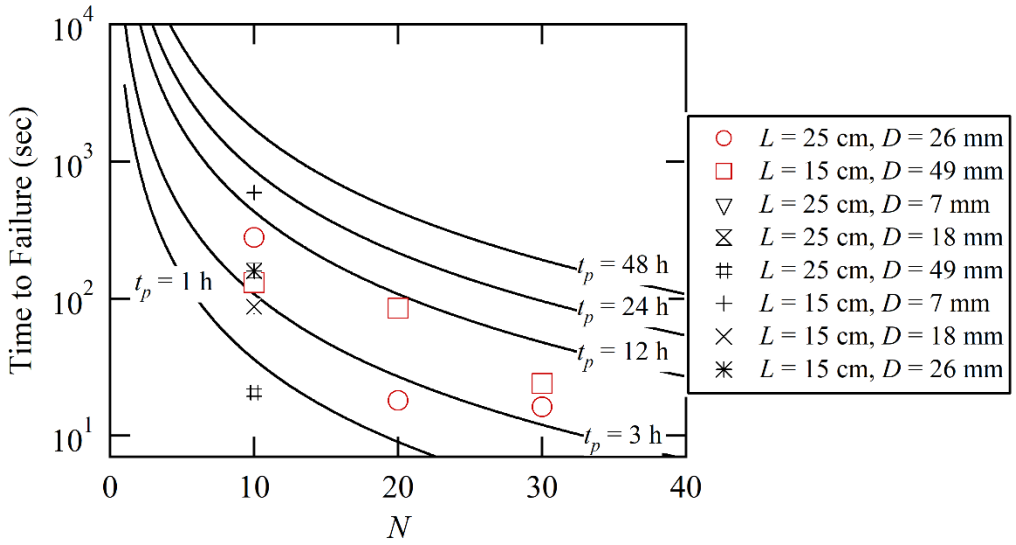

Figure 6. 16 Time elapsed during the development of backward erosion piping in centrifuge models.

6.5 CONCLUSIONS

The development of backward erosion piping in centrifuge models at 10g, 20g and 30g was analyzed using small-scaled models of a sandy foundation underlain by a clay cover with a local defect representing an exit for drainage causing the initiation of

erosion. The mechanism was observed similar to the literature, which included an initial ambient seepage across the model and towards the downstream side, and without changes in the porosity of the soil. Afterwards, the emerging flow occurred, which was described by the flow across the exit-hole and to the surface of the model. The emerging flow changed the flow direction leading to a localized increase in pressure loss near the exit-hole, and eventually to soil loosening. After that, the erosion was initiated as sand grains migrated through the exit-hole. At this time the piping erosion progressed backward until the failure occurred.

Observations of local pressure loss across different locations within the models indicated that a steady progression of backward erosion piping occurred in the models with lower seepage length, for which the soil loosening, initiation of erosion, and failure could be clearly identified. A much more rapid progression of erosion occurred in the models with longer seepage length, for which only initiation of erosion and failure were observed with no clear evidence of soil loosening. The difference between both seepage lengths was caused by the local hydraulic gradients developed near the exit-hole. It was found that the local hydraulic gradient was 30 to 260% higher in the models with longer seepage length at the imitation of erosion. Nonetheless, the critical global hydraulic gradients were very similar regardless of the seepage length. The critical hydraulic gradient between the upstream reservoir and the exit-hole was observed to increase as the diameter of the exit-hole increased between 7 mm and 26 mm, regardless of the seepage length. However, the trend was not extended to the models with a diameter of exit-hole 49 mm, for which the critical gradients were relatively lower. In addition, the exit-hole

size had an impact on the change of local gradients during the advancement of soil loosening to the initiation of erosion.

It was observed that for the centrifuge models with same soil and same model dimension, the pressure loss increased proportional to the centrifuge gravitational acceleration. The effect of centrifuge gravity on the amount of eroded soil and piping path were observed qualitatively and appeared to be contributing factors affecting the critical hydraulic gradients. The critical hydraulic gradient decreased slightly as the centrifuge gravity increased. Despite this, the values of critical hydraulic gradients observed from the centrifuge model tests were comparable to results available in the literature, especially the values obtained from full-scale models, which highlighted the potential of the centrifuge modeling technique to model backward erosion piping.

CHAPTER 7

SUMMARY, CONCLUSIONS AND FUTURE WORK

7.1 SUMMARY

The mechanism of internal erosion known as backward erosion piping is a potential hazard for dams, dikes and levees underlain by a sandy foundation. This mechanism has been extensively studied through physical and analytical modeling techniques, but a challenge still exists to replicate the behavior observed on the field. This challenge is due to, among others, the complexity of the mechanism and the difficulty to obtain reliable information from field studies. Scale effects derived from the use of reduced-scale models also make it difficult to study backward erosion piping under controlled laboratory conditions. There is a need to develop new and innovative modeling techniques as an alternative to the full-scale experiments to allow linking experimental results to field behavior more accurately.

The main goal of this investigation was to evaluate the use of the geotechnical centrifuge modeling technique as an innovative alternative to conventional methods for modeling backward erosion piping. This dissertation presented the results of an extensive series of centrifuge experiments performed to investigate the different phases comprising the phenomenon and to assess the effects of the centrifuge gravitational acceleration field. The effects of the exit size and the seepage length on the backward erosion piping mechanism modeled were also evaluated using global and local analysis of hydraulic

conditions. The results were compared and validated with relevant experimental results from the literature.

Since backward erosion piping is driven by seepage, the first part of this investigation focused on the evaluation of the seepage behavior reproduced in centrifuge models. This stage studied the effects of the gravitational acceleration on the flow behavior through fine-grained materials typically used in geotechnical centrifuge modeling. The experiments were performed using a customized permeability test configuration and tested granular materials with variable grain-shape and grain-size distribution under gravitational acceleration fields, relative to Earth's gravity, of 1g, 10g, 20g and 30g. The assessment covered the effect of the increase of the gravitational acceleration field on the limit of validity of Darcy's Law, which may be exceeded in centrifuge models due to the consequent increase in the velocity of flow, in addition to the effects on the permeability constants describing both laminar and nonlaminar flow conditions. Furthermore, the effects of the soil characteristics on the flow behavior were analyzed.

The second part of this investigation focused on the initiation phase of backward erosion piping that occurs at an exit point near the downstream toe of a water retaining structure. This stage studied the effects of modeling this initial phase under an increased gravitational acceleration based on observations of the hydraulic behavior reproduced across the exit-hole and the critical hydraulic conditions that trigger the mechanism. The experiments were performed using a one-dimensional configuration by inducing upward flow across columns of sands with uniform gradations and variable grain-size, and under gravitational acceleration fields of 1g, 10g, 20g and 30g. The analysis was performed

using direct measurements of pressure loss across different segments within the models and supported by real-time visual monitoring. The effect of the gravitational acceleration on the critical hydraulic gradients determined for different moments during the initiation phase were determined and validated using results from similar experiments available in the literature. In addition, the components of the seepage stress at a grain level driving the initiation mechanism were determined and analyzed using a simplified methodology derived for this purpose.

The third part of this investigation focused on the backward erosion piping that occurs across a confined foundation composed of a uniform, fine-grained sand, which is overlain by a clay cover layer with an exit-hole. This stage studied the effects of modeling the backward erosion piping mechanism under an increased gravitational acceleration, using the size of the exit-hole as the main variable. The experiments were performed following a three-dimensional configuration and under gravitational accelerations of 10g, 20g and 30g. The analysis was performed using direct measurements of pore pressure at different locations across the interface between the clay cover layer and the foundation and were supported by real-time visual monitoring. This part of the investigation used extensive visual information to describe the behavior observed before and after the failure. The assessments covered the effects of the gravitational acceleration on the behavior observed, the evolution of local and global hydraulic gradients and the critical gradients triggering the phenomenon. The results were also analyzed based on the size of the exit-hole and compared with estimations of critical hydraulic gradients from typical analytical models used in the practice of civil engineering.

The fourth and final part of this study expanded the assessments developed in the third part by including the seepage length as a main variable in the models. This part of the investigation focused on evaluating the effects of the seepage length and the exit-hole size in the behavior reproduced in centrifuge models of backward erosion piping tested at 10g, 20g and 30g. Such effects were compared with similar studies available in the literature to validate the estimations of both local and global critical hydraulic gradients from centrifuge models in addition to validate the general mechanism reproduced under and increased gravitational acceleration.

7.2 CONCLUSIONS

Overall, the backward erosion piping mechanism observed in the centrifuge models show an agreement with the sequential development of phases described in the literature for both the initiation phase occurring inside the exit-hole and the general evolution of the mechanism across the foundation soil. The piping path that characterizes this phenomenon was identified in the two-dimensional models from post-failure observations. Likewise, the backward evolution was identified based on the assessments of pore pressures within the models. The mechanism reproduced in the centrifuge models generally displayed an initiation-dominated behavior, which indicates that the mechanism initiated and progressed until failure for the same global hydraulic gradient that initiated the phenomenon. This behavior is typical of small-scale models. The estimations of critical hydraulic gradients obtained in this study showed good agreement with the values from full-scale models. It is important to understand that additional conditions such, as the geological conditions and other complexities of hydraulic conditions in the field, are typically not modeled in the laboratory.

The initial evaluation of the flow behavior in centrifuge models indicated that the effect of the gravitational acceleration was minimal on the Forchheimer coefficients describing the laminar and nonlaminar flow. This indicated that the evolution of the hydraulic gradient as a function of the velocity of flow, or vice versa, follows a unique behavior regardless of the gravitational acceleration. The main implication of this behavior is that the transition from a laminar, viscous flow condition, typical of geotechnical structures, to a nonlaminar flow, is also unaffected by the gravitational acceleration field induced on the model. Therefore, and considering that the velocity of flow in centrifuge models typically increases significantly as the gravitational acceleration field increases, the likelihood to exceed such a limit increases as the gravitational acceleration increases. Although this represents a potential challenge to use the centrifuge modeling technique, it was found that the flow likely remained laminar in the backward erosion piping experiments performed.

The initiation phase of backward erosion piping observed in one-dimensional centrifuge experiments showed two typical phases. The first phase, namely first visible movement, indicated the first visible expansion of the surface of the soil, which represented an initial localized loosening behavior of the soil located closest to the surface. The second phase, namely total heave, indicated the development of a preferential piping path across the exit-hole, which resembles the preceding moment to the progression phase in a backward erosion piping process. The hydraulic gradient observed before the loosening of the soil was constant regardless of the gravitational acceleration and followed the theoretical scaling law of $\boldsymbol{i_{cr}} = 1$. After the loosening of the soil began and progressed to the total heave, the hydraulic gradient varied as a function of

the gravitational acceleration following a different factor closer to $\boldsymbol{i_{cr}}$ = 0.8. The flow conditions experienced during the initiation of backward erosion piping were laminar based on a Moody Diagram evaluation, regardless of the gravitational acceleration. Nonetheless, the Reynolds Numbers estimated for the centrifuge models with coarser grains indicated that nonlaminar flow may have occurred.

Observations from one-dimensional centrifuge models also highlighted a major effect derived solely from the increased gravitational acceleration field. In these models, the expansion experienced while the loosening progressed was noticeably lower than in one-dimensional models tested under Earth's gravity. The deformation observed in centrifuge models decreased, compared to the deformation reproduced under Earth's gravity, due to the increase in self-weight, which led to a different scaling factor for the hydraulic gradient after the loosening. The limited expansion of the soil at the exit-hole was also observed in the three-dimensional centrifuge models for which loosening was barely visible from video recordings, in contrast to similar experiments available in the literature for which the loosening was often visible. This behavior likely contributed to the development of an initiation-dominated mechanism in centrifuge models, rather than the expected progression-dominated observed on the field.

The three-dimensional experiments that modeled the complete mechanism showed that the critical global hydraulic gradient slightly decreased as the gravitational acceleration increased, but the difference was minimal, and the overall estimations agreed with estimations from full-scale experiments. In addition, the centrifuge gravitational acceleration was found to affect the amount of eroded soil and the time for development of the mechanism.

The mechanism modeled in experiments with different seepage lengths was different in terms of rate of progression, maximum elevation of impoundment, extent of erosion after failure and hydraulic gradient triggering the initiation of erosion, which were caused by the different local hydraulic behaviors observed at the exit-hole. However, the critical global hydraulic gradients observed in models tested at the same gravitational acceleration were very similar, regardless of the seepage length. It was observed that the size of the exit-hole had a more noticeable effect on the mechanism modeled because of its influence on the initiation phase. The overall agreement between critical values obtained in this study and those reported in the literature using models with different scales highlights the great potential of the centrifuge modeling technique to study erosion mechanisms.

7.3 RECOMMENDATIONS FOR FUTURE WORK

The following research topics and recommendations are suggested to continue with the investigation of backward erosion piping using the geotechnical centrifuge modeling technique.

1. *Improvements to three-dimensional models*: the performance of the instruments used to analyze the models, such as pore pressure and differential pressure transducers, was satisfactory as they provided reliable data regardless of the challenges associated to the centrifuge environment. It is recommended to maintain the miniature pore pressure sensors for three-dimensional models but increase the number to cover a greater surface area of the foundation soil. This should be done with caution to maintain enough contact area with the cover layer as the sensor location usually provide unexpected weak points to develop erosion.

2. *Geometric parameters of the model*: the overall dimensions of the model and the type of exit strongly affected the characteristics of the backward erosion piping modeled and the critical hydraulic conditions that trigger the phenomenon. It was observed that the tendency of the critical gradients estimated from centrifuge models changed while the size of the exit-hole increased from 26 mm to 49 mm, which suggests that the overall behavior changes significantly for a certain exit size. It is recommended to expand the current analysis to exit-hole sizes between this range to develop a detailed analysis of the change in behavior, in addition to include exit-hole sizes beyond 49 mm to characterize the transition between a three-dimensional configuration to a two-dimensional configuration. It is recommended to develop a series of experiments with variable thickness of the foundation soil as it is expected to influence the evolution of the mechanism and perhaps contribute to a progression-dominated mechanism.
3. *The nonlinear flow problem*: the development of nonlinear flow while modeling seepage-driven phenomena in centrifuge models with the same soil existing in the prototype is virtually unavoidable, especially in coarse grained materials. An alternative solution proposed in the literature is reducing the size of the grains in proportion to the increase of the gravitational acceleration. By doing so, the permeability of the soil decreases, hence reducing the velocity of flow across the soil and the likelihood to develop nonlinear flow. However, a side effects for this approach is the development of intergranular forces that are representative of silts and clays, which implies the development of an erosion mechanism not representative of cohesionless soils. An alternative approach is increasing the viscosity of the seeping fluid, which would also decrease the velocity of flow. This alternative requires the

analysis of the change of the seepage forces acting on the grains relative to the gravitational acceleration field.

4. *Modeling the conventional solutions to piping problems*: the use of toe drain filters and cut-off walls in the foundation soil are typical solutions to avoid or control piping problems in water retaining structures. It is recommended to study the effects of this solutions in centrifuge models as they can be easily implemented in two- and three-dimensional models of backward erosion piping.
5. *Correlating with numerical approaches:* one of the main advantages observed in centrifuge models was the possibility of measuring pressure losses within very small seepage lengths, which is otherwise challenging under Earth's gravity. By replicating the control volumes of numerical analyses in physical experiments using centrifuge, a reliable comparison of the results is possible. Therefore, it is possible to analysis the effects of challenging factors, such as viscous shear stress, particle-shape effects, fluid viscosity or grain motion analysis.

REFERENCES

Abbood, D. W. (2009). An experimental model for flow through porous media using water filter. In *Thirteenth international water technology conference*, Hurghada, Egypt.

Alfortish, M., Brandon, T., …, Woodward, M. (2012). *Geotechnical Reconnaissance of the 2011 Flood on the lower Mississippi River.*

Alsaydalani, M. O. A., & Clayton, C. R. I. (2013). Internal fluidization in granular soils. *Journal of Geotechnical and Geoenvironmental Engineering*, *140*(3), 04013024.

Altinbilek, D. (2002). "The role of dams in development." *International Journal of Water Resources Development*, 18(1), 9-24.

Andreasen, R. R., Canga, E., Kjaergaard, C., Iversen, B. V., & Poulsen, T. G. (2013). Relating water and air flow characteristics in coarse granular materials. *Water, Air, & Soil Pollution*, 224(4), 1469.

Arulanandan, K., Thompson, P. Y., Kutter, B. L., Meegoda, N. J., Muraleetharan, K. K., & Yogachandran, C. (1988). Centrifuge modeling of transport processes for pollutants in soils. *Journal of Geotechnical Engineering*, *114*(2), 185-205.

ASTM D2434-68. (2006). *Standard Test Method for Permeability of Granular Soils (Constant Head) (Withdrawn 2015)*, ASTM International, West Conshohocken, PA, 2006

Baldassarre, G. D., Viglione, A., Carr, G., Kuil, L., Salinas, J. L., and Blöschl, G. (2013). "Socio-hydrology: conceptualizing human-flood interactions." *Hydrology and Earth System Sciences*, 17(8), 3295-3303.

Bear, J. (2013). *Dynamics of fluids in porous media*. Courier Corporation.

Beheshti, A. A., & Ataie-Ashtiani, B. (2008). Analysis of threshold and incipient conditions for sediment movement. *Coastal Engineering*, *55*(5), 423-430.

Bendahmane, F., Marot, D., & Alexis, A. (2008). Experimental parametric study of suffusion and backward erosion. *Journal of Geotechnical and Geoenvironmental Engineering*, *134*(1), 57-67.

Bezuijen, A., & Steedman, R. S. (2010). Scaling of hydraulic processes. In *Proc. 7th Intl. Conf. on Physical Modeling in Geotechnics (ICPMG 2010)* (pp. 93-98).

Biswas, A. K., and Tortajada, C. (2001). "Development and large dams: a global perspective." *International Journal of Water Resources Development*, 17(1), 9-21.

Bligh, W. G. (1910). Dams, barrages and weirs on porous foundations. *Engineering News*, *64*(26), 708-710.

Bo-Ming, Y., & Jian-Hua, L. (2004). A geometry model for tortuosity of flow path in porous media. *Chinese Physics Letters*, *21*(8), 1569.

Bonelli, S. (Ed.). (2013). *Erosion in geomechanics applied to dams and levees*. John Wiley & Sons.

Burcharth, H. F., & Christensen, C. (1991). On Non-Stationary One-Dimensional Porous Flow in Coarse Granular Materials.

Cargill, K. W., & Ko, H. Y. (1983). Centrifugal modeling of transient water flow. *Journal of Geotechnical Engineering*, *109*(4), 536-555.

Cao, Z., Pender, G., & Meng, J. (2006). Explicit formulation of the Shields diagram for incipient motion of sediment. *Journal of Hydraulic Engineering*, *132*(10), 1097-1099.

Casagrande, A. (1948). Classification and identification of soils. *Transactions, ASCE*, 113, 901-991.

Carman PC (1956) Flow of gases through porous media. Academic press

Carrier III, W. D. (2003). Goodbye, hazen; hello, kozeny-carman. *Journal of geotechnical and geoenvironmental engineering*, *129*(11), 1054-1056.

Chapuis, R. P. (2004). Predicting the saturated hydraulic conductivity of sand and gravel using effective diameter and void ratio. *Canadian geotechnical journal*, 41(5), 787-795.

Comiti, J., & Renaud, M. (1989). A new model for determining mean structure parameters of fixed beds from pressure drop measurements: application to beds packed with parallelepipedal particles. *Chemical Engineering Science*, *44*(7), 1539-1545.

Comiti, J., Sabiri, N. E., & Montillet, A. (2000). Experimental characterization of flow regimes in various porous media—III: limit of Darcy's or creeping flow regime for Newtonian and purely viscous non-Newtonian fluids. *Chemical Engineering Science*, *55*(15), 3057-3061.

Costa, G., & Prisco, C. D. (1999). On slope instability induced by seepage erosion. *Canadian Geotechnical Journal*, *36*(6), 1056-1073.

Dancey, C. L., Diplas, P., Papanicolaou, A., & Bala, M. (2002). Probability of individual grain movement and threshold condition. *Journal of Hydraulic Engineering*, *128*(12), 1069-1075.

Danka, J., & Zhang, L. M. (2015). Dike failure mechanisms and breaching parameters. *Journal of Geotechnical and Geoenvironmental Engineering*, *141*(9), 04015039.

Dean, R. G. (1973). Heuristic models of sand transport in the surf zone. In *First Australian Conference on Coastal Engineering, 1973: Engineering Dynamics of the Coastal Zone*(p. 215). Institution of Engineers, Australia.

De Wit, J. D., Sellmeijer, J. B., & Penning, A. (1981). Laboratory testing on piping. In *Tenth International Conference on Soil Mechanics and Foundation Engineering* (pp. 517-520).

De Wit, J. M. (1984). Onderzoek zandmeevoerende wellen Rapportage Modelproeven. Grondmechanica Delft Report CO220887/10, Delft.

Dewoolkar, M. M., Ko, H. Y., & Pak, R. Y. (2001). Seismic behavior of cantilever retaining walls with liquefiable backfills. *Journal of Geotechnical and Geoenvironmental engineering*, *127*(5), 424-435.

Dewoolkar, M. M., Ko, H. Y., & Pak, R. Y. S. (1999). Centrifuge modelling of models of seismic effects on saturated earth structures. *Geotechnique*, *49*(2), 247-266.

Dong, P., Newson, T. A., Davies, M. C. R., & Davies, P. A. (2001). Scaling laws for centrifuge modelling of soil transport by turbulent fluid flows. *International Journal of Physical Modelling in Geotechnics*, *1*(1), 41-45.

Dukhan, N., Bağcı, Ö., & Özdemir, M. (2014). Metal foam hydrodynamics: flow regimes from pre-Darcy to turbulent. *International Journal of Heat and Mass Transfer*, *77*, 114-123.

Ergun S, Orning AA (1949) Fluid flow through randomly packed columns and fluidized beds. Industrial & Engineering Chemistry, 41(6): 1179-1184.

Ergun S (1952) Fluid flow through packed columns. Chem. Eng. Prog., 48: 89-94.

Fand, R. M., Kim, B. Y. K., Lam, A. C. C., & Phan, R. T. (1987). Resistance to the flow of fluids through simple and complex porous media whose matrices are composed of randomly packed spheres.

Fell, R., Wan, C. F., Cyganiewicz, J., & Foster, M. (2003). Time for development of internal erosion and piping in embankment dams. *Journal of geotechnical and geoenvironmental engineering*, *129*(4), 307-314.

Fell, R., & Wan, C. F. (2005). *Methods for estimating the probability of failure of embankment dams by internal erosion and piping in the foundation and from embankment to foundation*. University of New South Wales, School of Civil and Environmental Engineering.

Fleshman, M. S., & Rice, J. D. (2013). Constant gradient piping test apparatus for evaluation of critical hydraulic conditions for the initiation of piping.

Fleshman, M. S., & Rice, J. D. (2014). Laboratory modeling of the mechanisms of piping erosion initiation. *Journal of Geotechnical and Geoenvironmental Engineering*, *140*(6), 04014017.

Fontana, N. (2008). Experimental analysis of heaving phenomena in sandy soils. *Journal of Hydraulic Engineering*, *134*(6), 794-799.

Foster, M., Fell, R., & Spannagle, M. (2000). The statistics of embankment dam failures and accidents. *Canadian Geotechnical Journal*, *37*(5), 1000-1024.

Fourar, M., Radilla, G., Lenormand, R., & Moyne, C. (2004). On the non-linear behavior of a laminar single-phase flow through two and three-dimensional porous media. *Advances in Water resources*, *27*(6), 669-677.

Gajan, S., Kutter, B. L., Phalen, J. D., Hutchinson, T. C., & Martin, G. R. (2005). Centrifuge modeling of load-deformation behavior of rocking shallow foundations. *Soil Dynamics and Earthquake Engineering*, 25(7-10), 773-783.

Garnier, J., Gaudin, C., Springman, S. M., Culligan, P. J., Goodings, D., Konig, D., ... & Thorel, L. (2007). Catalogue of scaling laws and similitude questions in geotechnical centrifuge modelling. *International Journal of Physical Modelling in Geotechnics*, *7*(3), 1.

Ghiassian, H., & Ghareh, S. (2008). Stability of sandy slopes under seepage conditions. *Landslides*, *5*(4), 397-406.

Gelhar, L. W., Welty, C., & Rehfeldt, K. R. (1992). A critical review of data on field-scale dispersion in aquifers. *Water resources research*, *28*(7), 1955-1974.

Goodings, D. J. (1982). Relationships for centrifugal modelling of seepage and surface flow effects on embankment dams. *Géotechnique*, *32*(2), 149-152.

Goodings, D. J. (1984). GEOTECHNICAL CENTRIFUGE MODELING OF SOIL EROSION. *Transportation Research Record*, (998).

Goodings, D. J. (1985). RELATIONSHIPS FOR MODELLING WATER EFFECTS IN GEOTECHNICAL CENTIFUGE MODELS. *Publication of: Balkema (AA)*.

Goodings, D. J. (1994). Implications of changes in seepage flow regimes for centrifuge models. In *Centrifuge* (Vol. 94, pp. 393-398).

Goodings, D. J., & Abdulla, W. A. (2002). Stability charts for predicting sinkholes in weakly cemented sand over karst limestone. *Engineering geology*, 65(2-3), 179-184.

Guo, J. (2002). Logarithmic matching and its applications in computational hydraulics and sediment transport. *Journal of Hydraulic research*, *40*(5), 555-565.

Hamilton, J. M., Phillips, R., Dunnavant, T. W., & Murff, J. D. (1991). Centrifuge study of laterally loaded pile behavior in clay. In *Proc., Int. Conf. Centrifuge* (Vol. 91, pp. 285-292).

Han, S. J., & Goodings, D. J. (2006). Practical model of frost heave in clay. *Journal of geotechnical and geoenvironmental engineering*, 132(1), 92-101.

Hanses, U. K. (1985). Zur Mechanik der Entwicklung von Erosionskanälen in geschichtetem Untergrund unter Stauanlagen. Universitätsbibliothek der TU Berlin.

Horikoshi, K., Noda, S., Takizawa, A., and Takahashi, A. (2019). "EWG-6 Centrifuge Modeling for Visualization of Backward Erosion Piping Progression". *In Book of Abstracts*, pp. 17.

Indraratna, B., & Radampola, S. (2002). Analysis of critical hydraulic gradient for particle movement in filtration. *Journal of Geotechnical and Geoenvironmental Engineering*, *128*(4), 347-350.

Israr, J., Indraratna, B., & Rujikiatkamjorn, C. (2016). Laboratory investigation of the seepage induced response of granular soils under static and cyclic loading. *Geotechnical Testing Journal*, 39(5), 795-812.

Joseph, P. G., Einstein, H. H., & Whitman, R. V. (1988). *A literature review of geotechnical centrifuge modeling with particular emphasis on rock mechanics*. Massachusetts Inst Of Tech Cambridge Dept Of Civil Engineering.

Kadlec, R. H., & Knight, R. L. (1996). Treatment Wetlands. Lewis. *Boca Raton*, 893.

Khalifa, A., Garnier, J., Thomas, P., & Rault, G. (2000, May). Scaling laws of water flow in centrifuge models. In *International Symposium on Physical Modelling and Testing in Environmental Geotechnics* (Vol. 56, pp. 207-216).

Khalifa, M. A., Wahyudi, I., & Thomas, P. (2000). A new device for measuring permeability under high gradients and sinusoidal gradients.

Khalifa, M. A. O., Wahyudi, I., & Thomas, P. (2002). New extension of Darcy's law to unsteady flows. *Soils and foundations*, *42*(6), 53-63.

Kim, D. S., Kim, N. R., Choo, Y. W., & Cho, G. C. (2013). A newly developed state-of-the-art geotechnical centrifuge in Korea. *KSCE Journal of Civil Engineering*, 1-8.

Ko, H. Y. (1988). Summary of the state-of-the-art in centrifuge model testing. *Centrifuges in soil mechanics*, 11-18.

Koenders, M. A., & Sellmeijer, J. B. (1992). Mathematical model for piping. *Journal of Geotechnical Engineering*, *118*(6), 943-946.

Koito, N., Horikoshi, K., & Takahashi, A. (2016). Physical modelling of backward erosion piping in foundation beneath levee. In *Scour and Erosion: Proceedings of*

the 8th International Conference on Scour and Erosion (Oxford, UK, 12-15 September 2016) (p. 445). CRC Press.

Kolb, C. R. (1975). *Geologic control of sand boils along Mississippi River levees* (No. AEWES-MISC-PAPER-S-75-22). Army Engineer Waterways Experiment Station Vicksburg Ms.

Kovács, G. (1981). Developments in water science—seepage hydraulics, Chap 3.2.

Kreibich, H., Piroth, K., Seifert, I., Maiwald, H., Kunert, U., Schwarz, J., ... & Thieken, A. H. (2009). Is flow velocity a significant parameter in flood damage modelling?. *Natural Hazards and Earth System Sciences*, *9*(5), 1679.

Kutter, B. L. (1995). Recent advances in centrifuge modeling of seismic shaking.

Lane, E. W. (1935). Security from under-seepage-masonry dams on earth foundations. In *Proceedings of ASCE*.

Lanzano, G., Bilotta, E., Russo, G., Silvestri, F., & Madabhushi, S. G. (2012). Centrifuge modeling of seismic loading on tunnels in sand. *Geotechnical Testing Journal*, 35(6), 854-869.

Laut, P. (1975). Application of centrifugal model tests in connexion with studies of flow patterns of contaminated water in soil structures. *Geotechnique*, *25*(2), 401-406.

Leavell, D. A., Wibowo, J. L., Yule, D. E., and Strange, R. C. (2014). "Geotechnical centrifuge experiments to evaluate piping in foundation soils (No. ERDC/GSL-TR-14-14)." Eng. Research and Development Center, Vicksburg.

Li, Y., Craven, J., Schweig, E. S., & Obermeier, S. F. (1996). Sand boils induced by the 1993 Mississippi River flood: Could they one day be misinterpreted as earthquake-induced liquefaction? *Geology*, *24*(2), 171-174.

Lin, C. P., Goodings, D. J., Bernold, L. E., Dick, R. D., & Fourney, W. L. (1994). Model studies of effects on lunar soil of chemical explosions. *Journal of geotechnical engineering*, 120(10), 1684-1703.

Ling, H. I., Mohri, Y., Kawabata, T., Liu, H., Burke, C., & Sun, L. (2003). Centrifugal modeling of seismic behavior of large-diameter pipe in liquefiable soil. *Journal of geotechnical and geoenvironmental engineering*, *129*(12), 1092-1101.

Macdonald, I. F., El-Sayed, M. S., Mow, K., & Dullien, F. A. L. (1979). Flow through porous media-the Ergun equation revisited. *Industrial & Engineering Chemistry Fundamentals*, *18*(3), 199-208.

Madabhushi, G. (2014). *Centrifuge modelling for civil engineers*. CRC Press.

Marot, D., Le, V. D., Garnier, J., Thorel, L., & Audrain, P. (2012). Study of scale effect in an internal erosion mechanism: centrifuge model and energy analysis. *European Journal of Environmental and Civil Engineering*, *16*(1), 1-19.

Mathias, S. A., Butler, A. P., & Zhan, H. (2008). Approximate solutions for Forchheimer flow to a well. *Journal of Hydraulic Engineering*, 134(9), 1318-1325.

Mazzoleni, M., Bacchi, B., Barontini, S., Di Baldassarre, G., Pilotti, M., & Ranzi, R. (2013). Flooding hazard mapping in floodplain areas affected by piping breaches in the Po River, Italy. *Journal of Hydrologic Engineering*, *19*(4), 717-731.

Mesquita, M., Testezlaf, R., & Ramirez, J. S. (2012). The effect of media bed characteristics and internal auxiliary elements on sand filter head loss. *Agricultural Water Management*, 115, 178-185.

Miesel, D. (1978). Rückschreitende erosion unter bindiger Deckschicht. Baugrundtagung Berlin.

Moutsopoulos, K. N., Papaspyros, I. N., & Tsihrintzis, V. A. (2009). Experimental investigation of inertial flow processes in porous media. *Journal of hydrology*, 374(3-4), 242-254.

Murillo, C., Thorel, L., & Caicedo, B. (2009). Ground vibration isolation with geofoam barriers: Centrifuge modeling. *Geotextiles and Geomembranes*, 27(6), 423-434.

Muskat, M. (1938). The Flow of Homogeneous Fluids Through Porous Media. *Soil Science*, *46*(2), 169.

Nichols, S. C., & Goodings, D. J. (2000). Physical model testing of compaction grouting in cohesionless soil. *Journal of Geotechnical and Geoenvironmental Engineering*, 126(9), 848-852.

Nielsen, P. (1992). *Coastal bottom boundary layers and sediment transport* (Vol. 4). World Scientific Publishing Co Inc.

Ojha, C. S. P., Singh, V. P., & Adrian, D. D. (2001). Influence of porosity on piping models of levee failure. *Journal of geotechnical and geoenvironmental engineering*, *127*(12), 1071-1074.

Ojha, C. S. P., Singh, V. P., & Adrian, D. D. (2003). Determination of critical head in soil piping. *Journal of Hydraulic Engineering*, *129*(7), 511-518.

Ovalle-Villamil, W., and Sasanakul, I. (2018) "A new insight into the behaviour of seepage flow in centrifuge modelling." Physical Modelling in Geotechnics, Volume 1: *Proc. of the 9th International Conference on Physical Modelling in Geotechnics (ICPMG 2018)*, London, United Kingdom, July 2018, pp.259.

Ovalle-Villamil, W., and Sasanakul, I. (2019) "Observation of Piping Erosion Initiation in a Centrifuge Model," *Geo-Congress 2019, 8th International Conference on Case Histories in Geotechnical Engineering*, Philadelphia, Pennsylvania, U.S., 2019.

Ovalle-Villamil, W., & Sasanakul, I. (2019). Investigation of non-Darcy flow for fine grained materials. *Geotechnical and Geological Engineering*, 37(1), 413-429.

Ovalle-Villamil, W., & Sasanakul, I. (2020). Assessment of Centrifuge Modelling of Internal Erosion Induced by Upward Flow Conditions. *International Journal of Physical Modelling in Geotechnics*, 1-40.

Ovalle-Villamil, W., and Sasanakul, I. (2021) "Centrifuge Modeling of the Backward Erosion Piping Process," Accepted to: *10th International Conference on Scour and Erosion ICSE 10*, Arlington, Virginia, U.S., 2021.

Ovesen, N.K. (1980) Discussion: The use of physical models in design. *Proc. 7th Eur. Regional Conf. Soil Mech. Found. Eng.*, Brighton, Vol. 4, pp. 315–323. British Geotechnical Society, London.

Parekh, M. L., Kanning, W., Bocovich, C., Mooney, M. A., & Koelewijn, A. R. (2016). Backward Erosion Monitored by Spatial–Temporal Pore Pressure Changes during Field Experiments. *Journal of Geotechnical and Geoenvironmental Engineering*, *142*(10), 04016050.

Peng, S., & Rice, J. D. (2020). Measuring Critical Gradients for Soil Loosening and Initiation of Backward Erosion-Piping Mechanism. *Journal of Geotechnical and Geoenvironmental Engineering*, 146(8), 04020069.

Philippe, P., & Badiane, M. (2013). Localized fluidization in a granular medium. *Physical Review E*, *87*(4), 042206.

Pokrovsky, G. I. (1936). Studies of soil pressures and soil deformations by means of a centrifuge. *Proc. of 1st ICSMFE*, *1*, 70-71.

Reddi, L. N., Lee, I. M., & Bonala, M. V. (2000). Comparison of internal and surface erosion using flow pump tests on a sand-kaolinite mixture.

Richards, K. S., & Reddy, K. R. (2007). Critical appraisal of piping phenomena in earth dams. *Bulletin of Engineering Geology and the Environment*, *66*(4), 381-402.

Richards, K. S., & Reddy, K. R. (2008). Experimental investigation of piping potential in earthen structures. In *Geocongress 2008: Geosustainability and geohazard mitigation* (pp. 367-376).

Richards, K. S., & Reddy, K. R. (2010). True triaxial piping test apparatus for evaluation of piping potential in earth structures. *Geotechnical Testing Journal*, 33(1), 83-95.

Richards, K. S., & Reddy, K. R. (2012). Experimental investigation of initiation of backward erosion piping in soils. *Géotechnique*, *62*(10), 933.

Richardson, J. F., & Harker, J. H. (2002). *Chemical engineering-Volume 2: Particle Technology and Separation Processes*. Butterworth-Heinemann.

Robbins, B. A., Stephens, I. J., Van Beek, V. M., Koelewijn, A. R., & Bezuijen, A. (2020). Field measurements of sand boil hydraulics. *Géotechnique*, 70(2), 153-160.

Salahi, M. B., Sedghi-Asl, M., & Parvizi, M. (2015). Nonlinear flow through a packed-column experiment. *Journal of Hydrologic Engineering*, *20*(9), 04015003.

Salem, H. S., & Chilingarian, G. V. (2000). Influence of porosity and direction of flow on tortuosity in unconsolidated porous media. *Energy Sources*, *22*(3), 207-213.

Santamarina, J. C. (2003). Soil behavior at the microscale: particle forces. In *Soil behavior and soft ground construction* (pp. 25-56).

Santamarina, J. C., & Goodings, D. J. (1989). Centrifuge modeling: a study of similarity.

Sasanakul, I., Vanadit-Ellis, W., Sharp, M., Abdoun, T., Ubilla, J., Steedman, S., and Stone, K. (2008). "New Orleans levee system performance during Hurricane Katrina: 17th Street Canal and Orleans Canal North." *Journal of geotechnical and geoenvironmental engineering*, 134(5), 657-667.

Sasanakul, I., Gassman, S. L., Pierce, C. E., Ovalle, W., Starcher, R., Gheibi, E., & Rahman, M. (2017). Dam Failures from a 1000-Year Rainfall Event in South Carolina. In *Geotechnical Frontiers 2017* (pp. 244-254).

Schmertmann, J. H. (2000). The no-filter factor of safety against piping through sands. In *Judgment and Innovation: The Heritage and Future of the Geotechnical Engineering Profession* (pp. 65-132).

Schmertmann, J. H., Foster, M., Fell, R., & Spannagle, M. (2002). A method for assessing the relative likelihood of failure of embankment dams by piping: Discussion/Reply. *Canadian Geotechnical Journal*, *39*(2), 495.

Schofield, A. N. (1981). Dynamic and earthquake geotechnical centrifuge modelling.

Sedghi-Asl, M., Rahimi, H., & Salehi, R. (2014). Non-Darcy flow of water through a packed column test. *Transport in porous media*, 101(2), 215-227.

Sellmeijer, J. B. (1988). On the mechanism of piping under impervious structures.

Sellmeijer, J. B., & Koenders, M. A. (1991). A mathematical model for piping. *Applied Mathematical Modelling*, *15*(11-12), 646-651.

Sellmeijer, H., de la Cruz, J. L., van Beek, V. M., & Knoeff, H. (2011). Fine-tuning of the backward erosion piping model through small-scale, medium-scale and IJkdijk experiments. *European Journal of Environmental and Civil Engineering*, *15*(8), 1139-1154.

Sharif, Y. A., Elkholy, M., Hanif Chaudhry, M., & Imran, J. (2015). Experimental study on the piping erosion process in earthen embankments. *Journal of Hydraulic Engineering*, *141*(7), 04015012.

Shields, A. (1936). Application of similarity principles and turbulence research to bed-load movement. *CalTech library*.

Sidiropoulou, M. G., Moutsopoulos, K. N., & Tsihrintzis, V. A. (2007). Determination of Forchheimer equation coefficients a and b. *Hydrological processes*, *21*(4), 534-554.

Silvis, F. (1991). Verificatie piping model: proeven in de deltagoot. Delft, the Netherlands: *Grondmechanica Delft* (in Dutch).

Singh, D. N., & Gupta, A. K. (2000). Modelling hydraulic conductivity in a small centrifuge. *Canadian Geotechnical Journal*, *37*(5), 1150-1155.

Snoeijers, R. (2016). *Non-linear Flow in Unconsolidated Sandy Porous Media-An Experimental Investigation* (Master's thesis).

Stephenson, D. J. (1979). *Rockfill in hydraulic engineering* (Vol. 27). Elsevier.

Stewart, J. P., Douglas, J., Javanbarg, M., Bozorgnia, Y., Abrahamson, N. A., Boore, D. M., ... & Stafford, P. J. (2015). Selection of ground motion prediction equations for the global earthquake model. *Earthquake Spectra*, 31(1), 19-45.

Suah, P. G., & Goodings, D. J. (2001). Failure of geotextile-reinforced vertical soil walls with marginal backfill. *Transportation research record*, 1772(1), 183-189.

Swamee, P. K., & Ojha, C. S. P. (1994). Criteria for evaluating flow classes in alluvial channels. *Journal of Hydraulic Engineering*, 120(5), 652-658.

Tao, H., & Tao, J. (2017). Quantitative analysis of piping erosion micro-mechanisms with coupled CFD and DEM method. *Acta Geotechnica*, 12(3), 573-592.

Taylor, R. E. (Ed.). (2018). *Geotechnical centrifuge technology*. CRC Press.

Technical Advisory Committee (1999). Technical report on sand boils (piping), Technical Advisory Committee on Flood Defenses. Delft, the Netherlands: Road and Hydraulic Engineering Institute.

Terashi, M., Kitazume, M. and Kawabata, K. (1989) Centrifuge modelling of a laterally loaded pile. *Proc. 12th Int. Conf. Soil Mech. Found. Eng.*, Vol. 2, pp. 991–994.

Terzaghi, K. V. (1922). Der grundbruch an stauwerken und seine verhutung. *Wasserkraft*, *17*, 445-449.

Terzaghi, K., & Peck, R. B. (1948). Soil mechanics in engineering practice.

Terzaghi, K., Peck, R. B., & Mesri, G. (1996). *Soil mechanics in engineering practice*. John Wiley & Sons.

Trussell, R. R., & Chang, M. (1999). Review of flow through porous media as applied to head loss in water filters. *Journal of Environmental Engineering*, *125*(11), 998-1006.

Ubilla, J., Abdoun, T., Sasanakul, I., Sharp, M., Steedman, S., Vanadit-Ellis, W., and Zimmie, T. (2008). "New Orleans levee system performance during hurricane Katrina: London Avenue and Orleans canal south." *Journal of Geotechnical and Geoenvironmental Engineering*, 134(5), 668-680.

US Army Corps of Engineers (2000). Design and Construction of Levees. Washington, DC.

US Army Corps of Engineers (2016) "Corps Map. Corps Map. National Inventory of Dams." <nid.usace.army.mil> (Oct. 6, 2018).

US Army Corps of Engineers (2018) "National Levee Database." <levees.sec.usace.army.mil> (Oct. 6, 2018).

USDIBR (2014). *Design Standards No. 13 Embankment Dams*.

Van Beek, V. M. (2015). *Backward erosion piping: initiation and progression*.

Van Beek, V. M., Koelewijn, A. R., Kruse, G. A. M., Sellmeijer, J. B., & Barends, F. B. J. (2008). Piping phenomena in heterogeneous sands–experiments and simulations. In *Proceedings of the 4th international conference on scour and erosion. Tokyo, Japan*.

Van Beek, V. M., Bezuijen, A., & Zwanenburg, C. (2010). Piping: Centrifuge experiments on scaling effects and levee stability. In *Physical Modelling in Geotechnics, Two Volume Set: Proceedings of the 7th International Conference on Physical Modelling in Geotechnics (ICPMG 2010), 28th June-1st July, Zurich, Switzerland* (Vol. 1, p. 183). CRC Press.

Van Beek, V. M., Knoeff, H., & Sellmeijer, H. (2011). Observations on the process of backward erosion piping in small-, medium-and full-scale experiments. *European Journal of Environmental and Civil Engineering*, *15*(8), 1115-1137.

Van Beek, V., Yao, Q., Van, M., & Barends, F. (2012). Validation of Sellmeijer's model for backward piping under dikes on multiple sand layers. In *ICSE6: sixth international conference on Scour and Erosion, Paris* (pp. 27-31).

Van Beek, V. M., Van Essen, H. M., Vandenboer, K., & Bezuijen, A. (2015). Developments in modelling of backward erosion piping. *Géotechnique*, *65*(9), 740-754.

Wahyudi, I., Montillet, A., & Khalifa, A. A. (2002). Darcy and post-Darcy flows within different sands. *Journal of Hydraulic Research*, *40*(4), 519-525.

Wan, C. F., & Fell, R. (2004). *Experimental investigation of internal instability of soils in embankment dams and their foundations*. University of New South Wales, School of Civil and Environmental Engineering.

White, C. M. (1940). The equilibrium of grains on the bed of a stream. *Proceedings of the Royal Society of London. Series A, Mathematical and Physical Sciences*, 322-338.

Xu, P., & Yu, B. (2008). Developing a new form of permeability and Kozeny–Carman constant for homogeneous porous media by means of fractal geometry. *Advances in water resources*, *31*(1), 74-81.

Yang, K. H., & Wang, J. Y. (2017). Experiment and statistical assessment on piping failures in soils with different gradations. *Marine Georesources & Geotechnology*, *35*(4), 512-527.

Yüksel, I. (2009). "Dams and hydropower for sustainable development." *Energy Sources, Part B*, 4(1), 100-110.

Zeng, Z., & Grigg, R. (2006). A criterion for non-Darcy flow in porous media. *Transport in porous media*, *63*(1), 57-69.

APPENDIX A

GEOTECHNICAL CENTRIFUGE FACILITIES

This appendix presents details of the geotechnical centrifuge facilities at the University of South Carolina and covers the details of the main features and capabilities of the centrifuge device, as well as details of the data acquisition system and the tools for in-flight video monitoring.

1.1 FACILITIES

The centrifuge is located within the Geotechnical Research Laboratories at the University of South Carolina. A plan view of this location is shown in Figure A. 1. The device is installed in an enclosed 45 m^2 (480 Ft^2) room, providing enough space for model and test preparation, as shown in Figure A. 2. The main control room is located adjacent to the centrifuge area in an isolated location to ensure the safety of the user, as shown in Figure A. 3. The main control desktop and the power control for the drive system are located in this room in addition to a small closed-circuit television system that provides different views of the centrifuge device during operation using a 42-inch monitor. The control room also includes a pressurized air line with a maximum capacity of 150 psi that is regulated using a conventional analog pressure gauge. A secondary control desk is also located in the centrifuge room to assist in the preparation and execution of centrifuge tests.

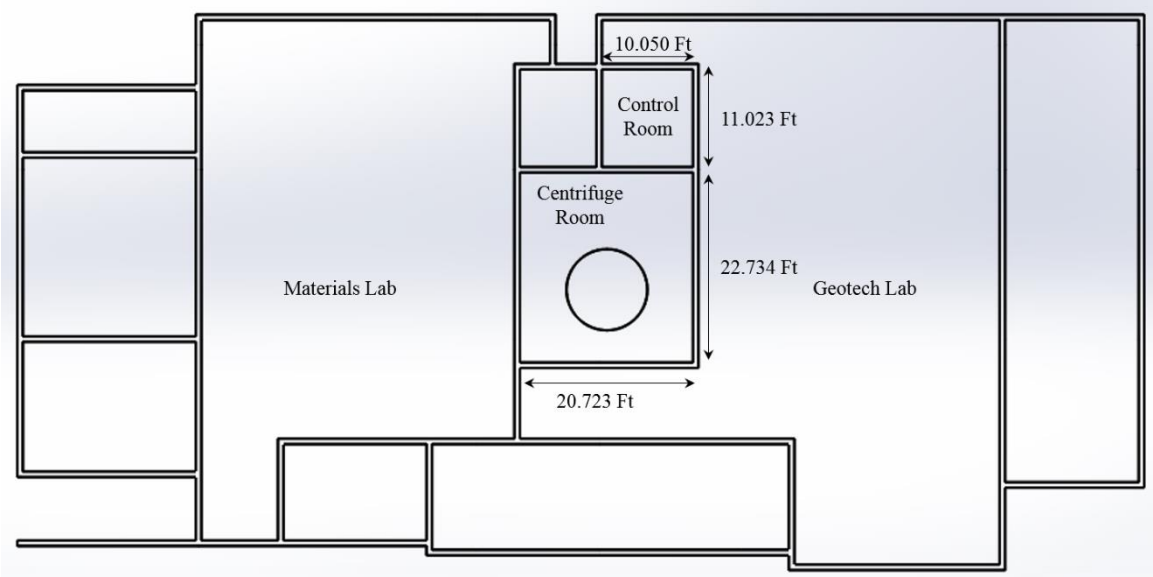

Figure A. 1 Geotechnical research facilities at the University of South Carolina.

Figure A. 2 Centrifuge room.

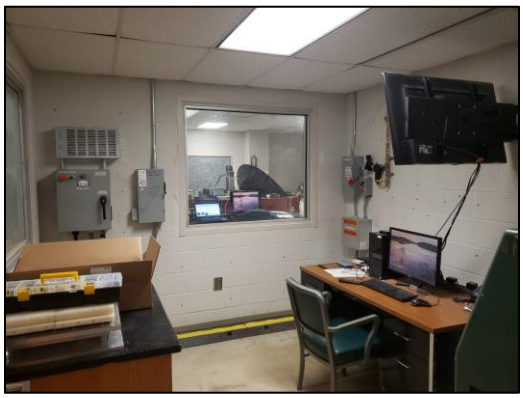

Figure A. 3 Control room.

1.2 GENERAL OVERVIEW

A sketch of the geotechnical centrifuge at UofSC is shown in Figure A. 4. The radius, r, from the central axis of the centrifuge to the basket floor is 1.3 m (51 inches). The speed range capacity of this device is 0 to 400 RPM, which can be translated to a range of increment of gravitational acceleration by:

$$N = \frac{r}{9.81\ m/s^2}\left(2\pi\frac{RPM}{60}\right)^2$$

where N = increment of gravitational acceleration with reference to Earth's gravity (i.e., $N = g_{model}/g_{Earth}$); r = radius of rotation; and RPM = radial acceleration in revolutions per minute.

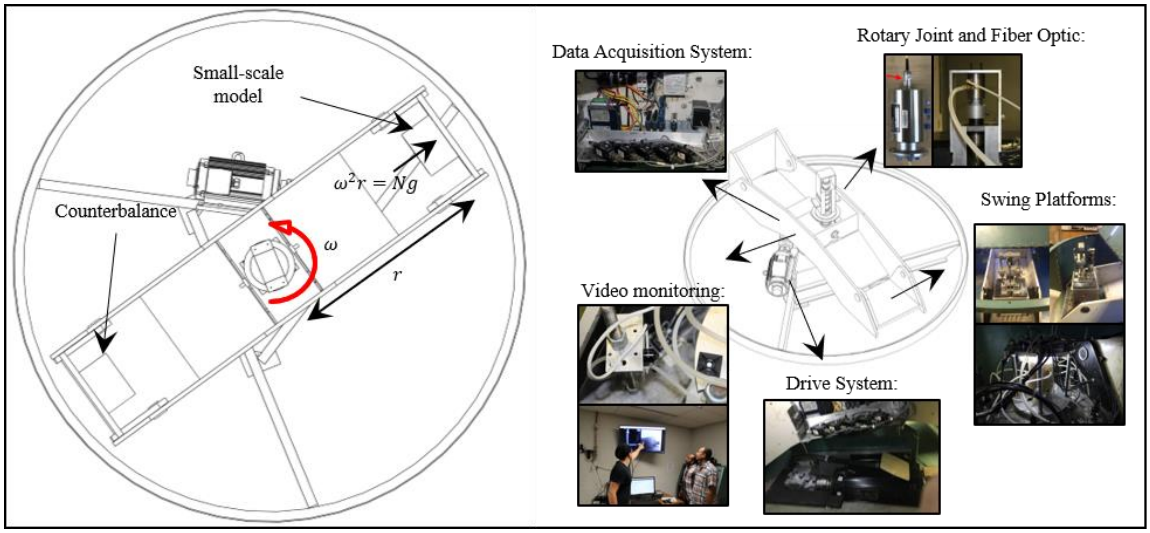

Figure A. 4 Geotechnical centrifuge at the University of South Carolina.

The range of N that the centrifuge can operate is shown in Figure A. 5a, as a function of RPM. It is observed that this centrifuge can perform experiments under values of N up to 230g, where g = 9.81 m/s^2 (i.e., Earth's gravity). The centrifuge capacity in terms of maximum acceleration multiplied by the maximum payload is 13.6 g-ton (30,000 g-lb) based on the manufacturer literature. Using the range of N aforementioned,

the maximum payload can be estimated as shown in Figure A. 5b. A maximum payload of 68 kg (150 lbs) is allowed at 200g, while 136 kg (300 lbs) is allowed at 100g.

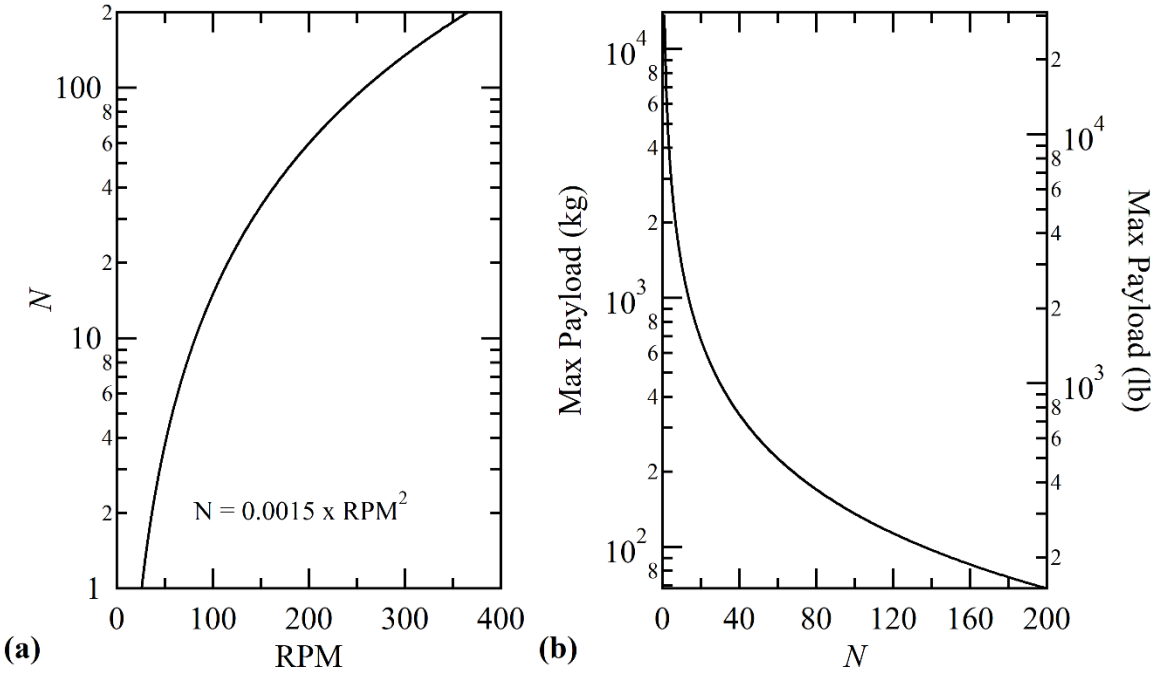

Figure A. 5 (a) Induced gravitational acceleration by centrifuge radial acceleration and (b) maximum payload in centrifuge models.

1.3 MAIN COMPONENTS

The original centrifuge setup is composed of a base support and centrifuge enclosure, the main drive shaft, which is hollowed and allows a passage to the interior of the centrifuge, the arm assembly with two swing platforms at each end and a set of electric sliprings. Two lateral containers were attached to the sides of the arm to store the devices and electronics required for operation. A new rotary joint and a new electric-drive system were also installed. The main components are described in this appendix and further information can be consulted from the original literature of the device. Figure A. 6 shows a general sketch of the centrifuge.

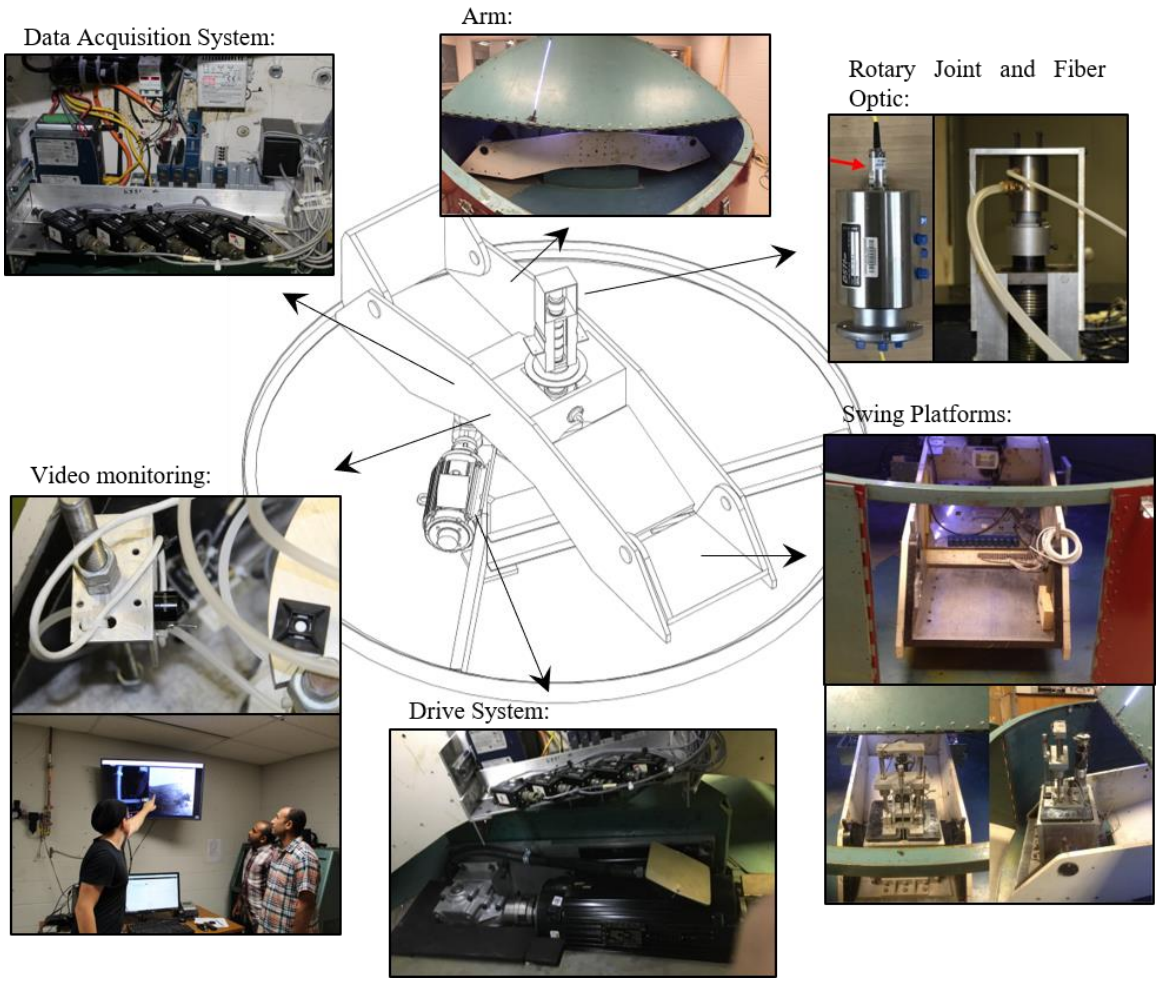

Figure A. 6 Main components of the geotechnical centrifuge.

1.3.1 Arm Assembly

The arm assembly is composed of the main arm and two swing platforms, as shown in Figure A. 7. The main arm is a symmetrical piece made of an aluminum alloy and has dimension of 275 cm (108 in) in length and 68.6 cm (27 in) in width. The two swing platforms are made of an aluminum alloy and are pivoted to both ends of the main arm. The useful area of the platforms is 61-by-61 cm^2 (24-by-24 in^2) and they can accommodate models with up to 61 cm (24 inches) in height. The approximated clearance between the base of the platforms and the centrifuge enclosure is of 2.9 cm in

vertical position, and 3.2 cm in horizontal position (during flight). The center of gravity of both empty platforms is located 23.5 cm below the pivot location. The arm assembly was specially designed with a model capacity of 13.6 g-ton.

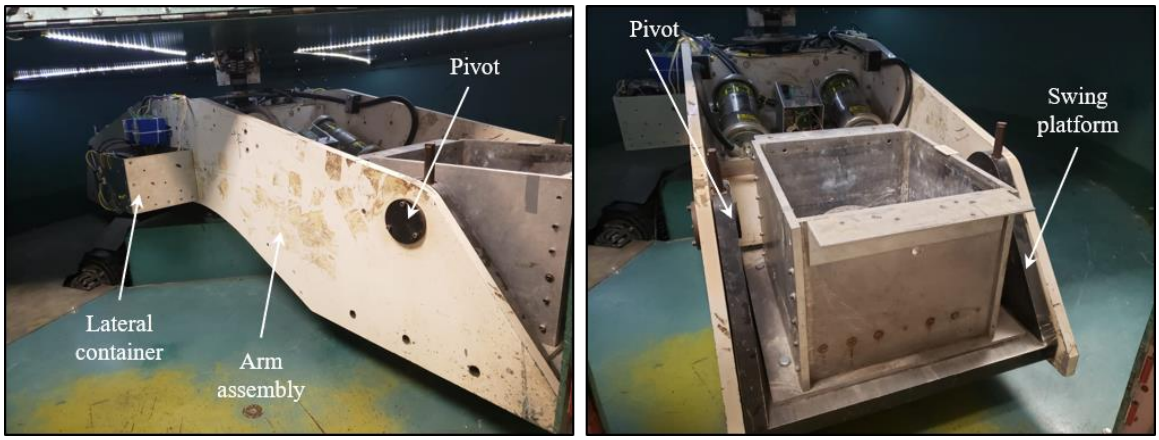

Figure A. 7 Arm assembly and swing platforms.

A set of six lateral holes were predisposed on the base of the platforms to fix a vertical position. Three holes with 1.35 cm in diameter and 7.62 cm in length are in parallel on both sides. The capability of securing the platforms in vertical position is a special feature of this centrifuge. These holes are particularly useful during the installation of model containers and experimental setting up. Although testing with the platforms in vertical position is possible, the capacity of the arm decreases to 5.4 g-ton. It is highly important to design a thorough security protocol for the model for testing with the platforms in vertical position.

1.3.2 Drive System

The centrifuge uses a 15 HP AC variable speed electric drive system, as shown in Figure A. 8. This system offers, among others, accurate speed indication and control, precise up and down ramping, robust emergency stop, increased efficiency, and large

reduction of mechanical parts compared to oil-driven systems. Major components include an ABB ACS355 15 HP VFD, 15 HP asynchronous induction motor with encoder feedback, right angle gearbox and mounting plate, a braking resistor and a LabVIEW based control program. This TVF 254THTL5726-000288 FH I system was manufactured by Marathon Black Max and allows a maximum safe radial acceleration of 4200 RPM. The motor has a standard diameter gear of 3 inches and is connected to the centrifuge main drive shaft using a standard time belt model 725H-150.

Figure A. 8 Electric drive system mounted in the centrifuge.

The drive system requires the customized electric installation shown in Figure A. 9, which is located inside the control room. The ABB ACS355 system in this figure is a customized mountable drive controller designed for this motor and uses an input voltage of 208 AC-V. The output is directly connected to the motor via cable. Figure A. 10 shows the simplified main circuit diagram of the ABB ACS 355 drive system. The rectifier converts the three-phase AC voltage to DC voltage. The capacitor bank of the intermediate circuit stabilizes the DC voltage. The inverter converts the DC voltage back

to AC voltage for the AC motor. The brake chopper connects the external brake resistor to the intermediate DC circuit when the voltage in the circuit exceeds its maximum limit.

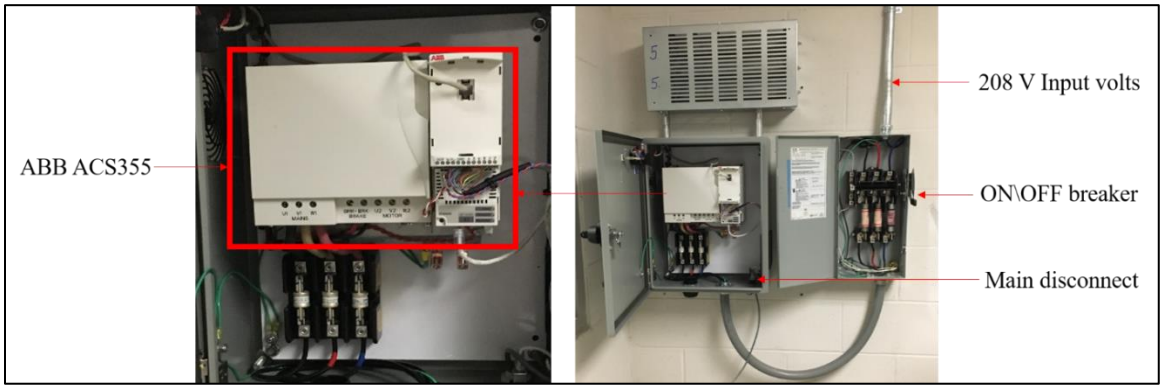

Figure A. 9 Electric assembly for the Electric Drive System.

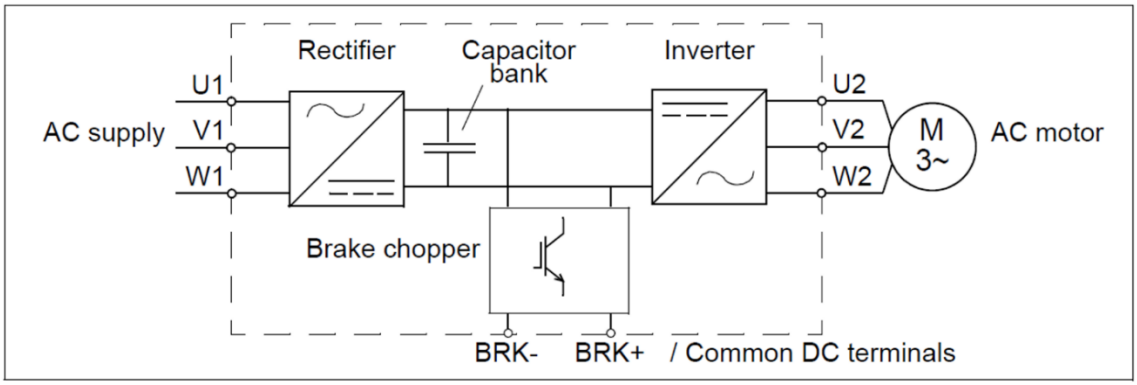

Figure A. 10 Simplified circuit diagram for ABB ACS355 drive.

1.3.3 Electric Slipring

A slip ring assembly made of coin silver and insulated with plastic is mounted over the main drive shaft, as shown in Figure A. 11. This assembly is part of the original design of the centrifuge and provides a connection for external devices that require a physical connection with the internal portion of the centrifuge while spinning. The assembly has 4 separated modules (labeled A, B, C and D), and each module has 8

independent rings. The rings within modules B, C and D are wired through the main drive shaft, to a dual-row electric strip with capacity of 24 positions located in the arm. The rings in module A are also wired through the main drive shaft, but the terminals inside the centrifuge are disconnected. Electrical continuity between the terminals of each ring (i.e., inside and outside the centrifuge) was checked on August 31st, 2018. Table A. 1 shows the current use of each ring. The rings numbered as 1 in this table correspond to the top left in each module and the numbering increases as the ring location moves downwards.

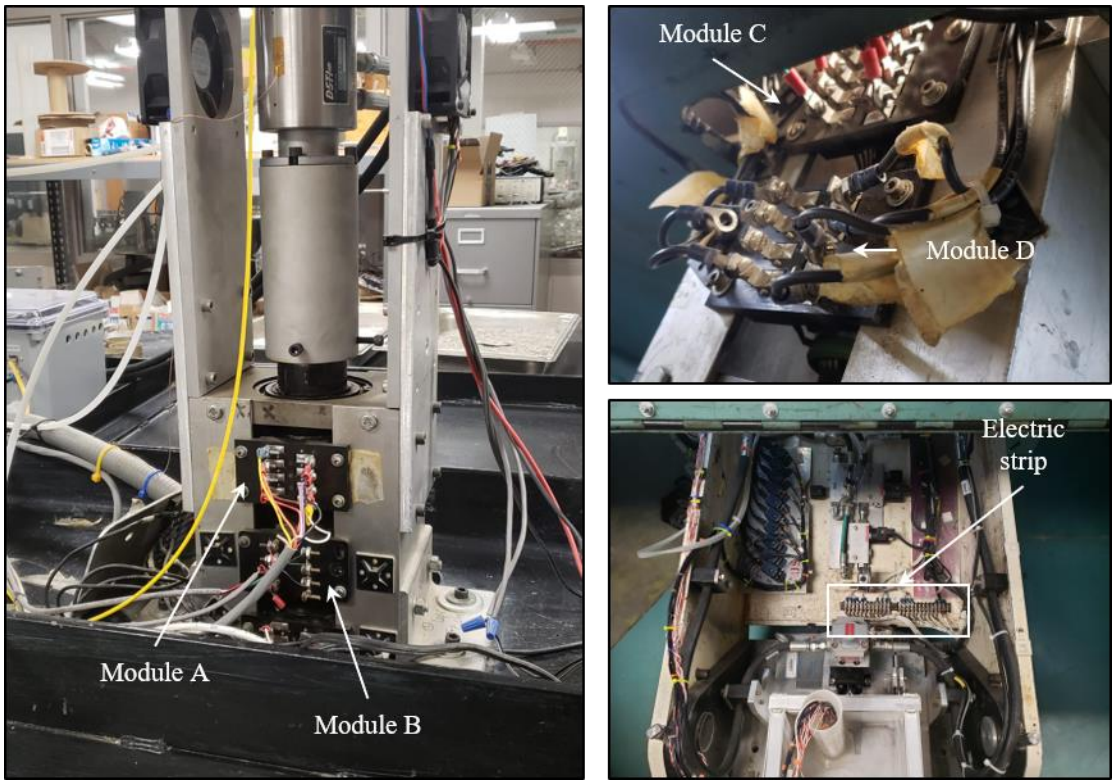

Figure A. 11 Electric slipring assembly.

Table A. 1 Current use of electric sliprings (Module-Ring).

M-R	Use	M-R	Use
A-1	Disconnected	B-1	MOOG -Shaker
A-2	Disconnected	B-2	MOOG -Shaker
A-3	Disconnected	B-3	MOOG - Shaker
A-4	Disconnected	B-4	MOOG - Shaker
A-5	Disconnected	B-5	MOOG - Shaker
A-6	Disconnected	B-6	MOOG - Shaker
A-7	Disconnected	B-7	Disconnected
A-8	Disconnected	B-8	Disconnected
C-1	24V (Stationary/Rotating Modules)	D-1	Disconnected
C-2	24V (Stationary /Rotating Modules)	D-2	Disconnected
C-3	0V (Stationary /Rotating Modules)	D-3	Disconnected
C-4	0V (Stationary /Rotating Modules)	D-4	Disconnected
C-5	48V (Stationary /Rotating Modules)	D-5	Disconnected
C-6	48V (Stationary /Rotating Modules)	D-6	Ground (120V AC source)
C-7	0V (Stationary /Rotating Modules)	D-7	Load (120V AC source)
C-8	0V (Stationary /Rotating Modules)	D-8	Neutral (120V AC source)

1.3.4 Rotary Joint or Rotary Union

The rotary joint is a stainless-steel GP-141 piece of equipment manufactured by Dynamic Sealing Technologies Incorporated and is used to drive fluids and gases in and out the centrifuge while spinning. The rotary joint is mounted on top of the main drive shaft using an aluminum adapter designed for this purpose, as shown in Figure A. 12. The adapter is an aluminum hollow cylinder attached to the main drive shaft through two lateral screws and to the rotary joint through four vertical screws. Four additional screws attached to the top of the rotary joint are used to prevent its rotation, but these screws do not lock the rotary joint in any other direction. Since the rotary joint is also hollowed, a continuous passage through the assembly exists and it is used to assemble the fiber optic system used for data communication (Fiber Optic Rotary Joint, FORJ).

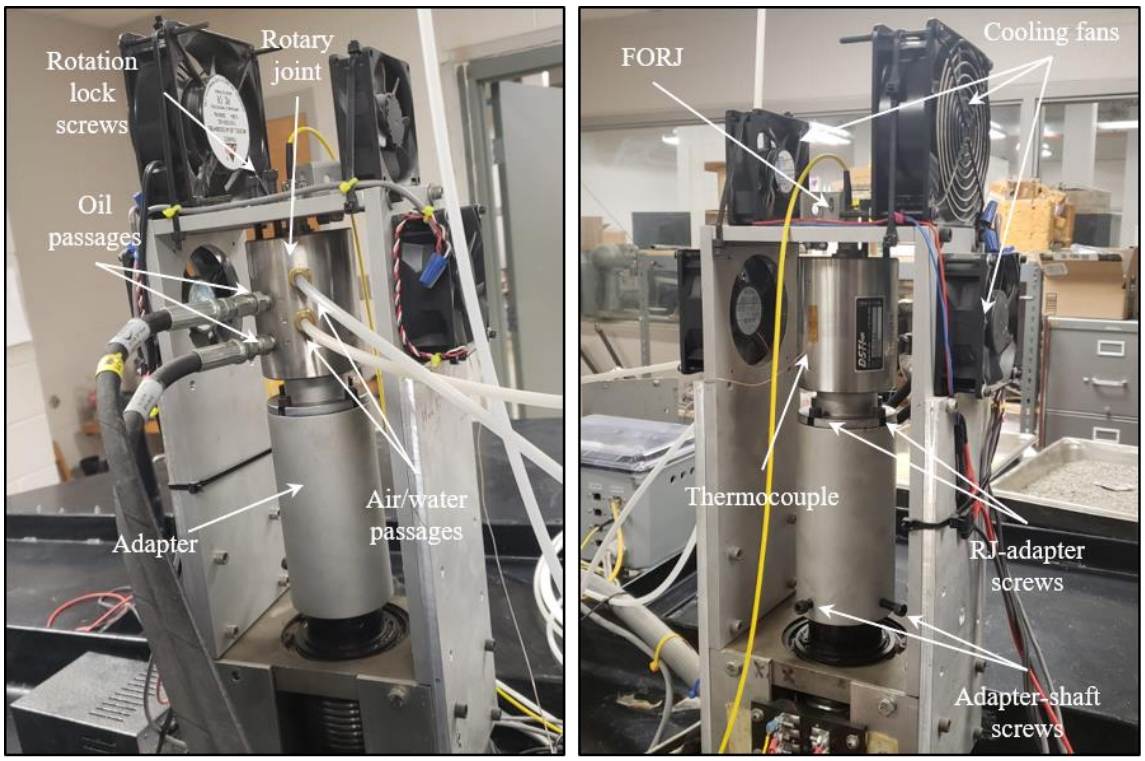

Figure A. 12 Rotary joint assembly.

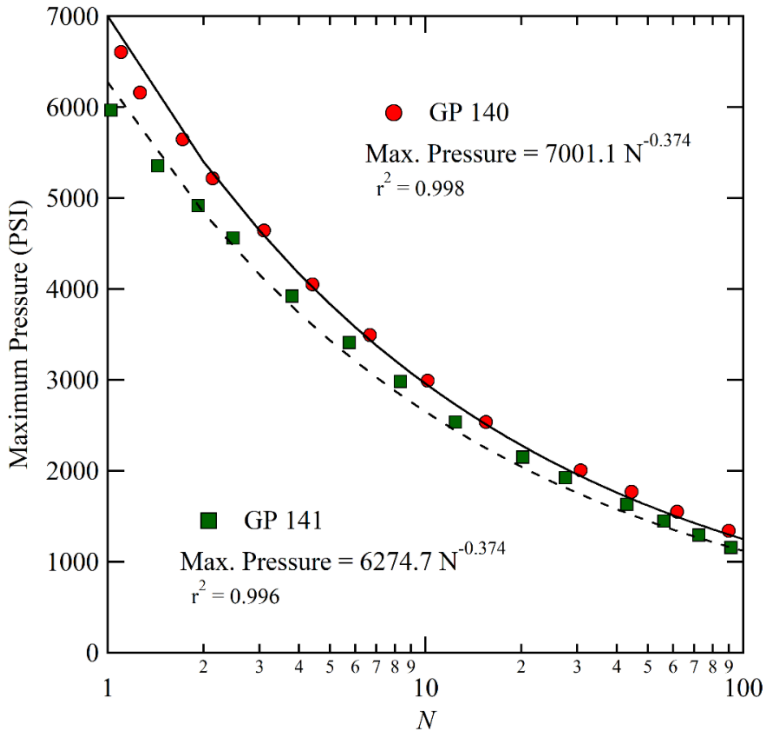

Figure A. 13 Pressure loss as a function of the increment of gravitational acceleration.

To drive fluids and gases, the device uses four internal passages with a maximum rated pressure of 515 Bar (7,500 PSI) and allows radial velocities of up to 500 RPM, although the maximum pressure reduces with acceleration, as shown in Figure A. 13. Two passages are currently used to drive oil during the operation of a one-dimensional shaking table, while the remaining two passages are used for air and water flow. A thermocouple was attached to the lateral wall of the rotary joint to monitor the temperature of the assembly and four cooling fans are used as protection.

1.3.5 Visual Monitoring System

A series of AXIS network cameras, as shown in Figure A. 14, are used to monitor the models and the arm assembly during flight. These cameras provide high quality video recordings and image captures with up to 1280x720 pixels resolution. A frame rate of 25 to 30 frames per second and a shutter time of 1/24500 seconds are allowed with these devices.

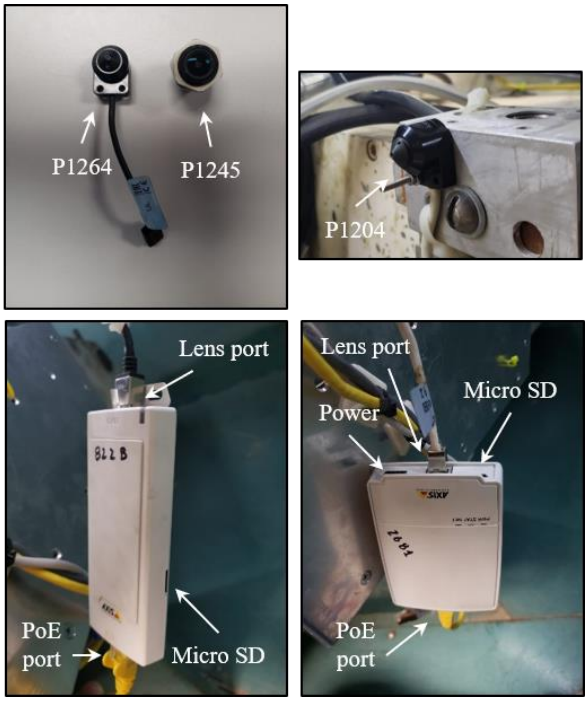

Figure A. 14 Details of cameras.

Each camera is composed of a sensor unit, or lens, and a main unit with network and power ports and a memory card slot. The depth of field can be adjusted by rotating the frame surrounding the lens. A P1204 camera is fixed to the inner wall of the centrifuge enclosure and is used to monitor the arm assembly during test, as shown in Figure A. 15. The main unit of this camera is in the control room and data communication is made through a physical connection with the main desktop.

Figure A. 15 Fixed camera to monitor the arm assembly.

Three additional cameras lenses (P1204, P1245 and P1264) are used to monitor the models and are strategically located depending on the experiment. The main units of these cameras are placed in the lateral containers of the arm assembly and data communication is made through the ethernet switch module and the fiber optic. Real-time

videos and video recordings are managed using the AXIS online portal, accessible through the IP address assigned to each camera, and the specialized software Bluecherry. Further details of the configuration of the cameras prior testing are presented later in this appendix.

1.3.6 Data Acquisition System

Data acquisition during centrifuge tests is done using a National Instrument cDAQ 9188 chassis, which allows acquiring data from 8 National Instrument modules simultaneously. The chassis and modules are placed in a lateral container of the arm assembly, as shown in Figure A. 16. Communication with the main desktop from models connected to the chassis is done using the fiber optic system.

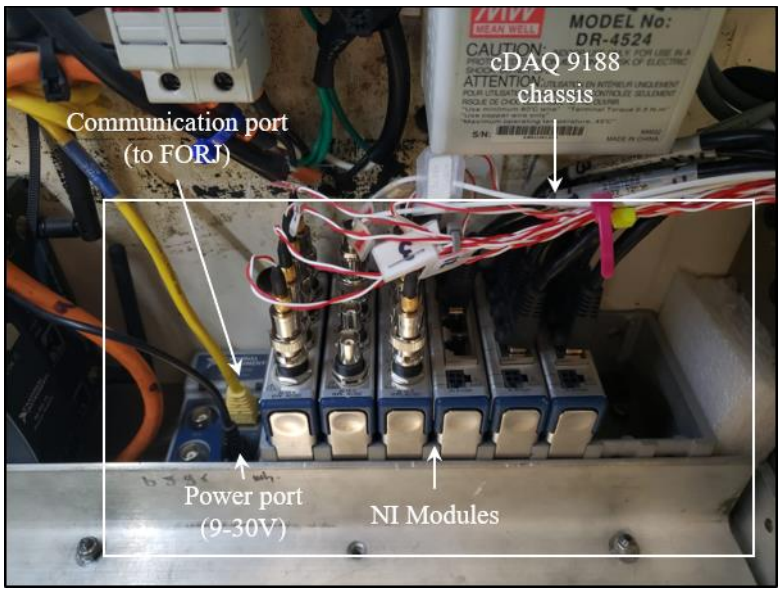

Figure A. 16 Data acquisition system.

Three different NI modules were used inside the centrifuge throughout this investigation. The NI 9205 module was used to acquire data from gauge pressure sensors (Omega PX409-100G5V) during centrifuge permeability and one-dimensional

experiments using a reference single ended (RSE) terminal configuration (i.e., the sensors shared the common port). The NI 9202 module was used to acquire data from differential pressure sensors during one-dimensional experiments using a differential terminal configuration (i.e., the sensors had isolated ports). The NI 9237 card was used to acquire data from Keller MI2 sensors during three-dimensional experiments using a full-bridge configuration. Data from displacement sensors was acquired using an external NI USB 6009 module. Likewise, data from the thermocouple attached to the rotary joint is continuously acquired using an external NI USB TC01.

1.3.7 Fiber Optic Communication System

Figure A. 17 shows the single-channel, Fiber Optic Rotary Joint (FORJ) used as main communication system of the centrifuge. The FORJ is screwed to the top of the rotary joint and is connected to the power supply and ethernet switch enclosure (see Figure A. 18), located outside the centrifuge, and to the rotating DC-DC converter and ethernet switch assembly (see Figure A. 19), located inside. The small form-factor pluggable (SFP) module on each connection is used to transmit and receive on different wavelengths of light, which allows a single fiber to be used for bidirectional communication. An anti-rotation assembly is also included to protect the FORJ during test.

1.3.8 Stationary Power Supply and Switch Enclosure

Figure A. 18 shows a picture of the power supply and switch assembly. This assembly is mounted over the centrifuge enclosure and contains a 24V/10A and a 48V/5A DC power supplies, and a four-port Gigabit Power Over Ethernet (PoE) switch with a Small Form-factor Pluggable (SFP) module. The SFP module provides the fiber

optic an interface to the FORJ. The power supplies are used to rout DC power to the centrifuge through the electric sliprings, as shown in Table A. 1. An additional non-PoE port available is used to connected and communicate to the centrifuge main desktop. The PoE ports can be connected to stationary network cameras.

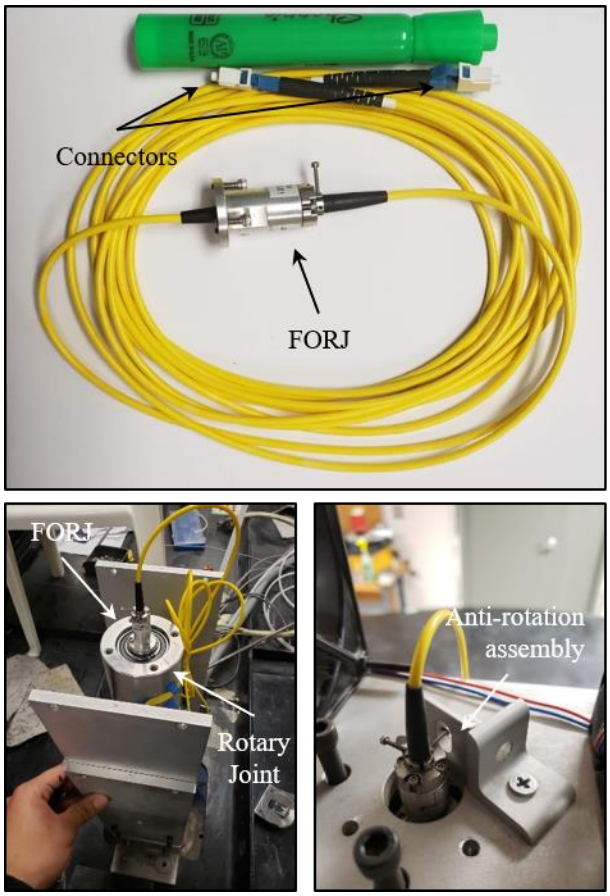

Figure A. 17 Fiber optic rotary joint assembly.

1.3.9 Rotating DC-DC Converter and Ethernet Switch Module

Figure A. 19 shows a picture of the rotating module. This assembly is mounted inside the centrifuge and is powered by the 24V and 48V DC supplied by the stationary power supplies through the electric sliprings, as shown in Table A. 1. The 48V supply is used to power the PoE Gigabit switch (four ports), which powers and transmits data from

the cameras, transmits data from the NI chassis and contains the SFP module connected to the FORJ. The 24V supply is used to power the internal DC-DC converters that create additional voltage supplies of 0V, 24V,48V, 5V, 10V, 12V and +/-15V. It is noted that a 120V AC supply is also provided through the electric sliprings, as shown in Table A. 1.

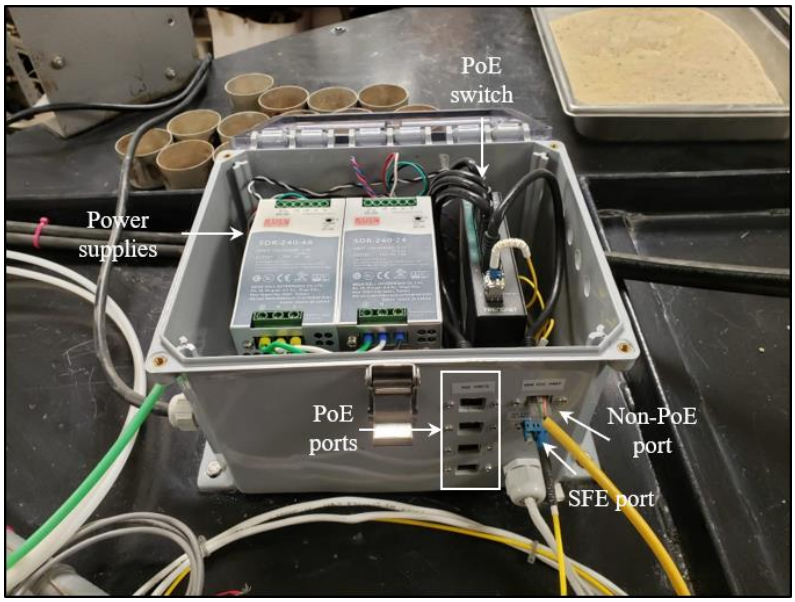

Figure A. 18 Stationary power supply and switch enclosure assembly.

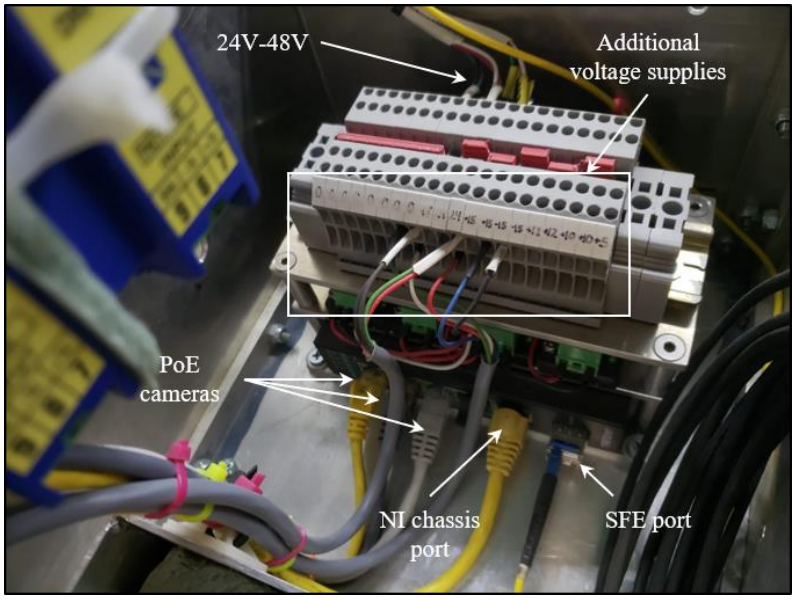

Figure A. 19 Rotating DC-DC converter and ethernet switch module assembly.

1.3.10 Control Desktop and Lateral Containers

Figure A. 20 shows a picture of the main control desktop and additional devices placed in the control room. The Giada device is a parallel computer operated by Linux and is used as storage for videos recorded using the Bluecherry software. The transfer of videos is done to maintain free space in the hard disk of the main desktop. The DVI device is used to extend the main control desktop capabilities to the secondary desktop. The AirRouter device is used to manage and protect the centrifuge local network and assign and manage the IP addresses the network electronic devices in the centrifuge, such as cameras, NI chassis and the Giada device.

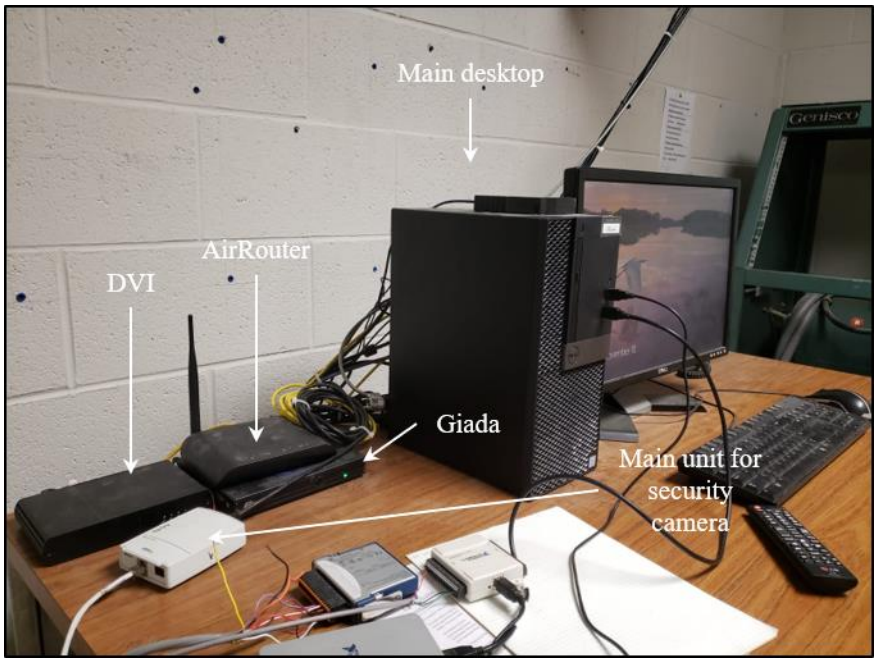

Figure A. 20 Control desktop in control room.

Figure A. 21 shows a picture of the lateral container containing the NI chassis. A class CC fuse is used as terminal of the 120V AC provided and is use as overcharge protection. This is particularly important to protect the chassis, which is powered using

this line. Two additional 24V power supplies are also placed in this container. Finally, an additional wireless Access Point bridge for communication is available in case of failure of the FORJ. The additional lateral container only includes the rotating DC-DC converter and switch module assembly and the main units of the cameras.

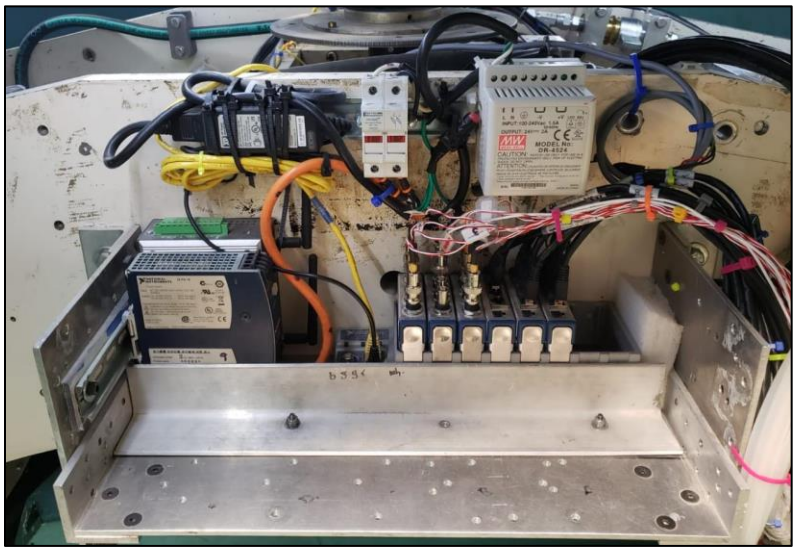

Figure A. 21 Lateral container.

1.3.11 General Wiring Map

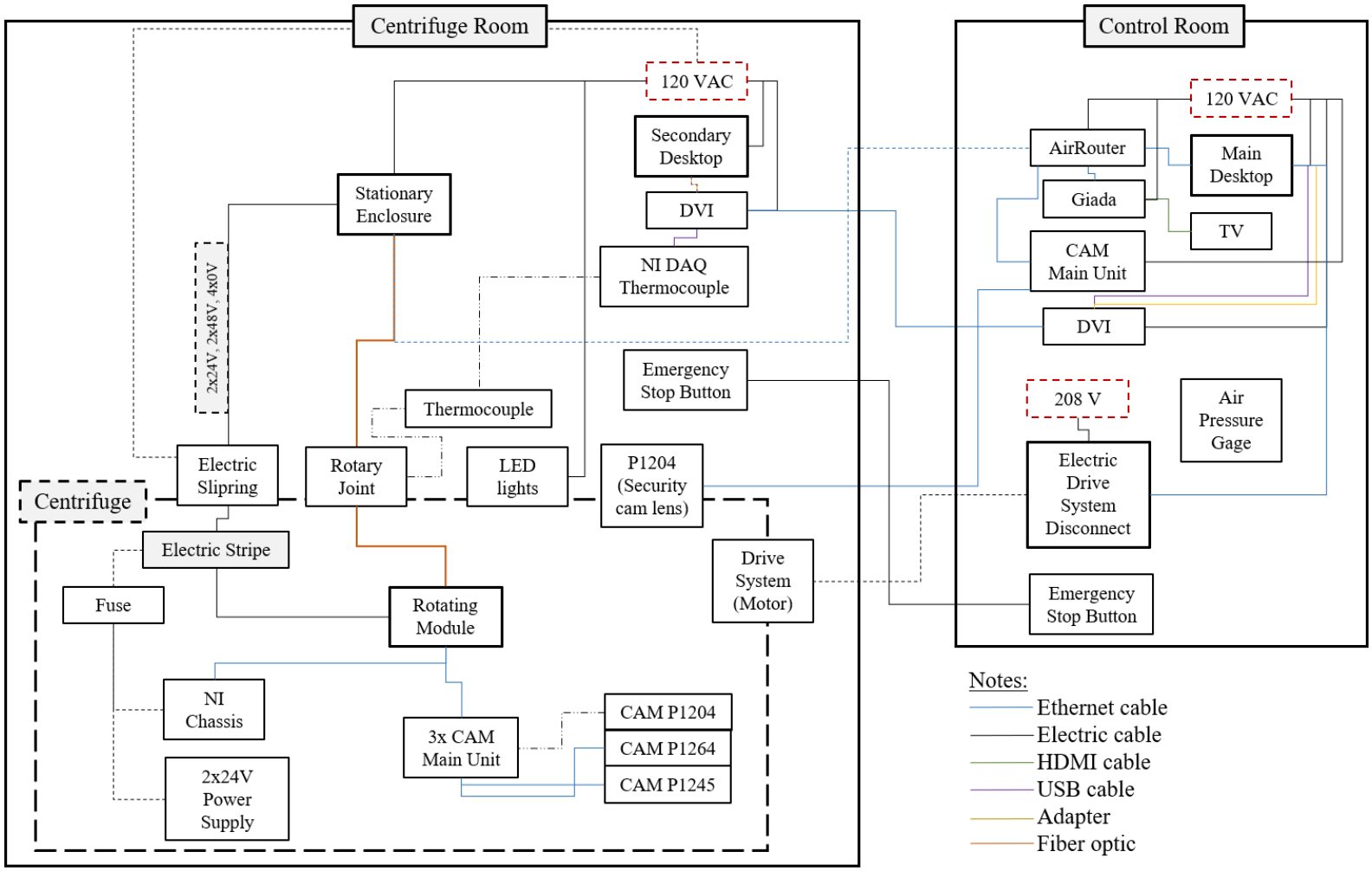

Figure A. 22 General wiring/connection map.

1.4 CENTRIFUGE SETTING UP

This section presents a step-by-step of the centrifuge setting-up covering the main components, safety measures, software use and centrifuge spin up. The process is presented under the assumption that a model has been already placed in the swing platforms and it is ready for testing. In addition, the order presented here is not mandatory, but every step is necessary before running an experiment.

1.4.1 COUNTERWEIGHT, ARM ASSEMBLY BALANCE AND SAFETY MEASURES

The main initial safety concern for the centrifuge operation is ensuring that adequate balance exists between both swing platforms. The initial step to provide balance is ensuring that the weight in both platforms is the same. To do so, it is best to keep record of the change in weight of the model as it is prepared and gradually increase the counterweight as the preparation progresses. Although the numerous devices and tools installed across the arm assembly make virtually impossible to ensure balance in the momentum forces induced on the platforms, which result from the displacement of the center of gravity on each platform, the user should try to the best of their possibilities to decrease momentum unbalance effects. Examples of how to address the momentum balance are presented in the original literature of the centrifuge device.

After the model and the counterweight are placed in the platforms, the user shall proceed to secure all the items involved in the experiment to a safe position. Such items include sensor cables across the arm assembly, air and water hoses, hose fittings, general wiring from the power supplies or data acquisition systems to sensing devices, camera lenses and camera cables, wiring connections, etc. This process varies from test to test and the following points are recommended:

- Using zip ties is very common to tide cables and hoses, among other items. It is recommended to consider the type and function of the cable or hose before tiding zip ties. Some cables are less robust than others and the zip tie may cause irreversible damages. For instance, fiber optic cables are extremely delicate and sensitive, and the ties should leave enough movement spaces. In addition, it is common to observe unexpected noises in sensor signals when its wiring is too close to other cables or power supplies.
- Consider the rotation of the platforms before securing hoses and cables. A certain loose length should be left to accommodate to this rotation. The loose cable or hose should not interact with the base platform, the enclosure or the rotation of the platforms.
- Hose fittings, wire fittings and any other item with a weight significantly greater than the wire or cable attached to are potential hazards due to the increase in self-weight during test. These fittings should be secured as well.
- Avoid using slender models without providing supporting frames.
- Remove unnecessary items, such as extensive cables or loose screws.
- Consider that the items tend to move in radial outward direction during flight.
- Secure the general items strategically, so it can be repeated easily for future tests.

After securing the items, the balance of the arm assembly shall be verified. Before doing so, the user should remove any unnecessary dead weights, such as screws locking the platforms to vertical position, tools or trash. Afterwards, the arm assembly is loosened by rotating the rod near the central axis of the centrifuge, as shown in Figure A. 23. A bubble level is place in the middle of the arm assembly to check that both sides are in

balance. Afterwards, the rod is rotated in opposite direction and tightened, and the bubble level is removed.

Figure A. 23 Centrifuge balance lock rod.

After this process, the centrifuge is ready to spin, but it is recommended to carefully rotate the arm assembly by hand to check for potential hazards. Once cleared, the enclosure lid and door can be closed and secured.

1.4.2 IP Address Verification – AirRouter/AirOS

This step is required to setup the cameras and to check that data communication between the centrifuge and the main desktop is stable. The user initially should power the devices inside the centrifuge. If a device is powered using the 120 VAC source, such as the NI chassis and modules, the respective cable located outside the centrifuge is plugged to a wall electric inlet. The stationary power supply and switch enclosure, which powers the main features inside the centrifuge, is also plugged. The next step is to verify the IP addresses assigned to each network device (i.e., NI chassis, each network camera and the Bluecherry Giada system). The user shall type the IP address 192.168.1.1 in an internet

browser to access airOS, which is the interface of the AirRouter, as shown in Figure A.24. After typing the credentials, the user will find a list of the devices and their respective IP addresses by accessing the “DHCP Leases” option, as shown in Figure A. 25.

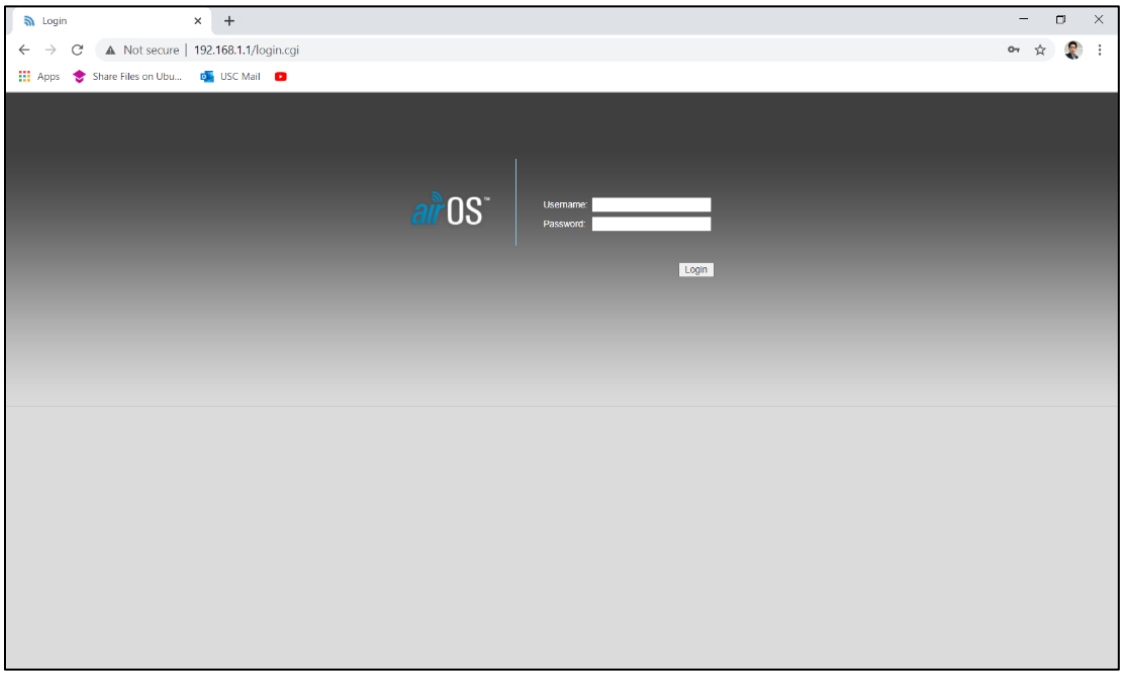

Figure A. 24 AirOS interface.

It is noted that a specific online interface can be accessed by typing the IP address in a browser and using the adequate credentials. However, this procedure is only required for the cameras as the remaining devices can be configured through available software. It is also important to highlight that any network device not listed in this section of the airOS interface is likely an indicator of problems with the physical connection of such device. Such problems may include the lack of power to the device and a bad or missing connection with the FORJ.

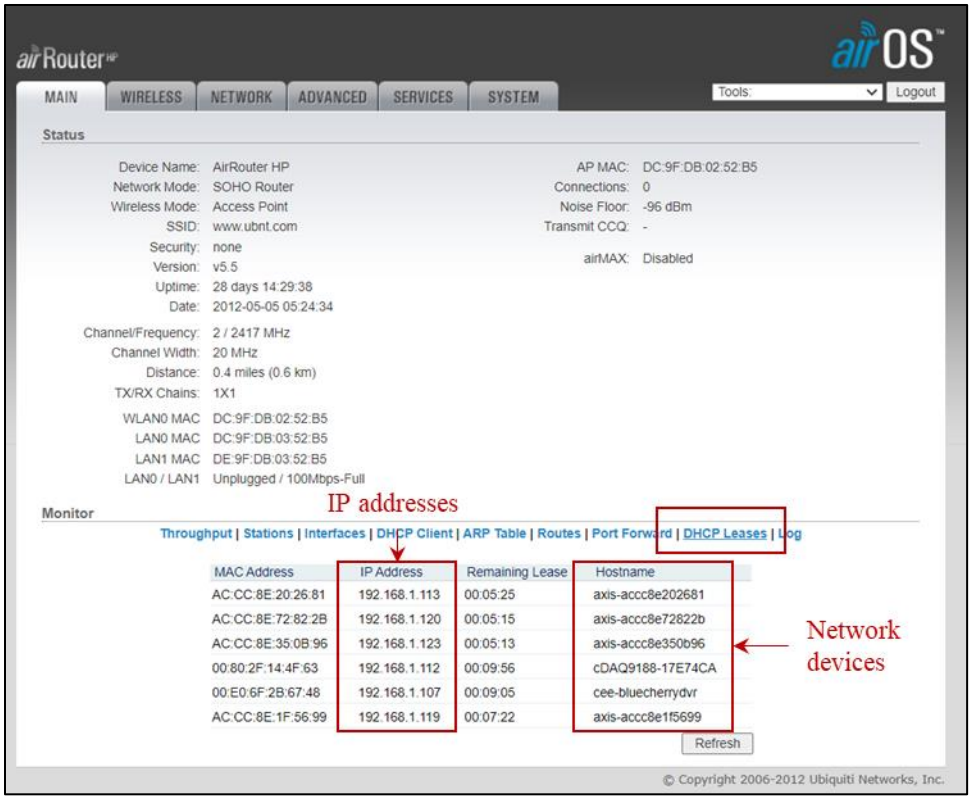

Figure A. 25 IP addresses and Network devices in AirOS.

1.4.3 Camera Setup – Axis and Bluecherry

The setup of the cameras for video monitoring and recording uses two correlated interfaces. The axis interface allows to set specific aspects of each camera, such as the quality of the video recordings or the protocol to record in microSD cards. The Bluecherry software allows to monitor the model and the arm assembly simultaneously and to manage and save video recordings. Both interfaces can perform video monitoring and recording individually, but each one has limitations. For example, Bluecherry is user friendly as it allows to manage different cameras on the same screen and videos recorded are easily accessed, while displaying multiple cameras using the axis interface requires multiple open browsers simultaneously and accessing video recordings is more

complicated. In contrast, the axis interface allows to modify multiple aspects of the cameras that are otherwise impossible through Bluecherry.

The first step in the process is to type the IP address of a given camera in an internet browser and access the credentials set for such device. Figure A. 26 shows the screen displayed, including the current view of the camera. If a black screen is displayed instead, it is possible that the camera lens is not connected to the main unit.

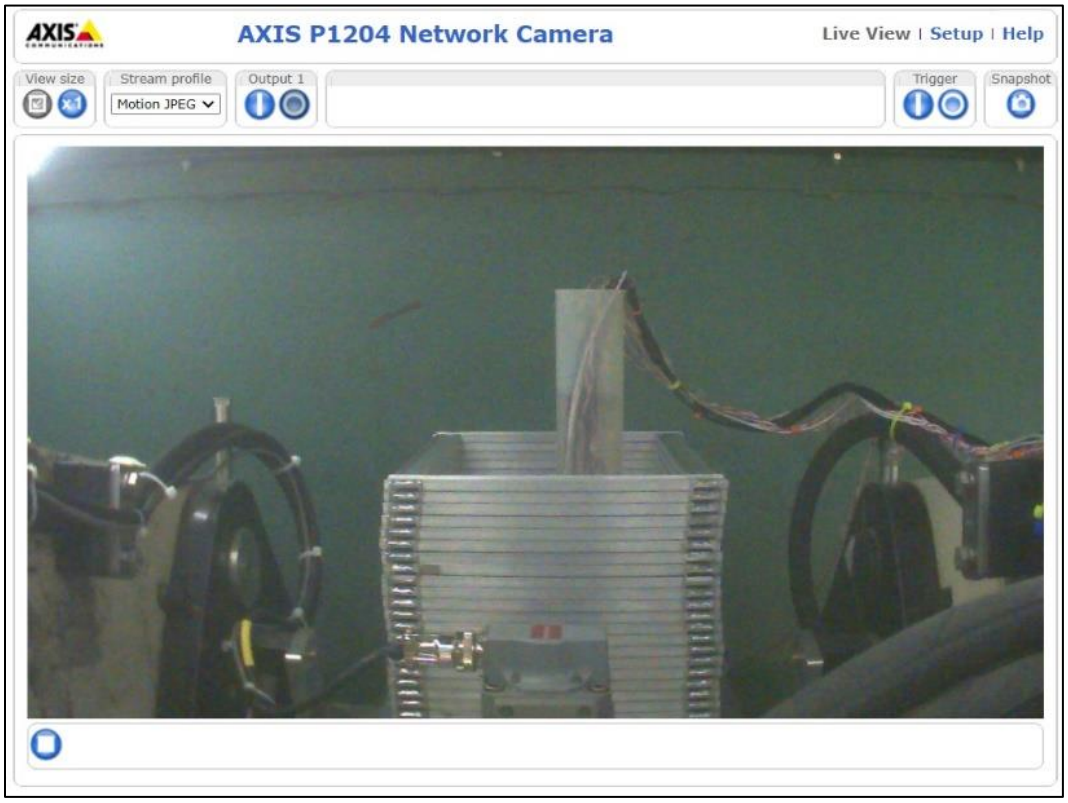

Figure A. 26 Online interface for AXIS cameras.

From the “Setup” option, the user can modify the frames per second and screen resolution of the video recordings, among others, using the “Basic Setup” and “Video” tools, as shown in Figure A. 27. These modifications are automatically applied to the videos from Bluecherry. By clicking the “Action Rules” tool in the “Events” option, the

user can set an action rule, which is a command for the camera to keep recording in a storage device if a predefined event occurs. Figure A. 28 shows the setup for a "Hardware" triggering event, which implies that the camera would keep recording in a microSD card if a hardware problem occurs. Such problem was experienced in the past with the failure of the local wireless system. This feature is ideal for backup purposes.

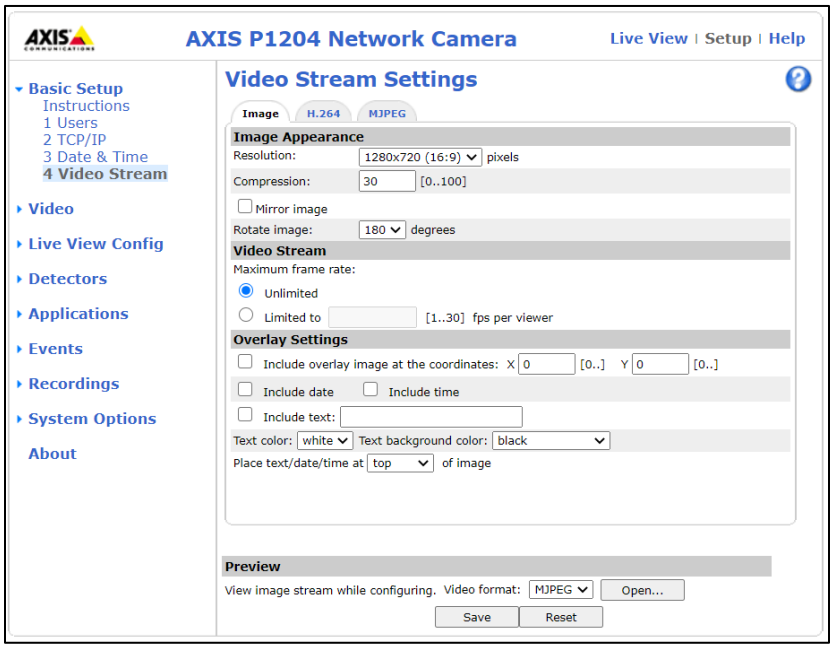

Figure A. 27 "Video Stream Settings" on AXIS cameras.

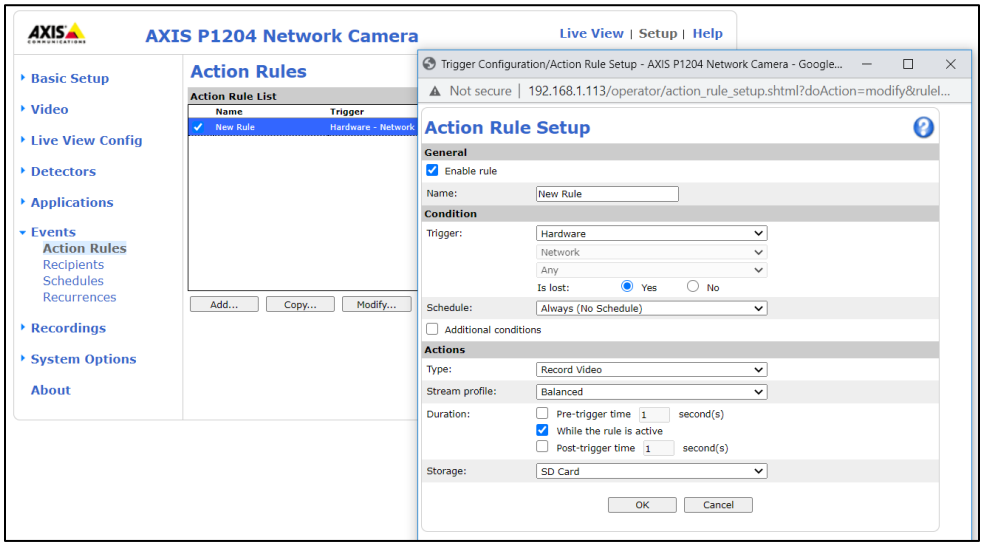

Figure A. 28 "Action Rule Setup" on AXIS cameras.

By clicking the “List” tool in the “Recordings” option, the user can access the recordings available. The “Continuous” tool allows the user to set whether the camera records continuously in addition to a location to save recordings and stream profile, which is the quality of the video expected. It is noted that the videos listed on the “List” tool depend on the status of the “Continuous” option. Figure A. 29 shows the interface for this last option.

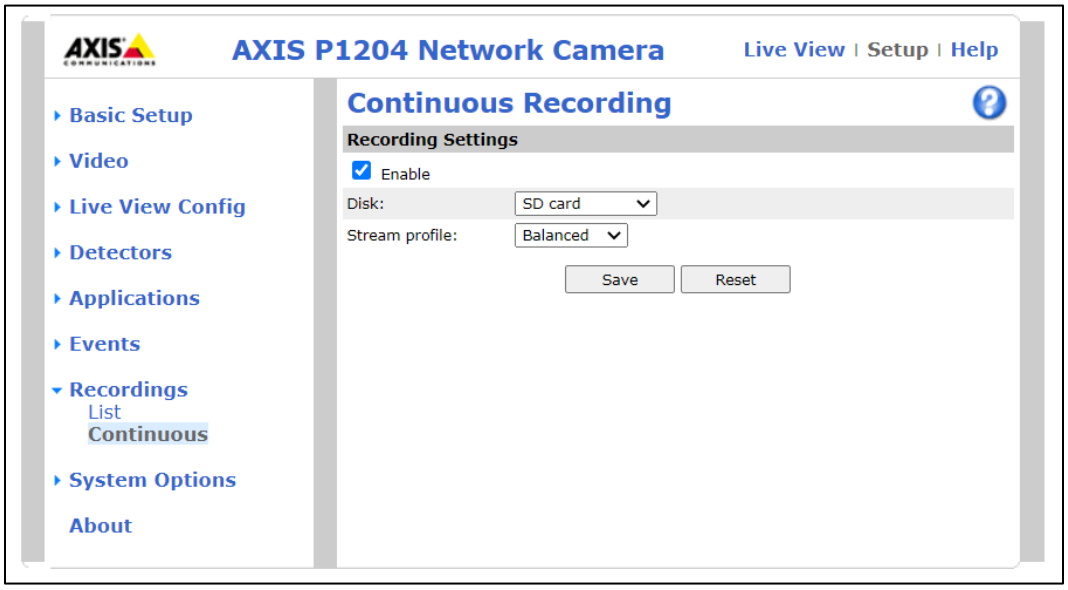

Figure A. 29 “Continous Recording” on AXIS cameras.

The last step in this section is to set a storage device, as shown in Figure A. 30. This is done through the “Storage” tool inside the “System Options” option. If a microSD card was placed in the camera’s main unit, the interface will display its status, total size and used space. Two main options are available by clicking on the SD Card First, the user can format the card to delete any current content and free space by clicking the “Format” button. This is ideal for setting up new experiments. And second, the user can safely

unmount the card by clicking the “Unmount button”. This option should be done at the end of every test to recover the video recordings.

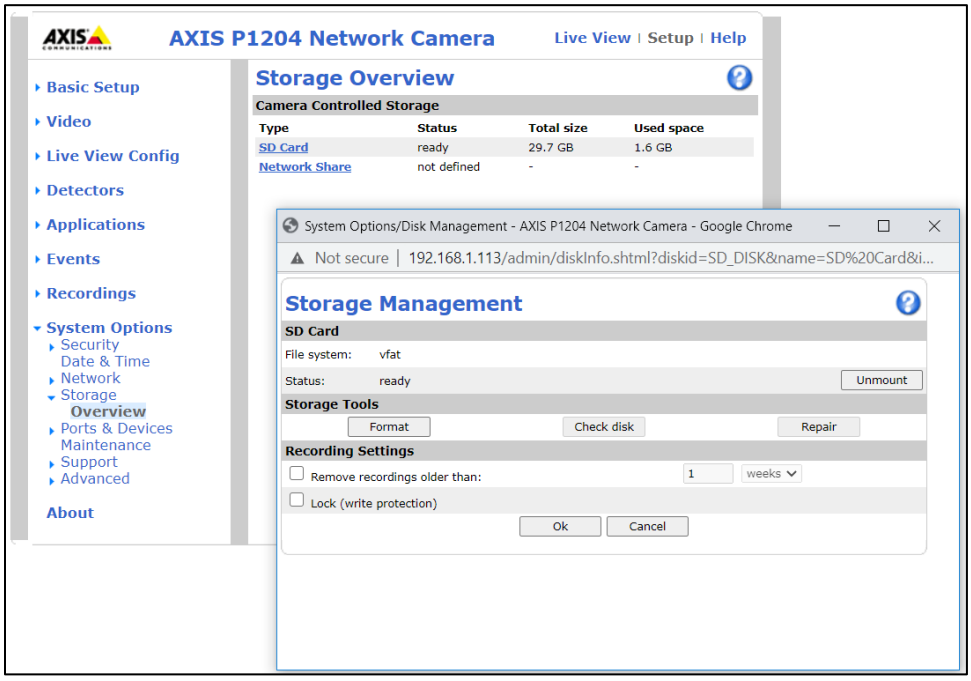

Figure A. 30 “Storage Overview/Management” on AXIS cameras.

On the other hand, and as mentioned previously, Bluecherry is a user-friendly software and allows displaying multiple videos simultaneously, as shown in Figure A. 31. This is ideal to monitor the experiments in real time. As highlighted for the online interface for AXIS cameras, a black screen in Bluecherry is also an indicator that the lens may be disconnected from the main unit. Furthermore, in the particular case of Bluecherry, this may also indicate that the IP address assigned for the camera is not up to date. The user may fix this by accessing the “Configure server” option as shown in Figures A. 32 and A. 33. After using the credentials for Bluecherry, the user may access to the configuration screen of the software as shown next, as shown in Figure A. 34.

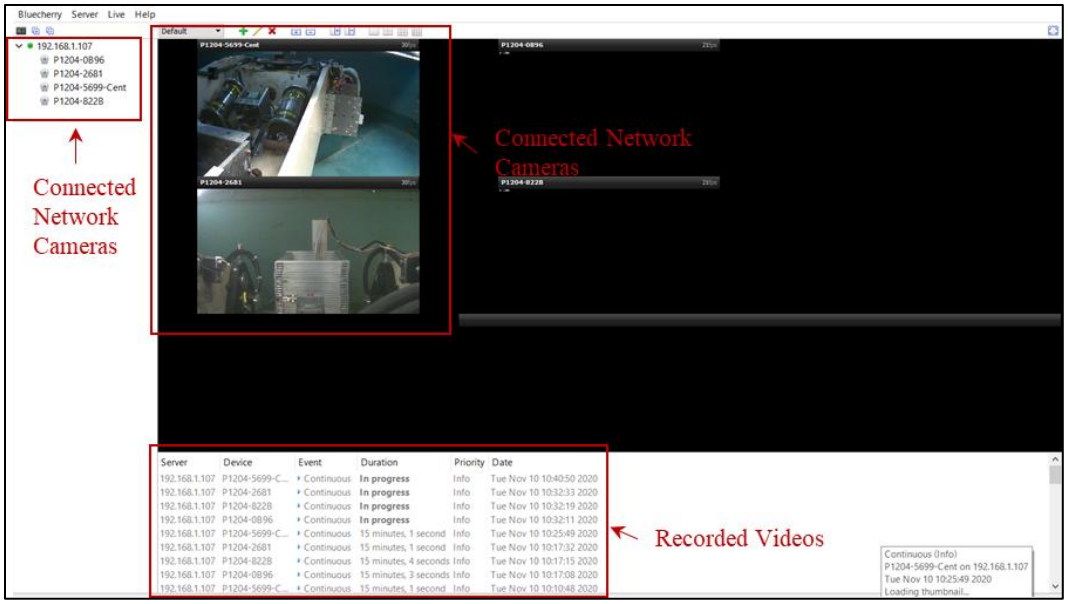

Figure A. 31 Bluecherry main interface.

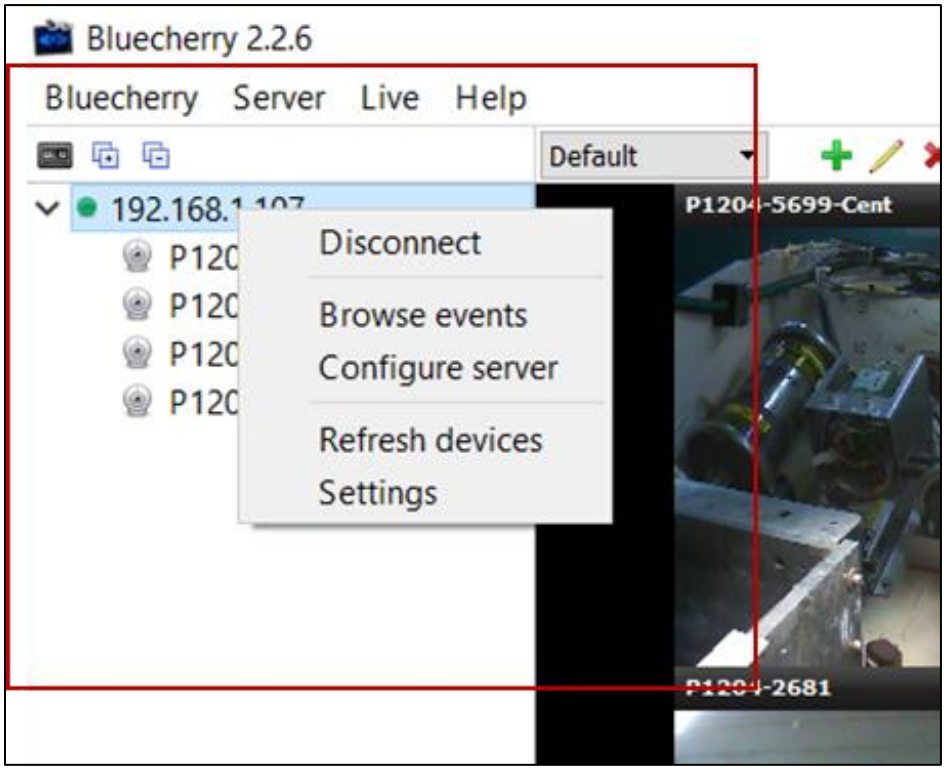

Figure A. 32 Accesing “Configure Server” option in Bluecherry.

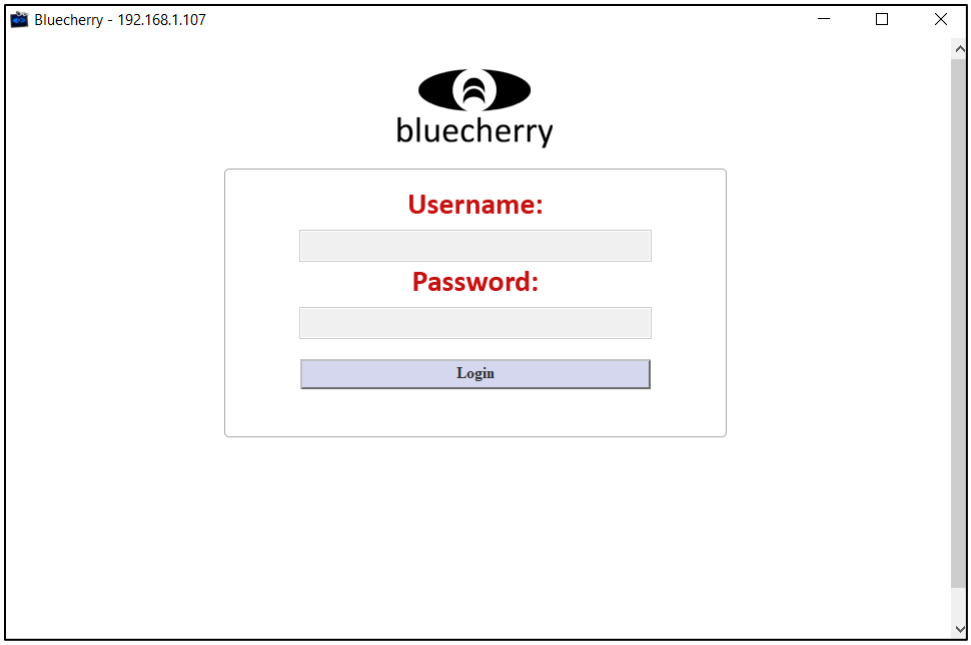

Figure A. 33 “Configure Server” option in Bluecherry.

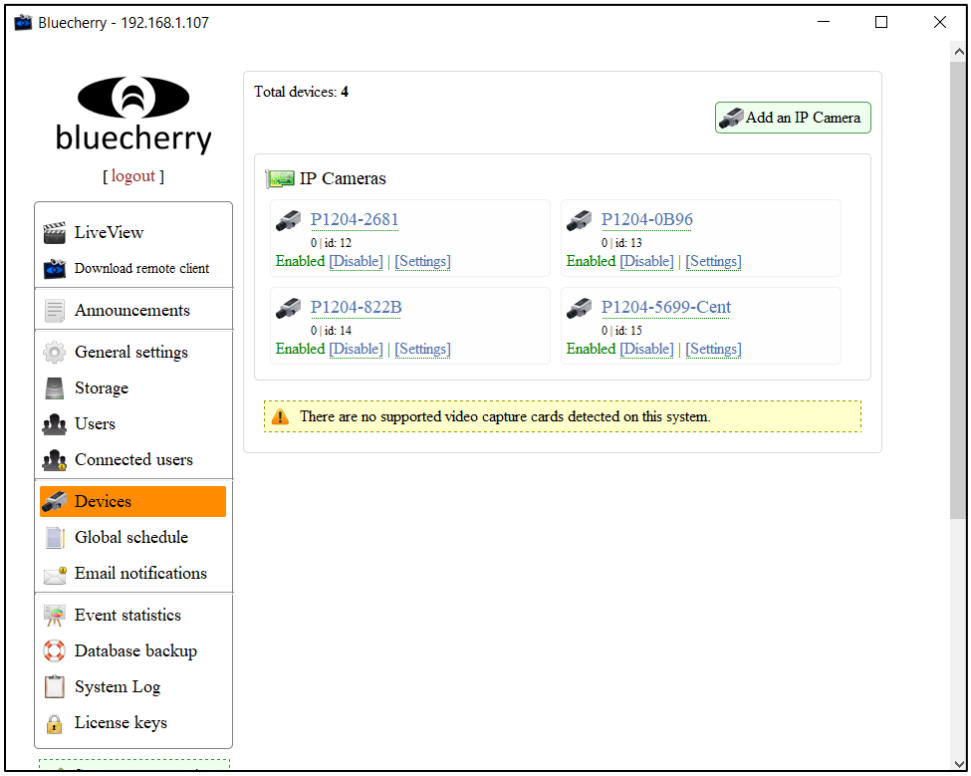

Figure A. 34 “Devices” option in Bluecherry.

The user may add a new network camera by clicking on the top left button, or may configure an existing camera by clicking on the “Settings” option, followed by the “Properties”, as shown in Figure A. 35. After typing the new IP address of the camera on the “Camera IP or Host” line, as shown in Figure A. 36, the user shall save the changes and the camera should be displayed in the main interface.

Figure A. 35 List of IP Cameras displayed in Bluecherry.

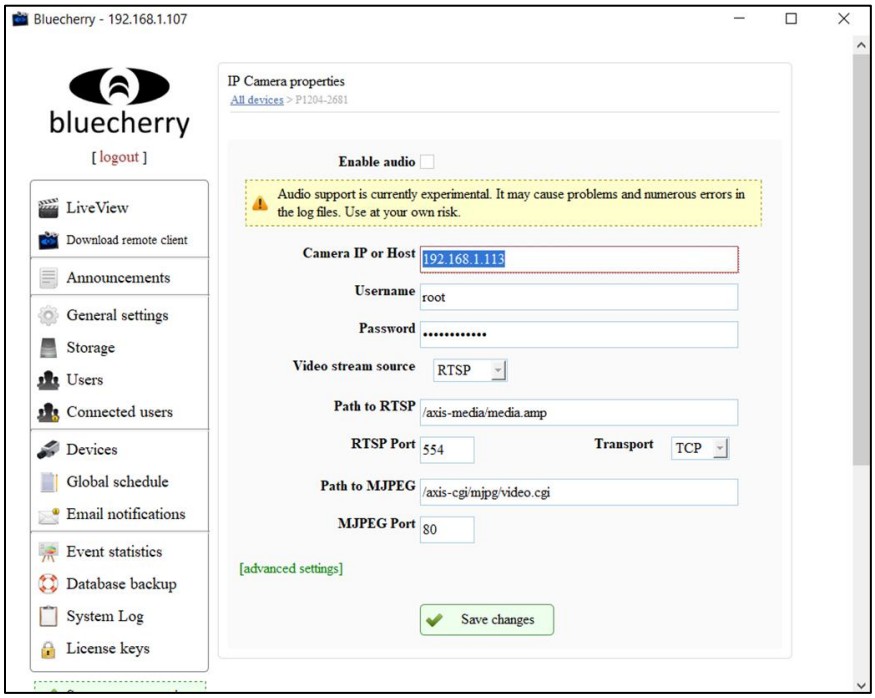

Figure A. 36 “Camera IP or Host” option in Bluecherry.

1.4.4 CENTRIFUGE DAQ SYSTEM – BLOOMY CO.

A LabView based software was designed specifically to provide control of data acquisition and sensors management before and after centrifuge tests. The software was developed by Bloomy Co. with the support of the Geotechnical Research Group of the University of South Carolina. The main interface of the software allows the simultaneous use of several acquisition modules (based on NI instruments only) and connected sensors, as well as to setup different aspects of the experiments. The main interface is shown in Figure A. 37.

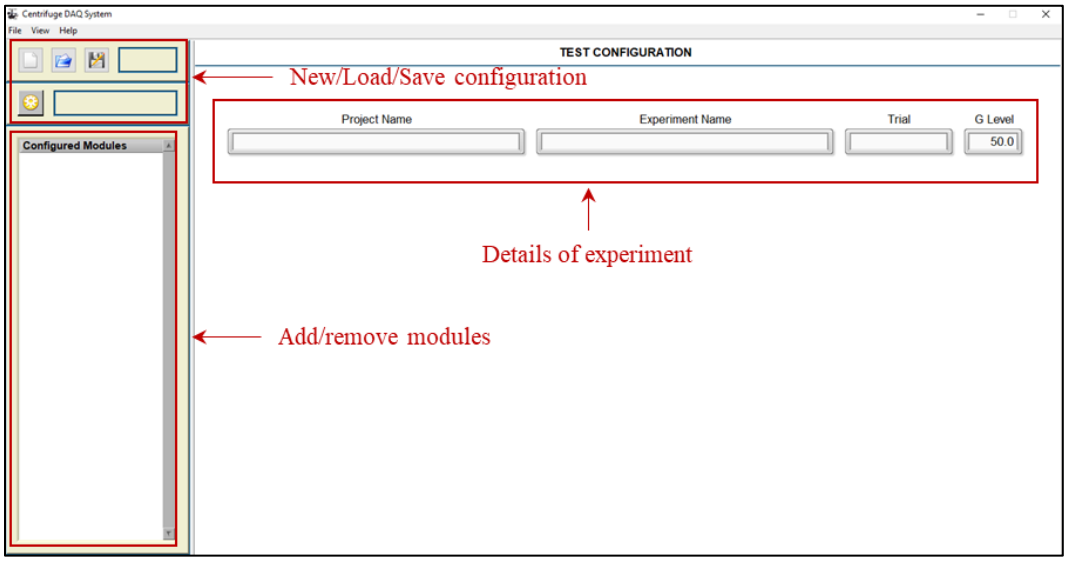

Figure A. 37 Main interface in Centrifuge DAQ System.

The main interface is composed of three panels. The top left panel includes the buttons for adding a new configuration, loading an existing configuration and saving the current configuration. The left panel shows the information of the modules included in each testing configuration and allows adding or removing modules. The central panel displays the information of the experiment. The names assigned in the central panel will be used by the software to create a series of folders and subfolders containing the data

from an experiment. The protocol followed by the software is exemplified in Figure A. 38.

To add or remove modules, the user shall right-click on the left panel and choose the adequate option, as shown in Figure A. 39. For the "Add Module" option, the software displays different alternatives that cover most of the sensing devices available, each one assigned to a specific NI module. It is recommended to explore the different configurations available to choose the best option. It is noted that the software only displays the NI modules that are connected to the network system (i.e., the NI Chassis connected to the FORJ).

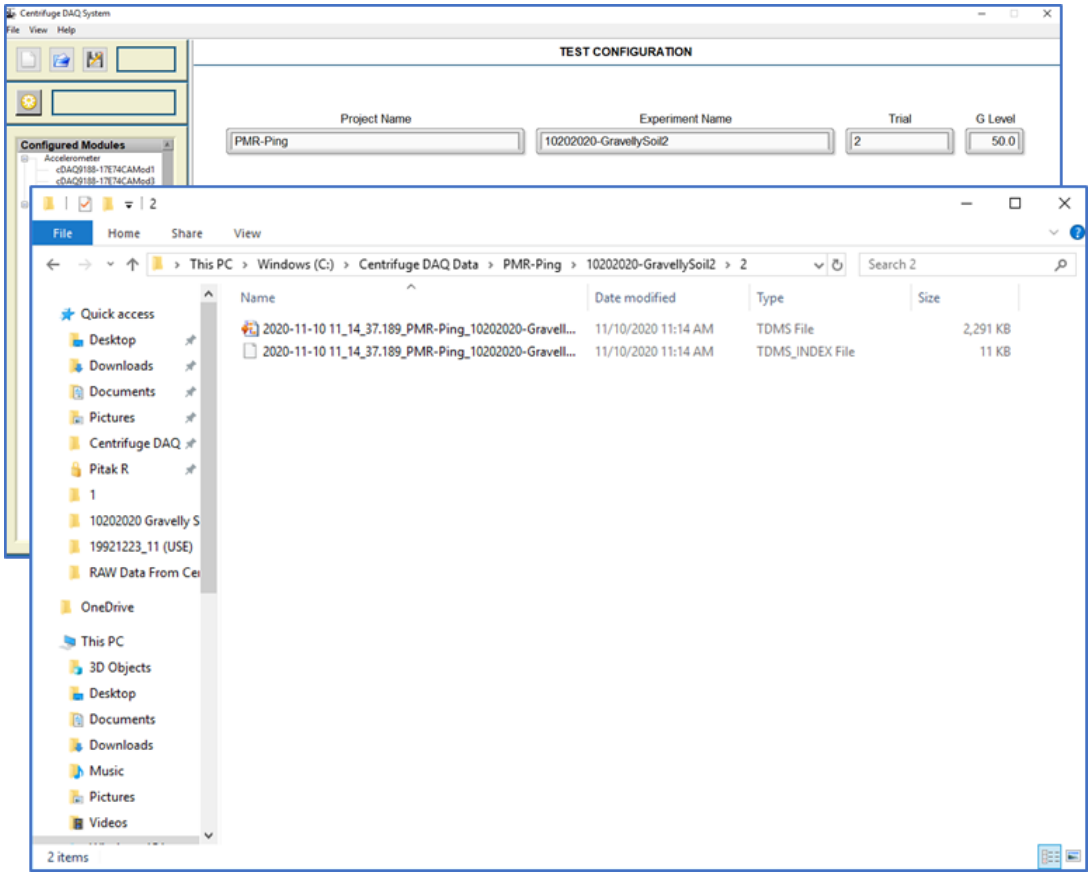

Figure A. 38 Saving protocol in Centrifuge DAQ System.

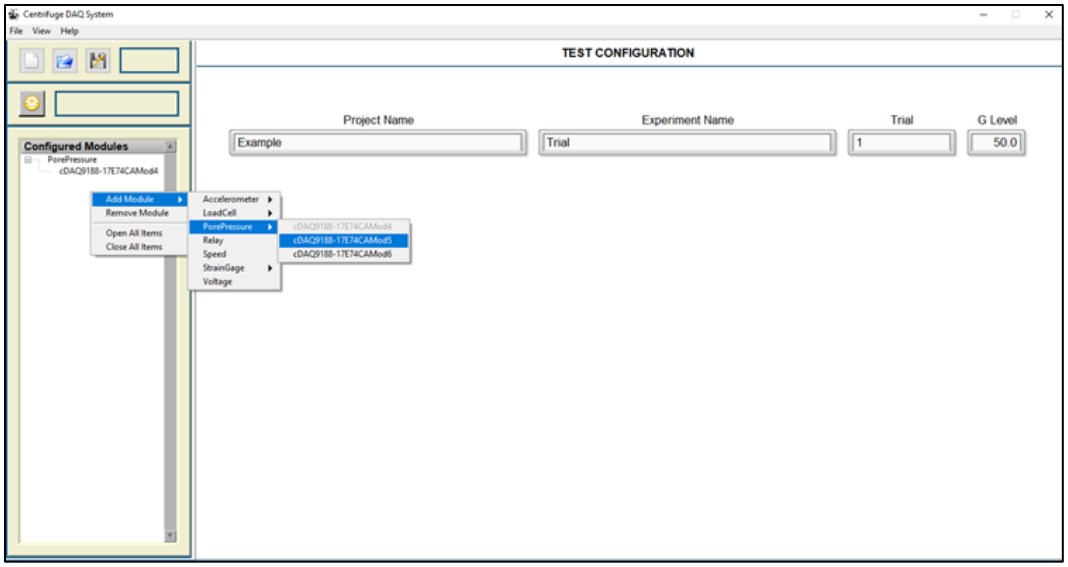

Figure A. 39 Adding a module in Centrifuge DAQ System.

The modules added to the software are displayed and discretized by type within the same panel. The user has access to the configuration panel of each module by clicking on the module wanted. It is noted that each module has a different number of submodules depending on the NI card used. Each submodule is, in turn, connected to an individual sensing device. Figure A. 40 shows an example of the configuration panel displayed for a module connected to accelerometers. The NI card used in this case has four submodules (or channels), and each one has a set of individual inputs defined by the user.

After the configuration of modules is completed, the user shall save the configuration and proceed to the testing interface by clicking on the “Acquire” option within the “View” tab, as shown in Figure A. 41. The central panel of this interface displays the current sensors readings. The left panel displays the submodules configured previously, which can be removed or added to the central panel. The bottom left panel allows the user to set a specific sampling rate for the test by clicking on the “Log Rate”

option. It is noted that the “Sampling Rate” option is for internal use of the software and should not be modified. There are two main buttons in the bottom left corner of the interface. The “Monitor/Stop DAQ” button allows the user to monitor the readings of the sensors without recording. The “Log Data/Stop Log” button allows the user to start and stop recording the readings from the sensors.

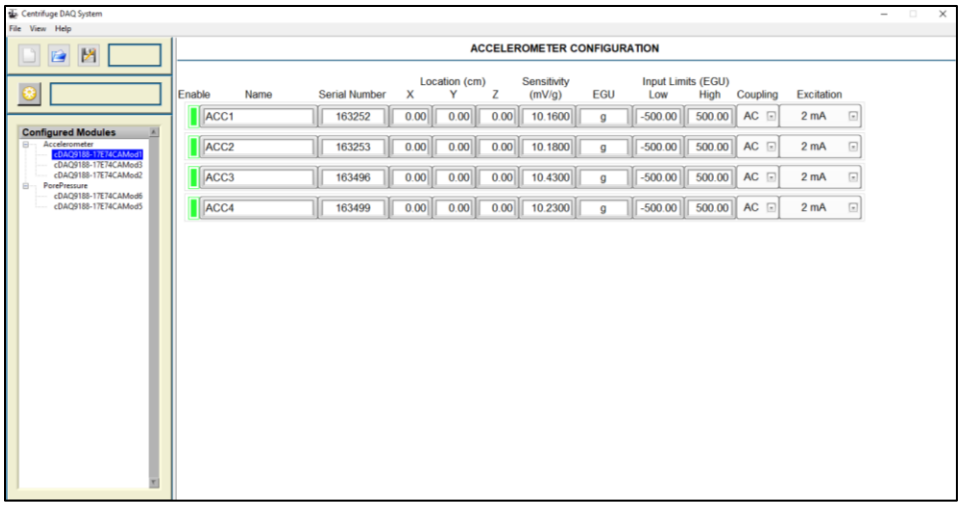

Figure A. 40 Configuration panel for an accelerometer.

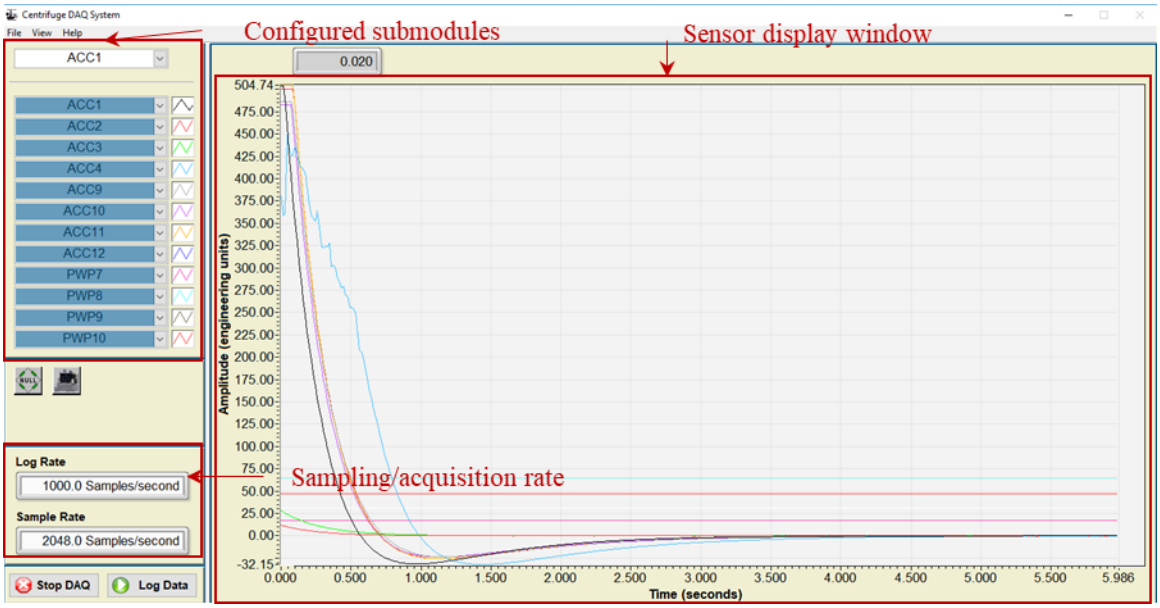

Figure A. 41 Acquire panel in Centrifuge DAQ System.

1.4.5 Centrifuge Speed Controller

The speed of rotation and the centrifuge gravitational acceleration is controlled using the operator interface implemented as a LabVIEW based human machine interface (HMI) with start, stop, ramp, target and experiment metadata inputs. The HMI displays the state of the centrifuge drive and a gravitational level time history. The LabVIEW program communicates with the ABB VFD using Modbus TCP, a standard industrial communication protocol. Modbus communication occurs over a dedicated EtherNET connection between the control computer and an ABB FENA-01 module installed in the ABB VFD. The FENA module facilitates Modbus access to the VFD's control and status words, speed command and feedback, and preselected operational data parameters. The VFD is configured to disallow local control and must be operated from the computer control program.

The interface of the control program is shown in Figure A. 42. In this interface, the user defines the characteristics of the experiment, the rates of increase of rotational speed for spin-up and spin-down in G/min and the targeted G for the experiment. Likewise, the user has access to buttons to start and stop the centrifuge. The interface also displays the current simulated gravitational acceleration in real-time, in addition to other parameters reflecting the performance of the driving motor. During operation, the LabVIEW program issues start and stop commands to the drive and provides speed command for the drive to follow. All speed profile generation is calculated by the LabVIEW control program. Internal ramping functions on the VFD are not used.

A hardwired emergency signal is connected to the ABB drive. This signal is active low, meaning the drive will activate an emergency stop if 24VDC is not applied to

the input. The emergency stop signal is chained through two pushbuttons (one on the drive panel and one remotely located next to the secondary desktop) and one key switch. The key switch is designed for use as a rotation inhibit, preventing unauthorized/accidental rotation of the centrifuge. Activation of the emergency stop during operation initiates a controlled, rapid deceleration of the centrifuge. The centrifuge will stop and remain in a latched emergency stop state until reset. During the emergency stop, kinetic energy from the centrifuge is transferred to the VFD DC bus by the inverter, then dumped to a braking resistor mounted above the centrifuge drive enclosure by a the VFD brake chopper circuit.

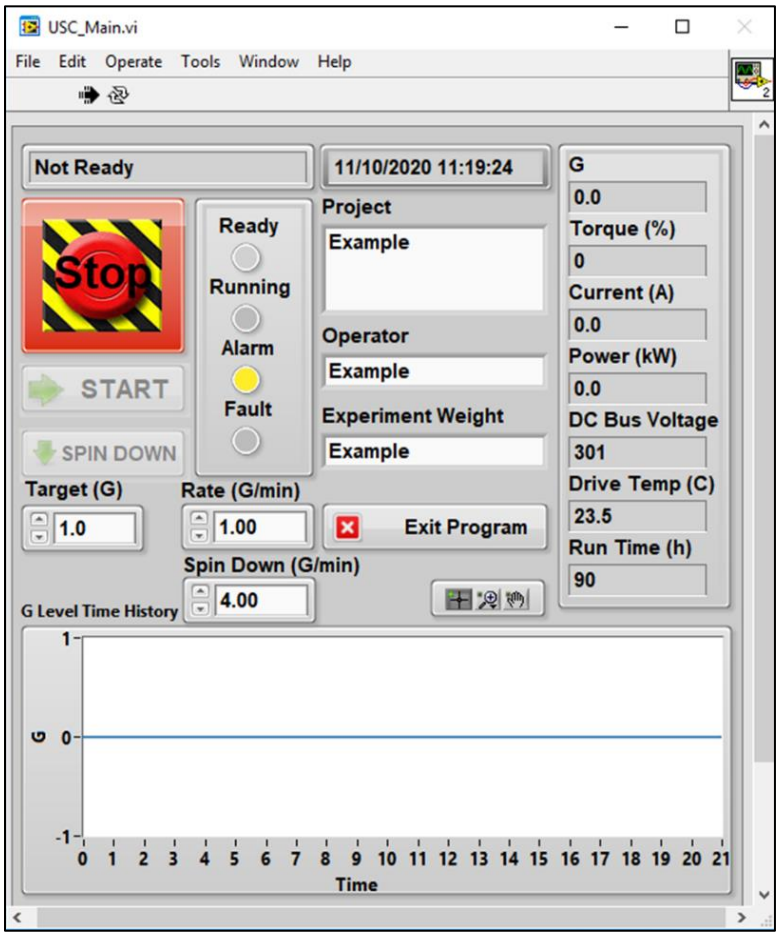

Figure A. 42 Centrifuge speed control software.

A step by step procedure to operating the speed is listed next:

1. Turn on the power from the main breaker (see Figure A. 43).
2. Turn the key on the main disconnect to ON position (rotate clockwise).
3. Release the stop buttons on the main disconnect and the centrifuge room.
4. If the stop button on the interface of the software is orange, click the stop button.
5. On the interface dialog, input the project name, operator and experiment details.
6. On the interface dialog, input the rates for spin-up and spin-down, and then the target gravitational acceleration.
7. Click the “Start” button.

The data will be recorded automatically, and the file will be saved, and it can be accessed anytime at (C:)CentrifugeLog.

Figure A. 43 Main breaker and key switch to power centrifuge drive system.

APPENDIX B

INVENTORY OF SENSING DEVICES

This appendix presents details of the sensors used throughout this investigation. It is noted that information relative to instruments used for data acquisition are described in Appendix A. Table B. 1 shows a summary of the sensors and their specific application in this study.

Table B. 1 Summary of sensors used.

Sensor	Type	Calibration	Experiments
Omega PX409-100G5V	Gauge pressure	Five-point	Centrifuge permeability (Chapter 3) One-dimensional (Chapter 4)
KELLER 2MI PAA81840.1	Absolute pressure	Modified five-point	Three-dimensional (Chapters 5, 6)
Valydine DP15	Differential pressure	Five-point	Centrifuge permeability (Chapter 3) One-dimensional (Chapter 4)
LVDT DC-EC5000	Displacement	Five-point	Centrifuge permeability (Chapter 3)
Baumer UNDK 09u6914/D1	Displacement	Five-point	Centrifuge permeability (Chapter 3)

1.1 PRESSURE SENSORS

These sensors provide a measure of pressure relative to a reference value. Two different brands of sensors were used throughout this study as described in the following sections. The Omega PX409-100 G5V sensor provides a measurement of pressure

relative to the atmospheric pressure, while the Keller 2MI PAA81840.1 sensor provides a measurement of pressure relative to the absolute zero.

1.1.1 OMEGA PX409-100G5V

General details of this sensor are shown in Figure B. 1. An internal embedded membrane containing a strain gage deforms in response to an applied pressure, which generates a readable proportional output voltage. The sensor includes a threaded head with a small orifice used as pressure input port and can be used for measurements of both air and water pressure.

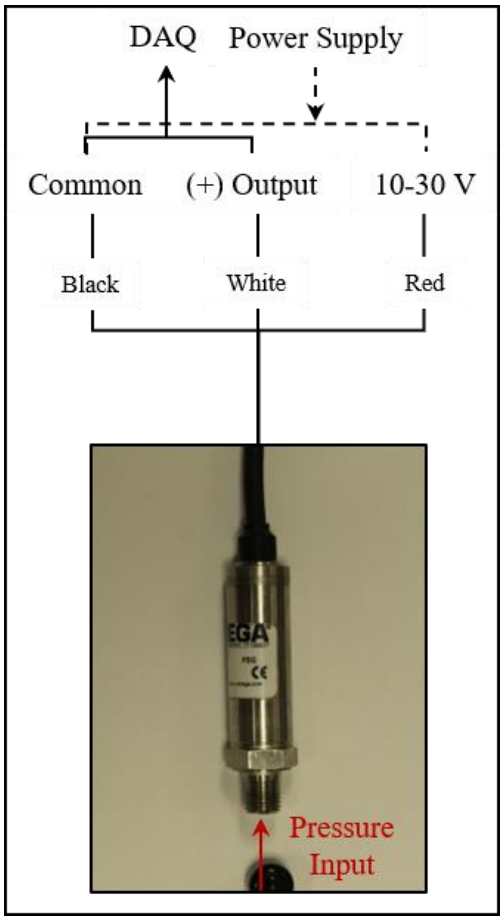

Figure B. 1 Wiring diagram for gauge pressure sensors used in this study.

The sensors used in this study provide an output voltage of 0 to 5V for a pressure range of 0 to 100 psi. As shown in Figure B. 1, a power supply system is required to provide an input voltage from 10 to 30 V, and a data acquisition system is required to record the outputs. A 5-point procedure was used for calibration. This procedure consists in recording the output voltages for pressure inputs of 20, 40, 60, 80 and 100% of the pressure capacity, which were induced using the building air pressure system. The calibration constant that relates the output voltage to the pressure induced was obtained from the slope of the best-fitting line of the calibration results. It is recommended to use the same power supply and data acquisition system during calibration and during test.

1.1.2 KELLER 2MI PAA81840.1

General details of this sensor are shown in Figure B. 2. This miniature sensor contains a high sensitivity piezoresistive chip, which generates a readable voltage proportional output voltage. The sensor includes a ceramic disk encased in a stainless-steel cover with a small orifice used as pressure input port. It is noted that the ceramic disk was removed and replaced with porous filters to increase the response speed of the device during the experiments. This sensor requires a NI-9237 module to perform a full-bridge configuration and allows pressure readings in a range of 0 to 50 psi. Figure B. 2 shows a sketch of the wiring and connections used in this study.

Although a similar procedure than the five-point calibration was used to prepare these sensors for testing, the actual calibration process was different compared to the remaining sensors used throughout this investigation. Such difference is the result of two main limitations. First, the sensors are too small and cannot be pressurized under controlled conditions using the tools available at the time. Second, the value that the

centrifuge software reports as reading or measurement depends on a complex combination of input parameters (i.e., scaling factor, voltage excitation and limit values in engineering units). Such reading should remain within limit voltage values that, for this particular NI module, also depend on the input parameters.

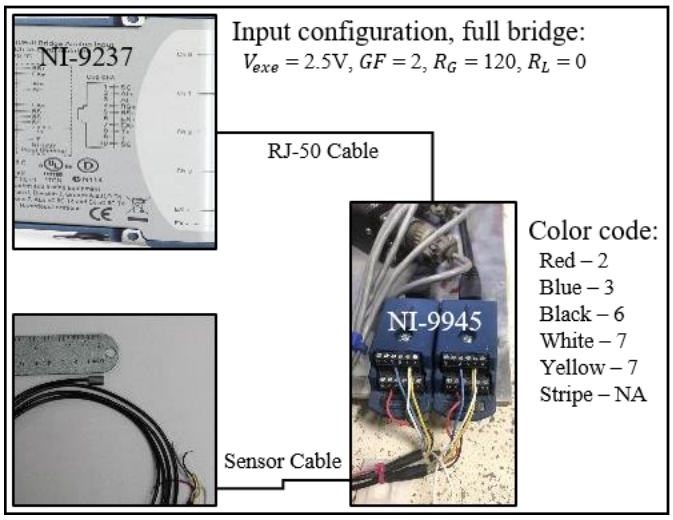

Figure B. 2 Wiring diagram for Keller 2MI sensors coupled to NI instruments.

To mitigate the first limitation, the sensors were calibrated using the centrifuge, as shown in Figure B. 3. As shown, the sensors are fixed to the inner bottom of a conventional permeameter cell, which is placed in the centrifuge basket with enough vertical support to avoid tilting. The elevation of the sensors relative to a fixed location, such as the base of the permeameter cell, is carefully measured. Afterwards, the permeameter is filled with water (known density and viscosity), up to a desired elevation that can be measured with high precision. Hence, the hydrostatic pressure head, h, at the sensor's location is known. The centrifuge is later spun to different gravitational accelerations, N_i, and the output readings achieved for each value of N are recorded.

After the experience, a pressure reading is obtained for each value of hydrostatic pressure induced by the gravity increase.

To mitigate the second limitation, a trial and error process is reproduced, which consists in repeating the procedure described in Figure B. 3 for different scaling factors inputted in the software. The remaining input parameters remain constant. This process is done with the main purpose of determining the range of values of scaling factor that result in no conflict with the limit values of the NI module. This process could also lead to the specific scaling factor that matches the software readings with the actual pressure induced in the sensors. However, it was found for some experiments that the matching scaling factor also caused conflicts. In that case, a different scaling factor should be used during test and an additional correction to the readings should be used for data processing.

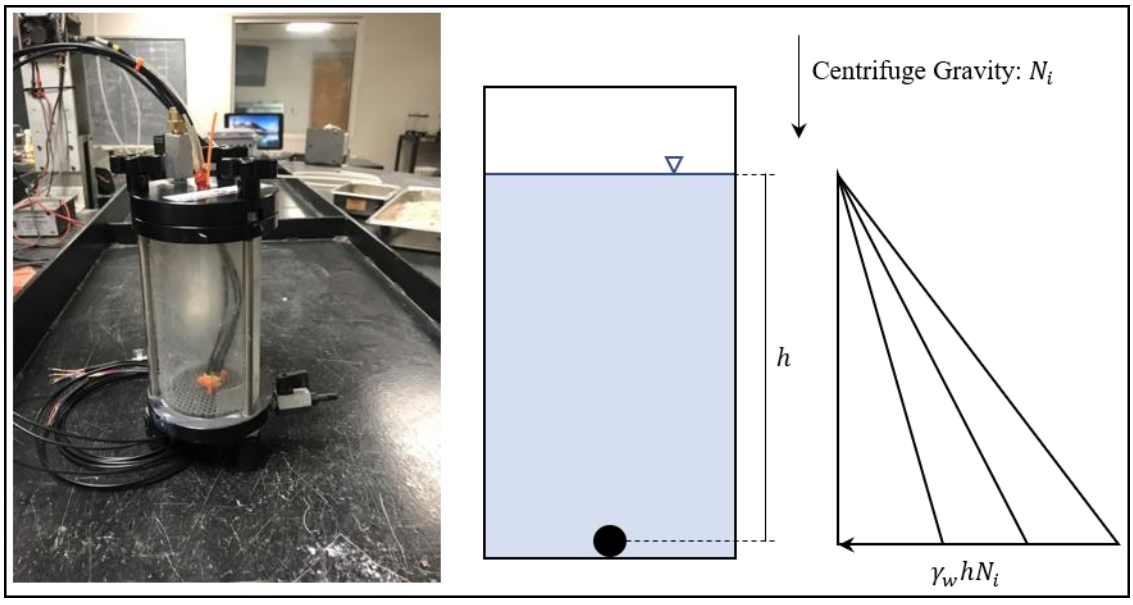

Figure B. 3 Calibration procedure for Keller 2MI sensors.

An example of this process is presented for the Keller 2MI sensor with serial number 6948. The sensor was submerged to a pressure head, h, of 15.3 cm and a series of pressure recordings were obtained at 1g (dry and submerged), 10g and 25g, which resulted in induced hydrostatic pressure values of 0 kPa, 1.5 kPa, 15 kPa and 37.5 kPa, respectively. By the time of this calibration, a tare option was not available in the software, which forced the use of pressure increments to perform the calibration. The pressure increments used were +13.5 kPa, +15 kPa, +22.5 kPa, +36 kPa and +37.5 kPa and were obtained by different combinations of the induced hydrostatic pressure values. Figure B. 4 shows the pressure increment readings obtained with the software as a function of the value inputted as scaling factor for an induced pressure increment of +15 kPa.

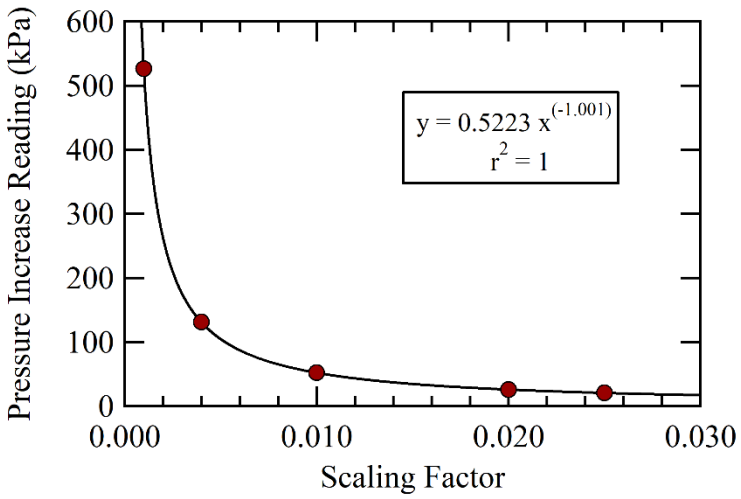

Figure B. 4 Pressure increase readings for different scaling factors under a constant applied increase of +15 kPa using Keller 2MI sensors.

From the best fitting power function displayed in Figure B. 4, the scaling factor that would fit the induced pressure increment is 0.035, for which a conflict with the NI

module occurred. It is noted that the same process for different induced pressure increments should give the same value of matching scaling factor. Otherwise, the sensor may have an internal damage that lead to a nonlinear response. This was verified for this sensor and the same value of scaling factor was obtained.

Since the value of scaling factor that fitted the value of induced pressure increments in this example led to conflicts with the NI module, a different scaling factor of 0.02 was used. Therefore, a correction was required for data processing. Figure B. 5 shows the correction required for readings obtained using this sensor. This figure relates the values of induced pressure increment (i.e., +13.5 kPa, +15 kPa, +22.5 kPa, +36 kPa and +37.5 kPa) with the readings obtained using the scaling factor of 0.02, and the best fitting linear regression shown in the figure is used to correct the readings obtained during test. The accuracy of the corrected pressures was verified by comparing with the increase of hydrostatic pressure occurred between 1g and Ng before each three-dimensional experiment. It is important to note that this calibration is applicable to an increase of pressure relative to a reference value. Therefore, it is important to define the initial pressure conditions before testing.

1.2 DIFFERENTIAL PRESSURE SENSORS

This type of sensor provides a measure of the difference between two acting pressure values. One brand was used throughout this study as described in the following section.

1.2.1 VALYDINE DP15

General details of this sensor are shown in Figure B. 6. An internal embedded flat diaphragm deforms by the action of two pressures acting in opposite directions, which

generates a proportional output voltage of 35 mV/V. The sensor includes two threaded orifices used as pressure input ports and can be used for measurements of both air and water pressure. Due to the small output range and the general characteristics of this sensor, an additional device for is required for signal processing before differential pressure readings are available. Single channel Valydine CD16 demodulators (one per sensor) were used in this study. The complete assembly provides an output voltage of 0 to 5V for a differential pressure range of 0 to 0.8 psi, 5 psi and 8 psi, depending on the sensor.

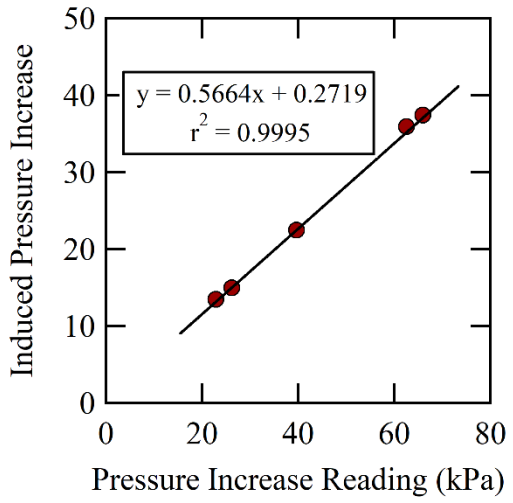

Figure B. 5 Determination of correction factor for pressure readings using Keller 2MI sensors and different scaling factors.

As shown in Figure B. 6, a power supply system is required to provide an input voltage from 28V, and a data acquisition system is required to record the outputs. A 5-point procedure was used for calibration. This procedure consists in recording the output voltages for pressure inputs of 20, 40, 60, 80 and 100% of the pressure capacity. Due to the low capacity range of pressures of the sensors used in this study, the calibration was

done using hydrostatic water pressures instead of the air pressure system of the building. This was done by connecting a conventional permeameter cell filled with water to each pressure port of the sensor, ensuring that the pressure head induced in each port was equal. Afterwards, the permeameter located on the positive port of the sensor was raised to different elevations and recording different values of known differential pressure. As mentioned, the calibration constant that relates the output voltage to the differential pressure induced was obtained from the slope of the best-fitting line of the calibration results. It is recommended to use the same power supply and data acquisition system during calibration and during test.

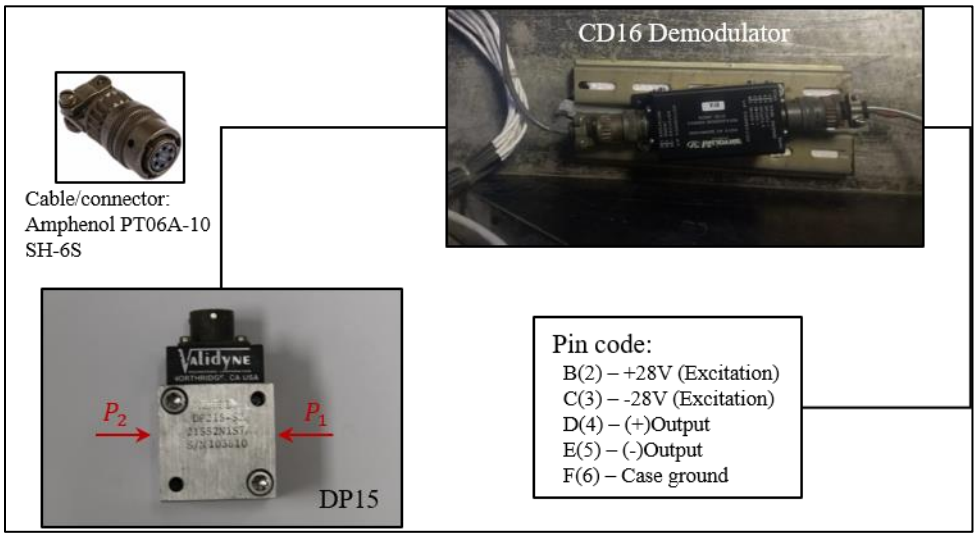

Figure B. 6 Wiring diagram for differential pressure sensors used in this study.

1.3 DISPLACEMENT SENSORS

This type of sensor provides a measure of linear distance relative to a reference initial position. Two different brands of sensors were used in this study as described in the following sections.

1.3.1 MEASUREMENT SPECIALTIES LVDT DC-EC5000

General details of this sensor are shown in Figure B. 7. This device is composed of a hollow rod and a core rod. The core rod can be displaced across the hollow rod, which causes a reaction with an internal embedded coil and generates a readable proportional output voltage depending on the location of the core. The sensor used in this study provides an output voltage of -10V to 10V for maximum linear displacement of 0 to 10 inches, depending on the initial location of the core. As shown in Figure B. 7, a power supply system is required to provide an input voltage of +/- 15 VDC, and a data acquisition system is required to record the outputs. A 5-point procedure was used for calibration. This procedure consists in recording the output voltages for displacements of 20, 40, 60, 80 and 100% of the total capacity. The calibration constant that relates the output voltage to the displacement of the core was obtained from the slope of the best-fitting line of the calibration results. It is recommended to use the same power supply and data acquisition system during calibration and during test.

1.3.2 BAUMER UNDK 09U6914/D1

General details of this sensor are shown in Figure B. 8. This is an ultrasonic distance measuring sensor that generates a readable output voltage as a response to the distance between a target object and an embedded beam columnator. Different from an LVDT, this device does not require to fix the target to the sensor body, but the target is only detected for a distance between 3 and 150 mm. The sensor used in this study provide an output voltage of 0 to 10V.

As shown in Figure B. 8, a power supply system is required to provide an input voltage from 15 to 30 V, and a data acquisition system is required to record the outputs.

This procedure consists in recording the output voltages for displacements of 20, 40, 60, 80 and 100% of the total capacity. The calibration constant that relates the output voltage to the distance between the target object and the sensor was obtained from the slope of the best-fitting line of the calibration results. It is recommended to use the same power supply and data acquisition system during calibration and during test.

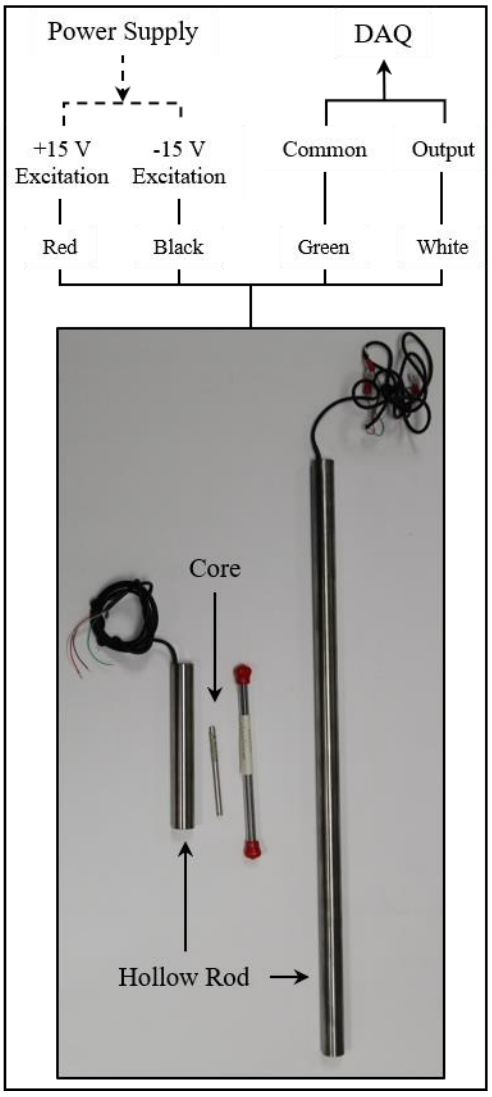

Figure B. 7 Wiring diagram for LVDT sensor used in this study.

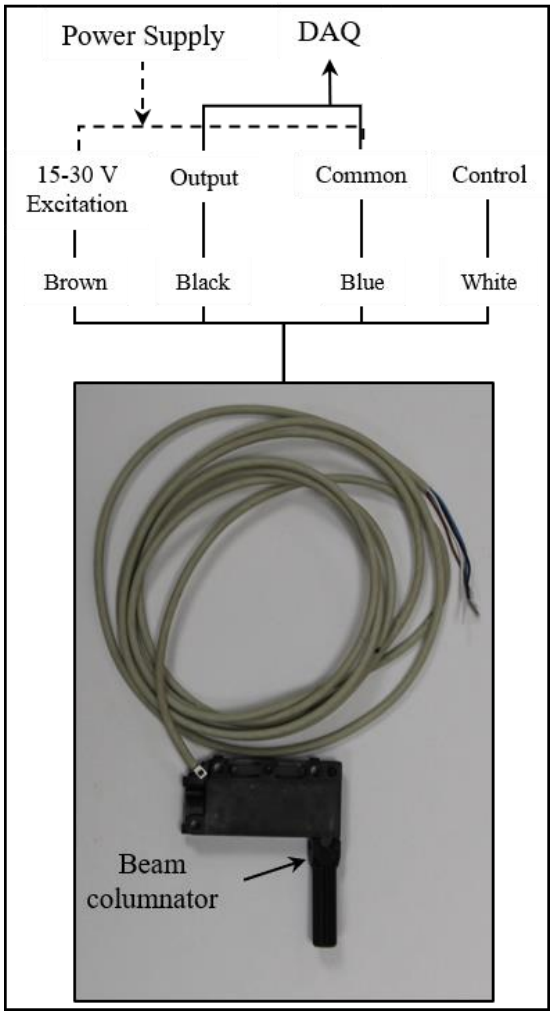

Figure B. 8 Wiring diagram for ultrasonic sensor used in this study.

APPENDIX C

CENTRIFUGE PERMEABILITY EXPERIMENTS

This appendix presents addition details and description of the experimental setup and testing procedure used for the centrifuge permeability tests described in Chapter 3.

1.1 HARDWARE

As shown in Figure 3. 1 and described in Section 3.2, in addition to the centrifuge device, the experimental setup included a customized permeameter, two gauge pressure sensors, three air water cylinders (NFPA Tie Rod Air Cylinders), one laser sensor and one LVDT. Details of the sensing devices are shown in Appendix B.

1.2 SAMPLE PREPARATION

The sample preparation procedure is detailed as follows:

1. The permeameter is assembled without the top lid by tightening the bottom three vertical screws and two of the top screws are placed to maintain the hollow inner portion aligned (see Figure C. 1a). The lateral threaded holes, which are later use to install the pressure sensors, are temporarily sealed to maintain the soil grains inside the permeameter. To minimize the lateral friction between the seeping water and the inner wall, an ultra-thin PTFE tape is placed inside the permeameter (see Figure C. 1b).
2. The oven-dried soil is placed inside the permeameter following the procedure described in Section 3.3 (see Figure C. 1c). A No. 200 stainless steel mesh is placed on top of the compacted sample to avoid migration of soils, together with a plastic

perforated plate, and a layer of glass beads is placed to ensure a homogeneous flow distribution to the sample (see Figures C. 1d and C. 1e). Note that the same filters and glass beads are installed initially on the bottom part of the permeameter and O-rings are used between the permeameter pieces. The top lid is placed and tightened afterwards.

3. The permeameter is placed in a wooden frame that maintains its vertical position during test, and the pressure sensors are installed (Figure C. 1f). It is noted that small pieces of the No. 200 stainless steel mesh are also placed on the head of the sensors to protect them from soil infiltration.
4. The saturation procedure is done as described in Section 3.3. After the sample and the water lines, in and out the centrifuge, are saturated, and additional plastic frame is placed to provide a protection bed to the sensors. This is done as a mitigation strategy to the increase in the self-weight of the sensors, which increases the shear force at the connection with the permeameter (See Figures C. 1g to C. 1i).

1.3 DRIVING SYSTEM

As described in Section 3.2, the permeameter and the three air-water cylinders are connected in a closed loop by a series of hoses passing through the centrifuge rotary joint. The flow is driven using the system of tanks located outside the centrifuge. Figure C. 2 shows photos of this drive system. Note that in the head and atmospheric tanks, the inner chamber located closest to the tip of the pistons is filled with air, while the opposite chamber is filled with water. In contrast, the chamber located closest the tip of the piston is filled with water in the backpressure tank.

Figure C. 1 Procedure of sample preparation in centrifuge permeability experiments.

The tips of the pistons in the head and atmospheric tanks are attached, and these tanks are enclosed in the reaction frame shown in Figure C. 2. Therefore, the displacement of both pistons is equal, while the location of the tanks remains fixed throughout the tests. Such displacement is continuously measured using the LVDT located on top of the atmospheric tank and it is later used to estimate the velocity of flow. The chambers filled with water in the atmospheric and backpressure tanks are connected

to the bottom of the permeameter, while the chamber filled with water in the head tank is connected to the top of the permeameter. In addition, independent pressurized air lines, each one controlled with analogic pressure gauges, are connected to the chambers filled with air in the head and backpressure tanks, while the chamber filled with air in the atmospheric chamber remains open to atmospheric pressure.

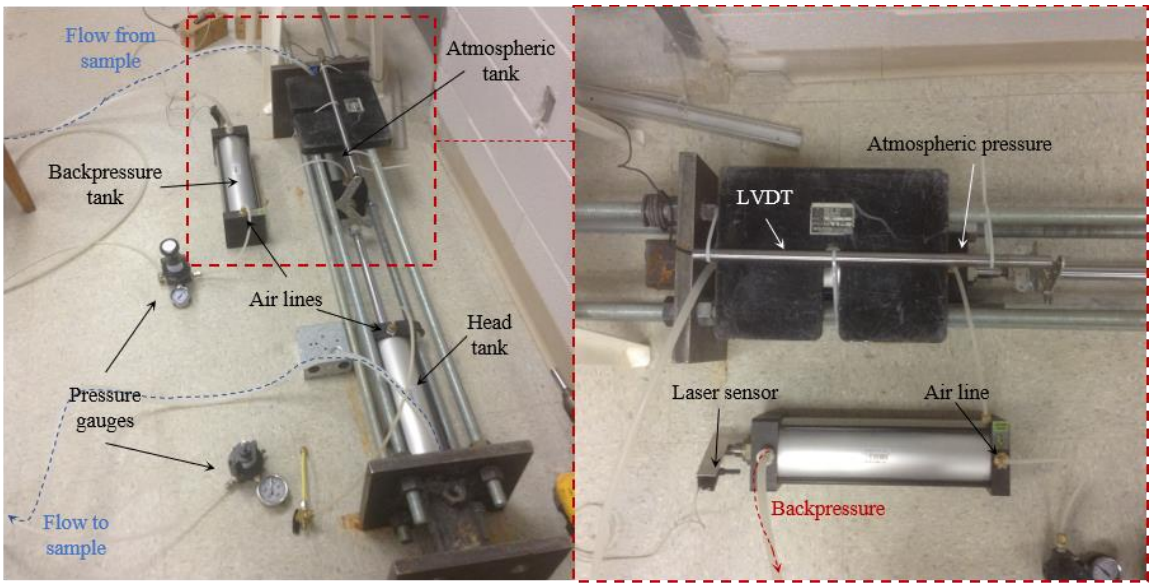

Figure C. 2 Driving system in centrifuge permeability experiments.

The initial state of the drive system, after the saturation of the sample and the hoses used as water lines, is as follows. The water chamber in the head tank is almost filled and the piston rod is outside of the tank. Therefore, the water chamber in the atmospheric tank is partially filled and the piston rod is mostly inside the tank. The water chamber in the backpressure tank is filled and piston rod is inside the tank.

The saturation procedure is finished by gradually increasing the air pressure in the backpressure tank, as described in Section 3.3. The water in the system is pressurized in this step, which reduces any existing volume of air, but flow across the specimen is not

developed. The displacement of the piston in this tank is monitored using the laser sensor located on the tip and the increasing of the backpressure is stopped after no displacement is observed, indicating that the volume of existing air decreased to the maximum possible. Once the system is pressurized, the flow through the sample is induced by continuously increasing the air pressure in the head tank, as described in Section 3.2.

APPENDIX D

ONE-DIMENSIONAL EXPERIMENTS

This appendix presents addition details and description of the experimental setup and testing procedure used for the one-dimensional experiments described in Chapter 4.

1.1 HARDWARE

As shown in Figure 4. 1 and described in Section 4.2, in addition to the centrifuge device, the experimental setup included a customized sample holder composed of a transparent cylinder and set of aluminum pieces, one gauge pressure sensor, five differential pressure sensors, four air-water cylinders and three video cameras. Details of this devices are shown in Appendix B.

1.2 SAMPLE PREPARATION

The sample preparation procedure used is detailed next:

1. The sample holder is assembled without the top lid by tightening the base plate, the manifold, the perforated disk, the transparent cylinder and the top plate using the four lateral rods (see Figure D. 1a). O-rings are used between the different pieces composing the sample holder.
2. A clear silicon coating is placed on the inner wall of the clear cylinder to provide friction with soil. Small pieces of a No. 200 stainless-steel mesh are placed inside the lateral push-to-connect fittings, which are later use to plug the differential pressure sensors, to maintain the soil grains inside the cylinder.

3. A No. 200 stainless-steel mesh is placed on top of the perforated disk to maintain the soil grains inside the cylinder.
4. The oven-dried soil is placed inside the permeameter following the procedure described in Section 4.3 (see Figure D. 1b to D. 1d). It is noted that the silicon coating is nearly 1 cm above the surface of the compacted sand at the end of the sample preparation. This is done to prevent the silicon coating from separating from the cylinder while the soil is compacted.
5. The sample holder is placed in the centrifuge basket. It is noted that the holder was designed to maintain its vertical position during test.
6. As described in Section 4.3, the saturation procedure is done by flushing water in upward direction, from the base of the sample, at a very low hydraulic gradient (i_{sat} < 0.1). This is done by connecting the manifold of the sample holder and a conventional permeameter with a hose. The permeameter continuously fills with water while the permeameter's position is carefully elevated to maintain the flow to the sample.

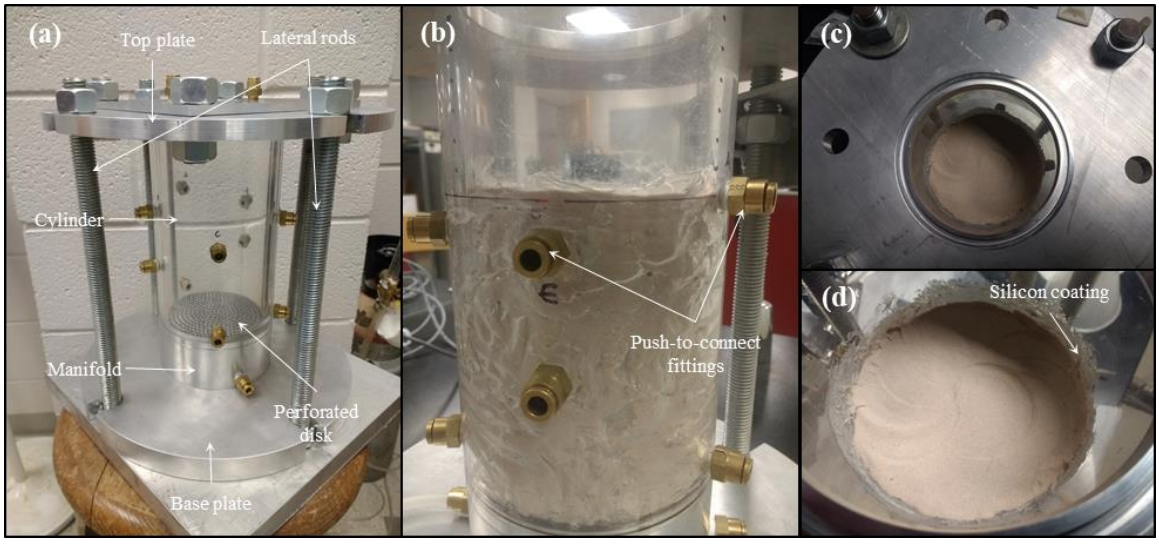

Figure D. 1 Sample preparation for one-dimensional experiments.

7. As the saturation progresses and the water level increases across the sample (see Figures D. 2a and D. 2b), water draining out of the lateral fittings is eventually observed. Once identified, an individual hose is connected to each draining fitting and the open end of the hose is positioned above the sample holder. This process allows to saturate the hose simultaneously with the sample. It is noted that the hoses are long enough to exceed to height of the sample holder to maintain the water inside the hose while the saturation of the sample progresses.
8. The saturation continues until the water level inside the cylinder emerges at the surface of the sample (Figure D. 2a) and the same water level is observed in the hoses plugged to the lateral fittings. Afterwards, the open ends of the hoses are connected to each port in the differential pressure sensors while maintaining the hoses saturated. As a reminder, the pressure loss towards the bottom of the sample is greater than towards the top during upward flow. Therefore, the hoses placed at the bottom should be connected to the positive port of the sensors (see Figure B. 6). It is noted that this process is carefully done to ensure full saturation of the hoses and the sensors, which implies that the overall water level may decrease substantially.
9. After the sensors are installed, the top lid, which includes the top camera (see Figure 4. 2), is attached to the sample holder. The conventional permeameter elevation is increased again to continue the saturation of the entire cylinder (Figure D. 2c).
10. The water lines, in and out the centrifuge, are saturated separately and are connected to the top and bottom of the sample holder. This process is carefully done to avoid upward flow across the sample. At the end of the procedure, the water line connected to the bottom of the sample holder is connected to the drive system, passing through

the rotary joint. The gauge pressure sensor is also connected to the manifold to provide a pressure reading of at the base of the sample. The water line connected to the top is left open to atmospheric pressure outside the centrifuge (see Figure 4. 1). During test, an empty container is placed at the open end of the water line outside the centrifuge to collect the drained water.

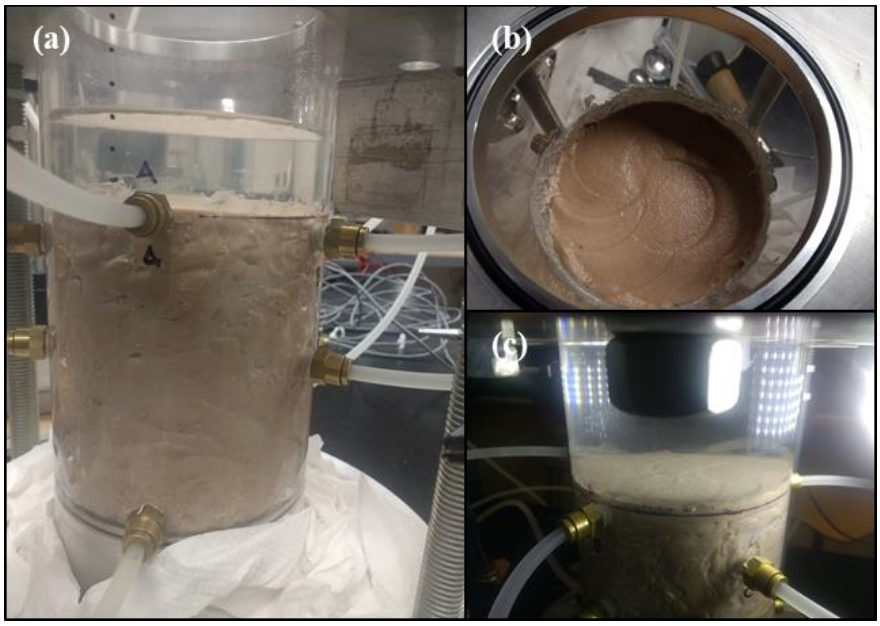

Figure D. 2 Saturation procedure for one-dimensional experiments:
(a) side view, (b) top view, and (c) top view of saturated sample.

1.3 DRIVING SYSTEM

As described in Section 4.2, four air-water cylinders connected in parallel to the manifold in the sample holder, passing through the centrifuge rotary joint, are used to drive the flow and control the progression of the experiments. The inner chamber of the tanks that provided more volume was filled with water, while the opposite chambers were connected to a pressurized-air line. Figure D. 3 shows a photo of the drive system used.

As shown in Figures 4. 2 and D. 3, the four tanks are connected to the same pressurized-air line, which is done using three-way, push-to-connect fittings. Therefore, after increasing the air pressure, all the tanks are pressurized simultaneously. Likewise, the water chambers in the four tanks are connected to each other using three-way hose fittings, and a unique water line is connected to the rotary joint and to the sample. A valve is connected to each water chamber to prevent or allow water flow from each tank.

In the initial state of the drive system, the valves must remain closed. This is particularly important for the centrifuge experience. There is no flow across the sample while the centrifuge is not spinning (i.e., 1g condition) and the valves could remain open. However, once the centrifuge starts spinning, the water in the hoses inside the centrifuge is pressurized by the increase in self-weight, leading to unexpected flow from the water chambers in the tanks, which cannot provide enough friction to prevent the displacement of the pistons.

Once the setup is ready and the centrifuge is spun to the g-level required for the experiment, the air pressure in the tanks is increased. The valve in the first tank is open, allowing water to flow to the sample only from this tank. Once the water inside the first tank is reaching its limit, which is monitored by the stroke of the piston, a transition to the next tank is done. This transition consists in simultaneously closing the valve of the first tank and opening the valve in the next tank. It is highly important to do the transition quickly to reduce the possibility of stopping the flow across the sample. Likewise, it is highly important to close the valve in the first tank because the water from the second tank may start filling the water chamber of the first instead of flowing to the sample. This process is repeated until the end of the experiment.

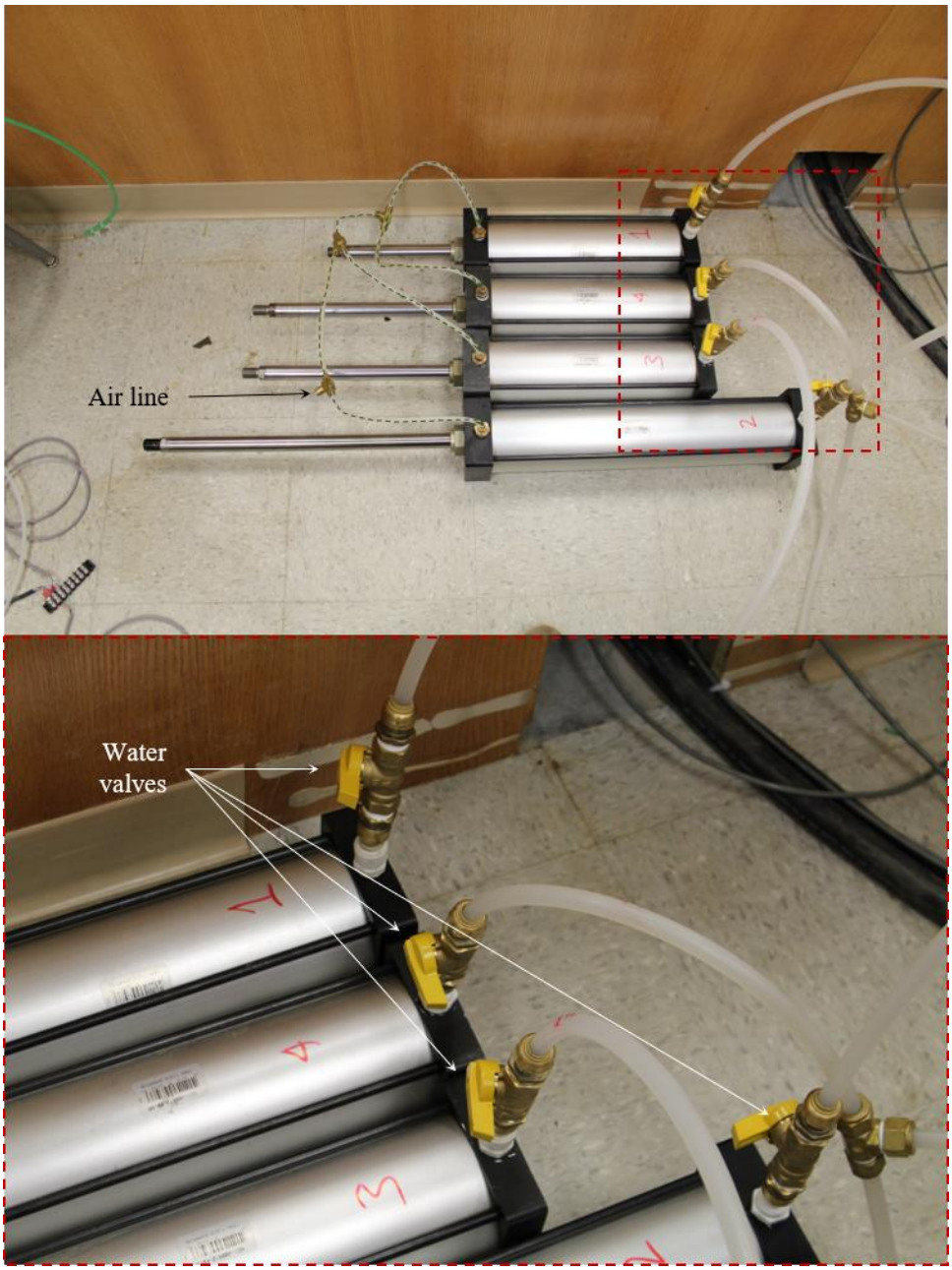

Figure D. 3 Driving system in one-dimensional experiments.

APPENDIX E

THREE-DIMENSIONAL EXPERIMENTS

This appendix presents addition details and description of the experimental setup and testing procedure used for the three-dimensional experiments described in Chapters 5 and 6.

1.1 HARDWARE

As shown in Figures 5. 1, 6. 1 and 6. 2 and as described in Sections 5.2 and 6.2, in addition to the centrifuge device, the experimental setup included a customized aluminum container, two to five differential pressure sensors, seven Keller 2MI pressure sensors and two video cameras. Details of the sensing devices are shown in Appendix B.

1.2 SAMPLE PREPARATION

The procedure used for sample preparation in three dimensional experiments is detailed next:

1. The inner edges of the empty and dry central reservoir are sealed using silicone to prevent leaks. A No. 200 stainless-steel mesh is placed to cover the circular holes perforated in the side walls (Figure E. 1). This is done to prevent grain migration to the upstream and downstream reservoirs. Temporary tape was placed on the upper edge of the mesh covers to help during the compaction of the sample.
2. The foundation soil is prepared following the procedure described in Sections 5.3 and 6.3 (see Figure E. 2a). Four layers of equal mass are compacted using flat steel hammer following the next process. The first layer of dry sand is placed inside the

empty container and spread evenly using a steel straight edge. The surface is flattened, and the sand is tampered across the surface until reaching a density of 1920 kg/m^3. The straight edge is used to verify the flat surface and the next layer of dry sand is carefully placed in the container using a spoon. The process is repeated for each layer carefully providing a final flat surface to the specimen. The tape, if used, is removed.

Figure E. 1 Stainless-steel mesh and lateral perforated holes.

3. The clay used as cover layer in three-dimensional experiments is a typical pottery clay available commercially. The clay slabs are cut as described in Section 5.3 and

are carefully placed above the soil. The overlapped portions between clay slabs and the interfaces between the slabs and the inner walls of the container are sealed by carefully pressing the clay (Figure E. 2b). Afterwards, the uneven resulting portions in the cover are filled with clay and are mixed by hand to provide a homogenous surface (Figure E. 2c).

4. A plastic with dimensions of the central reservoir and an acrylic plate are placed above the clay layer and dead weight is distributed across the surface to provide an adequate contact between the clay and the sand.
5. The downstream reservoir is filled with water to induce flow across the sample and toward the upstream reservoir. It is noted that erosion does not occur in this step due to the overburden applied. The model is covered with a plastic bag to maintain the moisture in the clay layer and is left overnight to allow a homogenous distribution of water across the container. Ideally, the resulting elevation of water in both reservoirs and across the sand at the end of this step should be nearly 4 cm from the base of the container. This partial saturation in clay layer also provides a suction stress on the soil grains near the interface with the clay layer.
6. The dead weight, acrylic plate and plastic cover are removed and the expected locations for sensors and exit-hole are marked on the surface of the clay. Afterwards, small holes are perforated at each location using a thin-walled straw. Small cylinders of clay should be removed at each location to prevent penetrating the sand.
7. At the location of the exit-hole, several small cylinders of clay are removed until matching the expected size of the exit. It is noted that the complete volume clay corresponding to the volume of the exit-hole should not be removed at once because

suction exists at the interface and may remove undesired amounts of sand. A PVC cylinder is inserted at the exit-hole and the outer portion is sealed by pressing the clay (Figure E. 2d). The container should be placed in the centrifuge platform at this moment.

8. The Keller 2MI sensors are inserted in the remaining perforated holes ensuring full contact with the sand.

Figure E. 2 Sample preparation for three-dimensional experiments.

9. Two additional Keller 2MI pressure sensors are attached and fixed to straight edges (or any other heavy flat tool). Each straight edge is submerged in a lateral reservoir

and its elevation is recorded with the best accuracy possible. It is noted that the position of these sensors inside the reservoirs must remain during the tests.

10. The cameras are installed as shown in Figure 6. 1. Likewise, the water inlet hose is attached to the upstream reservoir.
11. The container is covered again with a plastic bag and the saturation continues by slowly increasing the water level in the upstream reservoir, allowing enough time to reach an even elevation across the container. This is repeated until reaching the maximum elevation possible of 10 cm inside the downstream reservoir. Observation of the water level inside the exit-hole helps as check for this process.
12. After the saturation is completed, the model is ready for test.
13. After the test is completed, the sensors are removed, and the clay layer is carefully sliced in blocks and removed. Details of the surface of the sand are observed (Figure E. 3).

Figure E. 3 Post-test observations.

1.3 DRIVING SYSTEM

The flow in three-dimensional experiments is driven by differential water head between the upstream and downstream reservoirs. The upstream head is increased by opening the water inlet, which is connected to the rotary joint and to a water source located outside the centrifuge (conventional faucet). The head in the downstream reservoir remains constant throughout the test as two lateral holes were perforated at an elevation of 10 cm from the base of the sample and are used for drainage. It is noted that the water is allowed to drain to the sides of the centrifuge while spinning. Therefore, the centrifuge is carefully cleaned immediately after the test is completed.